Investigation on the link between microstructures and superconducting properties of MgB_2 bulk samples

Zilin Gao

The Queen's College



A thesis submitted for the degree of

Doctor of Philosophy

at the University of Oxford

Supervised by: Professor S. C. Speller &

Professor C. R. M. Grovenor

Hilary Term 2022

Abstract

The work in this thesis is part of an EPSRC project (reference: EP/P026427/1) that involves designing and building a desktop-sized magnet applied in magnetic drug targeting. Bulk superconductors can be used to substitute conventional ferromagnets because of the higher magnetic field they can generate. High temperature superconducting materials suffer from weak link behaviour of grain boundaries, so a complicated top-seed growth method is required. Among low temperature superconductors, MgB_2 has a reasonably high transition temperature (T_c = 39 K) and can be fabricated in the bulk form by simple and cheap powder processing methods, but the macroscopic J_c values ($J_{c,macro}$) require further improvement to provide a suitable magnetic field for practical applications. Improving intrinsic properties, such as upper critical field and flux pinning strength can increase the capability of superconductors generating high J_c values. To enable macroscopic current circulating the whole sample, density, grain connectivity and anisotropy need to be systematically investigated.

The goal of this thesis is to enhance the superconducting performance of MgB_2 bulk samples and explore how different microstructures influence magnetization and J_c values. Theoretical models are established to simulate the contribution of $J_{c,macro}$ and currents flowing locally ($J_{c,micro}$) to the total ΔM (the difference between the magnetization in the increasing and the decreasing field branches) when samples have anisotropy, inhomogeneity or connectivity problems. Five types of microstructures are

introduced and simulated by the duplex microstructure model as the references for the superconducting analysis in experimental chapters. The ultra-high pressure sintering method was applied to produce MgB_2 bulk samples with nano-scale structure. The sample processed at 900 °C and 5 GPa shows an extraordinary $\Delta M(B_{app})$ performance, achieved 5×10^6 A/m at 4.2 K, 6 T, 30 times and more than 100 times higher than samples prepared at 800 °C and 1100 °C at 5.5/5 GPa. Field-assisted sintering combined with high-energy ball milling is another ex-situ method to prepare MgB_2 bulk samples within a short time (5 min). 5 wt% Mg addition is demonstrated to improve the low- and medium-field ΔM performance. The hBN addition in nanoparticle form is more effective than cBN additions with large sizes. 0.5 wt% hBN+MgB_2 samples with powder milled for 12 h and 1 wt% hBN +MgB_2 samples with powder milled for 6 h have ΔM values around 2.6 times than pure MgB_2 at 20 K, 2 T, which may result from good macroscopic connectivity as well as the increased pinning strength by Mg(N,B) nano impurities. Co-doping 5 wt% Mg and 1 wt% hBN and 6 h of milling have a synergistic effect on the improvement of $\Delta M(B_{app})$ curves. However, the combination of 5wt% Cu and 2wt% cBN is detrimental to the MgB_2 performance. All results in this dissertation stressed the necessity of the wide microstructural characterisation to interpret the superconducting results reliably.

Acknowledgements

Throughout my time at Oxford, I have received many supports from my supervisors, family and friends, to whom I am extremely grateful. This thesis would not be completed without their encouragement and assistance.

Thanks first to my dear supervisors, Prof. Chris Grovenor and Prof. Susie Speller, who are always there when I encounter tough problems throughout my DPhil. Every time I am stuck in the microstructural analysis and the explanation of superconducting data, your guide helps me a lot to clear my mind and to establish the framework linking both parts together. Your instructions as supervisors and kindness as life mentors show me the way to be a researcher with a serious attitude, critical thinking and an ongoing curiosity about the unknown field.

I am grateful to Dr. Amalia Coldea and Kieran McCall at the Clarendon Laboratory who assisted me with PPMS measurements. All conversations with you are inspiring and pleasant. Many thanks to Prof. Patrick Grant for allowing me to do powder processing in Advanced Processing Laboratory. I really appreciate all the support staff in the David Cockayne Centre for Electron Microscopy especially Mr. Graham Wyatt and Mrs. Jennifer Holter who keep SEM in good condition. Thanks also go to the industrial collaborator in Element Six for preparing MgB_2 bulk samples under ultra-high pressure. Also, I would like to thank my assessors, Prof. Angus Wilkinson and Prof. Richard Todd, for assessing my progress and giving useful suggestions on my work.

I would also like to acknowledge my group members for their support and advice. Thanks to Dr. Clara Baker who helps me order items as a lab manager. Special thanks to Dr. Junliang Liu, Dr. Sangeeta Santra, Dr. Timothy Davies and Dr. Guillaume Matthews for teaching me a lot of experimental skills and knowledge on superconductivity. A big thank you to Dr. Sajjad Amirkhanlou and Kailing Huang for providing TEM characterization and graphene nanosheets respectively for their courtesy. To my colleagues, William Iliffe, Stephen Turrell and Marco Siniscalchi, you are always so kind to give me a hand in PPMS and XRD measurements!

I also appreciate Chinese Scholarship Council for supporting my tuition fees and living costs at Oxford. Last but not least, thanks must go to my family. Mom and dad, thanks for comforting me whenever I feel depressed. Your love motivates me to pursue my dreams bravely. Thanks to my best friends, Xuehao and Chaoying, my strongest backup who always keep me company. Even in our nineties, we are still the youngest dreamers. Thanks also to my other good friends, Xiaowen Cao, Haoran Wu, Feng Zhu, etc.

This is not an end. This is a start. All that comes next will be marvelous.

Statement of Originality

The work reported in this thesis was carried out by the author in the Department of Materials at the University of Oxford between October 2018 and Jan 2022, under the supervision of Professor S.C. Speller and Professor C. R. M. Grovenor. No part of this thesis has been previously submitted for a degree at this or any other university. All of the work is original, and the work of others has been freely drawn upon and is duly acknowledged in the text.
Part of the work in this thesis has been presented at conferences and will be published in journals are listed below:

Z.L. Gao, S. Santra, C.R.M. Grovenor, S.C. Speller. *Effect of cubic and hexagonal boron nitride additions on the microstructure and properties of bulk MgB_2 superconductors*, Superconductor Science and Technology (Submitted)

Z.L. Gao, S. Santra, S. Amirkhanlou, E. Eardley, C. Wort, C.R.M. Grovenor, S.C. Speller. *Effect of ultra-high pressure and temperature on the phase evolution, microstructure and superconducting properties of MgB_2*, Superconductor Science and Technology (prepared for submission)

Z.L. Gao, C.R.M. Grovenor, S.C. Speller. *Effect of hBN and Mg additions on the microstructure and superconducting properties of MgB_2 bulk samples fabricated from ball-milled powder using field assisted sintering technology*, Superconductor Science and Technology (prepared for submission)

Z.L. Gao, C.R.M. Grovenor, S.C. Speller. *Reliable analysis of magnetization data from MgB_2 bulk superconductors featured by different microstructures*, Applied physics letters (Under preparation)

15th European Conference on Applied Superconductivity, Moscow, Russia, September 2021, *A systematic study on microstructural evolution and corresponding changes in superconducting performance of ex-situ MgB_2 bulk superconductors doped with cubic and hexagonal BN*, Poster Presentation

The 2020 Applied Superconductivity Conference, Florida, USA, October 2020, *Microstructure, crystallographic texture and superconducting properties of ex-situ MgB_2 bulk superconductors*, Oral presentation

The 14th European Conference on Applied Superconductivity, Glasgow, UK, *Microstructural Characterization of MgB_2 superconductors for operation at 27 K*, September 2019, Poster Presentation

Contents

Abstract ..... **i**
Acknowledgements ..... **iii**
Statement of Originality ..... **v**
Contents ..... **vi**
List of Tables ..... **x**
List of Figures ..... **xii**
Chapter 1 Introduction **1**
1.1 Fundamentals of superconductivity 3
1.2 Critical superconducting parameters 4
1.3 Theories of Superconductivity 6
1.4 Intrinsic factors influencing critical current density 8
1.5 Extrinsic factors influencing critical current density 11
Chapter 2 Literature review **12**
2.1 Electronic structure and two-gap superconductivity 13
2.2 Fabrication of MgB_2 bulk samples 16
2.3 How to improve the superconducting performance of MgB_2? 18
2.3.1 Irradiation 19
2.3.2 High-energy ball milling 20
2.3.3 Chemical doping 23
2.4 Applications of MgB_2 bulk samples in magnetic drug targeting 32
2.5 Summary 34
Chapter 3 Experimental methods and characterisation techniques **36**
3.1 Processing methods 36
3.1.1 High-energy ball milling of powders 36
3.1.2 Field-assisted sintering technology 39
3.1.3 Ultra-high pressure-assisted sintering 41
3.2 Characterisation techniques 41
3.2.1 X-ray diffraction 42
3.2.2 Scanning electron microscopy and energy dispersive X-ray spectroscopy 43
3.2.3 Electron backscatter diffraction 46
3.2.4 Transmission Kikuchi diffraction 48
3.2.5 Physical property measurement system 49
3.3 Sample preparation for characterisation 52
3.3.1 Bulk samples for EBSD 52

3.3.2 Thin foils for TKD 52
Chapter 4 Theoretical analysis of magnetization data 54
4.1 Magnetic measurements and Bean's critical state model 55
4.1.1 Magnetic hysteresis 55
4.1.2 Bean's critical state model 57
4.2 Reliable J_c extraction 59
4.2.1 Cell model for isotropic superconductors 59
4.2.2 Percolation model for anisotropic superconductors 65
4.2.3 Anisotropic superconductors with connectivity problems 76
4.2.4 Duplex microstructure model for practical superconductors 77
4.2.5 Horvat's analysis 80
4.2.6 Practical simulation 83
4.3 Self-field corrections 93
4.3.1 The origin of calculating pinning curves 93
4.3.2 Methods of self-field corrections 94
4.4 Conclusions 99
Chapter 5 Microstructures and superconducting properties of MgB_2 bulk samples processed by ultra-high pressure-assisted sintering 101
5.1 Introduction 101
5.2 Experimental Methods 102
5.3 Effect of processing temperature on microstructure 102
5.3.1 Phase identification and quantitative analysis by Rietveld refinement 103
5.3.2 Microstructural analysis 105
5.3.3 Detection of grain size and grain defects 110
5.4 Effect of ultra-high pressure on microstructures 112
5.5 Effect of time on microstructure 117
5.6 Discussion on microstructural evolution and mechanisms of densification 119
5.7 Effect of temperatures and ultra-high pressure on superconducting properties 123
5.7.1 Critical transition temperatures and transition width 123
5.7.2 ΔM performance 124
5.8 Conclusions 127
Chapter 6 Effect of high-energy ball milling and Mg additions on MgB_2 bulk samples prepared by field-assisted sintering 129
6.1 Introduction 129
6.2 Experimental details 130
6.3 Phase analysis and microstructural characterisation of MgB_2 powders prepared by high-energy ball milling 132

6.4 Effect of milling time on phase evolution and microstructures of MgB_2 bulk samples 137
6.5 Effect of Mg addition on phase evolution and microstructures of MgB_2 bulk samples 142
6.5.1 Effect of ball milling time on bulk samples with added Mg 142
6.5.2 Effect of processing temperatures on Mg-added bulk samples 145
6.6 Analysis of superconducting properties 147
6.7 Analysis of pinning mechanisms 153
6.8 Conclusions 156
Chapter 7 Microstructures and superconducting properties of cubic BN added MgB_2 bulk samples 158
7.1 Introduction 158
7.2 Experimental methods 159
7.3 Characterisation of ball-milled precursor powders 159
7.3.1 Phase identification and quantitative analysis by Rietveld refinement.....160
7.3.2 Characterisation of microstructures and chemical composition 162
7.4 Investigation of cBN addition on phase and microstructural evolution of MgB_2 bulk samples.....165
7.4.1 Characterisation of MgB_2 bulk samples with 0.5 wt% cBN addition.....165
7.4.2 Characterisation of MgB_2 bulk samples with 2 wt% cBN addition 168
7.4.3 Characterisation of MgB_2 bulk samples with 5 wt% cBN addition 175
7.5 The formation and growth mechanisms of $MgNB_9$ impurities 185
7.6 Analysis of superconducting properties 187
7.7 Conclusions 192
Chapter 8 Microstructures and superconducting properties of hexagonal BN added MgB_2 bulk samples 194
8.1 Introduction 194
8.2 Experimental methods 195
8.3 Investigation on phase evolution and morphologies of milled powders 196
8.4 Investigation on phase evolution, morphology and chemical composition of hBN added bulk samples.....198
8.4.1 Characterisation of bulk samples with 0.5 wt% hBN addition 202
8.4.2 Characterisation of bulk samples with 1 wt% hBN addition 205
8.4.3 Characterisation of bulk samples with 2 wt% hBN addition 208
8.5 Investigation of effect of hBN addition on grain sizes and phase transformations 211
8.6 The influence of hBN addition on milled powders and green compacts 213
8.6.1 The influence of hBN addition on milled powders.....214

8.6.2 The influence of hBN addition on green compacts 214
8.7 The influence of hBN addition on MgB_2 bulk samples.....217
8.8 Analysis of superconducting properties.....218
8.9 Conclusions.....222
Chapter 9 Microstructures and superconducting properties of Metal (Mg/Cu) and BN (hBN/cBN) co-doped MgB_2 bulk samples.....224
9.1 Introduction.....224
9.2 Experimental details 225
9.3 On the role of Mg and hBN addition on microstructural evolution of MgB_2 bulk samples 226
9.4 On the role of Cu and cBN additions on the microstructural evolution of MgB_2 bulk samples.....234
9.5 Superconducting properties of Mg and hBN co-doped MgB_2 bulk samples...237
9.6 Superconducting properties of Cu and cBN co-doped MgB_2 bulk samples....239
9.7 Conclusions.....241
Chapter 10 Conclusions and future work.....243
10.1 Conclusions.....243
10.2 Future work 247
References.....249

List of Tables

Table 2.1 Some crystal and superconducting parameters of MgB_2..... 12

Table 2.2 The influence of milling parameters on the milling energy per mass [88] (Copyright © (2013) by IOP Publishing. Used with permission.)..... 21

Table 2.3 The doping effects of RE oxides on the superconducting parameters of MgB_2. HPS refers to high pressure sintering process..... 31

Table 3.1 The precision of MgB_2 crystallite size, strain and lattice parameters calculated by Rietveld refinement (Copyright © 2020 by IOP Publishing. Reproduced from [67] licensed by CC BY 4.0)..... 43

Table 3.2 Analysis of MgB_2 and MgB_4 from 8 measurements at E_0 = 10 keV. Analysis performed with Mg K_α and B K_α. σ refers to standard deviation and σ_{rel} is relative standard deviation. 45

Table 4.1 Lists of phenomenological $J_c(B)$ models..... 58

Table 4.2 Summary of intervals of b_{app} and B_{app}. B_{self} and B_{app} are compared to determine the B_{av} direction. 98

Table 5.1 Processing conditions of MgB_2 samples 102

Table 5.2 The phase content, lattice parameters, crystallite size and strain are obtained by Rietveld refinement. Refinement results from FAST samples from [67] are presented as a comparison. 105

Table 5.3 The phase content, lattice parameters, crystallite size and strain extracted from XRD results by Rietveld refinement. 113

Table 5.4 The critical transition temperature (T_c) and transition width (ΔT) of samples in the temperature and pressure series.....124

Table 6.1 Processing parameters for ball milling and field-assisted sintering.....131

Table 6.2 Phase content, lattice parameters, crystallite size and strain calculated by Rietveld method in powders ball-milled for different times.....133

Table 6.3 Lattice parameters, crystallite size and strain of MgB_2 bulk samples produced by powders after different hours of milling. These results are calculated by the Rietveld method. 139

Table 7.1 The processing conditions applied in the field-assisted sintering.....159

Table 7.2 Quantitative results of MgB_2 lattice parameters, crystallite size and strain of 5 wt% cBN added MgB_2 powders milled for selected times.....161

Table 7.3 Chemical composition results from point analysis by EDX in Figure 7.10. 173

Table 7.4 Chemical composition of different sites in the 5cBN-F30min and 5cBN-24hM samples by point analysis. The sites are labelled in Figure 7.14. 181

Table 8.1 Structural and physical properties of cubic BN and hexagonal BN [224] (Copyright © (2017) by John Wiley & Sons, Inc. Used with permission).....194
Table 8.2 Processing conditions applied in high-energy ball milling and field-assisted sintering process.....195
Table 8.3 The crystallographic parameters and three strongest peaks of MgB_2 and $MgNB_9$ from the standard PDF cards in the ICSD database: MgB_4 PDF 00-015-0299; Mg PDF 01-089-4894; $MgNB_9$ PDF 96-201-2797. The percentages in parentheses refer to the relative peak intensities.....199
Table 8.4 Chemical composition analysis of 0.5hBN-6hM. The corresponding sites are labelled in Figure 8.5b.....204
Table 9.1 Processing conditions applied in the FAST apparatus 226

List of Figures

Figure 1.1 Periodic table of superconducting elements (Reprinted from [2] with permission from IOP Publishing)..... 2

Figure 1.2 The discovery process of superconducting materials in the past 120 years (Reprinted from [8] licensed by CC BY-SA 4.0)..... 3

Figure 1.3 Magnetization as a function of the applied magnetic field for type I and type II superconductors..... 4

Figure 1.4 Magnetic phase diagrams of type I and type II superconductors..... 5

Figure 1.5 Schematic of the critical surface of a low temperature superconductor (MgB_2) and cuprate high temperature superconductors..... 6

Figure 1.6 The variation of magnetic penetration depth (λ) and coherence length (ξ) at the interface between normal regions and superconducting regions for type I and II superconductors..... 8

Figure 1.7 Schematics of vortices in the type II superconductor with the screening currents flowing in the surface layer; the partial magnified view shows a vortex that consists of a normal core surrounded by supercurrents..... 9

Figure 1.8 Pinning diagrams showing different regimes defined by strong pinning and collective pinning scenarios. n_p refers to the density of pins. a_0 is a constant and ξ is coherent length (Reproduced from [25] with permission from American Physical Society)..... 10

Figure 2.1 The crystal structure of MgB_2 with hexagonal Mg and B layers. Each Mg atom is located above the center of the B hexagons (Reproduced from [42] with permission from Elsevier)..... 13

Figure 2.2 (a) Band structures and superconducting energy gaps of MgB_2 on the Fermi surface at 4 K with the colour scale linked with (b) the distribution of energy values of gaps. (c) shows the temperature dependence of two gaps (Reprinted from [41] with permission from Springer Nature)..... 15

Figure 2.3 SEM images of (a)(d) MgB_2 bulk samples without ball milling, (b)(e) with milling energy of 2.1×10^6 MJ/kg and (c)(f) with milling energy of 1.7×10^7 MJ/kg. The gray and black contrast in these images are from MgB_2 and voids (Reprinted from [90] with permission from IOP Publishing)..... 22

Figure 2.4 Milling energy dependence of (a) full width at half maximum (FWHM), (b) unit cell parameters (Reproduced from [90] with permission from IOP Publishing). 22

Figure 2.5 Experimental data and fitting lines showing the correlation between critical current density and average grain sizes of pure samples (red points) and samples doped with nanoparticles (black points) (Reproduced from [92] by permission from IOP Publishing)..... 23

Figure 2.6 (a) shows XRD scans for the pure MgB_2 and B_4C doped MgB_2 samples. (b)

highlights the evolution of (110) and (002) peaks. (c) plots the dependence of lattice parameters on the concentration of C-containing dopants. (d) shows T_c values and estimated carbon substitution (X_i) as a function of C dopants (Reproduced from [102] licensed by CC BY 4.0). 24

Figure 2.7 SEM images of B_4C doped MgB_2 samples produced at (a) 1530 °C, (b) 1600 °C and (c) 1700 °C. (d) and (e) are bright field TEM and HAADF images of the 1530 °C sample; (f) EDX spectra of the three spots marked in (e) (Reproduced figure from [98] with the permission from AIP Publishing). 26

Figure 2.8 (a) and (b) SEM images of $(Mg_{1.1}B_2)_{0.92}Cu_{0.08}$ and pure MgB_2 samples. (c) temperature dependence of resistivity for both samples. (Reproduced figure from [112] with permission from Elsevier). (d) the influence of sintering temperatures on the transport self-field current measured at 30 K (Reproduced figure from [113] with permission from AIP Publishing). 28

Figure 2.9 (a) TEM image of 10 wt% Y_2O_3 doped MgB_2; (b) J_c(B) curves of Y_2O_3 doped MgB_2 at 20 K and 4.2 K (inset). (c) TEM image of 0.5 wt% Dy_2O_3 doped MgB_2 samples. (d) J_c(B) curves of Dy_2O_3 doped MgB_2 at 6 K. Inset: temperature dependence of normalized magnetic moment (Reproduced figures from [123, 124] with permission from AIP Publishing). 30

Figure 2.10 Schematic of the desktop-type MgB_2 superconducting 34

Figure 3.1 Schematic diagrams of ball milling process and particle composites when milling different powder mixtures. 38

Figure 3.2 (a) Schematic diagrams of a FAST apparatus (Reproduced from [150] with permission from John Wiley & Sons, Inc) and the graphite die. (b) shows an example of variation in pressure, actual travel of punches and temperature during field-assisted sintering of 1 wt% hBN doped MgB_2 bulk sample. The inset figure shows a processed MgB_2 (D ≈ 2 cm, h ≈ 3.5 mm) cylinder. 40

Figure 3.3 Schematic of a part of the cylindrical sample prepared by ultra-high pressure-assisted sintering. On the right, an SEM image taken by the previous group member Dr. Sajjad Amirkhanlou shows the different layers at the edge of the sample. 41

Figure 3.4 Schematics of (a) the scattering process to generate Kikuchi patterns and (b) the EBSD setup when characterising bulk samples. 47

Figure 3.5 Schematics of experimental configurations for (a) off-axis TKD and (b) on-axis TKD. 49

Figure 3.6 (a) shows Physical Property Measurement System (PPMS) with the Quantum Design Vibrating Sample Magnetometer (VSM) option (b) is the interior schematic diagram of the standard coilset puck and the touchdown centering operation. (c) shows the configuration of the mounted sample. 50

Figure 3.7 Schematic showing steps of preparation for TEM foils. 53

Figure 4.1 Hysteresis loop measured for a MgB_2 bulk sample at 4.2 K in the axial magnetic field. The right figure sketches the flux density gradient in the surface layer when B_{app} initially increases from 0. The bottom subfigures depict B and corresponding

J_c profiles across the diameter of the sample. 57
Figure 4.2 Sketch of a cell in the cylindrical sample with height H and diameter D. 60
Figure 4.3 Schematic diagram showing a part of fully-dense and homogeneous samples that consists of well-connected superconducting cells. 61
Figure 4.4 Schematic diagram showing a part of fully-dense and homogeneous samples that consists of unconnected superconducting cells. 62
Figure 4.5 Schematic diagram showing a part of fully-dense and homogeneous samples that consists of partially connected superconducting cells. 63
Figure 4.6 Schematic diagram showing a part of fully dense but inhomogeneous samples that consists of partially connected superconducting cells and non-superconducting cells. 65
Figure 4.7 Schematic diagrams of (a) B_{c2} dependence of grain orientation and current paths at (b) low applied fields ($B_{c2}^{||c} \leq B_{app} \leq B_{c2}^{||ab}$) and (c) high applied fields ($B_{app} \geq B_{c2}^{||ab}$) where $J_{c,macro}$ and $J_{c,micro}$ flow on the different length scales. 66
Figure 4.8 Numerically simulated $\Delta M(B_{app})$ curves by the percolation theory with different (a) anisotropy γ, (b) percolation threshold p_c, (c) upper critical field Bc2||ab and (d) ΔM_0 values. 70
Figure 4.9 Illustration of percolation results with different p values in a 400 × 400 site percolation system. The p_c of a 2D system with square units is 0.59 above which the percolation cluster exists. The clusters are coloured by the size of clusters (S), and S_{max} is the maximum cluster size. 71
Figure 4.10 Plots of the fraction of the percolating/local clusters and the maximum local cluster size depending on p values in a 400 × 400 percolation system. The area labelled by star shows the dramatic changes in clusters when p is close to $P_c \approx 0.59$. 72
Figure 4.11 (a) Schematic diagrams of pressure applied in field-assisted sintering process and the spherical coordinate system showing **t** and **g**. (b) plots simulated $\Delta M(B_{app})$ curves with different extent of texture when $B_{app} \perp$ c axis and $B_{app} \parallel$ c axis.. 74
Figure 4.12 Two-dimensional schematic diagrams of situations in Percolation model A and B showing changes in K and K^* values as well as current paths in the presence of impurities/pores with comparable size to MgB_2 grains. 75
Figure 4.13 Theoretical $\Delta M(B_{app})$ curves show the effects of impurities with a comparable size to MgB_2 grains. 76
Figure 4.14 Schematic diagram showing duplex microstructures with the presence of Type A and Type B cells. Black regions in Type A cells represent non-superconducting grains. The grey cells can be Type A or Type B cells. 78
Figure 4.15 (a) $-d\ln(\Delta M)/dB_{app}$ vs. B_{app} curves on a log-log scale of the MgB_2 sample prepared by FAST at 1200 °C. The inset figure is the $\Delta M(B_{app})$ curve. (b) the curve fitting results using a stretched exponential function proposed by Horvat et al [183].81
Figure 4.16 (a) theoretical $\Delta M(B_{app})$ curve generated from the percolation theory and its fitting curve using a stretched exponential function proposed by Horvat et al [183]

with $\alpha=1.2\times10^6$ A/m, $B_1 = 1.1$ T, $n_1 = 1.9$, $\beta = 3.4\times10^4$ A/m, $B_2 = 2.4$ T, $n_2 = 2.9$. (b) the $-d\ln(\Delta M)/dB_{app}$ vs. B_{app} log-log plot of the theoretical curve. 82
Figure 4.17 Schematic diagram of Type I microstructure that consists of Subarray A and Subarray B. The parameters used in the simulation are shown on the right table. 84
Figure 4.18 Theoretical ΔM curves of Type I microstructure as a function of B_{app} when $\alpha = 0$ or $\alpha = 1$ 85
Figure 4.19 Schematic diagram of Type II microstructure that consists of Subarray A and Subarray B. The parameters used in the simulation are shown on the right table. 85
Figure 4.20 Theoretical ΔM curves of Type II microstructure as a function of B_{app} when (a) $f_B = 0.5$ and (b) $f_B = 0.3$ under different interconnectivity conditions. 87
Figure 4.21 Schematic diagram of Type III microstructure that consists of Subarray A and Subarray B. The parameters used in the simulation are shown on the right table. 88
Figure 4.22 ΔM dependence of Type III microstructure on the B_{app}. The curves are simulated by Cell model D with J_c calculated by the percolation theory. 88
Figure 4.23 Schematic diagram of Type IV microstructure that consists of Subarray A and Subarray B. The parameters used in the simulation are shown on the right table. 90
Figure 4.24 $\Delta M(B_{app})$ curves of Type IV microstructure when (a) $f_B = 0.3$ and $A_b = 0.6$, (b) $f_B = 0.3$ and $A_b = 0.3$, (c) $f_B = 0.5$ and $A_b = 0.6$ and (d) $f_B = 0.5$ and $A_b = 0.3$. 91
Figure 4.25 Schematic diagram of Type V microstructure that consists of Subarray A and Subarray B. The parameters used in simulation are shown on the right table. 91
Figure 4.26 $\Delta M(B_{app})$ curves of Type IV microstructure when (a) $f_A = f_B = 0.3$, (b) $f_A = 0.3$ and $f_B = 0.6$, (c) $f_A = 0.6$ and $f_B = 0.3$ and (d) $f_A = f_B = 0.3$ ($\alpha = 1$). 92
Figure 4.27 Sketch of a cylindrical sample in cylindrical polar co-ordinates. The right figure shows D values under various r_a/d and the fitting curve. 96
Figure 4.28 The distribution of normalised axial and radial self-field values ($b_{self,z}$ and $b_{self,r}$) in samples with $r_a/d = 0.57$. 97
Figure 4.29 (a) shows field correction functions C_B for different r_a/d and important b values are labeled in (b). (c) depicts the B_{app} ranges divided by different lines of b. (d) presents the corrected moment and J_c curves 99
Figure 5.1 X-ray diffraction patterns (XRD) of MgB_2 samples processed at 700 °C, 800 °C, 900 °C and 1100 °C. The right figure shows an expanded region around the (002) and (110) peaks of MgB_2. 104
Figure 5.2 Backscattered electron (BSE) micrographs showing (a) different contrasts of MgB_2, MgO and MgB_4 (along with EDX maps of Mg, B and O elements) in the sample processed at 1100 °C and 5 GPa for 15 min and (b) the existence of dense regions, porous matrix of MgB_2 and large MgB_4 phases in sample processed at 800 °C and 5.5 GPa for 15 min. (c) and (d) present high magnification images of dense regions and porous matrix in T800. 106
Figure 5.3 Scanning electron microscope (SEM) micrographs of samples processed at (a, b) 700 °C, (c, d) 800 °C, (e, f) 900 °C and (g, h) 1100 °C captured at 500× and 3000×

magnifications respectively.....109
Figure 5.4 EBSD IPF maps from Z direction (IPFZ) of samples produced at (a) 700 ºC, (b) 800 ºC, (c) 900 ºC and (d) 1100 ºC. The black grain boundaries represent misorientations larger than 15°. (e) and (f) are phase maps of T1100 taken by traditional EBSD and by TKD. (g) shows the grain size distribution. Image (f) was captured by Dr. Sangeeta Santra. 111
Figure 5.5 Transmission electron microscopy (TEM), scanning TEM and High-resolution TEM images of a single MgB_2 grain in (a) T900 and (b) T1100. All images were taken by Dr. Sajjad Amirkhanlou.....112
Figure 5.6 XRD diffraction patterns of P4.5, P5.5, P6.5 and P7.5 processed at 800 ºC for 15 min. The right enlarged figure shows the (002) and (110) peaks of MgB_2.....113
Figure 5.7 SEM images of samples processed under (a) 4.5 GPa, (b) 6.5 GPa, (c) 7.5 GPa at 800 ºC. (d) and (e) show the transition zone and fine-grained matrix in P7.5. (f) shows nanograins situated between large MgB_2 grains in P7.5.....114
Figure 5.8 EBSD IPFZ maps of samples produced at (a) 4.5 GPa and (b) 7.5 GPa for 15 min at 800 ºC. In the phase maps, black grain boundaries represent misorientations larger than 15°, while white lines inside the grains represent boundaries with misorientation angle between 2° to 15°. Local angular misorientation (LAM) maps of smaller areas identified in the IPFZ sections reveal the deformation substructures. (c) shows the grain size distribution histogram from EBSD analysis. The colour key of MgB_2 IPFZ maps is at the bottom-right corner.....116
Figure 5.9 SEM images of (a) t5, (b) t10 and (c) t20. (d-f) are corresponding micrographs in dense MgB_2 regions at high magnification.....118
Figure 5.10 EBSD IPFZ maps of (a) t5, (b) t10 and (c) t20 processed at 800 ºC and 5.5 GPa. The colour key of MgB_2 IPFZ maps is at the right hand. (d) is the gran size distribution histogram.....119
Figure 5.11 Schematic diagram of evolution from green compacts to three types of final microstructures in the MgB_2 bulk samples under different processing parameters...121
Figure 5.12 DC susceptibility curves of bulk samples in the (a) temperature series and (b) pressure series measured under 5 mT. 124
Figure 5.13 (a)(b) $\Delta M(B_{app})$ curves of T700, T800, T900 and T1100 at 4.2 K and 20 K. (c)(d) $\Delta M(B_{app})$ curves of P4.5, P5.5, P6.5 and P7.5 at 4.2 K and 20 K.....126
Figure 6.1 XRD patterns of MgB_2 powders after ball milling for 0 min, 10 min, 30 min, 1 h, 3 h, 6 h, 12 h and 24 h. The right two figures highlight (110) and (002) peaks corresponding to changes in the a and c axes. 132
Figure 6.2 (a) BSE images (500×) and EDX maps of as-received MgB_2 powders. (b) BSE images taken at higher magnification showing the porosity in MgB_2 agglomerates and MgB_4 phases.....134
Figure 6.3 BSE images (500×) of MgB_2 powders after (a) 0 min; (b) 10 min; (c) 1 h; (d) 3 h; (e) 12 h and (f) 24 h of milling. 135

Figure 6.4 BSE images show microstructural evolution of MgB_2 powders after (a) 10 min; (b) 3 h; (c) 6 h and (d) 12 h of milling. (e) and (f) show newly-formed MgB_4 in powders milled for 12 h and 24 h.....136
Figure 6.5 (a) XRD patterns of bulk samples processed by powders milled for various lengths of time and processed at 1200 ºC for 5 min. (b) compares XRD patterns of powders and bulk samples. (c) shows the pressure direction and the comparison of (002) and (110) peaks of powders and bulk samples. 138
Figure 6.6 BSE images showing cross-sections of MgB_2 bulk samples along the direction parallel to the axial pressure. These samples processed at 1200 ºC for 5 min were prepared from precursors after (a)(b) 0 h, (c)(d) 3 h, (e) 12 h and (g) 24 h of milling. (f) and (h) SEM images highlight different matrix structures in samples produced from MgB_2 powder milled for 12 h and 24 h. 140
Figure 6.7 (a) Three-dimensional schematic of pressing direction and sample position in EBSD characterisation. (b) EBSD IPF Y1 maps of bulk samples with powder milled for 0 h, 6 h and 12 h processed at 1200 ºC for 5min. (c) (0001) pole figures of MgB_2 grains in the un-milled and MgB_2-12hM samples. (d) shows the grain size distribution. 141
Figure 6.8 XRD patterns of MgB_2 bulk samples with the addition of 5 wt% Mg. 6 hM and 12 hM mean that MgB_2 powders were milled for 6 and 12 h before being processed at 1200 ºC. The right figure compares the changes in MgB_4 peaks. 143
Figure 6.9 BSE images of (a-c) MgB_2, (e-g) MgB_2 + 5 wt% Mg, (h-j) 6 h ball-milled MgB_2 and (k-m) 6 h ball-milled MgB_2 + 5 wt% Mg samples processed at 1200 ºC.144
Figure 6.10 XRD patterns of Mg-added MgB_2 samples processed at temperatures from 900 ºC to 1200 ºC. The right figure highlights the change in the MgB_4 peaks. 145
Figure 6.11 BSE images of (a)(b) un-milled MgB_2 and (c)(b) MgB_2 + 5 wt% Mg samples with powder milled for 6 h. Since porous areas are easily removed in the sample preparation, the uneven surface contributes to regions with the brightest contrast in (a).....146
Figure 6.12 DC susceptibility curves of (a) MgB_2 samples, (b) Mg added MgB_2 samples made from powder milled for different times, (c) Mg added samples processed at different temperatures. (d) compares susceptibility curves of MgB_2 samples with/without Mg addition. 148
Figure 6.13 SEM micrographs of MgB_2 samples and the corresponding schematics (Chapter 4) to identify the currents flowing on different length scales. 149
Figure 6.14 (a) and (b) show $\Delta M(B_{app})$ curves at 4.2 K and 20 K of pure MgB_2 samples. (c) presents J_c curves calculated by Bean's model. (d) and (e) show ΔM curves at 4.2 K and 20 K of MgB_2 + 5 wt% Mg samples with powder milled for various lengths of time. (f) presents $J_c(B)$ curves calculated by Bean's model. 150
Figure 6.15 (a) and (b) compare $J_c(B)$ curves at 20 K of MgB_2 samples with and without Mg addition. 151
Figure 6.16 DC susceptibility curves of the MgB_2+5 wt% Mg bulk specimens processed

at different temperatures. 152
Figure 6.17 (a) and (b) are $\Delta M(B_{app})$ and $J_c(B_{app})$ curves at 20 K of MgB_2+5 wt% Mg samples processed at different temperatures.....153
Figure 6.18 (a) and (b) show J_c curves at 20 K before and after self-field corrections. (c) and (d) show the comparison of pinning curves calculated from original and corrected J_c curves. 155
Figure 7.1 (a) XRD patterns of 2 wt% and 5 wt% cBN doped MgB_2 ball-milled powders. (b) the changes of MgB_2 lattice parameters, crystallite sizes and strain with the increasing milling time. 161
Figure 7.2 (a) BSE image along with elemental mapping of B and N of as-received cBN powders. (b) SEM images of 5 wt% cBN added MgB_2 precursor powders after 12 h of milling.....162
Figure 7.3 BSE images of (a) as-received powder and 5 wt% cBN doped MgB_2 powder after (b) 10 min, (c) 30 min, (d) 1 h, (e) 3 h, (f) 12 h and (g) 24 h of milling. (h) shows the particle size vs. milling time for the two powder sets. 164
Figure 7.4 XRD patterns of 0.5 wt% cBN added MgB_2 bulk samples with powder milled for selected times and then processed at 1200 °C for 5 min. The lower figure highlights the phase evolution of MgB_4 and MgO after different milling times. 166
Figure 7.5 BSE micrographs of 0.5 wt% cBN added MgB_2 samples with powder milled for (a)(b) 12 h and (c)(d) 24 h and then processed at 1200 °C for 5 min. 167
Figure 7.6 EDX results of 0.5cBN-12hM processed at 1200 °C for 5 min. 168
Figure 7.7 (a) XRD patterns of 2 wt% cBN added MgB_2 samples with powder processed at selected milling times or at different temperatures. (b) and (c) highlight the phase evolution of MgB_4 impurities.....169
Figure 7.8 BSE micrographs of 2 wt% cBN added MgB_2 samples with powder milled for (a) 6 h, (b) 12 h, (c) 24 h before processed at 1200 °C for 5 min and (d) 24 h before processed at 950 °C for 5 min. 170
Figure 7.9 BSE images of 2 wt% cBN added MgB_2 samples with powder milled for (a)(b) 12 h, (c)(d) 24 h and then processed at 1200 °C for 5 min. (e) and (f) are SEM micrographs of the matrix. (g) and (h) shows morphologies of 2 wt% cBN doped MgB_2 samples with powder milled for 24 h and then processed at 950 °C for 5 min. 171
Figure 7.10 Chemical composition analysis of (a-c) 2cBN-12hM (bulk samples) showing the existence of N-containing phases and (d) 2cBN-24hM (thin foils) showing the reaction layers at the cBN/MgB_2 interface. 174
Figure 7.11 (a) XRD patterns of 5 wt% cBN added MgB_2 bulk samples with powder milled for various times and processed at different processing conditions. The processing temperature is 1200 °C unless labelled and the processing time is 5 min unless labelled. (b-d) the phase evolution of MgB_4, $MgNB_9$ and Mg impurities under various processing conditions. 176
Figure 7.12 BSE micrographs of 5 wt% cBN added MgB_2 bulk sample with powder

milled for (a) 6 h and (b) 24 h and then processed at 1200 ºC for 5 min. BSE images of 5 wt% cBN added MgB_2 bulk sample with powder milled for 24 h and then processed at (c) 1200 ºC for 30 min and (d) 1050 ºC for 5 min. 177
Figure 7.13 BSE images of dense regions and the matrix in (a)(b) 5cBN-6hM, (c)(d) 5cBN-24hM, (e)(f) 5cBN-30 min and (g)(h) 5cBN-1050C. 178
Figure 7.14 SEM images and EDX analysis of gaps between MgB_2 grains in dense regions of 5cBN-F30min with powder milled for 24 h and then processed at 1200 ºC for 30 min. 180
Figure 7.15 SEM images and EDX analysis of (a)(c)(e) 5cBN-F30min and (b)(d)(f) 5cBN-24hM. (g) and (h) show the corresponding line scan data. The only difference in the processing conditions of two samples is the sintering time (5 and 30 min). 182
Figure 7.16 SEM image, phase map and IPFZ map taken by typical bulk EBSD. The colour key is the same as Figure 7.17. 183
Figure 7.17 Two TKD image sets of two sites in TEM foils of 5cBN-F30min, showing (a)(b) bright-field, (c)(d) band contrast, (e)(f) phase maps and (g) IPFZ images.....184
Figure 7.18 (a) The phase diagram of the binary Mg-B system under the pressure of 1 atm (Reproduced figure from [217] with permission from AIP Publishing). (b) P-T phase diagram of ternary Mg-B-N system (Reproduced figure from [218] with permission from Elsevier).....186
Figure 7.19 Schematic of the possible reaction between MgB_2 and cBN during high temperature sintering process. 187
Figure 7.20 DC susceptibility under 5 mT as a function of temperature in (a) 0.5 wt% cBN, (b) 2 wt% cBN and (c) 5 wt% cBN added MgB_2 bulk sample series. (d) compares T_c of samples with different cBN percentages. 188
Figure 7.21 SEM micrographs of cBN added MgB_2 and the corresponding schematics (Chapter 4) to identify the currents flowing on different length scales.....189
Figure 7.22 $\Delta M(B_{app})$ curves on the log-log scale of (a) 0.5 wt% cBN, (b) 2 wt% cBN and (c) 5 wt% cBN added MgB_2 sample series processed at 1050/1200 ºC for 5/30 min. (d) $J_c(B_{app})$ curves of MgB_2 samples added different percentages of cBN.....191
Figure 8.1 (a) XRD scans of x wt% hBN+MgB_2 (x = 0.5, 1 and 2) powder milled for 6 and 12 h and 0.5 wt% graphene+MgB_2 powders milled for 12 h. (b) schematic diagram showing the role of hBN/graphene layers on MgB_2 powders during the ball milling process. (c) compares the (002) and (110) peaks of undoped MgB_2 and MgB_2 powders with hBN, graphene and cBN addition.....197
Figure 8.2 BSE images of (a) 0.5 wt% hBN and (b) 2 wt% cBN added MgB_2 powders after 12 h of milling.....198
Figure 8.3 (a) XRD patterns of x wt% hBN + MgB_2 (x = 0.5, 1 and 2) and 0.5graphene-12hM bulk samples with powder milled for 6 or 12 h and processed at 1200 ºC for 5 min. (b-e) show the dominant impurity in different samples. 200
Figure 8.4 BSE micrographs of x wt% hBN added MgB_2 samples (x = 0.5, 1 and 2)

produced from mixtures milled for 6 h and 12 h. 201
Figure 8.5 BSE images of 0.5 wt% hBN added MgB_2 bulk samples produced by powders milled for (a)(b) 6 h and (c)(d) 12 h. (e)(f) 0.5 wt% graphene added MgB_2 samples produced by powders milled for 12 h and processed at 1200 °C for 5 min. 203
Figure 8.6 BSE images and EDX analysis of 0.5hBN-6hM. (a) shows the line scan analysis across MgB_4 and Mg(N,B) impurities. 205
Figure 8.7 SEM images of dense regions and the matrix in 1 wt% hBN doped MgB_2 samples with powder milled for (a, b) 6 h and (c, d)12 h and processed at 1200 °C for 5 min. 206
Figure 8.8 EDX analysis of 1 wt% hBN added MgB_2 samples processed at 1200 °C for 5min. (a, b) show N and B element maps from porous matrix and dense regions and line scans in the 1hBN-6hM sample. (c, d) show equivalent data from Region A and Region B in the 1hBN-12hM sample. 207
Figure 8.9 BSE images of 2 wt% hBN added MgB_2 samples with powder milled for (a)(b) 6 h and (c-f)12 h before processed at 1200 °C for 5 min. 209
Figure 8.10 (a) BSE image and EDX analysis of 2hBN-6hM. (b) SEM image and EDX analysis of porous regions in 2hBN-12hM. 210
Figure 8.11 BSE image and line scan results of 2hBN-12hM. 210
Figure 8.12 EBSD inverse pole figure maps from Y-direction (IPFY) of (a) 0.5hBN-12hM, (b) 1hBN-12hM, (c) 2hBN-12hM and (d) 2hBN-6hM. The black grain boundaries represent misorientations larger than 15°. (e) presents the grain size distribution. 212
Figure 8.13 (a) and (b) show band contrast and phase maps of different regions in 1hBN-6hM thin foils. 213
Figure 8.14 Schematic diagrams comparing role of (a) soft, small hBN nanoparticles and (b) hard, large cBN particles on ball-milled mixture powder and green compacts. (c) and (d) BSE images of 2hBN-12hM and 2cBN-12hM showing the microstructures of processed samples with hBN/cBN addition. 216
Figure 8.15 Schematic diagrams showing the role of hBN nanoparticles on microstructures of MgB_2 bulk samples. The enlarged figure shows that the Mg-N-B liquid phase exists in the sintering process. 218
Figure 8.16 DC susceptibility curves under 5 mT in (a) 0.5 wt% hBN/graphene, (b) 1 wt% hBN and (c) 2 wt% hBN added MgB_2 bulk samples processed at 1200 °C for 5 min. (d) compares the T_c of samples with different percentages of hBN addition. ...219
Figure 8.17 SEM micrographs and the corresponding schematics (Chapter 4) to identify the currents flowing on different length scales. 220
Figure 8.18 $\Delta M(B_{app})$ curves on the log-log scale of (a) 0.5 wt% hBN/graphene, (b) 1 wt% hBN and (c) 2 wt% hBN added MgB_2 sample series. All samples are processed at 1200 °C for 5 min. (d) compares $J_c(B)$ curves of selective MgB_2 samples. 222
Figure 9.1 XRD patterns of hBN and Mg co-doped bulk samples processed from

powder milled for 6 h (or 12 h) and processed at 1200 ºC (or 1100 ºC) for 5 min....227
Figure 9.2 XRD results showing the impurity contents of samples under different processing conditions. 228
Figure 9.3 BSE images showing the morphologies of Mg and hBN co-doped samples. 229
Figure 9.4 SEM images showing microstructures of hBN and Mg co-doped MgB_2 bulk samples at higher magnification.....230
Figure 9.5 SEM image and elemental mapping of (a) 1hBN-6hM-1100C and (b) 2hBN-5Mg-6hM-1200C. (c) shows the line scan data of 2hBN-5Mg-6hM-1200C. 231
Figure 9.6 SEM images and phase maps of 1 wt% hBN + 5 wt% Mg co-doped MgB_2 bulk samples processed at (a)(b)1100 ºC and (c)(d)1200 ºC. (e) highlights impurities situated between MgB_2 grains in dense regions. (f-h) shows SEM, band contrast and IPFZ images of 2hBN-5Mh-6hM-1200C. 233
Figure 9.7 (a) XRD patterns of cBN and Cu co-doped powder milled for 12 h and bulk samples processed at different temperatures for 5/15 min. (b) binary phase diagram for Cu-Mg the system (Reproduced from [239] with permission from Springer nature). 235
Figure 9.8 BSE images showing the microstructures of cBN and Cu co-doped MgB_2 bulk samples processed at (a-c) 1000 ºC and (d-f) 1100 ºC. 236
Figure 9.9 BSE image and EDX results from 2cBN-5Cu-12hM-1100C with line scan data and element maps.....237
Figure 9.10 DC susceptibility under 5 mT as a function of temperature in hBN and Mg co-doped MgB_2 samples processed at 1100 ºC or 1200 ºC for 5 min. 238
Figure 9.11 $\Delta M(B_{app})$ curves of MgB_2 samples with Mg and hBN additions processed at 1200 ºC for 5 min on (a) a log-log scale and (b) a linear scale. 239
Figure 9.12 DC susceptibility curves under 5 mT in Cu and MgB_2 co-doped MgB_2 samples processed at different processing conditions. 240
Figure 9.13 $\Delta M(B_{app})$ curves of MgB_2 samples with Cu and cBN additions processed at 1200 ºC for 5 min on (a) a log-log scale and (b) a linear scale. 241
Figure 10.1 $J_c(B_{app})$ curves measured at 20 K and calculated by Bean's critical model of (a) MgB_2 samples processed under ultra-high pressure sintering, (b) 5wt% Mg+MgB_2 and unmodified samples prepared from milled powders, (c) 5 wt% cBN+MgB_2 samples processed under different conditions and (d) MgB_2 samples with 1 or 2 wt% hBN addition. 244

Chapter 1 Introduction

The liquefaction of helium (He) made it possible to easily cool materials to temperatures down to 4.2 K. In 1911, Onnes discovered that the resistance of mercury was unmeasurable at the boiling point of helium [1]. In their study, the resistance jumped to zero suddenly at what was later defined as the critical transition temperature (T_c), and the mercury itself entered a 'superconducting state'. The discovery of superconductors aroused great interest in finding if other metals or alloys could also exhibit superconducting properties at low temperatures. The periodic table of superconducting elements in Figure 1.1 shows that many elements can achieve superconductivity, though some require application of high pressure or fabrication in thin film form [2]. Until 1986, the highest T_c reported among metals and alloys was Nb_3Ge with 23.3 K [3].

High temperature superconductors (HTS) were first discovered in 1986 when scientists in Zurich IBM found superconductivity in an oxide ceramic $La_{2-x}Ba_xCuO_4$ at 35 K [4]. This led to an explosion of interest in copper oxide materials, resulting in T_c values exceeding the boiling point of liquid nitrogen (about 77 K) in 1987 with Y-Ba-Cu-O systems superconducting over 90 K [5]. After this, the T_c record kept increasing incrementally till 1994 when Zhu et al reported that $Hg_2Ba_2Ca_2Cu_3O_{10}$ could enter superconducting state at temperatures as high as 164 K [6]. With these higher T_c values, HTS materials are expected to reduce cooling costs and enable a wider range of

commercial applications. About twenty years later, another superconducting family, the iron-based superconductors [7], set off a new upsurge of HTS research (the orange line in Figure 1.2) [8].

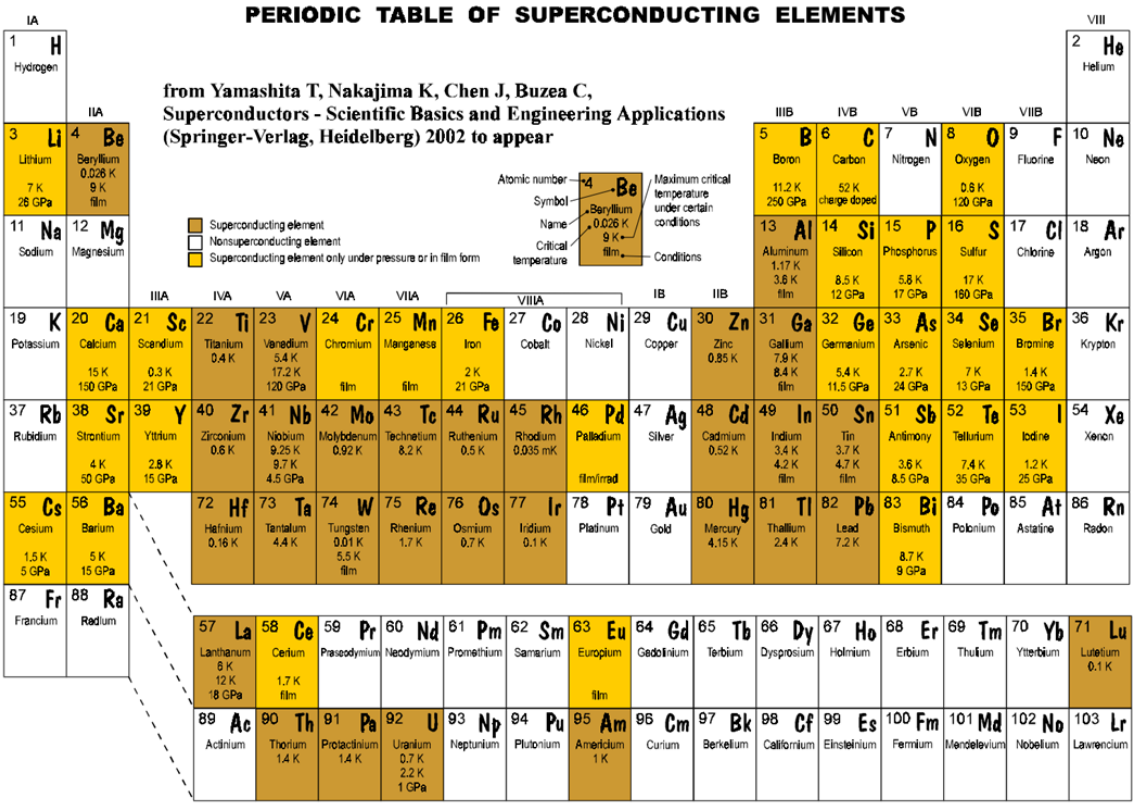


Figure 1.1 Periodic table of superconducting elements (Reprinted from [2] with permission from IOP Publishing).

With the boom of research on HTS, light element superconductors were not so widely studied. It was not until 2001 that superconductivity in magnesium diboride (MgB_2) was reported, with T_c of 39 K, the highest possible T_c for conventional superconductors defined by McMillan [9]. Even though MgB_2 behaves like a conventional metallic superconductor, its unique two-band structure makes T_c much higher than in metallic materials like NbTi alloys and the Nb_3Sn compound, and nearly the maximum theoretical T_c predicted by the Bardeen-Cooper-Schrieffer (BCS) theory. Additionally,

unlike cuprate HTS, MgB_2 does not show weak link coupling across grain boundaries so can be cheaply processed in polycrystalline form with reasonable properties [10, 11].

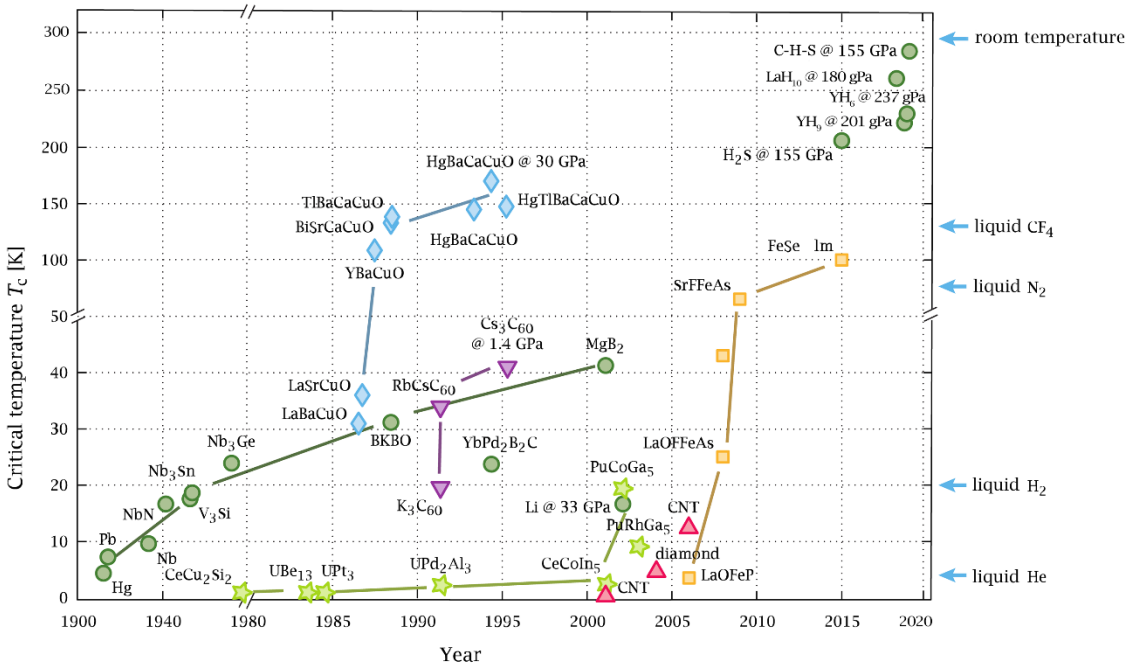


Figure 1.2 The discovery process of superconducting materials in the past 120 years (Reprinted from [8] licensed by CC BY-SA 4.0).

1.1 Fundamentals of superconductivity

Zero resistivity, Meissner effects [12] and the isotope effect [13] are three basic features of superconducting materials. The absence of resistance in ideal superconductors occurs below T_c, so in a superconducting ring, any transport current should be persistent over time. The Meissner effect refers to the superconducting state that superconductors perfectly expel the magnetic field and behave like a perfect diamagnet [12]. The field-shielding behavior takes place regardless of whether the field is applied followed by cooling, or decreasing temperature below T_c before the applied field (H); i.e., this phenomenon is path-independent. Actually, the thermodynamic Meissner state exists

only when H is below a critical field, known as H_c. If superconductors are in the Meissner state, they have perfect diamagnetism ($\chi = -1$).

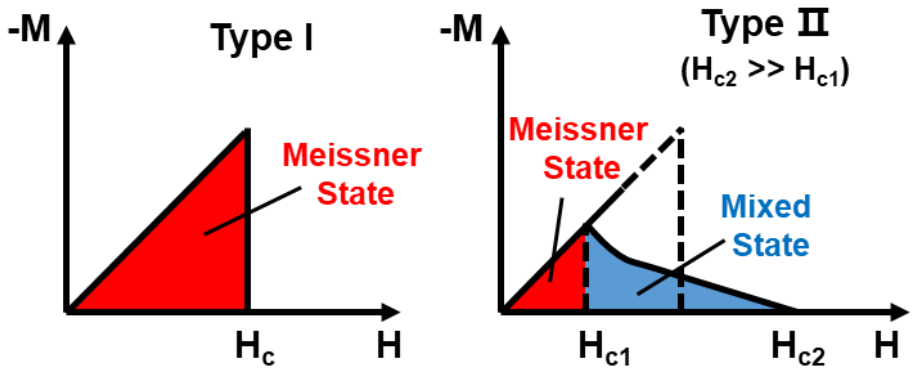


Figure 1.3 Magnetization as a function of the applied magnetic field for type I and type II superconductors.

According to the magnetization behavior, superconducting materials can be classified as type I or type II superconductors (Figure 1.3) [14]. For type I superconductors, the absolute value of magnetization (M) would suddenly drop to zero when H exceeds H_c, and the Meissner state is completely destroyed. However, type II superconductors maintain superconducting properties over a large range of H from the lower critical magnetic field (H_{c1}) to the upper critical magnetic field (H_{c2}). The M-H curves of type II superconductors in the low H range ($H < H_{c1}$) are the same as type I, but in the range $H_{c1} < H < H_{c2}$ the magnetic field begins to penetrate the superconductors so |M| decreases gradually with H to zero at H_{c2}. This state between the Meissner state and the normal state is called the 'mixed state'.

1.2 Critical superconducting parameters

There are three important parameters describing superconducting properties: critical

temperature (T_c), critical field (H_c) and critical current density (J_c). T_c refers to the sharp drop of resistance to zero during four-point probe measurements or the onset of the transition from the normal to the superconducting state at low application fields measured by a sharp change in the susceptibility. H_c is the maximum magnetic field that superconductors can support before they enter the normal state and depends roughly parabolically on temperature as [14],

$$H_c(T) = H_0\left[1 - \left(\frac{T}{T_c}\right)^2\right] \quad (1.1)$$

where H_0 is the critical field value at 0 K. H-T curves indicate the conditions under which the superconducting state exists, so can also be called phase diagrams. Figure 1.4 shows the phase diagram of two types of superconductors, where the phase diagram of type II superconductors is more complex due to the existence of the mixed state. It is worth mentioning that there is a $H_{irr}(T)$ line between H_{c1} and H_{c2} in practical conditions which will be defined later.

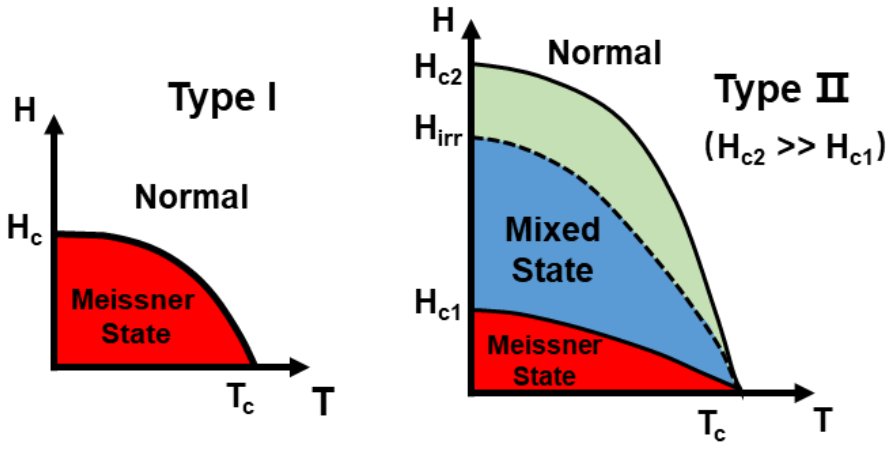


Figure 1.4 Magnetic phase diagrams of type I and type II superconductors.

The critical current density (J_c) depends on both H_c and T_c. For type I superconductors, when the total magnetic field on the surface of the sample exceeds H_c, the

superconducting state disappears. In type II superconductors, however, J_c values can be measured all the way up to the upper critical field (H_{c2}). Since J_c drops as the field and temperature increases, the critical surface defined by these three parameters for conventional low temperature superconductors such as MgB_2 and cuprate HTS are presented in Figure 1.5.

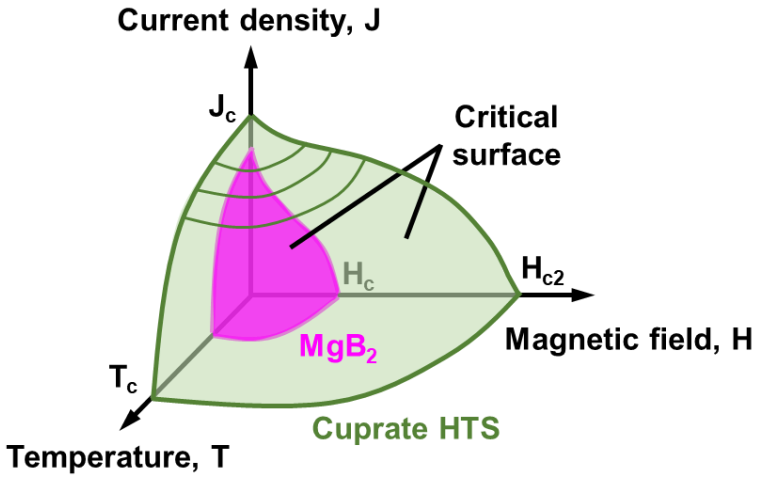


Figure 1.5 Schematic of the critical surface of a low temperature superconductor (MgB_2) and cuprate high temperature superconductors.

1.3 Theories of Superconductivity

The two fluid model is a phenomenological theory that was first suggested to explain the phenomenon of superconductivity [15]. In this theory, superfluid electrons and normal electrons are supposed to simultaneously flow through the superconductor. These two types of electrons spatially coexist but do not interact with each other. Normal electrons scattered by crystal lattice contribute to resistance while superfluid electrons are free to move without any scattering or resistance. After the discovery of the Messner effect, two London equations were proposed [16].

$$\nabla J = -\frac{n_s e^2}{m} B \tag{1.2}$$

$$\frac{\partial J}{\partial t} = -\frac{n_s e^2}{m} E \tag{1.3}$$

where J refers to the current density. n_s is related to the number of superconducting electrons. E and B are electric and magnetic fields in the superconductor, and e is the electron charge. If Ampere's law, $\nabla B = \mu_0 J$, was applied, Eq. 1.2 can be transformed to,

$$\nabla^2 B = -\frac{\mu_0 n_s e^2}{m} B \tag{1.4}$$

The London penetration depth, $\lambda = \sqrt{\frac{m}{\mu_0 n_s e^2}}$, in the equation denotes the characteristic distance over which the magnetic field is attenuated in a superconductor with the interior of the sample unaffected. i.e., the Messner state. The current flowing in the surface layer with a thickness of λ is called the screening current.

Introducing non-localised effects to the London equations, Pippard proposed the coherence length (ξ) to describe the distance over which n_s can change [17]. Abrikosov applied Ginzburg-Landau parameter κ, defined as $\kappa = \lambda(T)/\xi(T)$, to classify type I and type II superconductors based on the Ginzburg-Landau theory [18]. As shown in Figure 1.6, ξ is much larger than λ in type I materials ($\kappa < 1/\sqrt{2}$), where the interface energy between superconducting and normal regions is positive. The situation for type II superconductors is the opposite, with $\xi < \lambda$ and negative interface energy. Therefore, normal/superconducting interfaces are favorable to form in type II superconductors, which leads to the mixed state.

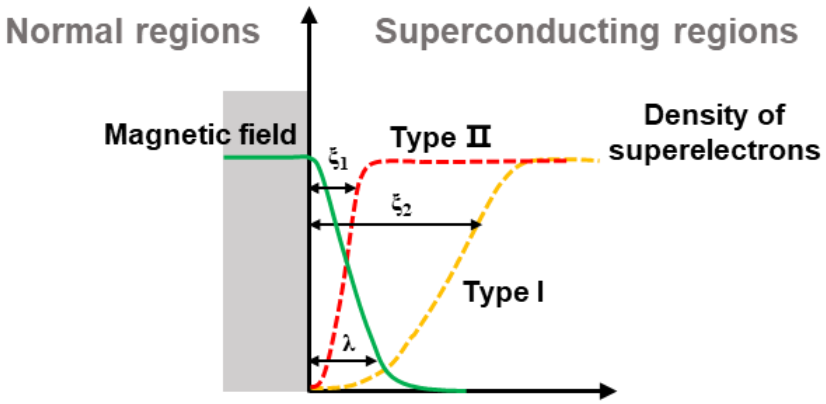


Figure 1.6 The variation of magnetic penetration depth (λ) and coherence length (ξ) at the interface between normal regions and superconducting regions for type I and II superconductors.

In 1957, J. Bardeen, L.N. Cooper and J.R. Schrieffer came up with the famous BCS theory to explain the superconducting mechanism of conventional superconductors [19]. The basic idea of this theory is that two electrons (Cooper pairs) with opposite spins and momentum can have an attractive interaction through a phonon, thus forming a low-energy stable state. There is an energy gap Δ between the BCS ground state and the first excited state, and the binding energy of a Cooper pair is 2Δ. T_c can be estimated by $T_c \approx \frac{2\Delta(0K)}{3.5k_B}$, where k_B is the Boltzmann constant [14].

1.4 Intrinsic factors influencing critical current density

As mentioned above, normal cores with the radius ξ can be penetrated by the external field. Each core accommodates a quantum of flux (Φ_0) with small currents circulating over the radius of λ, which are known as the vortex. Interaction between vortices can arrange them to form flux line lattice [20]. The Lorentz force generated by small currents will lead to the movement of vortices and energy dissipation when a small

external field is applied. However, if defects that immobilize flux lines are introduced, the elementary pinning force (f_p) due to the interaction between defects and each single flux line can compensate for the driving force. These defects trapping flux lines are known as pinning centres. Only when the external field increases to a higher critical value, flux lines de-pin, and the J_c of materials is enhanced due to the presence of pinning centres. Defining the pinning force density (F_p) as the vector addition of the individual pinning force per unit volume, the maximum pinning force $F_{p,max}$ (i.e., the onset of the flux motion) can be written as,

$$\mathbf{F}_{p,max} = \mathbf{J}_c \times \mathbf{B} \tag{1.5}$$

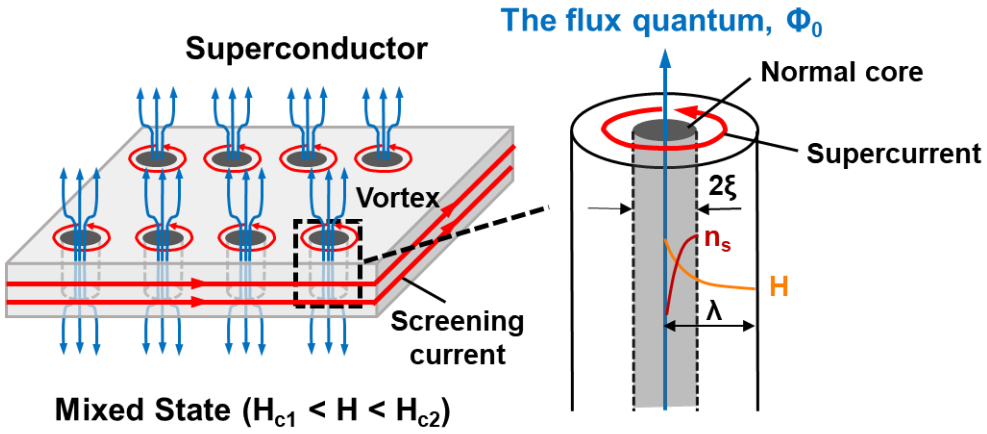


Figure 1.7 Schematics of vortices in the type II superconductor with the screening currents flowing in the surface layer; the partial magnified view shows a vortex that consists of a normal core surrounded by supercurrents.

The types of pinning in the superconducting crystal lattice include point pins (atomic defects), line pins (irradiation-induced tracks, dislocations, etc.), surface pins (stacking faults, grain boundaries, etc.) and volume pins (large precipitates, voids, etc.) according to the dimension of pinning centres [21]. Depending on the type of defects and their densities, one can make two major scenarios for vortex pinning: strong pinning and

collective pinning [22]. When the normal region has a similar size as the coherence length, it can act as strong pinning centres and each vortex interacts with strong pins independently [23]. The strong pinning force is proportional to the density of pins (n_p). In contrast, collective pinning considers the interaction of flux lines with a large number of weak pinning centers. The individual flux line cannot move independently so a bundle of flux lines should be treated as an object that experiences elastic lattice deformation when interacting with the pinning landscape [24]. Figure 1.8 presents pinning diagrams for both pinning scenarios at a fixed magnetic field [25]. Each scenario can be further subdivided into single-line pinning (1D) and lattice pinning regimes (3D). The threshold for an effective pinning force, f_{Lab}, is proposed by Labusch, and only pins with $f_p > f_{Lab}$ and proper n_p can have opportunities to be strong pins [26].

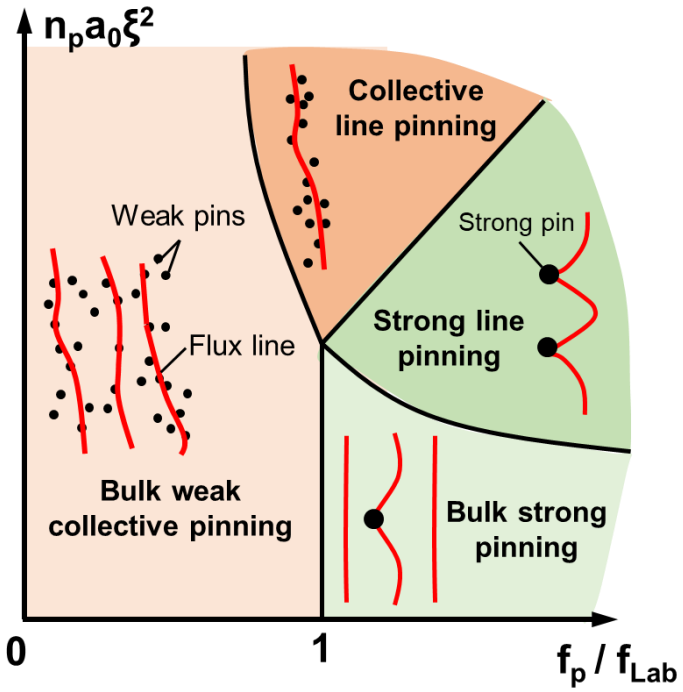


Figure 1.8 Pinning diagrams showing different regimes defined by strong pinning and collective pinning scenarios. n_p refers to the density of pins. a_0 is a constant and ξ is coherent length (Reproduced from [25] with permission from American Physical Society).

1.5 Extrinsic factors influencing critical current density

The microstructures affect J_c flowing on different scales in bulk samples and change the spatial distribution of the total magnetic field, and the influence varies in different types of superconductors. For example, cuprate HTS materials suffer from grain boundaries where J_c can drop exponentially because of weak-link grain boundaries [27], while grain boundary pinning is the dominant pinning mechanism in MgB_2 [28, 29]. In NbTi, the pinning from clusters of normal precipitates (non-superconducting α-Ti) has the strongest effect [30, 31]. Porosity reduces the area of available current paths for all superconductors so it should be carefully controlled [32-34] Poor grain/interface connectivity impeding the flow of supercurrent across different regions should also be avoided in polycrystalline samples [35, 36]. In a word, reliable interpretation of superconducting data requires support from microstructural characterisation, which is the focus of this thesis when investigating the superconducting properties of bulk MgB_2 materials.

Chapter 2 Literature review

MgB_2 is a conventional BCS superconductor, and the isotope effect directly verifies that superconductivity in MgB_2 derives from an electron-phonon interaction [37, 38]. Some crystal and superconducting parameters of MgB_2 are listed in Table 2.1.

Table 2.1 Some crystal and superconducting parameters of MgB_2.

Parameter	Values	Ref
Crystal system	Hexagonal	[39]
Space group	P6/mmm	[39]
Theoretical density	ρ = 2.63 g/cm^3	[39]
Lattice parameters	a = 0.3085 nm, b = 0.3524 nm	[39]
*Decomposition temperature	T = 883 ~ 1135 K	[40]
Coherence length	$\xi_{ab}(0)$ = 3.7~ 12.8 nm, $\xi_c(0)$ =1.6 ~ 5 nm	[2]
Penetration length	$\lambda(0)$ = 85 ~ 180 nm	[2]
Band gaps	$\Delta_\pi(0)$= 1.2 ~ 3.7 meV, $\Delta_\sigma(0)$= 6.4 ~ 7.2 meV	[41]
Upper critical magnetic field	$H_{c2}^{\|ab}(0)$ = 13 ~ 20 T	[2]

* $2MgB_2(s) = MgB_4(s) + Mg(g)$

As shown in Figure 2.1, MgB_2 has the AlB_2-type hexagonal structure with two types of layers along the c axis: B layers and Mg layers. The arrangement of B atoms is similar to carbon planes in graphite. Each hexagonal Mg layer interleaves between two B planes. The B-B interaction in the planes is stronger than that between planes, so MgB_2 shows a strong anisotropy along the a and c axes.

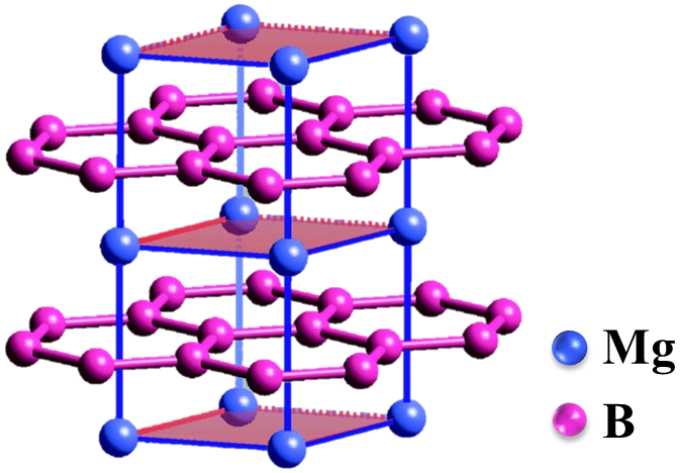


Figure 2.1 The crystal structure of MgB_2 with hexagonal Mg and B layers. Each Mg atom is located above the center of the B hexagons (Reproduced from [42] with permission from Elsevier).

As introduced in Chapter 1, MgB_2 possesses a remarkably high T_c (39 K), and grain boundaries in MgB_2 do not act as weak links so bulk materials can have reasonable superconducting properties even when prepared as polycrystalline samples by simple powder processing [10]. The cheap raw materials of MgB_2 also highlight its potential for industrial use [43]. Therefore, MgB_2 is an ideal alternative for high J_c magnets in modest field applications.

2.1 Electronic structure and two-gap superconductivity

The special superconducting properties of MgB_2 are attributed to its multiple bands and gaps. There are 2D σ covalent bands localized in boron layers arising from the 2s and $p_{x,y}$ orbitals of B atoms and delocalised 3D π bands between layers mainly from the p_z orbital [44]. As Figure 2.2a shows, blue tubular networks are π bands, and the top and bottom components are hole types from the bonding p_z bands while the middle one is from the antibonding p_z band (electron-like). The vertical cylinders refer to σ bands that

are hole-like, which have a greater contribution to the density of states at the Fermi surface than π bands [41]. The band structure of MgB_2 is dominated by B atoms but the contribution of Mg is also of importance. According to the BCS theory, the collective excitation of atoms (photons) is critical to the superconductivity of conventional superconductors [19].

There are four distinct phonon modes in MgB_2: A_{2u}, B_{1g}, E_{2g} and E_{1u}, among which E_{2g} is high anharmonic and denotes the in-plane B-B stretching mode [45]. The coupling of E_{2g} mode and two bands (boron σ and π bands) is well-accepted as the reason for MgB_2 superconductivity, especially the strong pairing between E_{2g} mode and boron σ bands that is responsible for a high T_c [46-48]. As Figure 2.2b shows, the coupling between different bands and phonons generates two distinct superconducting energy gaps. The colour scale is associated with that of the band structure representing different values of energy gaps (Δ) on the Fermi surface at 4 K. The Δ of σ bands along vertical Γ-Γ lines is around 7.2 meV on the red cylindrical sheet, while the broader orange sheet has an energy gap varying from 6.4 to 7.2 meV. The broad Δ_π gap ranges from 1.2 to 3.7 meV [41].

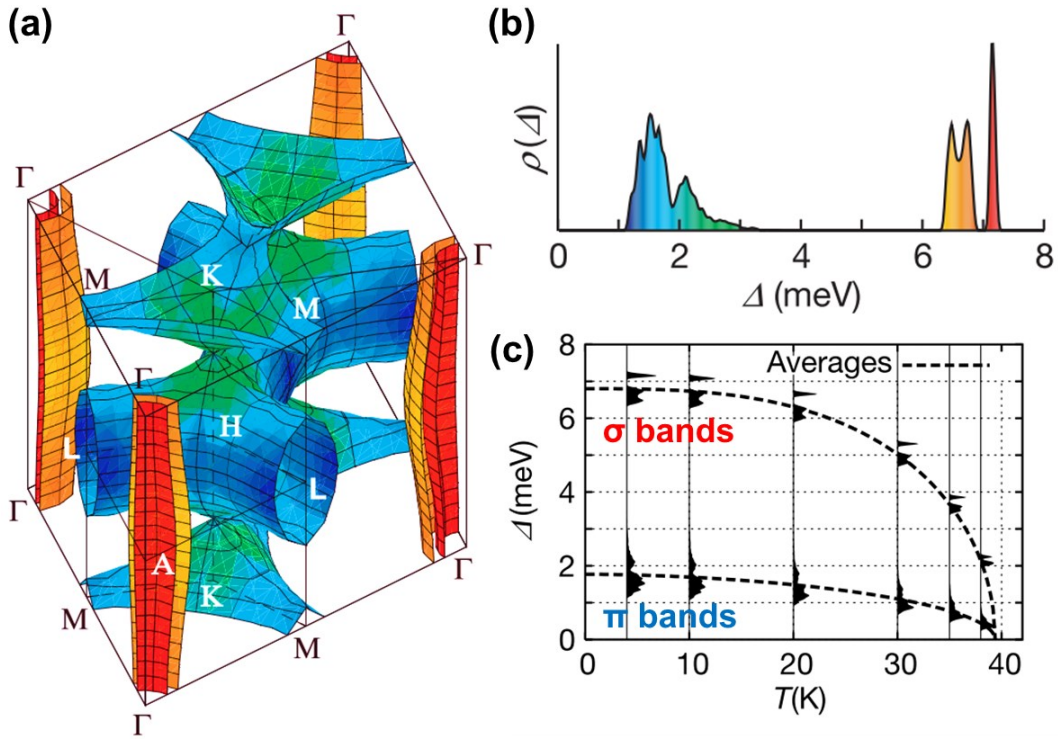


Figure 2.2 (a) Band structures and superconducting energy gaps of MgB_2 on the Fermi surface at 4 K with the colour scale linked with (b) the distribution of energy values of gaps. (c) shows the temperature dependence of two gaps (Reprinted from [41] with permission from Springer Nature).

T_c of MgB_2 is influenced by the density of states at the Fermi level, phonons (changes in phonon modes or phonon frequency) and the strength of coupling between bands and phonons [49]. The modifications of Fermi surface and changes in the phonon properties will reduce T_c. The impurity scattering (chemical disorder) that consists of interband scattering and intraband scattering, also has a prominent influence in T_c [50, 51]. As Figure 2.2c shows, there is a link between the values of these energy gaps and the corresponding T_c values, with a relation $\Delta(0\ \mathrm{K}) = Ck_BT_c$ (for σ sheets, C = 2; for π sheets, C = 0.53), which leads to a prediction of T_c of 45 K and 15 K respectively if inter-band scattering is ignored. However, due to the finite interband coupling, two gaps become narrower with the increasing temperature and finally merge at T_c no more than

39 K [41, 52].

The two-band and two-gap structures have been experimentally demonstrated by point-contact spectroscopy, tunnelling spectroscopy, electronic Roman spectra and other experimental investigations [53-56]. These studies provide new approaches to tune the superconducting performance of MgB_2 such as irradiation and selective alloying on Mg or B sites [57], as will be discussed in Section 2.3.

2.2 Fabrication of MgB_2 bulk samples

There are three common approaches to processing bulk MgB_2: ex-situ, in-situ and Mg infiltration processing (MIP). In the in-situ method, MgB_2 is formed by the reaction of mixed Mg and B powders during a heat treatment process. Mg melting at a lower melting point can diffuse to boron grains, which activates liquid phase sintering to form MgB_2. During this process, voids are left in samples, leading to a low density but the inter-grain coupling is usually strong [58]. In contrast, pre-reacted MgB_2 powders are directly sintered in the ex-situ route so bulks with high density can be produced by the field-assisted sintering method [59], although as will be discussed below finding an optimum sintering process for MgB_2 is not easy. MIP can be used to prepare dense bulks with complex geometries by infiltrating liquid Mg into a B green body [60], but an inhomogeneous phase distribution such as residual intermediate boride in samples produced by this method tends to have a detrimental effect on MgB_2 superconducting performance [61, 62].

The application of high pressures during sintering is commonly used to improve the densities of ceramic materials. Several kinds of pressure-assisted processing methods, such as hot-pressing, field-assisted sintering and ultra-pressure sintering, have already been used to produce MgB_2 bulk samples with improved microstructures and superconducting performance [63-65]. With the assistance of current flow, field-assisted sintering enables the production of dense nanocrystalline MgB_2 samples with short process times due to high-heating rates, so the crystal growth and microstructure coarsening can be retarded [63, 66, 67]. Ultra-high pressure-assisted sintering (>2 GPa) is another method that can process samples with high density in a short time so is widely applied in producing nanostructured ferroelectric ceramics and dense engineering ceramics [68-72]. The application of high pressure may alter phonon behaviour and bring lattice distortion, therefore changing the superconducting performance of MgB_2 [73]. Moreover, plastic deformation of particles under extreme external pressure may promote the elimination of pores and local atomic diffusion at interfaces or grain boundaries during the sintering process [74]. Compared with field-assisted sintering, this method allows a lower sintering temperature benefiting from ultra-high pressures. No matter which method is adopted, careful choice of processing conditions such as temperature and pressure are vital in achieving the optimum microstructure and hence superconducting performance of bulk MgB_2 samples, and this is another focus of the work reported in this thesis.

2.3 How to improve the superconducting performance of MgB_2?

Irreversibility field (H_{irr}) is defined as the magnetic field that flux lines de-pin due to strong Lorentz forces and begin to move [75]. The $H_{irr}(T)$ and the $H_{c2}(T)$ curves form the green area in the H-T diagram of MgB_2, as shown in Figure 1.4. Since the flux flow leads to energy loss, H_{irr} is also a useful parameter to judge the use of the material in practical applications.

As introduced in 2.1 T_c as an intrinsic property of MgB_2 relates to the density of states (DOS) at the Fermi level, the impurity scattering (especially the interband scattering), lattice distortion (especially the lattice parameter along a axis), etc. However, either the application of pressure during the sintering process or the irradiation to induce disorder will suppress T_c [49]. Moreover, extensive research attempted the substitution of Mg or B atoms by chemical doping, but dopants always result in the T_c of MgB_2 going down to a varying extent [2, 49]. Since T_c is difficult to be enhanced, improving the performance of MgB_2 mainly focuses on the enhancement of J_c, H_{c2} and H_{irr} in moderate fields without severe reduction in T_c.

From the aspect of intrinsic properties, flux pinning is critically important in increasing the supercurrent density (Section 1.4). J_c of MgB_2 can be improved by introducing defects as effective flux pinning centres if the defect sizes are comparable to the coherence length of MgB_2. As to extrinsic properties (Section 1.5), grain connectivity, density and microstructural homogeneity are critical factors affecting the current flowing through the bulk sample. For example, Rowell et al demonstrated that high

porosity and insulating impurities at grain boundaries reduce the effective area carrying supercurrents. They used measurements of normal state resistivity (which would also be influenced by these microstructural features) to make correlations of J_c in the superconducting state [36, 76]. This chapter will review processes that are often used to improve the superconducting properties of MgB_2; irradiation, ball milling or impurity phase additions.

2.3.1 Irradiation

Irradiation by high-energy neutrons, protons or heavy ions can introduce different types of defects in the MgB_2 lattice by the exchange of Mg and B on lattice sites (anti-site defects), the displacement of atoms from their initial sublattice or nanometric amorphous defects [77, 78]. This lattice disorder increases the interband impurity scattering and is associated with the high resistivity in irradiated specimens [79]. Besides, the change of lattice parameters after irradiation was identified by X-ray diffraction studies. The MgB_2 unit cell is expanded after irradiation, with the c axis expanding more than the a axis, as a result of the anisotropy of MgB_2 [80]. These disorders are related to the significant suppression of T_c, especially when samples are exposed to a high fluence [49].

The variations of MgB_2 electronic structure and coupling strength between phonons and σ bands contribute to changes in H_{c2} values. Putti et al summarised that defects created by irradiation increase H_{c2} by decreasing the mean free path and lowering the

coherence length. However, the dH_{c2}/dT behaviour depends on the fluence value and H_{c2} will be suppressed at a high fluence [79]. The effect of irradiation on J_c varies with different irradiation species and the fluence values [81-83]. Energetic neutrons may form nanometric-sized defects [77], while protons will form mostly point defects [82]. Even though defects with a size comparable to the coherent length of MgB_2 may serve as strong pinning centres, Eisterer et al thought that the main contribution to J_c improvement after irradiation is from the reduction of the anisotropy rather than changing the grain boundary pinning mechanism [84, 85].

Irradiation is a good approach to studying the effect of scattering centers on the superconducting properties of MgB_2. However, it is impractical to produce large-diameter MgB_2 bulk samples with higher supercurrent because of the cost of accessing nuclear facilities and the radioactivity of the irradiated samples.

2.3.2 High-energy ball milling

High-energy ball milling is applied to produce fine nanoparticles, uniform powder mixtures and even mechanically-alloyed powders for a wide range of materials followed by the sintering process, including alloys, intermetallics, ceramic, etc. [86, 87]. Brittle particles subjected to high-energy collision will fracture into small pieces, and crystallite refinement can be achieved after milling by the introduction of lattice damage. Haßler et al changed milling parameters when milling Mg and B starting powders to alter milling energies (E_t) calculated by modelling the motion of a single ball in

planetary ball milling [88]. Table 2.2 shows that E_t in their experiments varies over a range of $10^7 \sim 10^{10}$ J/Kg. It was found that the transition from simple mixing to mechanical alloying happens at the milling energy of 10^8 J/Kg, and the size of alloyed MgB_2 grains can effectively drop to some ten nanometers [88].

Table 2.2 The influence of milling parameters on the milling energy per mass [88] (Copyright © (2013) by IOP Publishing. Used with permission.)

Number	Ball to powder ratio	Time (h)	Rotation speed (min^{-1})	E_t/m (J/kg)
1	18	50	250	2.6×10^9
2	18	50	100	1.7×10^8
3	18	5	100	1.7×10^7
4	18	5	250	2.6×10^8
5	36	50	100	3.4×10^8
6	36	5	100	3.4×10^7
7	36	50	250	5.3×10^9
8	36	100	250	1.0×10^{10}

Many studies have demonstrated that ball milling contributes to the microstructural improvement of both green powders and processed samples [89-91]. SEM images in Figure 2.3 show that average void sizes in MgB_2 bulk samples reduce with increasing milling energy. The XRD peak broadening presented in Figure 2.4a indicates effective grain refinement, and Figure 2.4b shows that higher milling energies can create substantial shrinkage of the a axis in the MgB_2 lattice [90]. Mikheenko et al found that the relation of J_c and the average grain size follows $J_c \propto 1/D$ (Figure 2.5), which demonstrates that the grain size is critical to MgB_2 superconducting performance [92].

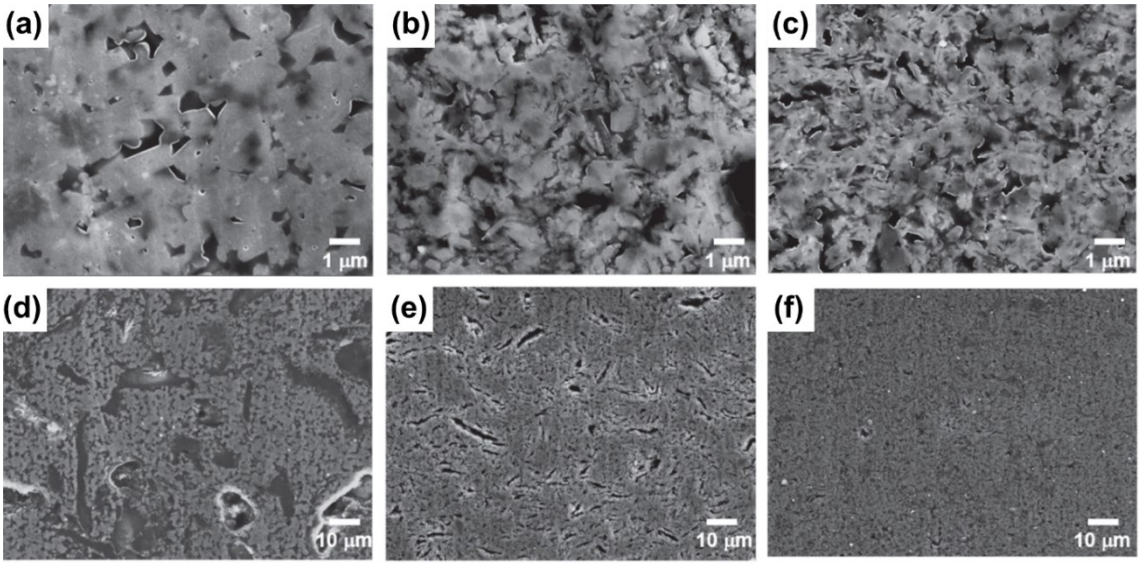


Figure 2.3 SEM images of (a)(d) MgB_2 bulk samples without ball milling, (b)(e) with milling energy of 2.1×10^6 MJ/kg and (c)(f) with milling energy of 1.7×10^7 MJ/kg. The gray and black contrast in these images are from MgB_2 and voids (Reprinted from [90] with permission from IOP Publishing).

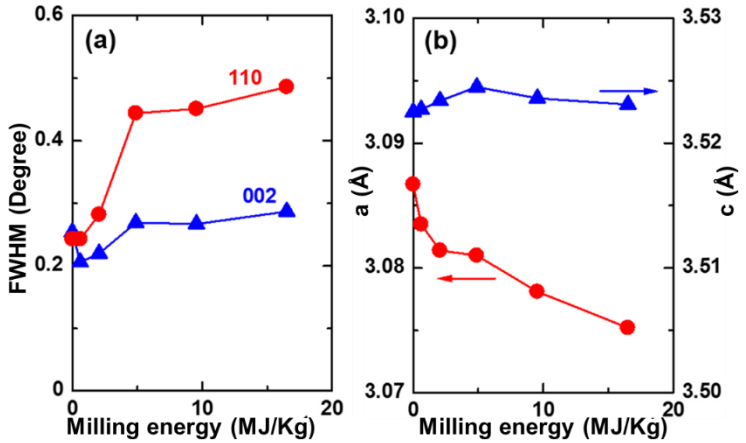


Figure 2.4 Milling energy dependence of (a) full width at half maximum (FWHM), (b) unit cell parameters (Reproduced from [90] with permission from IOP Publishing).

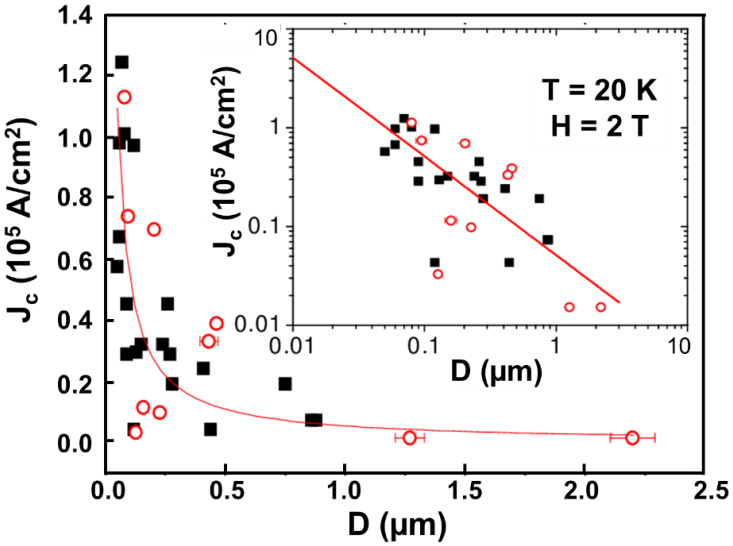


Figure 2.5 Experimental data and fitting lines showing the correlation between critical current density and average grain sizes of pure samples (red points) and samples doped with nanoparticles (black points) (Reproduced from [92] by permission from IOP Publishing).

2.3.3 Chemical doping

The effect of chemical doping on the superconducting properties of MgB_2 is complex. On the atomic scale, atoms with a radius comparable to Mg or B atoms may be substitutional atoms in the MgB_2 lattice, creating strain and disorder. In terms of flux pins on a larger scale, stable nano-sized impurities or new phases formed during the process may act as effective pinning centres. From the microstructural aspect, some dopants may situate at MgB_2 grain boundaries and retard grain growth while others may dissolve into MgB_2 lattice in the high-energy ball milling and then precipitate within grains in the sintering process [93].

2.3.3.1 Carbon and carbides

Carbon is the most widely accepted dopant to increase J_c in MgB_2 for high-field

applications. To date, the addition of various forms of carbon sources have been reported, including carbon nanoparticles [94], carbon nanotubes [95], graphite/graphene [96, 97], boron carbide [98] and organic matter [99]. C atoms substituting for B sites dope the material with excess electrons and decrease the DOS at the Fermi level, which leads to a decrease in T_c [100]. Another effect of C substitution is the increased intraband scattering, resulting in the reduced anisotropy and higher H_{c2} values in C-doped MgB_2 samples [51, 101].

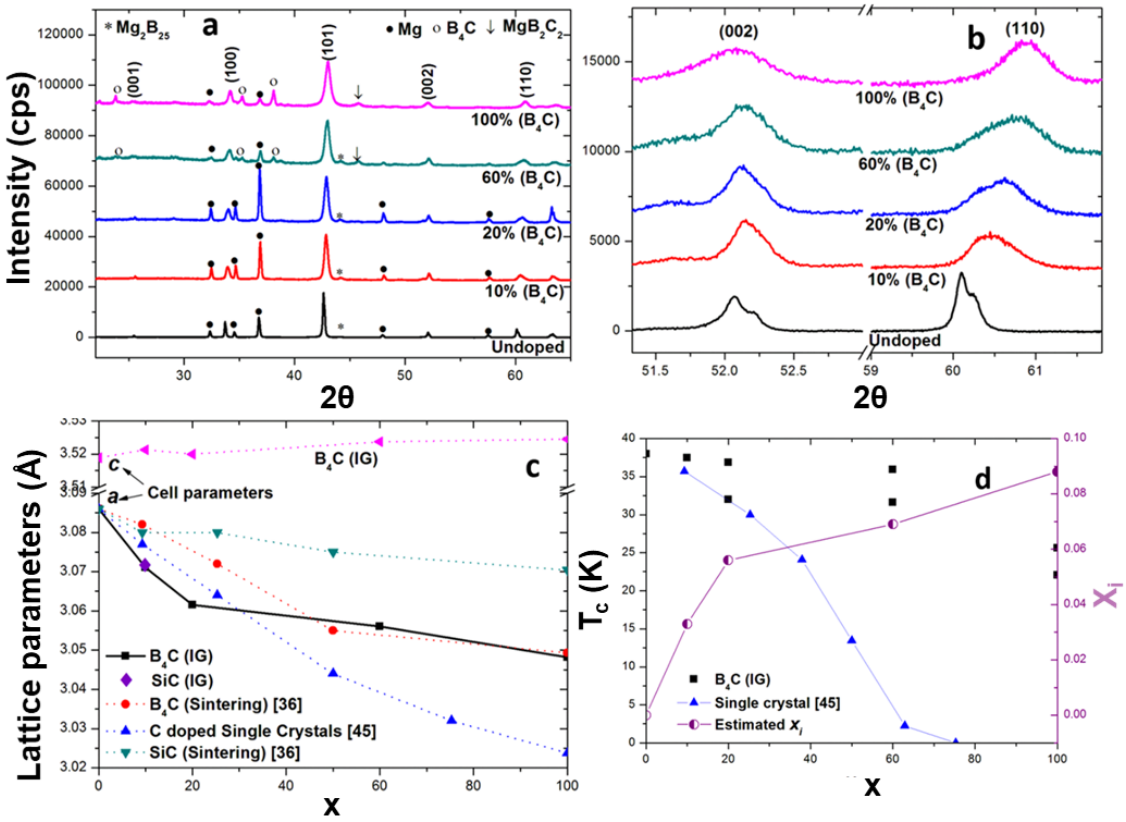


Figure 2.6 (a) shows XRD scans for the pure MgB_2 and B_4C doped MgB_2 samples. (b) highlights the evolution of (110) and (002) peaks. (c) plots the dependence of lattice parameters on the concentration of C-containing dopants. (d) shows T_c values and estimated carbon substitution (X_i) as a function of C dopants (Reproduced from [102] licensed by CC BY 4.0).

Doping carbon sources can also cause lattice contraction [98, 102, 103]. As Figure 2.6 shows, the in-plane a axis lattice parameter decreases with a higher concentration of C,

while the out-plane c axis lattice parameter remains nearly unchanged [102]. This is easy to understand because C in B sites forms covalent bands with surrounding B atoms, so mainly introduces in-plane distortion in the MgB_2 lattice.

Additionally, nano impurities brought by the addition of C-containing compounds may further contribute to the improved performance of C-doped MgB_2 samples [94, 98]. Figure 2.7 shows the distribution of main phases in B_4C-doped MgB_2 samples produced by in-situ method at high temperatures (>1530 ^oC) [98]. Excess carbon precipitates as MgB_2C_2 due to C saturation in $MgB_{2-x}C_x$ phases. With the increase in the sintering temperature, samples became denser and excess Mg was detected in the matrix (Figure 2.7b and c). The authors thought that small MgO inclusions, as shown in the high-angle annular dark field (HAADF) image marked as X_i (i = 2, 3, 4), could serve as second phase pinning sites.

Even though carbon or carbide doping is demonstrated as an effective way to improve MgB_2 superconducting performance, C-containing dopants should be avoided if MgB_2 superconductors are designed to operate at a higher temperature (>20 K) because of the heavy suppression in T_c resulting from C substitution [104].

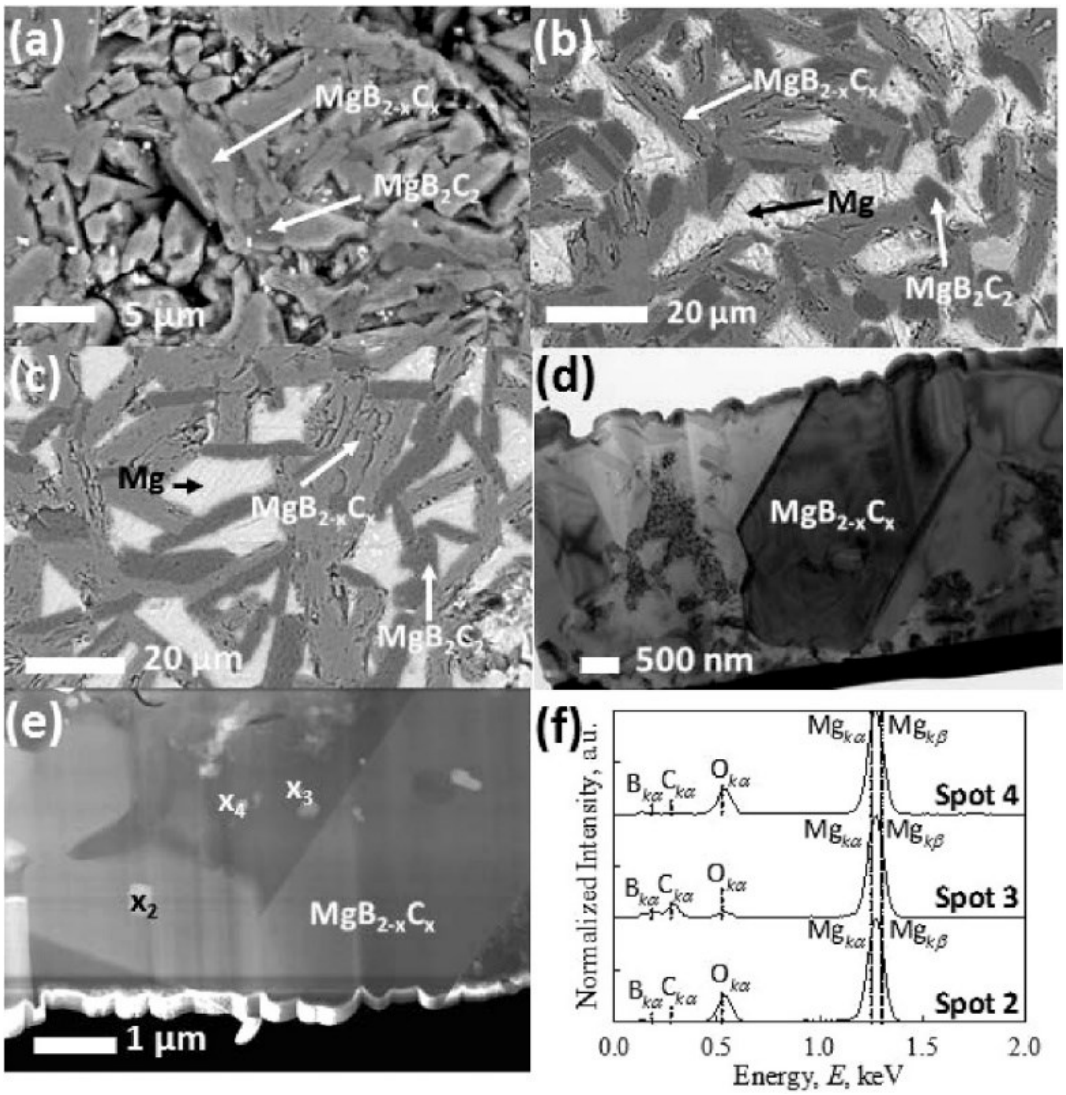


Figure 2.7 SEM images of B_4C doped MgB_2 samples produced at (a) 1530 ºC, (b) 1600 ºC and (c) 1700 ºC. (d) and (e) are bright field TEM and HAADF images of the 1530 ºC sample; (f) EDX spectra of the three spots marked in (e) (Reproduced figure from [98] with the permission from AIP Publishing).

2.3.3.2 Metal element additions

Extensive research has been carried out on the effect of metal doping on the T_c and J_c of MgB_2. Aluminum can serve as an electron dopant to Mg. Due to band filling effects, i.e., holes in the σ band of the B atoms being filled by electron doping, the coupling between holes in the σ band and phonons is suppressed by Al substitution, leading to a

dramatic decrease in T_c [100]. Additionally, the increasing Al concentration leads to lower T_c values [105]. Al-doping is demonstrated far less effective than C-doping in improving the J_c performance. It was reported that up to 2.5 wt% Al addition could double the self-field J_c values at 20 K, but excessive Al content (>5 wt%) impaired the J_c performance which may result from the segregation of impurities to the grain boundaries [106].

Since the electron doping failed to make a positive difference, one expects that hole doping might have the opposite effect. Upon Li doping, the lattice parameter a shows a dramatic decrease but the lattice parameter c does not show systematic change, and Li doping also reduces the T_c to around 34 K in $Mg_{1-x}Li_xB_2$ (x = 0.2) from 38 K in pure samples [107]. Daghero et al co-doped Al and Li in MgB_2 to balance the charge and studied the superconducting behavior of MgB_2. They found that T_c is mainly influenced by the content of Al rather than Li [108]. Pallecchi et al explained that the Li dopant effect primarily π bands while Al doping causes σ band filling [109]. Since T_c mainly depends on carrier concentrations in the σ band, Li doping does little to determine T_c. The influence of Li-doping on H_{c2} and J_c still lacks believable investigation.

Transition metal elements such as Ag, Cu and Zn can react with Mg to form intermetallic precipitates [110, 111]. Ma et al showed that doping Cu lowers the sintering temperature to 550 ^oC in the in-situ method by forming Mg-Cu eutectic liquid [112]. They thought lamellar MgB_2 grains formed during the sintering process have better grain connectivity in Cu-added samples compared with un-doped ones, as shown

by the lower values of normal state resistivity (Figure 2.8a-c). Varghese et al studied J_c in Cu added samples produced at different sintering temperatures by the in-situ method [113]. Their results suggested that J_c values in undoped samples strongly depend on processing temperatures, while the J_c(T) curve in Cu-doped bulks is quite flat over the whole temperature range (Figure 2.8d), indicating that the sintering can even be activated at 550 °C with Cu addition. Moreover, the higher percentage of Cu beyond the optimal Cu content (~2.5 wt%) decreases the transparency of grain boundaries to the current because of normal Mg-Cu precipitates at MgB_2 grain boundaries.

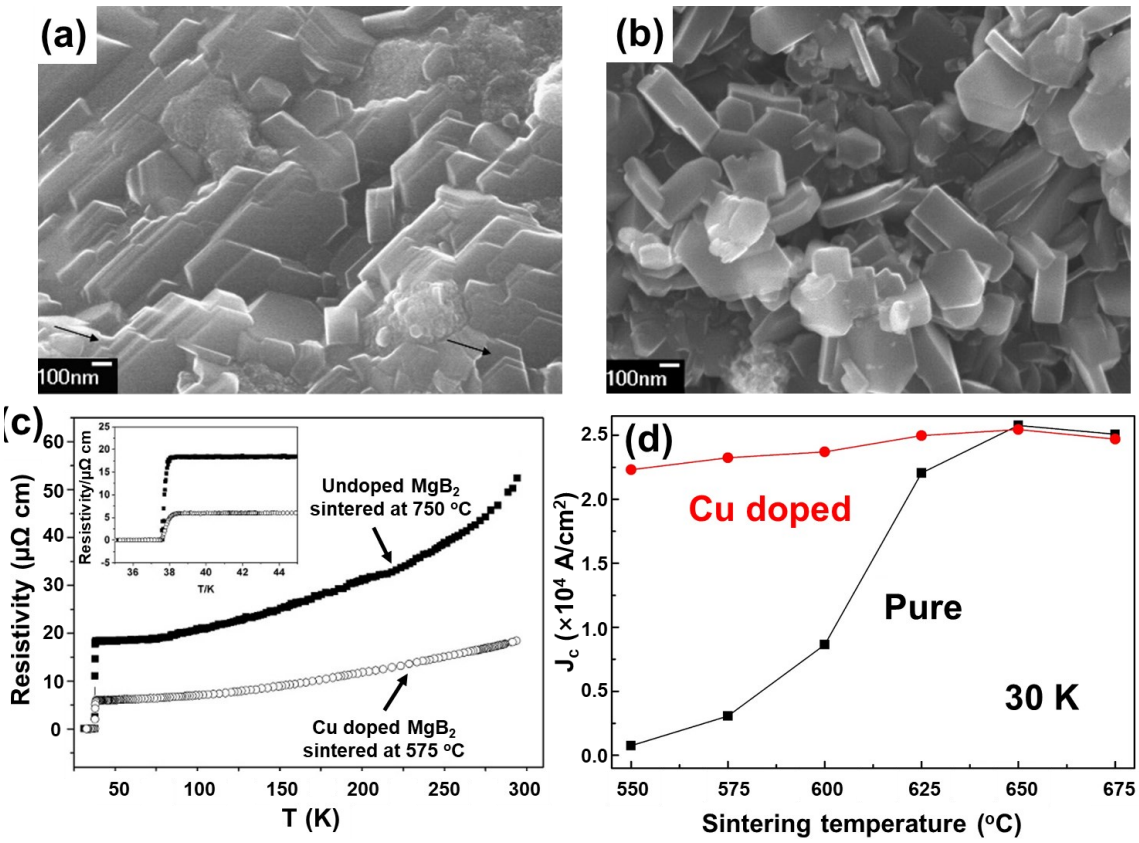


Figure 2.8 (a) and (b) SEM images of $(Mg_{1.1}B_2)_{0.92}Cu_{0.08}$ and pure MgB_2 samples. (c) temperature dependence of resistivity for both samples. (Reproduced figure from [112] with permission from Elsevier). (d) the influence of sintering temperatures on the transport self-field current measured at 30 K (Reproduced figure from [113] with permission from AIP Publishing).

Possible improvement of MgB_2 superconducting properties is expected with ferromagnetic dopants considering that these impurities have a stronger interaction with flux lines [114]. However, Li et al found that T_c values of Fe and Co-doped MgB_2 are suppressed due to weak magnetic scattering effects [115]. Ni doping could enhance J_c in some studies [116], while Fe and Co have negative effects in most studies [117-119]. Novosel et al concluded that the overall effect of the addition of ferromagnetic nanoparticles may be the balance between detrimental magnetic influence and improved flux pinning [120].

2.3.3.3 Oxides

The presence of oxygen is considered to be harmful to MgB_2 superconducting performance because the formation of MgO particles at grain boundaries may degrade the intergranular connectivity and/or decrease the area of transport current paths. However, if nanoscale precipitates are generated inside the MgB_2 grains, they can improve the superconducting properties by providing more pinning sites [121].

Rare earth (RE) oxide doping has been demonstrated to significantly enhance J_c with only a slight suppression of T_c [122]. Y_2O_3 doped MgB_2 bulks produced by the in-situ process were the first attempt [123]. XRD analysis demonstrated the formation of YB_4 in the in-situ liquid phase reaction. As shown in Figure 2.9a, the diameter of these nano precipitates was found to be around 10 nm at the MgB_2 grain boundaries. Smaller impurities (3~5 nm) comparable with the coherence length of MgB_2 were found inside

MgB_2 grains. The T_c of 10 wt% Y_2O_3-doped MgB_2 bulks was similar to un-doped material, but the uniform distribution of YB_4 significantly increases J_c in the high magnetic field range (>3 T, 20 K). Inspired by the successful results of adding Y_2O_3, other groups later tried Dy_2O_3, and the results are shown in Figure 2.9c and d [124]. The reaction between RE oxides and MgB_2 can form REB_x precipitates where RE = Y, Dy, Ho, Eu, etc., as summarized in Table 2.3. Among these dopants, Ho_2O_3 doping gives the best results because HoB_4 has a strong magnetic moment, which is supposed to provide strong interaction with flux lines [125].

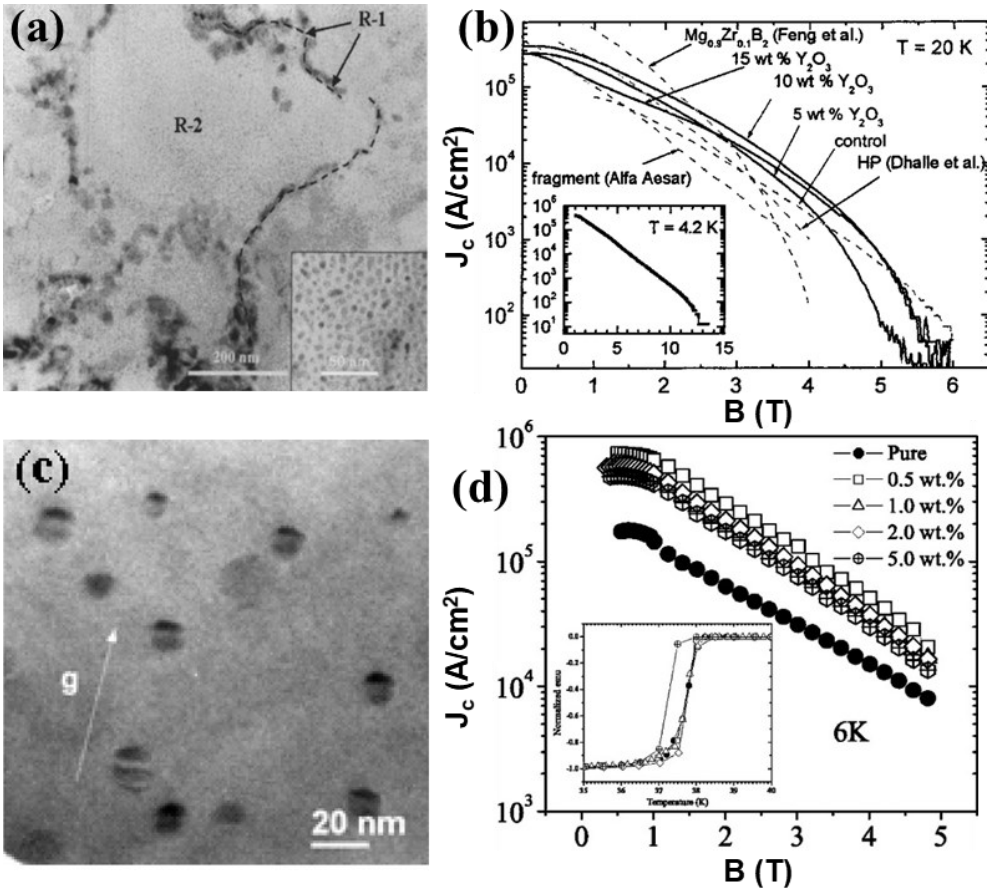


Figure 2.9 (a) TEM image of 10 wt% Y_2O_3 doped MgB_2; (b) J_c(B) curves of Y_2O_3 doped MgB_2 at 20 K and 4.2 K (inset). (c) TEM image of 0.5 wt% Dy_2O_3 doped MgB_2 samples. (d) J_c(B) curves of Dy_2O_3 doped MgB_2 at 6 K. Inset: temperature dependence of normalized magnetic moment (Reproduced figures from [123, 124] with permission from AIP Publishing).

Table 2.3 The doping effects of RE oxides on the superconducting parameters of MgB_2. HPS refers to high pressure sintering process.

Dopants	Size of dopants	Processing method	T_c	J_c	H_{c2}	H_{irr}	Reference
Y_2O_3	10 ~ 20 nm	In-situ HPS	~38 K	8×10^5A/cm^2 (20 K ,0 T)	-	-	[123]
CeO_2 (2 wt%)	10 ~ 20 nm	In-situ HPS (650 ºC, 1h; 800 ºC, 2h; 950 ºC, 1h)	~38 K	8×10^5A/cm^2 (20 K ,0 T)	-	-	[126]
Pr_6O_{11} (3 wt%)	-	In-situ HPS (850 ºC, 3h)	36.1 ~ 37.6 K	1.15×10^4 A/cm^2 (10 K, 5 T)	Improved	Improved	[127]
Nd_2O_3 (5 at%)	-	In-situ HPS (800 ºC, 1h)		2.46×10^3 A/cm^2 (4.2 K, 10 T)	-	-	[128]
Eu_2O_3 (4 wt%)	-	In-situ HPS (850 ºC, 3h)		1.1×10^4 A/cm^2 (10 K, 5 T)	Improved	Improved	[127]
Dy_2O_3 (0.5 wt%)	1 ~ 3 μm	In-situ HPS (900 °C, 15 min)	37.5 K	6.5×10^5 A/cm^2 (6 K, 1 T) 3.5×10^5 A/cm^2 (20 K, 1 T)	-	-	[124]
Ho_2O_3 (3 wt%)	50 nm	In-situ HPS (850 ºC, 2h)	37.1 ~ 37.3 K	2.0×10^4 A/cm^2 (10 K, 5 T) 1.0×10^3 A/cm^2 (20 K, 5 T)	Little effects	~9 T (10 K) improved	[125]
Tb_4O_7	<60 nm	In-situ HPS (800 ºC, 2h)	38.6 K	2.6×10^3 A/cm^2 (5 K, 6 T)	-	8.1 T (5 K) improved	[129]
Lu_2O_3 (<5 wt%)	~100 nm	In-situ HPS (750 ~ 850 ºC, 0.5 ~ 1 h)	~37.3 K	2.0×10^4 A/cm^2 (20 K, 2 T)	Little effects	Little effects	[130]

2.3.3.4 Borides

Doping with metal borides only brings one new element to the MgB_2 matrix. Possible roles of metal borides are either acting as pinning centres themselves or providing metal elements to substitute on the Mg sites. For example, the low-field J_c performance of MgB_2 is reported to be improved by doping TiB_2 [131]. An overall enhancement of J_c(B) performance was found in ZrB_2 doped MgB_2 samples and was ascribed to an increase in the density of pinning centers [132, 133]. In contrast, Yang et al did a systematic study on the superconducting properties of x wt% MB_2 doped MgB_2 bulk samples (x = 1 ZrB_2; x = 1.7 for TiB_2; x = 2.7 for NbB_2) [134]. They found all doped samples had reduced J_c values, especially at high magnetic fields. The contradictory results may come from dopant sizes and the various microstructures achieved under different processing conditions. The studies with positive results sintered Mg, B and ZrB_2 powders at around 800 ºC for up to 1 h, while the negative studies used the Mg infiltration method heating up to 1700 ºC for 20 min or 1500 ºC for 30 min. This indicates that other factors besides the choice of dopants, such as processing conditions and final microstructure are critical to the performance of superconducting samples.

2.4 Applications of MgB_2 bulk samples in magnetic drug targeting

Advances in medical science have resulted in the discovery of new drugs to cure a wide range of human diseases, and many of these drugs are designed to target specific

abnormal tissue, for example to attack cancerous tumours. Since drugs circulating in the bloodstream are also absorbed by normal tissue in traditional therapies, a high drug dose is required and side effects are inevitable. A good solution to solve these problems is to accumulate drugs specifically in the desired sites by magnetic drug targeting (MDT). In MDT, magnetic carriers bound with active ingredients are injected into the human body and manipulated by an external field to reach the desired location. The magnetic force on a carrier is given by [135, 136]:

$$\mathbf{F_m} = \mathrm{A}(\mathbf{M} \cdot \boldsymbol{\nabla})\mathbf{B} \qquad (2.1)$$

where A is a constant. $\mathbf{M}$ and $\boldsymbol{\nabla}\mathbf{B}$ are the particle's magnetisation and magnetic field gradient, respectively. Therefore, to maximise the magnetic steering force needs both $\mathbf{B}$ and $\boldsymbol{\nabla}\mathbf{B}$ to be optimised. Permanent magnets such as those based on neodymium iron boron alloys have initially been utilised in MDT, but the maximum magnetic field at the patient surface can only achieve less than 2 T [137, 138]. Magnetic resonance targeting based on superconducting coils is a good alternative and can be combined with magnetic resonance imaging [139, 140]. The main drawback of this approach is the large volume of devices when dealing with only a small target region. Compared with the options above, compact bulk superconductors incorporated into desktop devices show promise because they are portable and relatively inexpensive, as shown in Figure 2.10. Optimizing the superconducting properties of bulks can improve magnet field strength and field gradient. This not only can improve the magnetic forces on nanoparticles but also increase the penetration depth of the field which is a significant factor when dealing with diseased tissue lying deeper in the human body.

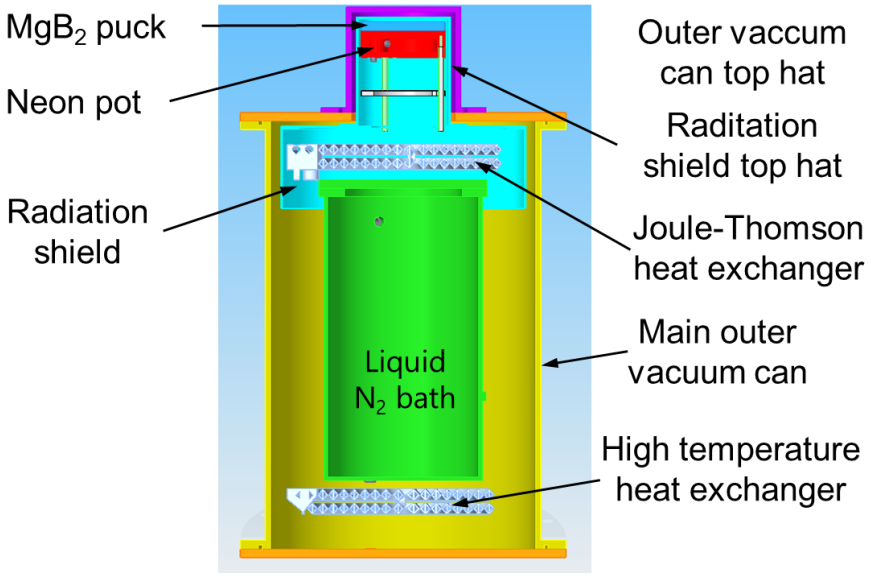


Figure 2.10 Schematic of the desktop-type MgB_2 superconducting bulk magnet system (Copyright © 2019 by IOP Publishing. Reproduced from [141] licensed by licensed by CC BY 3.0)

2.5 Summary

Although MgB_2 is a simple binary intermetallic compound, many studies have demonstrated that it is a two-band and two-gap superconductor with a useful T_c value of nearly 40 K. The intrinsic superconducting properties (T_c and H_{c2}) are mainly determined by boron atoms, so there is anisotropy in the direction parallel and perpendicular to B layers. Electronic structures and phonon behaviour can be modified by electron dopants or the application of high pressure during the sintering process. Inter- or intra-band scattering affects the anisotropy and upper critical field apart from T_c, which can be achieved by irradiation or the substitution of B atoms. Another way to change the intrinsic properties of MgB_2 is the introduction of strong flux pinning sites such as second phase inclusions of size comparable to the coherence length of MgB_2. The processing conditions are critical in determining the composition and

microstructure of bulk samples. Careful phase and microstructural characterisation are necessary to optimize processing conditions as well as to interpret the superconducting properties. The development of improved MgB_2 magnets incorporated into desktop devices offers the advantages of cheap precursors, simple processing and high trapped field gradients, so could make a difference in the magnetic drug targeting field.

Chapter 3 Experimental methods and characterisation techniques

This chapter consists of three parts, giving an overview of (i) methods of processing MgB_2 powders and bulk samples, (ii) techniques for characterising phases, microstructures and superconducting properties of MgB_2 bulk samples and (iii) sample preparation steps for Electron Backscatter Diffraction (EBSD) and Transmission Kikuchi Diffraction (TKD).

3.1 Processing methods

As introduced in Section 2.3.2, grain size is critical to the improvement of MgB_2 superconducting performance. Therefore, high-energy ball milling was adapted in this project to get refined MgB_2 powder. To avoid the grain growth during processing, field-assisted sintering was applied in the lab and the ultra-high pressure-assisted sintering method was used in Element Six. The mechanisms and operation steps are described in each section.

3.1.1 High-energy ball milling of powders

Apart from grain refinement [92, 142, 143], high-energy ball milling can introduce crystal defects due to plastic deformation brought by high-energy impacts. Moreover, it can lead to mechanical alloying if two or more components are co-milled. There are

several stages in the milling of different powder combinations with different ductility as shown in Figure 3.1 [144, 145].

i. In ductile-ductile systems (A+B), soft powders are first forged and flattened by the milling balls. The flattened layers will then combine to form a composite lamellar structure before being work hardened. With continued milling, these layer-structured particles fracture into small fragments. After long milling times, mechanical alloying (MA) may occur, which leads to the formation of new phases.

ii. In ductile-brittle systems (A+C), ductile components experience deformation while brittle particles undergo fragmentation. Thus, the fragmented brittle particles will be trapped and distributed uniformly in the ductile binder as the welding progresses [146]. Further milling promotes the fracture of composite particles and microstructure refinement.

iii. The milling stages of brittle-brittle systems (C+D) lack adequate studies up to now, but both components are considered to be fragmented in the initial stage of milling [145]. Moreover, harder particles (component C) with a larger size than the softer component D may assist the size reduction of D by acting like a milling medium. During this process, component C can also absorb the collision energy to reduce its particle size, generating small fragments distributed uniformly with the less brittle particles. If harder particles (component C) have a smaller size, they may insert into softer

particles (component D) like small wedges, accelerating the size reduction of softer particles. The relevant study will be described in Chapter 6 and Chapter 7.

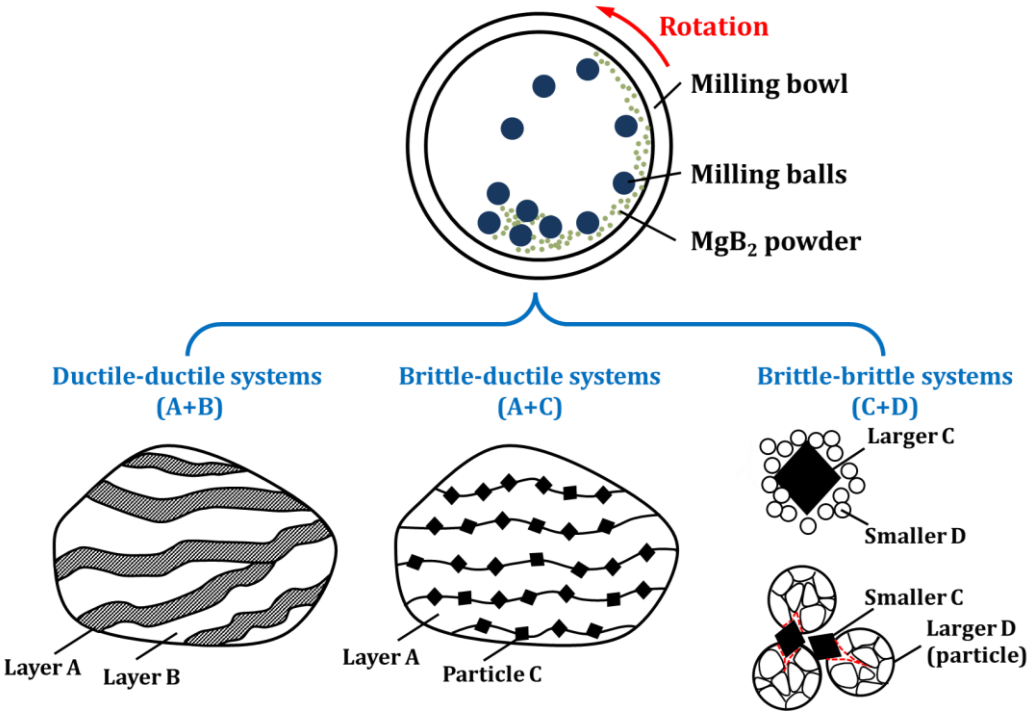


Figure 3.1 Schematic diagrams of ball milling process and particle composites when milling different powder mixtures.

Process variables, such as milling time, rotation speed and ball-to-powder weight ratio, are critical to the final microstructures of particles and their sintering behaviour [145]. In this project, a Fritsch PULVERISETTE 5 planetary ball milling machine was used. Prepared powders were sealed in a 250 ml hardened stainless grinding bowl under Argon. Stainless steel balls (D = 5 mm) were chosen as milling medium with a ball-to-powder ratio of 10:1. The rotation speed was set as 350 rpm, and grinding cycles were performed with 10 min working time separated by 20 min pauses to avoid overheating. These milling variables were suggested by previous group members Dr. Guillaume

Matthews and Dr. Sangeeta Santra. Commercial MgB_2 powder (purity: 99%, Alfa Aesar) was used, and detailed information on the properties of this powder will be presented in Chapter 6.3.

3.1.2 Field-assisted sintering technology

Field-assisted sintering technology (FAST) is a relatively novel sintering technique to process refractory metals and intermetallic, nanostructured materials, amorphous materials and ceramic-metal or ceramic-intermetallic composites [147, 148]. The apparatus can supply low voltages (<10 V) and high direct current up to 10 kA. Schematic diagrams of the setup are shown in Figure 3.2a [149]. The powders are sealed in the graphite die by two punches before cold compacted in a uniaxial pressing. Subsequently, the green compact is placed in the water-cooled vacuum chamber of the field-assisted sintering machine. Pulsed DC electrical current is then applied through electrodes along with uniaxial mechanical pressure [149]. The specimen is sintered by Joule heating for conductive powders or heat transfer from die and punches for insulating powders. The temperature is monitored by pyrometers or thermocouples. Compared with conventional hot pressing, this technique benefits from producing dense samples in a short time.

In this project, a Dr Fritsch DSP 507 FAST apparatus was used to sinter bulk samples under vacuum. The uniaxial pressure was ramped up as the temperature increased and held at 50 MPa once the temperature reached the preset values. After sintering, the

power was cut off and the sample was cooled down under the water-cooling system in the machine to room temperature. Figure 3.2b shows the changes in applied pressure, actual displacement of punches and temperature during processing. The sintering parameters will be described in detail in the experimental chapters. The pressure in the chamber fluctuates around 0.6 bar (60 Pascal), and the dimensions of the consolidated cylindrical samples are around 2 cm in diameter and 3.5 mm in height (Figure 3.2b).

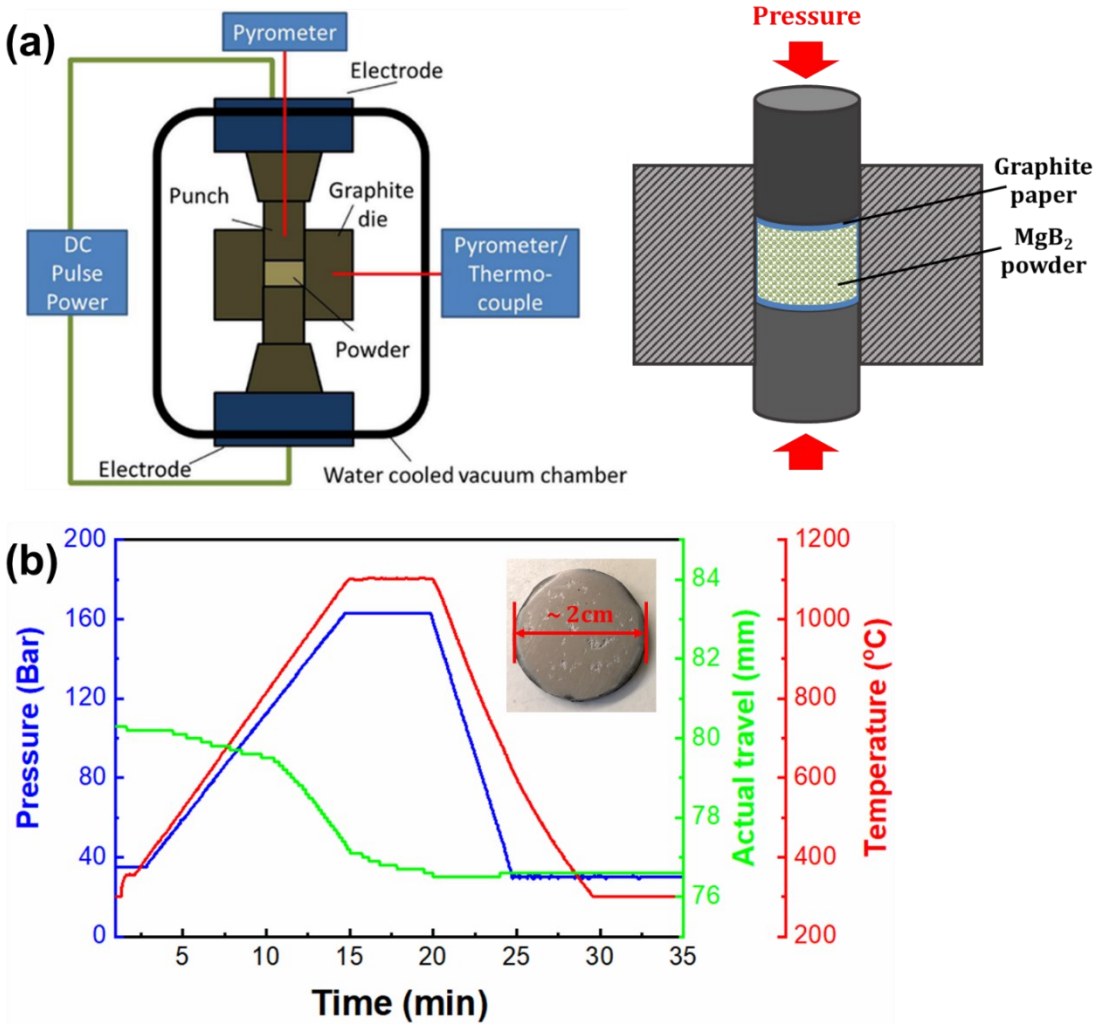


Figure 3.2 (a) Schematic diagrams of a FAST apparatus (Reproduced from [149] with permission from John Wiley & Sons, Inc) and the graphite die. (b) shows an example of variation in pressure, actual travel of punches and temperature during field-assisted sintering of 1 wt% hBN doped MgB_2 bulk sample. The inset figure shows a processed MgB_2 (D ≈ 2 cm, h ≈ 3.5 mm) cylinder.

3.1.3 Ultra-high pressure-assisted sintering

An industrial-scale cubic press was used to apply a high pressure (>4 GPa) to the large bulk samples in ultra-high pressure-assisted sintering, and for the samples studied in this thesis, the preparation was done by industrial collaborators from Element Six. Cu/Ti layers were used as sheath materials for preparing MgB_2 samples, as Figure 3.3 shows. An additional Nb layer acts as a chemical barrier to prohibit the reaction between the outer sheath and MgB_2 powders during heat treatment. The processing parameters will be described in Chapter 5 in detail.

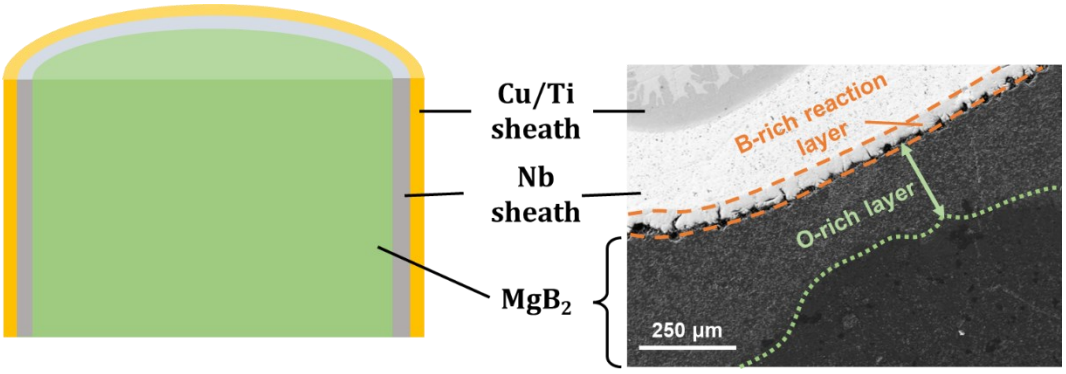


Figure 3.3 Schematic of a part of the cylindrical sample prepared by ultra-high pressure-assisted sintering. On the right, an SEM image taken by the previous group member Dr. Sajjad Amirkhanlou shows the different layers at the edge of the sample.

3.2 Characterisation techniques

The characterisation involves phase analysis by X-ray diffraction (XRD), the microstructural investigation by microscopes and superconducting properties by physical properties measurement system (PPMS).

3.2.1 X-ray diffraction

X-ray diffraction (XRD) is based on Bragg reflections of the incident X-ray beam by the crystal lattice, revealing structural information on materials. In addition to simple qualitative analysis such as phase identification, one can separate the contributions of crystallite size broadening and microstrain broadening by deconvoluting the peak profile using X-ray diffraction line profile analysis. Analysis of X-ray peak broadening is mainly divided into two categories. One type is to empirically fit the peak profile and obtain accurate peak information such as position, shape (full width at half maximum) and intensity. These data are used by the Scherrer equation, Williamson–Hall or Warren-Averbach plots to calculate crystallite size and/or microstrain [150, 151]. Whole pattern fitting such as Rietveld refinement is another way to characterise nanocrystalline or severely deformed grains [152, 153]. In this method, an ideal diffraction pattern calculated from crystal structures is fitted to the actual experimental data by the least square method. The optimal set of fitting parameters can be used to obtain quantitative data on the sample.

In this project, phase identification and quantitative analysis were carried out via powder X-ray diffraction using Cu-K_α radiation of 0.154 nm generated at 40 kV and 40 mA in a PANalytical Empyrean diffractometer in Bragg-Brentano geometry with parafocusing optics [154]. Rietveld refinement in the HighScore Plus software was applied to calculate phase fraction, lattice parameters, crystallite size and microstrain.

The XRD errors in analyzing MgB_2 powders and bulk samples have been studied previously by Dr. Guillaume Matthews in my group (Table 3.1) [67]. The precision of different parameters was defined as half the difference of the maximum and minimum values calculated by Rietveld methods after analysing five nominally identical bulk samples prepared by field-assisted sintering.

Table 3.1 The precision of MgB_2 crystallite size, strain and lattice parameters calculated by Rietveld refinement (Copyright © 2020 by IOP Publishing. Reproduced from [67] licensed by CC BY 4.0).

	Crystallite size (nm)	Microstrain (%)	a axis (Å)	c axis (Å)
Precision	±12	±0.005	±0.0002	±0.0003

3.2.2 Scanning electron microscopy and energy dispersive X-ray spectroscopy

Scanning electron microscopy (SEM) and energy dispersive X-ray spectroscopy (EDX) are used for microstructural characterisation and elemental analysis. When a focused beam of electrons interacts with a specimen, several kinds of signals, such as secondary electrons (SE), backscattered electrons (BSE) and characteristic X-rays, will be produced. SE imaging is used to gain insight into the surface roughness and topography of samples. In contrast, BSE imaging probes a larger depth of the sample as backscattered electrons have higher energy than secondary electrons. In addition, the intensity of backscattered electrons is much more dependent on the average atomic number, so the BSE imaging mode reveals chemical variations in the sample. Collecting

characteristic X-rays produced by electronic transitions in atoms of the sample excited by the primary SEM beam with EDX detectors can be used to give the elemental composition of a point, line or region in the specimen. Light elements with atomic numbers below 11 complicate the situation because signals with longer wavelengths are easily absorbed in the sample itself (or the EDX detector) and so have a low yield at a low voltage [155]. However, a higher accelerating voltage for the SEM beam will increase the interaction volume so surface details will be lost, and rapid X-ray absorption in the sample can lead to the generation of additional X-rays [156].

The characteristic K_α X-rays for the relatively light elements Mg, B, N and O are at 1.254 keV, 0.183 keV, 0.392 keV and 0.525 keV [157]. An accelerating voltage of 10 kV has been chosen in this study to fully excite the X-rays from these elements. Moreover, thin foils were prepared to reduce the interaction volume of the electron beam, which improves the spatial resolution of EDX analysis so allows the chemistry of particles tens of nanometers in diameter to be analysed. The preparation steps will be described in Section 3.3.2.

This part of work was conducted in the David Cockayne Centre for Electron Microscopy. Microstructural evolution and composition analysis were characterised on a Zeiss Merlin field-emission scanning electron microscope (FE-SEM) equipped with an Oxford Instruments XMax 150 mm^2 EDX detector. The applied accelerating voltage and the current were set as 10 kV and 2 nA for bulk samples, while voltage was adjusted to 5 kV when characterising thin foils. Quantitative analysis of EDX data was done

using the Aztec software. Simple element maps based on peak selection in the EDX spectrum do not deal with peak overlaps, and strong background signals produced by heavier elements can lower the detection sensitivity of light and minor elements. Therefore, TruMap corrections were used to remove false data from the X-ray background and eliminate map artifacts. Similarly, QuantLine utilizing the Tru-Q routines in the Aztec software was used to obtain quantitative element variations [158]. For point analysis, the position and shape of peaks in the spectrum were fitted by an algorithm to calculate the concentration of different elements. The raw mass fraction and standard deviation (σ) can be given by the software, and the relative standard deviation was calculated by dividing by the mean mass fraction. Here I chose eight replicate analyses to calculate the mean value from which atom fractions were obtained E_0 = 10 keV (Table 3.2). Taking the stoichiometric formula as the expected value of atom fractions, the relative error can be calculated by [159],

$$\text{Relative error} = \frac{\text{analyzed value} - \text{expected value}}{\text{expected value}} \times 100\%$$

Table 3.2 Analysis of MgB_2 and MgB_4 from 8 measurements at E_0 = 10 keV. Analysis performed with Mg K_α and B K_α. σ refers to standard deviation and σ_{rel} is relative standard deviation.

Compounds	MgB_2		MgB_4	
Elements	Mg	B	Mg	B
Raw mass fraction (8 replicates)	0.5241	0.4589	0.3730	0.6122
Standard deviation (σ)	0.0080	0.0082	0.0043	0.0045
σ_{rel} (%)	1.5	1.8	1.2	0.73
Atom fraction (8 replicates)	0.3368	0.6632	0.2132	0.7868
Relative error (%)	1.1	-0.52	6.6	-1.6

3.2.3 Electron backscatter diffraction

Electron backscatter diffraction (EBSD) as an add-on technique to SEM instruments has been widely applied to characterising texture, grain morphology, strain and different phases in crystalline materials [160]. This analysis is based on Kikuchi patterns giving crystallographic information about the sample surface. When electrons interact with solid matter, they will be scattered by the crystal lattice. Three scattering mechanisms are classified according to the energy loss (elastic or inelastic) and phase changes (coherent or incoherent) of emitted electrons compared with the incident electrons. The elastic and coherent scattering obeys Bragg's law so there is a significant direction change and no energy loss. Thermal diffuse scattering, also known as phonon scattering, arises from energy exchange with lattice vibrations in the crystal. In this process, scattered electrons only lose a small amount of energy so they are quasi-elastic but incoherent. Electrons that have lost a lot of energy from inelastic and incoherent scattering contribute to the background of Kikuchi patterns. The generation of Kikuchi bands in electron backscatter diffraction patterns involves two steps: thermal diffuse scattering of the incident beam, followed by Bragg reflections by specific crystallographic planes [161, 162]. Kikuchi bands rather than diffraction spots are observed, positions of which can be indexed to calculate the grain orientation. Tilting the sample (~70^{o}) is beneficial for the escape of BSE from the specimen surface and increases BSE yield. The best lateral resolution parallel to the tilt axis and longitudinal

resolution in the perpendicular direction varies over the range of 20 ~ 35 nm and 60 ~ 100 nm respectively, depending on the composition of the material and accelerating voltages [163, 164]. The conventional EBSD setup is shown in Figure 3.4. It is worth mentioning that the grain size measured by EBSD is defined by misorientation angles larger than 15°, and this differs from the crystallite size extracted from XRD data that may be influenced by grain defects such as dislocations, especially when arranged into low angle grain boundaries.

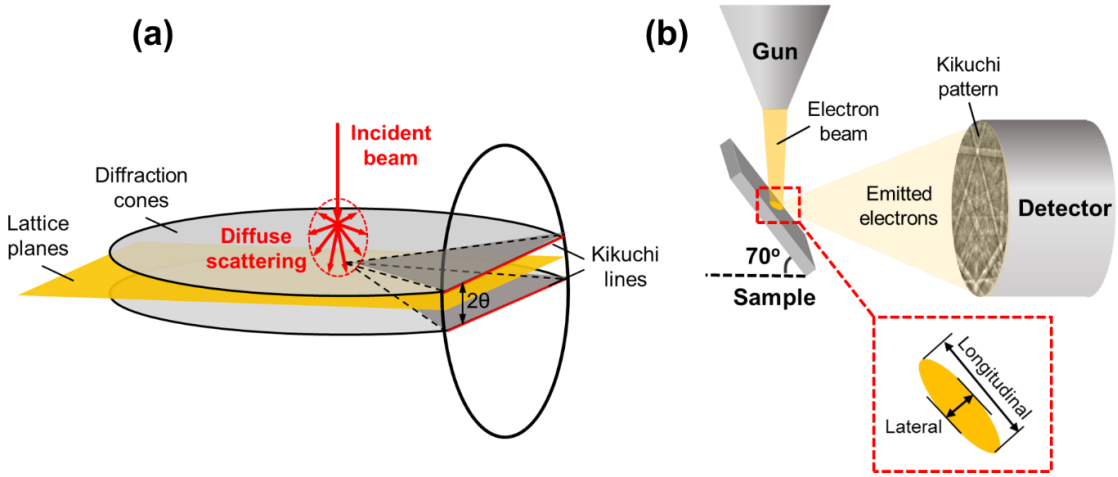


Figure 3.4 Schematics of (a) the scattering process to generate Kikuchi patterns and (b) the EBSD setup when characterising bulk samples.

In this project, the Carl Zeiss Merlin (FEG-SEM) fitted with a Bruker Quantax EBSD system and eFlash camera and forward scattered electron detectors were applied for high resolution EBSD patterning. The working distance and the detector distance were set as 18 mm. Data acquisition was performed using Esprit software with the accelerating voltage and beam current of 20 kV and 10 nA respectively. The post-processing was conducted using HKL Channel 5 software. A high misorientation angle (15°) was chosen to define the grains when plotting the grain size distribution. The black

pixels in EBSD maps are the unindexed points where the Kikuchi pattern was not recognized, maybe as a result of highly-deformed grains or 2 overlapping patterns from small crystals.

3.2.4 Transmission Kikuchi diffraction

Transmission Kikuchi diffraction (TKD) is a newly developed technique to characterise ultrafine-grained materials [162, 165]. Benefiting from a much smaller beam-specimen interaction volume in electron-transparent samples, this technique significantly improves the spatial resolution to a few nanometers. The incident beam also undergoes thermal diffuse scattering before Bragg reflections, as above, but Kikuchi patterns are formed by transmitted electrons passing through thin samples. There are two kinds of arrangements for TKD: off-axis and on-axis as shown in Figure 3.5. The main configuration differences are the sample tilt angle and the detector position. A low tilting angle ($10^{o} \sim 40^{o}$) is required in off-axis geometry because of the conventional vertical detector. In contrast, detectors are inserted horizontally below the foils in on-axis TKD, which greatly enhances the yield of signals and minimizes gnomonic distortions of Kikuchi patterns brought by sample tilt [166, 167].

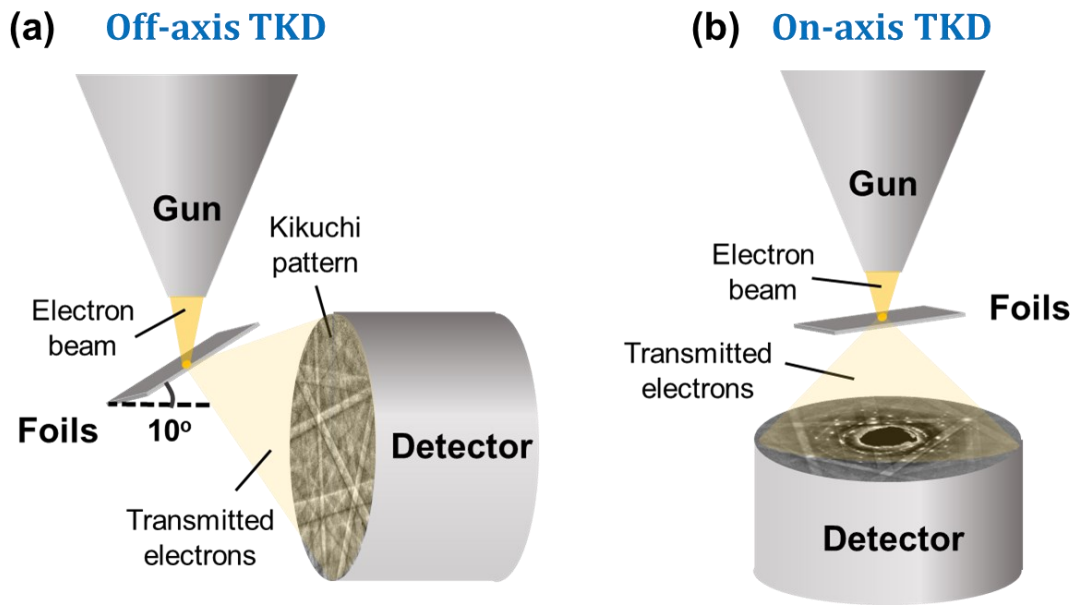


Figure 3.5 Schematics of experimental configurations for (a) off-axis TKD and (b) on-axis TKD.

The detailed configuration of on-axis geometry used in this project has been described elsewhere [162]. In a Zeiss Merlin FEG-SEM system, a Bruker eFlash EBSD detector configured with the OPTIMUS™ TKD head was used to characterise small nano-impurities within and/or among MgB_2 grains. The accelerating voltage and the probe current were set as 30 kV and 1.5 nA, and the working distance was fixed as 5 mm.

3.2.5 Physical property measurement system

Magnetic properties were measured using a 16 T Quantum Design physical properties measurement system (PPMS) with a Vibrating Sample Magnetometer (VSM) in the Clarendon Laboratory as shown in Figure 3.6a and b. The basic theory of VSM is that oscillation of a superconducting sample in a magnetic field can induce a voltage in a compact gradiometer pickup coil that is expressed as,

$$V_{coil} = 2\pi fCmAsin(2\pi ft) \quad (3.1)$$

where f is oscillation frequency, C is a constant, m is the DC magnetic moment of the sample, A is oscillation amplitude and t is the time. The sample position and oscillation amplitude are controlled, and position encoder signals can be generated as a reference. The VSM detection module then processes encoder signals and detected voltages from the pickup coil to give data on the moment of the sample. By adopting a counter-wound configuration to the pickup coil, this system has an oscillation amplitude over 1 ~ 3 mm and a frequency of 40 Hz. With a data rate of 1 Hz, changes in the magnetization less than 10^{-6} emu can be resolved. A non-magnetic brass holder is used for mounting cuboid MgB_2 samples that are fixed tightly by two quartz cylindrical holders. Kapton tape is used to avoid the loosening of holders during vibration as shown in Figure 3.6c. The automation and control of VSM operations are carried out by MultiVu software.

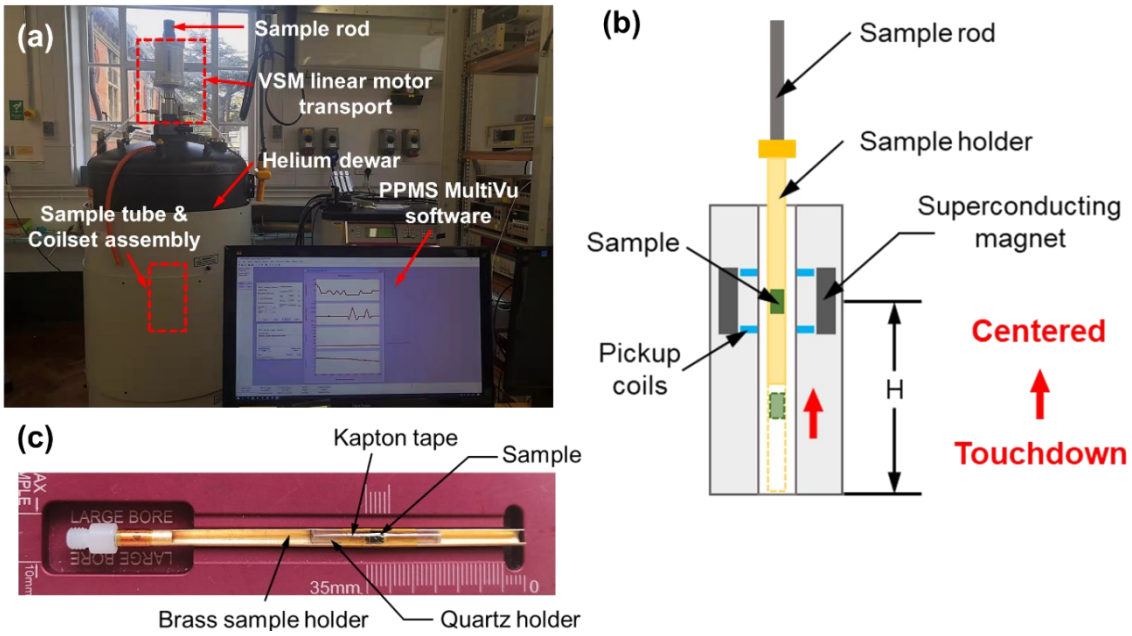


Figure 3.6 (a) shows Physical Property Measurement System (PPMS) with the Quantum Design Vibrating Sample Magnetometer (VSM) option (b) is the interior schematic diagram of the standard coilset puck and the touchdown centering operation. (c) shows the configuration of the mounted sample.

The cuboid samples are around 2 × 2 × 3 mm in size. All samples were cooled under the zero field. T_c was measured during moment-temperature sweeping at a fixed applied magnetic field (5 mT). DC susceptibility was calculated by $\chi_{eff} = \frac{\chi}{1+n\chi}$, where χ is the local material property and χ_{eff} is the effective susceptibility, taking into account demagnetization effects. The demagnetisation factor, n, is related to the geometry of the samples, and $n \approx \frac{4ab}{4ab+3c(a+b)}$ for cuboid samples in this study, where a, b are the dimensions of the cross-section (b > a) and c is the dimension parallel to the applied field [168]. Moment-field (M-H) sweeps were taken at 4.2 K and 20 K. 4.2 K (boiling point of liquid helium). 20 K were chosen because they are standard measurement temperatures used for assessing the properties of MgB_2. This allows comparison with work in the literature. The current density was calculated by Bean's critical state model, $J_c = \frac{2\Delta M}{a(1-a/3b)}$. ΔM is obtained from the hysteresis loops and will be introduced in detail in Chapter 4. To examine the homogeneity of the bulk samples, three cuboid samples were cut from the central regions to the outer regions along the axis, and when measured, little difference was found. Details about M-H measurements and methods for extracting effective J_c values will be discussed in Chapter 4. Additionally, prior to cooling a new sample, the sample chamber was warmed up to 100 K and the magnetic field is set to 0 in the oscillate mode. The system would stabilise for at least 16 hours to eliminate the residual field in the PPMS superconducting magnet. %Uncertainty in measured ΔM estimated by analysing 3 hysteresis loops of the same sample ($\frac{\text{Uncertainty}}{\text{average number}} \times 100\%$) was around 4 %.

3.3 Sample preparation for characterisation

Unlike SEM and EDX, EBSD has high requirements for a good sample surface, and the thickness of thin foils is critical for TKD characterisation. Therefore, details for the preparation of sample/thin foils are introduced in this section.

3.3.1 Bulk samples for EBSD

Since EBSD is surface-sensitive, the preparation of samples with a flat surface free of mechanical strain needs extra care. Cylindrical pellets produced by FAST or ultra-high pressure-assisted sintering were cut into small pieces using a Buehler IsoMet Low Speed Saw. Subsequently, samples were polished by SiC grinding discs from #800 to #4000 before chemical polishing with colloidal silica suspension for 3 ~ 4 h. The microstructures of the polished cross-sections were checked by an optical microscope. After polishing, samples were first immersed in ethanol and ultrasonically cleaned for around 5 min. Residual silica nanoparticles (~90 nm) that adhere to the surface when the organic solvent is evaporated were removed by wiping several times with soft tissue. Further ultrasonic cleaning for around 10 min was used to get a good and clean sample finish.

3.3.2 Thin foils for TKD

Ion milling using an energetic ion beam to gently remove the sample surface is effective for preparing thin foils of non-conductive materials, which has been used exclusively

in this project to prepare electron transparent MgB_2 samples. Initially, thin discs with the thickness of central regions below 20 μm were prepared by cutting, grinding and dimpling, as shown in Figure 3.7. The samples were then thinned further using conventional Ar ion milling using a Fischione Model 1010.

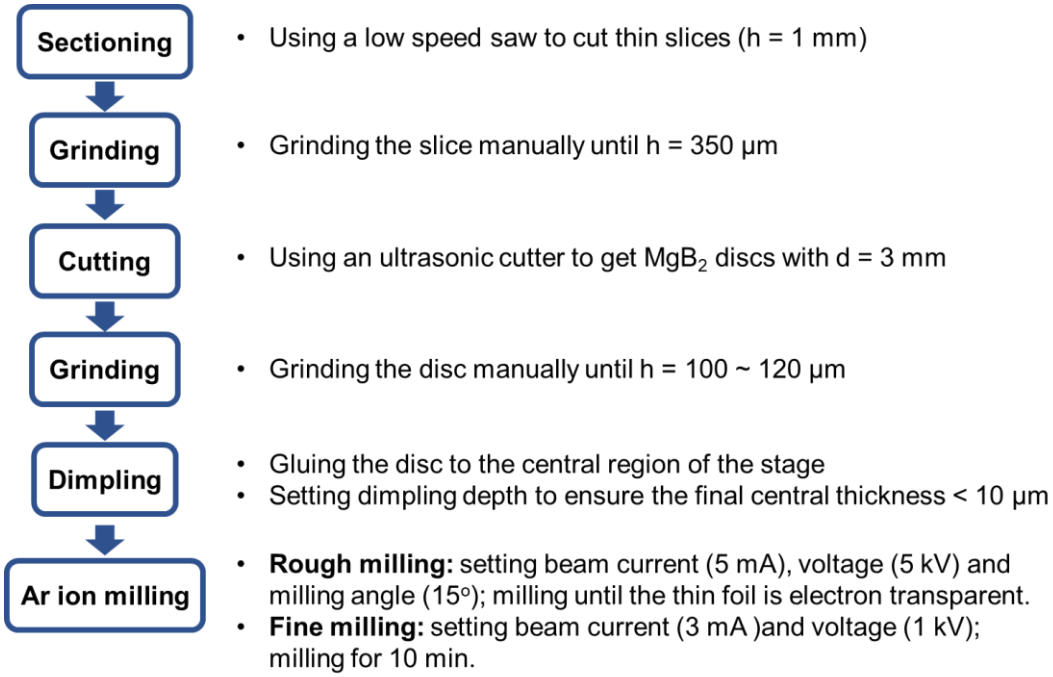


Figure 3.7 Schematic showing steps of preparation for TEM foils.

Chapter 4 Theoretical analysis of magnetization data

This chapter mainly deals with two primary problems that are often ignored in the analysis of data from superconducting measurements. One is the extraction of J_c using Bean's critical state model assuming that currents circulate uniformly through the whole superconducting sample, without proper consideration of sample microstructure. The other is the identification of possible flux pinning mechanisms in superconductors by plotting pinning curves directly from J_c data without applying self-field corrections. A brief introduction of magnetic measurements and Bean's critical state model is given in Section 4.1 . In Section 4.2 , I develop or modify three models step by step: the cell model, the percolation model and the duplex microstructure model. These models are the basics for discussing the effects on the magnetic moment from currents flowing on different length scales that are influenced by microstructural homogeneity, anisotropy, impurities, etc. in processed bulk samples. Only if the dominant current flowing dimension is figured out, can the superconducting performance be interpreted reliably. To show the application of these models intuitively, some typical types of microstructures in bulk samples are discussed. By applying sensible parameters in the theoretical models, the $J_c(B)$ performance of different types of microstructures is simulated, providing templates for data processing in subsequent experimental chapters. In Section 4.3 , the necessity to correct self-field is introduced, followed by instructions for carrying out self-field corrections on the $J_c(B)$ experimental data.

The implications of the systematic discussion in this Chapter lie in two aspects: (i) establishing the link between the microstructures and superconducting properties theoretically and (ii) pointing out important issues in data processing that has been overlooked in previous studies. From this chapter on, the term magnetic field refers to magnetic flux density (B) instead of magnetic field strength (H).

4.1 Magnetic measurements and Bean's critical state model

The current density can be derived from measuring spatial magnetic field distribution or magnetic moments contributed from all current loops over the sample volume:

$$\nabla \times \mathbf{B} = \mu_0 \mathbf{J} \tag{4.1}$$

$$\mathbf{m} = \frac{1}{2} \iiint \mathbf{r} \times \mathbf{J}(\mathrm{r})\, \mathrm{dV} \tag{4.2}$$

Eq. 4.1 refers to Ampere's law and maps of local current density distribution can be obtained via scanning hall probe microscopy [169]. In contrast, bulk current density (J_c) can be obtained at a given applied magnetic field (B_{app}) by measuring the magnetic moment generated by currents circulating in a superconducting sample (Eq. 4.2).

4.1.1 Magnetic hysteresis

A hysteresis loop for a typical MgB_2 bulk sample, taken by sweeping the magnetic field after cooling in the zero field, is shown in Figure 4.1. As the applied field (B_{app}) increases from 0, initially flux is expelled from the interior of the superconductor as the superconductor is in the Meissner state and the initial slope is the Meissner slope. For

fields up to the lower critical field (B_{c1}) the surface layer accommodates shielding currents producing a field to cancel out B_{app} so the field in bulk of the superconductor is still zero. When B_{app} exceeds B_{c1}, the flux begins to penetrate from the outside edge of the superconductor towards the interior in the form of quantized flux lines and the magnitude of the negative moment starts to drop. At the penetration field (B^*), flux reaches the centre of the sample, and the superconductor is said to be fully penetrated. Only when the absolute value of the maximum field (B_{max}) reaches the upper critical field (B_{c2}) of the superconductor will the moment reach 0. If $B_{max} < B_{c2}$ as the field is ramped down, flux lines are trapped within the superconductor and the current flow in the outer region of sample changes direction to shield the interior of the sample from the reduction in the applied field. This reverse leg, where the currents are gradually reversing direction from the edge to the centre of the sample, has the same slope as the Meissner slope (Figure 4.1).

In the rest of the descending-field branch, the average field inside the superconductor is in the same sense as B_{app} so the moment is positive. Because, in practice, the critical current density increases as B_{app} is reduced, the moment also increases in magnitude. The maximum moment is not achieved until the direction of B_{app} is reversed and its value reaches $-B_{peak}$. This is because, at $B = 0$, the currents flowing in the sample generate a self-field that suppresses the value of J_c. When the reversed B_{app} compensates this self-field, the local field inside the samples is minimized and J_c (and the magnetic moment of the sample) reaches its highest value. After finishing the branch where the

negative field magnitude increases to B_{max}, the remaining branches of the hysteresis curve are completed by sweeping the field from $-B_{max}$ back to $+B_{max}$ again.

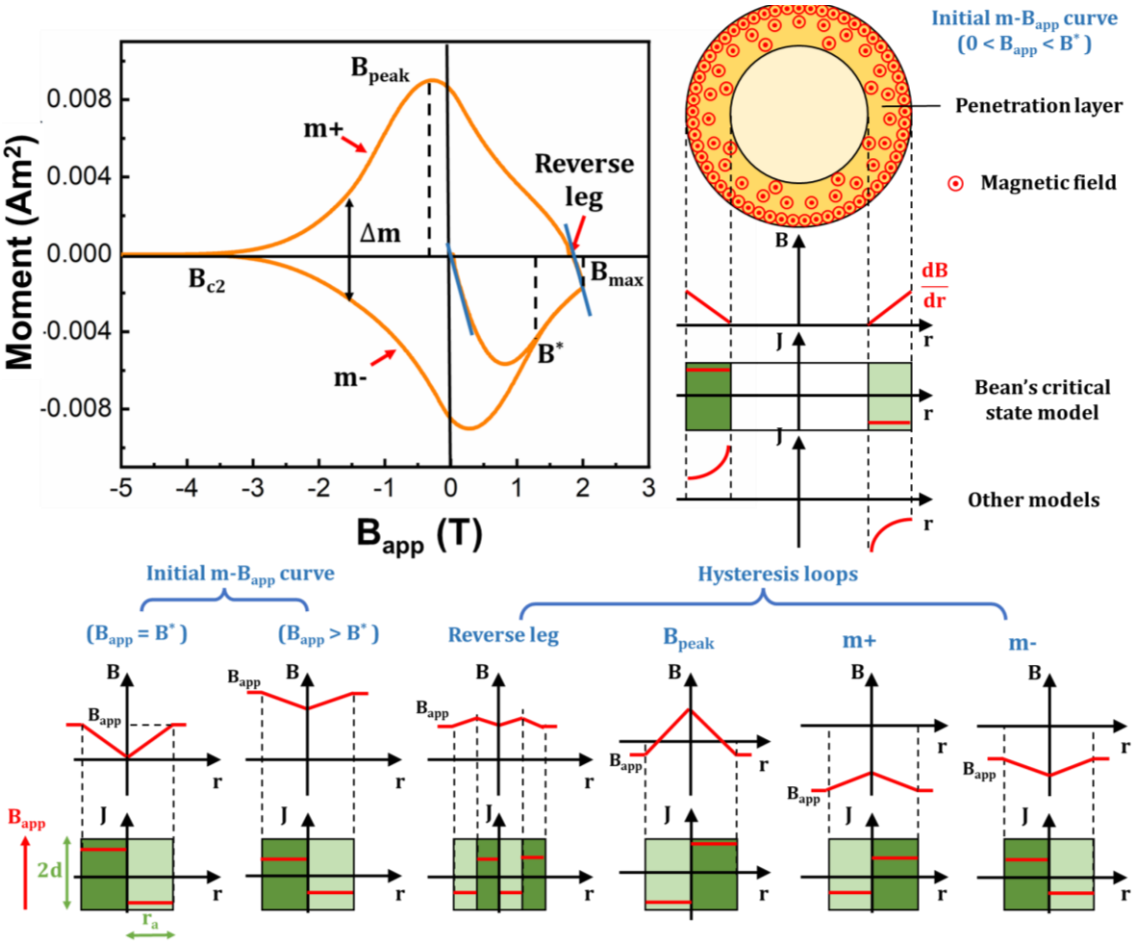


Figure 4.1 Hysteresis loop measured for a MgB_2 bulk sample at 4.2 K in the axial magnetic field. The right figure sketches the flux density gradient in the surface layer when B_{app} initially increases from 0. The bottom subfigures depict B and corresponding J_c profiles across the diameter of the sample.

4.1.2 Bean's critical state model

If both the magnetic field and the axis of cylindrical sample are in the z direction, the critical currents flow azimuthally and Eq. 4.1 can be simplified as:

$$\mu_0 J = -\frac{\partial B}{\partial r} \qquad (4.3)$$

Some models, such as Kim model, that apply different $J_c(B)$ functions have been proposed from the phenomenological point view, which are summarised in Table 4.1.

Table 4.1 Lists of phenomenological $J_c(B)$ models.

Model	Formula	Reference
Bean's model	$J_c = \text{costant}$	[170]
Kim model	$J_c(B) = \frac{k}{B + B_0}$ ($B_0$and k are constants)	[171, 172]
Power-law model	$J_c(B) = k_1\|B\|^{-q}$ ($k_1$and q are constants)	[173]
Exponential-law model	$J_c(B) = J_{c0}\exp(B/B_1)$ (J_{c0} and B_1 are constants)	[174]

The most commonly used critical state model is Bean's critical state model which assumes that J_c is independent of B and only three current density values (0, J_c and $-J_c$) exist in the sample. At a given applied field, if samples have already been fully-penetrated, the same J_c will flow everywhere in the sample, so the magnitude of field gradient is constant, but its sign can be negative or positive. J_c is deduced from the magnetization (if the sample geometry and dimensions are known) by assuming that currents circulate in perfect macroscopic loops throughout the entire sample. In general, the magnetization of a superconductor has two contributions, reversible and irreversible, and it is only the irreversible magnetization (M_{irr}) that is related to J_c. To subtract the reversible background, the width of the hysteresis loop Δm (the difference between the moment in the increasing and the decreasing field branches) is used: $\Delta m = m^+ - m^-$. M_{irr} can be calculated once the sample volume is known,

$$M_{irr} = \frac{\Delta M}{2} = \frac{\Delta m}{2V} = \frac{\frac{1}{2} J_c \iiint r \, dV}{V} \tag{4.4}$$

4.2 Reliable J_c extraction

If viewing a superconductor as an assembly of many cells, the cell inside is homogeneous and has consistent superconducting performance, but the current may have limited interconnectivity between adjacent cells. The cell defined here can refer to grains or other large features in bulk samples. Superconducting currents are classified according to two different criteria. The first is the length scale of current loops flowing. Currents circulating in the entire sample are called $J_{c,macro}$ while those flowing within cells are called $J_{c,cell}$. Under the second criterion of intrinsic or extrinsic factors that affect current density, two types of J_c can also be defined. Intrinsic factors include pinning strength and upper critical field (B_{c2}). As introduced in Section 1.4 , grain boundary pinning is the dominant mechanism in polycrystalline MgB_2 samples. Theoretical $J_c(B)$ curves calculated using Dew-Hughes's grain boundary pinning formula are notated here as $J_{c,int}$ which refers to the maximum current density that can be sustained in the sample without loss. $J_{c,int}$ value is only affected by intrinsic properties. Correspondingly, extrinsic factors refer to the microstructure features that influence macroscopic current transport, such as sample homogeneity, anisotropy, connectivity, etc. Besides, when considering anisotropy in polycrystalline MgB_2 samples, $J_c(B)$ calculated using current percolation models [175] is defined as $J_{c,\,perc}$.

4.2.1 Cell model for isotropic superconductors

The assumption in this model is that cells with the same sizes and shapes in fully-dense

samples pack perfectly to completely fill the volume. For simplicity, the 3D critical state of superconductors is studied by a 2D model. Take a cylinder as an example, the cell has the same height (H) as the cylindrical sample but its size in the horizontal planes is much smaller than the sample diameter D. In a standard magnetization measurement, B_{app} is applied along the Z direction which induces current loops within planes throughout the whole sample.

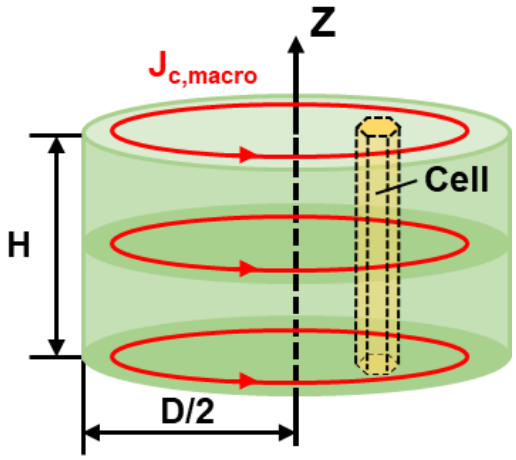


Figure 4.2 Sketch of a cell in the cylindrical sample with height H and diameter D.

When grain boundary pinning is dominant, Dew-Hughes's GB pinning formula gives the dependence of J_c on the magnetic field B [21]:

$$J_c = F_0 \frac{[1 - B/B_{c2}]^2}{\sqrt{B_{c2}B}} \tag{4.5}$$

4.2.1.1 Well-connected cells in homogenous superconductors (Cell model A)

Figure 4.3 shows the $J_{c,macro}$ flows through the whole sample without impairment. Bean's critical model is directly applied in this case has the form as,

$$\Delta M = \frac{2J_{c,macro}\int_0^H \int_0^{D/2} \pi(D/2)^2 drdh}{V} = \frac{J_{c,macro}D}{3} = G_{sample}J_{c,macro}D \qquad (4.6)$$

where r is the radius of the cylindrical sample and V is sample volume. G_{sample} is related to the sample geometry. It can be seen that $J_{c,macro} = J_{c,int}$ in isotropic, fully-dense and homogenous samples with well-connected cells.

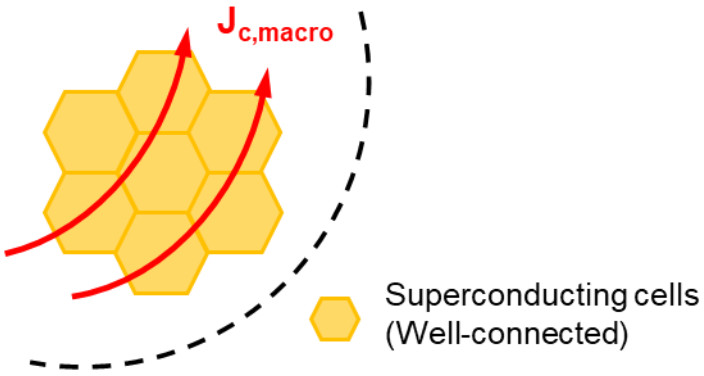


Figure 4.3 Schematic diagram showing a part of fully-dense and homogeneous samples that consists of well-connected superconducting cells.

4.2.1.2 Unconnected cells in homogenous superconductors (Cell model B)

The other limit for fully dense, homogeneous samples is the case where the cell boundaries are impervious to superconducting current flow, so the cells are completely isolated from one another. As shown in Figure 4.4, currents cannot flow across the cell boundaries ($J_{c,macro} = 0$) so are confined within cells and form isolated current loops, $J_{c,cell}$. If cells are approximately viewed as cylinders with diameter d_{cell}, the cell volume is given by $V_{cell} = \pi(d_{cell}/2)^2 H$. The moment of each cell, m_{cell} can be obtained from

$$m_{cell} = J_{c,cell}\int_0^H \int_0^{d_{cell}/2} \pi(d_{cell}/2)^2 drdh = J_{c,cell}\frac{\pi(d_{cell}/2)^3 H}{3} \qquad (4.7)$$

Since, in this case, the sample is fully-dense, the number of cells N can be calculated

from the sample volume V using $N = V/V_{cell}$. Therefore,

$$M = \frac{m}{V} = \frac{\sum_{i=1}^{N} m_{cell}}{V} = \frac{m_{cell}}{V_{cell}} = \frac{J_{c,cell} d_{cell}}{6} \quad (4.8)$$

ΔM can be calculated by,

$$\Delta M = \frac{J_{c,cell} d_{cell}}{3} = G_{cell} J_{c,cell} d_{cell} \quad (4.9)$$

where G_{cell} depends on the cell geometry. It can be seen that $J_{c,cell} = J_{c,int}$ in isotropic, fully-dense and homogenous samples with unconnected cells. Moreover, the magnitude of the magnetization is directly proportional to the cell size d_{cell}. If $G_{sample} \approx G_{cell}$, one can see that ΔM in unconnected samples is smaller than the fully-connected samples by a factor of $\approx \frac{d_{cell}}{D}$.

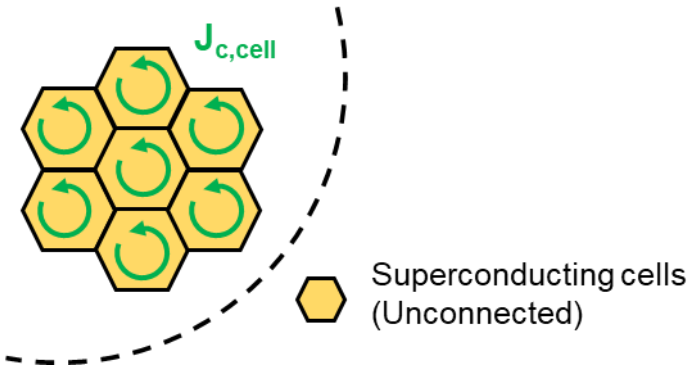


Figure 4.4 Schematic diagram showing a part of fully-dense and homogeneous samples that consists of unconnected superconducting cells.

4.2.1.3 Partially connected cells in homogenous superconductors (Cell model C)

If some current can pass through cell boundaries, two types of currents, $J_{c,macro}$ and $J_{c,cell}$, co-exist in homogeneous samples with partially connected cells (Figure 4.5). The fraction of connectivity is represented by A_{con} ($0 < A_{con} < 1$), where $A_{con} = 0$ and $A_{con} = 1$ correspond to the previously-introduced models for completely unconnected and fully

connected cells, respectively. $J_{c,int}$ is the sum of the $J_{c,cell}$ and $J_{c,macro}$ values. Therefore,

$$J_{c,macro} = A_{con} J_{c,int} \tag{4.10}$$

$$J_{c,cell} = J_{c,int} - J_{c,macro} = (1 - A_{con}) J_{c,int} \tag{4.11}$$

The total magnetic moment is the summation of moments generated by macroscopic current flowing around the bulk sample ($J_{c,macro}$) and smaller local current loops circulating within unit cells ($J_{c,cell}$) as,

$$\Delta m = \Delta m_{macro} + \sum_{i=1}^{N} \Delta m_{cell,i} \tag{4.12}$$

Therefore,

$$\begin{aligned} \Delta M &= G_{sample} J_{c,macro} D + G_{cell} J_{c,cell} d_{cell} \\ &= \left[G_{sample} A_{con} D + G_{cell} (1 - A_{con}) d_{cell} \right] J_{c,int} \\ &= \left[A_{con} D + (1 - A_{con}) d_{cell} \right] G J_{c,int} \left(\text{if } G_{sample} \approx G_{cell} \approx G \right) \end{aligned} \tag{4.13}$$

As to practical microstructures in processed MgB_2 samples, connectivity problems arise from impurities or pores with much smaller sizes than the cell size.

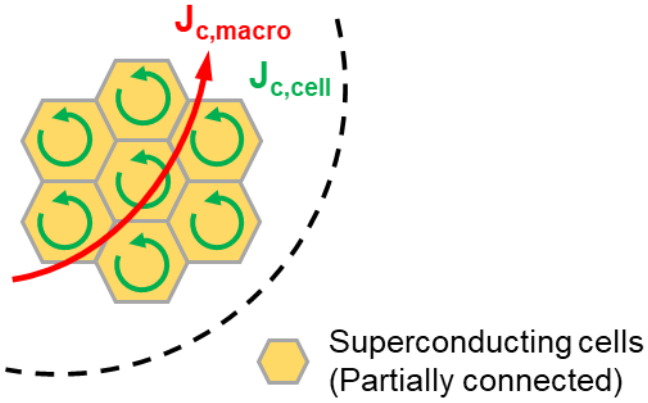


Figure 4.5 Schematic diagram showing a part of fully-dense and homogeneous samples that consists of partially connected superconducting cells.

4.2.1.4 Partially-connected cells in inhomogeneous superconductors (Cell model D)

This case is based on Cell model C but the superconductor is inhomogeneous due to the presence of non-superconducting cells. The size of these non-superconducting cells is assumed to be the same as superconducting cells but superconducting currents cannot pass through these regions (Figure 4.6). A prerequisite for the validity of this model is the fraction of superconducting cells (p_s) far exceeds that of non-superconducting cells, so the model can be simplified as the reduction of superconducting cross-section. $J_{c,macro}$ is viewed as nominal current density by dividing by the entire cross-section instead of the effective current density ($J'_{c,macro}$) that excludes the non-superconducting area.

$$J_{c,macro} = p_s J'_{c,macro} = A_{con} p_s J_{c,int} \tag{4.14}$$

However, when estimating $J_{c,cell}$, the local $J'_{c,macro}$ should be subtracted from $J_{c,int}$, giving

$$J_{c,cell} = (1 - A_{con}) J_{c,int} \tag{4.15}$$

Δm can be expressed by,

$$\Delta m = \Delta m_{macro} + \sum_{i=1}^{N_s} \Delta m_{cell,i} \tag{4.16}$$

where N_s is the number of superconducting cells with $N_s = p_s N$. Therefore,

$$\begin{aligned} \Delta M &= G_{sample} J_{c,macro} D + p_s G_{cell} J_{c,cell} d_{cell} \\ &= \left[G_{sample} A_{con} D + G_{cell} (1 - A_{con}) d_{cell} \right] p_s J_{c,int} \\ &= \left[A_{con} D + (1 - A_{con}) d_{cell} \right] G p_s J_{c,int} \left(\text{if } G_{sample} \approx G_{cell} \approx G \right) \end{aligned} \tag{4.17}$$

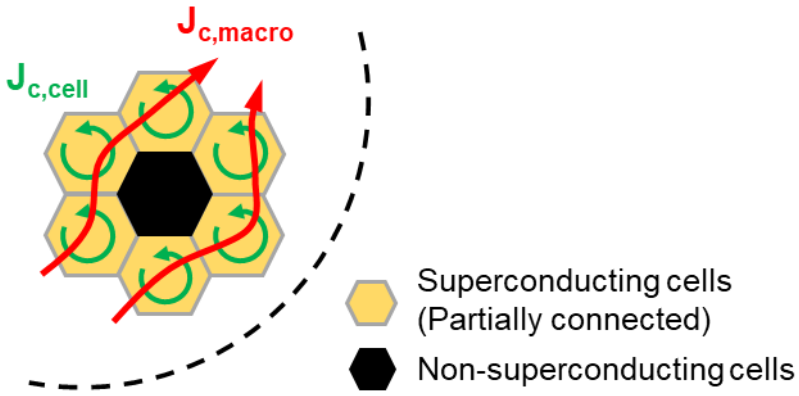


Figure 4.6 Schematic diagram showing a part of fully dense but inhomogeneous samples that consists of partially connected superconducting cells and non-superconducting cells.

4.2.2 Percolation model for anisotropic superconductors

Percolation concepts were initially employed to study the granularity in high temperature superconductors where grain boundaries severely limit J_c, but are also applicable to study the effects of anisotropy in polycrystalline MgB_2 samples, as explained by Eisterer et al [175]. Since the upper critical field of MgB_2 is much smaller along the direction parallel to the c axis than perpendicular to the c axis, the current-carrying capacity of superconducting grains varies with the angle (θ) between the c axis of MgB_2 unit cell and the direction of B_{app} (Figure 4.7a). Unfavourably aligned grains will lose their superconductivity at a low magnetic field, so the supercurrent has to divert around them (Figure 4.7b). The $J_{c,macro}$ drops as a result of the reduced cross-sectional area for current transport at higher B_{app} until all percolative paths are cut off and only microscopic current loops ($J_{c,micro}$) remain (Figure 4.7c).

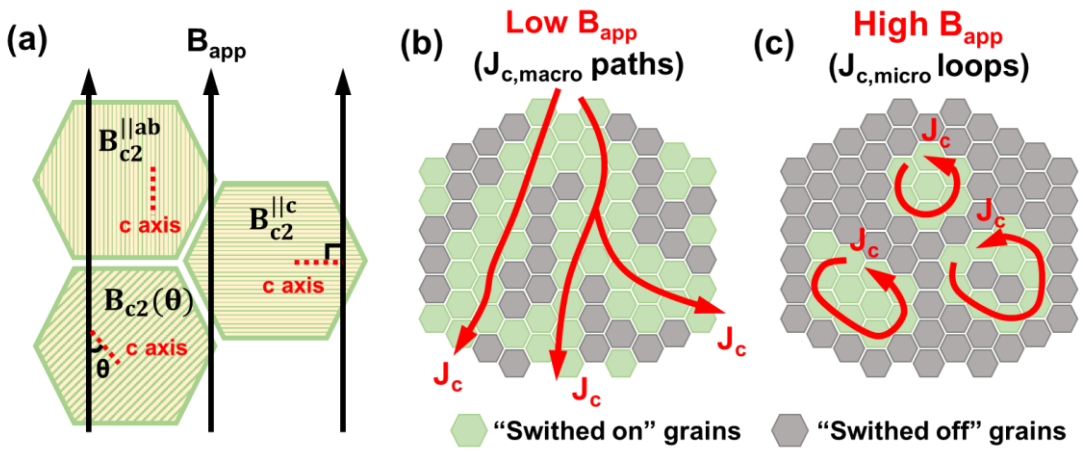


Figure 4.7 Schematic diagrams of (a) B_{c2} dependence of grain orientation and current paths at (b) low applied fields ($B_{c2}^{||c} \leq B_{app} \leq B_{c2}^{||ab}$) and (c) high applied fields ($B_{app} \geq B_{c2}^{||ab}$) where $J_{c,macro}$ and $J_{c,micro}$ flow on the different length scales.

$B_{c2}(\theta)$ of any grain can be calculated by the anisotropic Ginzburg-Landau relation [176],

$$B_{c2}(\theta) = \frac{B_{c2}^{||ab}}{\sqrt{\gamma^2 \cos^2(\theta) + \sin^2(\theta)}} \quad (\gamma > 1, \theta \in [0, \frac{\pi}{2}]) \qquad (4.18)$$

γ is the anisotropy parameter ($\gamma = B_{c2}^{||ab}/B_{c2}^{||c}, B_{c2}^{||ab} > B_{c2}^{||c}$). $B_{c2}^{||ab}$ and $B_{c2}^{||c}$ are the upper critical field values parallel to the a/b and c axis, respectively. In MgB_2, γ depends on how 'clean' the MgB_2 is [177]. For a certain B_{app}, there is a minimum angle (θ_{sc}) of the c axis of an MgB_2 grain with respect to the field for which grains are 'switched on' and can transport superconducting current. If p is the fraction of superconducting ('switched on') grains and all grains are randomly orientated, p is geometrically related to θ_{sc} by the following equation:

$$p = \frac{N_s}{N} = \frac{\int_{\theta_{sc}}^{\frac{\pi}{2}} \sin\theta d\theta}{\int_{0}^{\frac{\pi}{2}} \sin\theta d\theta} = \cos\theta_{sc} \qquad (4.19)$$

where N_s is the number of superconducting grains and N is the total number of grains.

Combining Eq. 4.18 and 4.19,

$$p = \sqrt{\frac{\left(\frac{B_{c2}^{||ab}}{B_{c2}(\theta_{sc})}\right)^2 - 1}{\gamma^2 - 1}} \tag{4.20}$$

$B_{c2}(\theta_{sc})$ is the upper critical field value of the grains aligned at the minimum angle to be superconducting in the applied field. Since $B_{app} = B_{c2}$ in the grains at the minimum angle for superconductivity, $B_{c2}(\theta_{sc})$ in Eq. 4.20 can be replaced with B_{app}, and the relation of p and B_{app} can be expressed by,

$$p = \sqrt{\frac{\left(\frac{B_{c2}^{||ab}}{B_{app}}\right)^2 - 1}{\gamma^2 - 1}} \quad (B_{c2}^{||c} \leq B_{app} \leq B_{c,macro}) \tag{4.21}$$

In a simple model where we just consider all grains that are "switched on" to carry the same J_c as each other, when B_{app} is below $B_{c2}^{||c}$, there is no effect of anisotropy because all grains are superconducting. In the field regime between $B_{c2}^{||c}$ and $B_{c2}^{||ab}$, p will gradually decrease from 1 to 0, and there will be a certain value ($B_{c,macro}$) above which no percolation path for superconducting current will exist, so the p value when $B = B_{c,macro}$ is known as the percolation threshold (p_c). i.e., above $B_{c,macro}$, the macroscopic J_c of the sample is zero.

In reality, the situation is more complex than this. Apart from the orientation with respect to B_{app}, the J_c value of a particular grain can be reduced by ΔJ due to the decreasing current paths. The more unfavourably aligned the grain is, the lower its J_c

will be even if B_{app} is not strong enough to switch off superconductivity altogether (i.e. $B_{app} < B_{c2}(\theta)$). $J_{c,int}$ of each grain with different orientation (θ) is calculated using Eq. 4.5 and the appropriate $B_{c2}(\theta)$ value for the grain. The fraction of superconducting grains at a given applied field is related to the current density, J. By employing a random resistor network model, the dependence of the percolating current density, $J_{c,perc}$, on the applied field in dense, fully-connected pure MgB_2 polycrystalline superconductors can be simulated [175, 177]. A_p, the density of percolation paths, represents the reduction in percolation cross-section and is given by $A_p = \sigma_p/\sigma_0$, where σ_0 is the geometric cross-sectional area and σ_p is the actual cross-sectional area the macroscopic current flowing through.

$$A_p = \left(\frac{p(J) - p_c}{1 - p_c}\right)^t \tag{4.22}$$

If the V-I characteristic is taken as a power law with the exponent tending to infinity, t is 1.76 for a 3D network [175]. Macroscopic critical current density for a polycrystalline sample estimated by percolation theory can be calculated by the integration function as follows,

$$J_{c,perc} = \int_0^{J_{c,max}(B_{app})} \left(\frac{p(J) - p_c}{1 - p_c}\right)^t dJ \tag{4.23}$$

To summarise, four parameters are important to the $J_c(B_{app})$ curves when applying the percolation theory: anisotropy γ, percolation threshold p_c, upper critical field $B_{c2}^{||ab}$ and J_0 values, where J_0 is the J_c value when B_{app} is zero. The basic formulas developed by

this theory so far only consider the anisotropy brought by grain orientation and do not take any other microstructural features into account. Therefore, instead of simulating $J_c(B_{app})$ curves using this model, I have written python code to simulate theoretical $\Delta M(B_{app})$ curves that can be directly compared with experimental data in later chapters. 1000 grains with θ angles varying systematically between 0 and π/2 were generated. The effects of changing four key parameters on the simulated curves only account for the macro current loops and ignore micro loops, as shown in Figure 4.8. Decreasing anisotropy (γ) from 3.5 to 2.5 (whilst keeping $B_{c2}^{||ab}$ constant) can apparently enhance ΔM performance at high magnetic fields (Figure 4.8a). Decreasing the percolation threshold, p_c, leads to slightly improved high field performance, but the effect is relatively weak (Figure 4.8b). Unsurprisingly, increasing $B_{c2}^{||ab}$greatly improves high field performance (Figure 4.8c). However, in practice $B_{c2}^{||ab}$ and anisotropy cannot be varied independently; high $B_{c2}^{||ab}$ values are accompanied by low anisotropy values [178]. The strategy of increasing $B_{c2}^{||ab}$ to improve J_c at high field is exploited by C doping of MgB_2 (Section 2.3.3). Larger ΔM_0 values can move the overall curves upwards (Figure 4.8d).

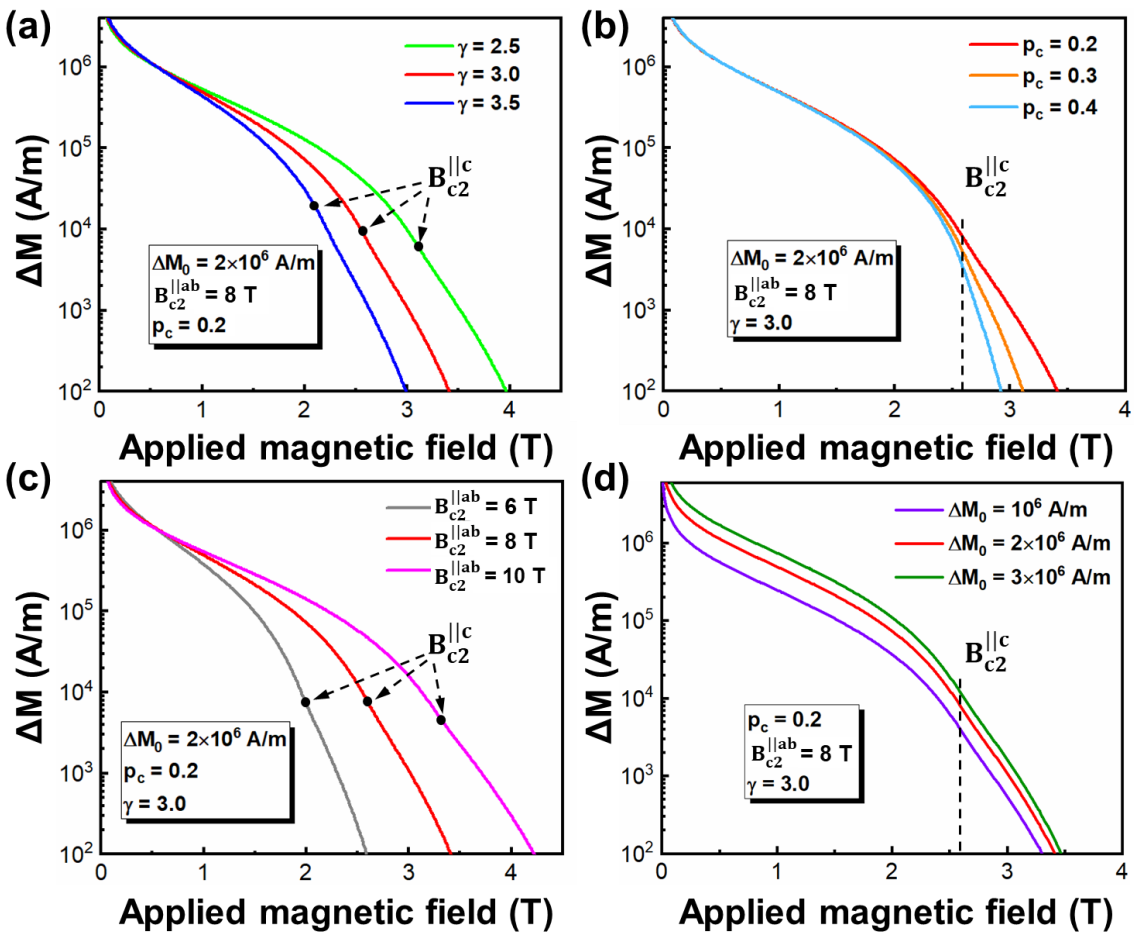


Figure 4.8 Numerically simulated $\Delta M(B_{app})$ curves by the percolation theory with different (a) anisotropy γ, (b) percolation threshold p_c, (c) upper critical field $B_{c2}^{||ab}$ and (d) ΔM_0 values.

If $p < p_c$, only local superconducting regions have flowing currents ($J_{c,micro}$). However, even when $p > p_c$, as the field increases, the density of percolation paths will also decrease. In moment measurements, it is possible that some superconducting areas confined by "switched off" grains can still be capable to carry microscopic current loops which do not need to be considered when modelling a transport current but will contribute to the signal in a magnetization measurement. Therefore, the magnitude of possible contribution of micro current loops to the total magnetic moment needs to be checked. Before discussing possible models under the percolation theories, I will first

use a simple 2D model to figure out if it is reasonable to neglect these additional micro current loops. The details of using a numerical approach to study percolation systems adopted by this study have been introduced elsewhere [179].

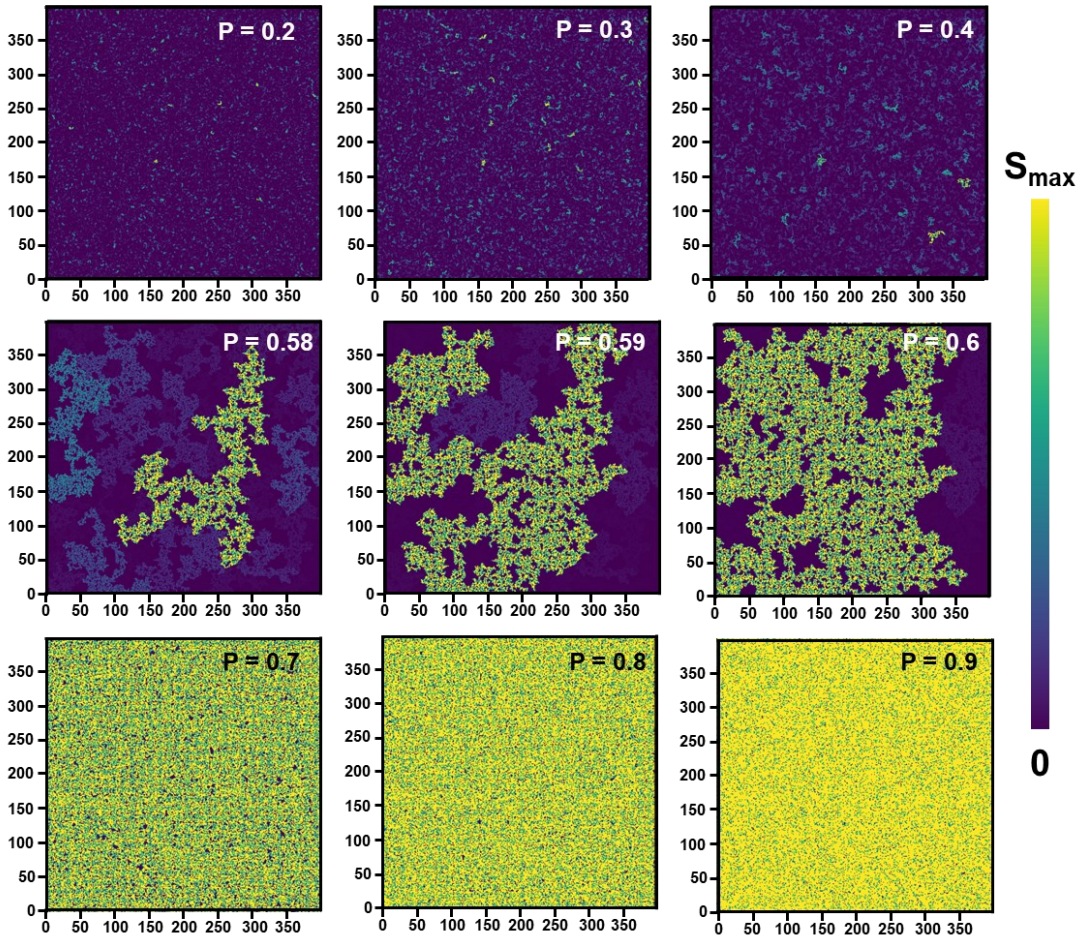


Figure 4.9 Illustration of percolation results with different p values in a 400 × 400 site percolation system. The p_c of a 2D system with square units is 0.59 above which the percolation cluster exists. The clusters are coloured by the size of clusters (S), and S_{max} is the maximum cluster size.

If creating an L × L lattice with square grains, percolating clusters that connect one side to the opposite side of the lattice represent the paths carrying $J_{c,macro}$, while local clusters refer to the confined area where local currents flow. The density of percolating clusters is represented by P(p,L) and equals the fraction of percolating clusters in the total lattice.

The fraction of the local clusters is P_{local}. A "switched on" site either belongs to the percolating cluster or local clusters.

$$P_{local} = p - P(p, L) \tag{4.24}$$

where p is the fraction of superconducting grains. Plots of clusters for different p values are shown in Figure 4.9 in a 400 × 400 site percolation system with the probability of each site generated randomly. One can see when $p \approx p_c$ the shape and size of clusters change dramatically. i.e., some unconnected local clusters have opportunities to interconnect and form the large percolating cluster at p_c.

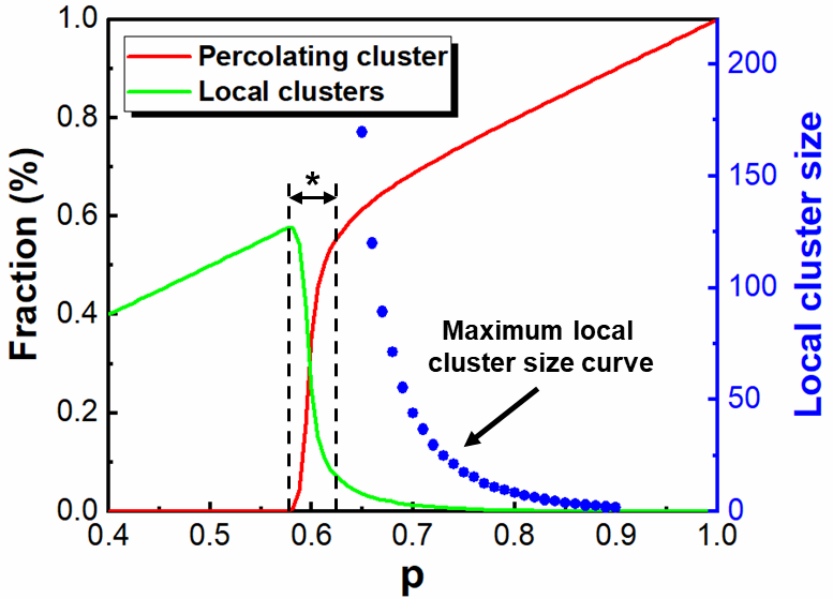


Figure 4.10 Plots of the fraction of the percolating/local clusters and the maximum local cluster size depending on p values in a 400 × 400 percolation system. The area labelled by star shows the dramatic changes in clusters when p is close to $P_c \approx 0.59$.

The main focus is how P(p,L) and P_{local} change when p decreases from 1 to 0.59 (for 2D square lattice, $p_c \approx 0.59$). Figure 4.10 plots P(p,400) and P_{local} as a function of p values, where one can see that the fraction of local clusters can be neglected when p is far away from p_c. Only in the narrow range labelled by *, a dramatic increase in the

fraction of local clusters occurs, accompanied by the increasing size of local clusters. These results show that the contribution of currents in local clusters is small when $p > p_c$ and p is not close to p_c. The maximum local cluster size is also plotted in Figure 4.10, which shows a dramatic decrease with increasing p values from 0.65 to 0.9. In a word, it is reasonable to ignore these local clusters in the following sections if p is higher than p_c and not close to p_c.

4.2.2.1 Dense and anisotropic superconductors with fully-connected grains and textures (Percolation model A)

Texture, also known as the preferred orientation of grains, can affect the superconducting performance of superconductors with high anisotropy. For MgB_2 grains, the c axis direction is represented by a unit vector **g** (1, φ, θ) in the spherical coordinate system (Figure 4.11a), where the Z-axis is the direction in which the uniaxial pressure is applied in the processing of the sample. **t** represents the direction of B_{app}, and the texture can be described by a normal distribution,

$$f(\theta, \sigma) \propto e^{-\frac{\theta^2}{2\sigma^2}} \ (\theta \in [0, \frac{\pi}{2}]) \qquad (4.25)$$

where θ represents the angle between **g** and **t** (also Z axis). σ refers to the standard deviation, indicating the degree of texture. Figure 4.11b shows the results of $\Delta M(B_{app})$ curves when a varying extent of texture exists. Lower σ values mean less angular deviation of MgB_2 grains and therefore a stronger texture in the sample. If B_{app} is perpendicular to the Z-axis, a strong texture (small σ) leads to better high field

performance. As σ increases from 5° to 45°, ΔM values drop dramatically with the increasing field, but the deterioration rate slows down when σ > 45°, indicating that weak texture does not make a substantial difference to the superconducting behaviour. This conclusion is consistent with experimental results [180, 181]. When B_{app} is parallel to c axis, J_c performs worse in the most strongly-textured samples, because the field is being applied in the direction where the B_{c2} value is lowest for most grains.

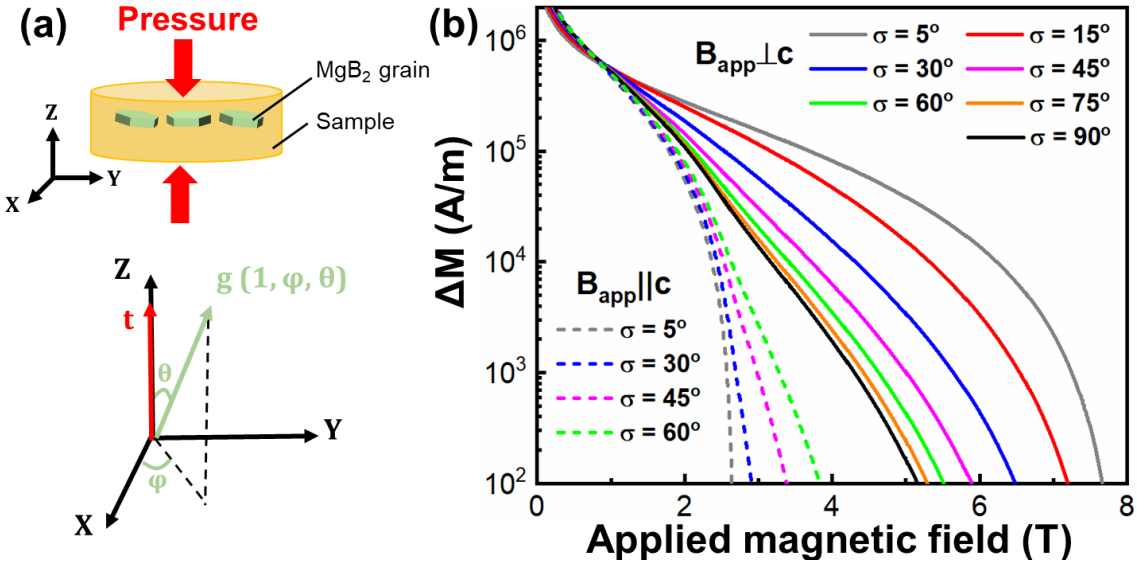


Figure 4.11 (a) Schematic diagrams of pressure applied in field-assisted sintering process and the spherical coordinate system showing **t** and **g**. (b) plots simulated ΔM(B_{app}) curves with different extent of texture when B_{app}⊥c axis and B_{app}∥c axis.

4.2.2.2 Anisotropic superconductors with fully-connected grains and non-superconducting impurities/pores (Percolation model B)

A small fraction of impurities or pores with sizes comparable to MgB_2 grain size can just be treated as reducing the cross-section where currents flow. However, when these impurities/pores occupy a larger percentage, their influence on percolation paths should be considered. Coordination number, K, is defined as the number of connections of one

MgB_2 grain to its neighbours. Due to the presence of impurities/pores, the effective coordination number K^* refers to the number of contacts of one MgB_2 grain to its MgB_2 neighbours. Eisterer et al introduced an additional parameter p_{MgB_2} to the percolation model which represents the fraction of MgB_2 grains [35]. A decrease in p_{MgB_2} will bring a reduction in K^*. As Figure 4.12 shows, grey represents grains with B_{c2} values below B_{app} so they are 'switched off', while green grains still keep superconducting. Compared with Percolation model A, the presence of impurities/pores shown as black grains reduce K^* instead of K values. Correspondingly, the density of percolation paths significantly drops.

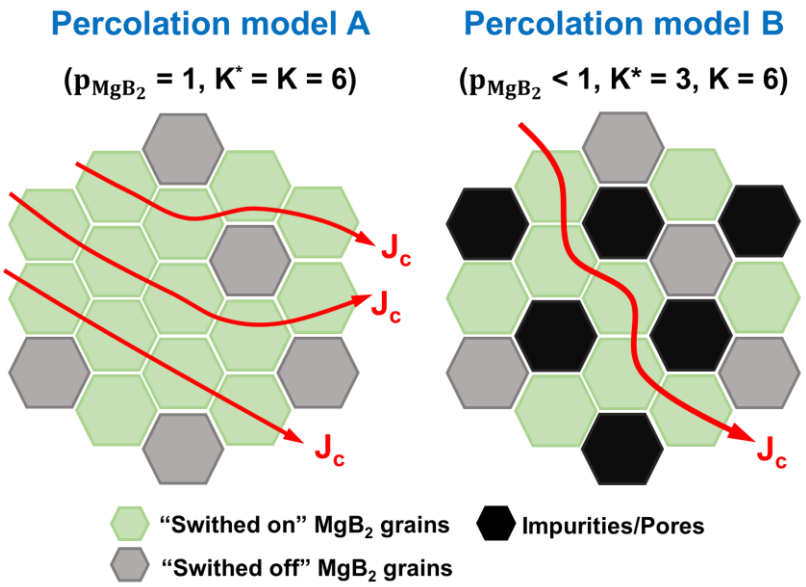


Figure 4.12 Two-dimensional schematic diagrams of situations in Percolation model A and B showing changes in K and K^* values as well as current paths in the presence of impurities/pores with comparable size to MgB_2 grains.

The earlier Eq. 4.22 is modified as [35],

$$A_p(p, p_{MgB_2}, p_c) = \left(\frac{p_{MgB_2} p(J) - p_c}{1 - p_c}\right)^t \qquad (4.26)$$

This formula can be expressed as the product of two components,

$$A_p\left(p, p_{MgB_2}, p_c\right) = \left(\frac{p - p_c^*}{1 - p_c^*}\right)^t \left(\frac{p_{MgB_2} - p_c}{1 - p_c}\right)^t \quad (4.27)$$

where $p_c^* = p_c / p_{MgB_2}$. Conditions, when p_{MgB_2} varies from 0.6 to 1 with an interval of 0.2, are simulated as shown in Figure 4.13. The change in pinning strength ($J_{c,int}$) brought by non-superconducting grains is neglected here, so decreasing p_{MgB_2} lowers the overall ΔM values, owing to the decreasing cross-section for supercurrent paths.

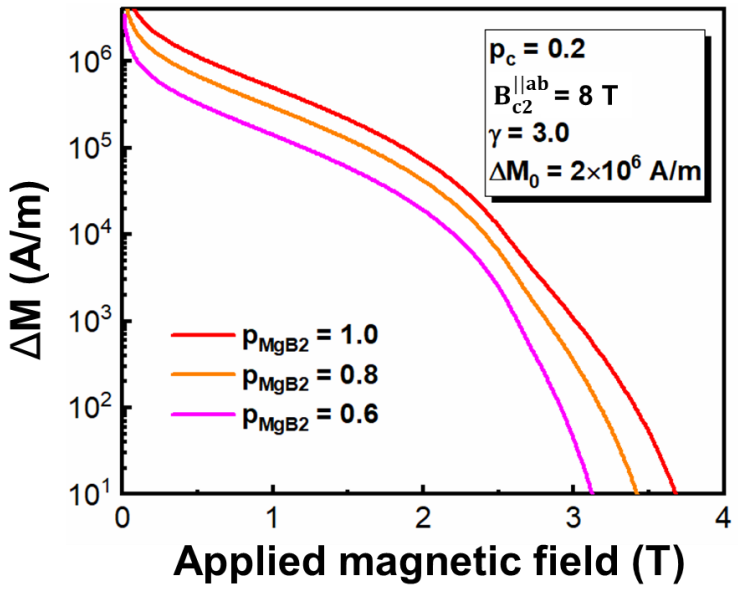


Figure 4.13 Theoretical $\Delta M(B_{app})$ curves show the effects of impurities with a comparable size to MgB_2 grains.

4.2.3 Anisotropic superconductors with connectivity problems

In this case, the percolation model should be introduced in the Cell model (Section 4.2.1) to deal with anisotropy and connectivity issues. If the cell refers to grains, one can replace $J_{c,int}$ in Cell models with $J_{c,perc}$ calculated by the percolation theory. However, if the cell represents larger features consist a group of grains, the specific conditions in

each cell may be different. Therefore, a more complex model describing the duplex microstructure model should be established (Section 4.2.4).

4.2.4 Duplex microstructure model for practical superconductors

There are two types of cells in the samples: Type A and Type B. Type B cells are dense and consist of well-connected grains while impurities or pores situate in Type A cells, impairing the grain connectivity and/or cell density. The cell size of both types of cells is assumed to be the same. The fraction of Type A cells is f_A and the fraction of Type B cells is f_B (if samples are totally dense, $f_A + f_B = 1$). A_a and A_b are parameters describing the connectivity within Type A cells and Type B cells. The schematic diagram below shows the current flow in the duplex microstructure model, where macro currents may have components from two types of cells (Figure 4.14). Besides, local currents flow within each kind of cell. The possibility of current flowing between Type A cells and Type B cells is defined as interconnectivity (α) with $0 \leq \alpha \leq 1$. $\alpha = 0$ means Type A subarrays are completely disconnected from Type B subarrays while $\alpha = 1$ means they are fully connected.

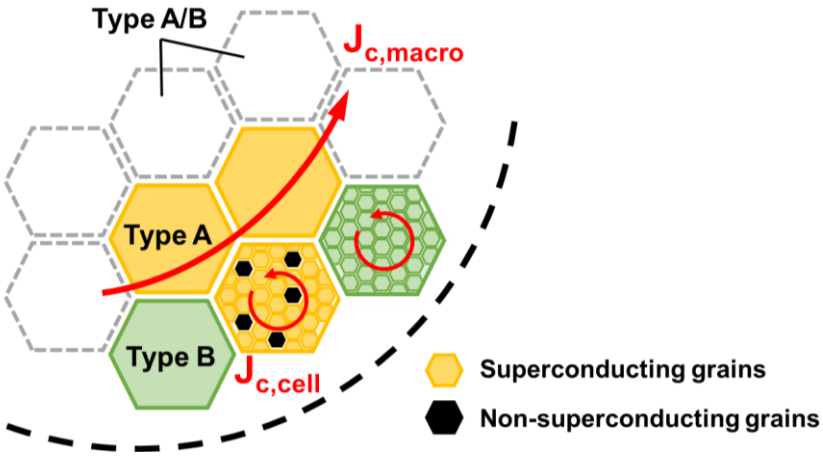


Figure 4.14 Schematic diagram showing duplex microstructures with the presence of Type A and Type B cells. Black regions in Type A cells represent non-superconducting grains. The grey cells can be Type A or Type B cells.

4.2.4.1 Duplex microstructure model I ($\alpha = 0$, unconnected)

Since there is no connectivity between two types of cells, the total ΔM can be expressed by,

$$\Delta M = \Delta M_{macro,A} + \Delta M_{cell,A} + \Delta M_{macro,B} + \Delta M_{cell,B} \qquad (4.28)$$

Applying Cell model D (Section 4.2.1.4) to Type A and Type B cells respectively, one can obtain,

$$\text{Type A cells: } \begin{cases} J_{c,macro,A} = A_a f_A^* J_{c,perc,A} \\ J_{c,cell,A} = [(1 - A_a) f_A^* + (f_A - f_A^*)] J_{c,perc,A} \end{cases} \text{ with } f_A^* = \left(\frac{f_A - p_c}{1 - p_c}\right)^t \qquad (4.29)$$

$$\text{Type B cells: } \begin{cases} J_{c,macro,B} = A_b f_B^* J_{c,perc,B} \\ J_{c,cell,B} = [(1 - A_b) f_B^* + (f_B - f_B^*)] J_{c,perc,B} \end{cases} \text{ with } f_B^* = \left(\frac{f_B - p_c}{1 - p_c}\right)^t \qquad (4.30)$$

The reason that f_A^* and f_B^* are used instead of f_A and f_B is that percolation should also be revised due to the existence of non-superconducting regions. Cell currents consist of currents flowing in the cells in the percolation paths and in the 'cut off' cells with the

fraction of $(f - f^*)$ in the Subarray A (or B). If $G_{sample} \approx G_{cell} \approx G$, ΔM can be expressed as,

$$\Delta M = G\left[(J_{c,macro,A} + J_{c,macro,B})D + (f_A J_{c,cell,A} + f_B J_{c,cell,B})d_{cell}\right] \quad (4.31)$$

4.2.4.2 Duplex microstructure model II ($0 < \alpha \leq 1$, partially-connected)

If two types of cells are partially or even fully connected, there will be current flowing through cell boundaries. Type A cells are assumed to serve as the connected matrix where Type B are isolated regions distributed within Subarray A. Therefore, the macro currents flow through the paths formed by Type A cells while two kinds of local currents still flow within cells.

$$\Delta M = \Delta M_{macro} + \Delta M_{cell,A} + \Delta M_{cell,B} \quad (4.32)$$

The $J_{c,cell}$ are the same with the discussion in Section 4.2.4.1, so the focus is on the calculation of $J_{c,macro}$. In the simple case, if both type of cells are fully connected ($\alpha = 1$). One could view that $A_a J_{c,perc,A}$ is the part of background macro currents that can flow through the whole sample. On this basis, since $J_{c,perc,B} > J_{c,perc,A}$, extra macro currents from Type B cells are introduced.

$$J_{c,macro}(\alpha = 1) = A_a J_{c,perc,A} + A_b f_B^* \left(J_{c,perc,B} - J_{c,perc,A}\right) \quad (4.33)$$

If $0 < \alpha < 1$, the situation can be viewed as the linear combination of two extremes $J_{c,macro}$ ($\alpha = 0$) and $J_{c,macro}$ ($\alpha = 1$),

$$J_{c,macro}(0 < \alpha < 1) = \alpha J_{c,macro}(\alpha = 1) + (1 - \alpha) J_{c,macro}(\alpha = 0) \quad (4.34)$$

4.2.5 Horvat's analysis

Even though discussion on currents flowing on different length scales has been less explored in previous experiments, Horvat et al noticed this inhomogeneity problem of their samples and made explanations by a stretched exponential function [182]. I will briefly process magnetization data from my samples to introduce how they conducted the analysis and point out where I think their conclusions are debatable.

Figure 4.15 shows the field dependences of $-d(\ln(\Delta M))/dB$, where the curve is divided into three parts by two special fields: B_t and B_i. In the field range of $B_{app} < B_t$, the data points show reasonable linearity. Above B_i, a dramatic decrease is observed. Between B_t and B_i, the curvature changes are sample-dependent. In the B_{app} range below B_i, Horvat et al fit the experimental data by a stretched exponential function [182, 183],

$$\Delta M = \alpha e^{(-B/B_1)^{n_1}} + \beta e^{(-B/B_2)^{n_2}} \ (B_1 < B_2) \qquad (4.35)$$

There is no physical justification for using the stretched exponential form, beyond the fact that it reproduces the experimental $-d(\ln(\Delta M))/dB_{app}$ vs. B_{app} behaviour. Horvat thought that coefficients α and β contain the cell and sample size information, but it is not possible to extract the sizes directly from the fit of α and β. B_1 and B_2 can only be obtained by fitting the experimental data. From experiments in which the sample size was gradually reduced, Horvat concluded that the first term of Eq. 4.35 represents microscopic currents flowing within the cells, which has a great contribution to the field dependence of ΔM at low fields. The second term was attributed to screening currents

circulating the whole sample and defines the field dependence of ΔM in the range of B_t < B_{app} < B_i. Their conclusions are debatable for two reasons: (i) the shape of ΔM(B_{app}) curves at a low magnetic field range may be influenced by the presence of self-field, and (ii) the curve shape can also be affected by percolation effects even in a homogenous sample. The first problem can be solved by applying suitable self-field corrections that will be introduced in Section 4.3. Another obvious problem of Horvat's interpretation is that the first exponential term decreases more dramatically with fields compared with the second term. This implies the contribution from the microscopic currents within MgB_2 cells drops off much more quickly with the applied field than the macroscopic current loops. They attributed this to a redistribution of current between the cells and the matrix, but a believable physical explanation for why the moment from the microscopic current loops would drop more rapidly in increasing field is lacking.

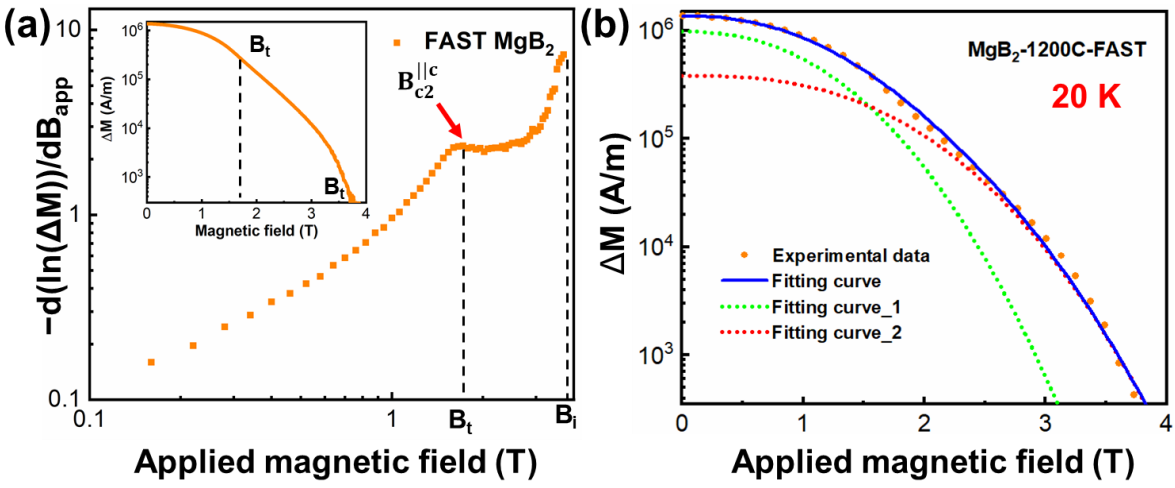


Figure 4.15 (a) −dln(ΔM)/dB_{app} vs. B_{app} curves on a log-log scale of the MgB_2 sample prepared by FAST at 1200 °C. The inset figure is the ΔM(B_{app}) curve. (b) the curve fitting results using a stretched exponential function proposed by Horvat et al [182].

To explain the percolation effects on the curve shape, I generated a theoretical ΔM(B_{app})

curve by the percolation theory to simulate a homogenous but anisotropic sample. Figure 4.16 shows the results of using the stretched exponential formula to do curve fitting on this homogeneous sample. Curve 1 and Curve 2 correspond to the first and second terms of the stretched exponential respectively. A good fit could be obtained (except in the region below ~0.5 T where uncorrected self-field effects will be present) but both curves do not represent the J_c flowing on different scales because the simulated sample is homogeneous. Therefore, even though one can use Eq. 4.35 to perform curve fitting, there are no necessary links between microstructures and the stretched exponential form. However, it is interesting to note that the first peak in the $d\ln(\Delta M)/dB_{app}$ curves occurs at values close to $B_{c2}^{||c}$, the lowest upper critical field which suggests that plotting this dependence for real samples may allow us to estimate their $B_{c2}^{||c}$ values.

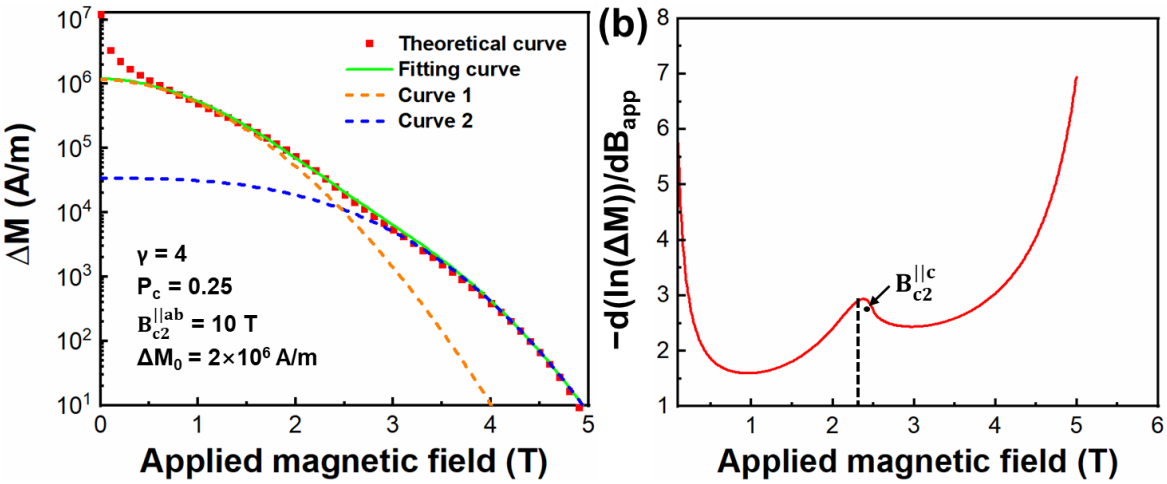


Figure 4.16 (a) theoretical $\Delta M(B_{app})$ curve generated from the percolation theory and its fitting curve using a stretched exponential function proposed by Horvat et al [182] with α=1.2×10^6 A/m, B_1 = 1.1 T, n_1 = 1.9, β = 3.4×10^4 A/m, B_2 = 2.4 T, n_2 = 2.9. (b) the $-d\ln(\Delta M)/dB_{app}$ vs. B_{app} log-log plot of the theoretical curve.

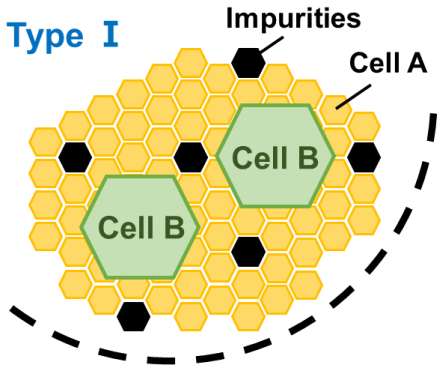
4.2.6 Practical simulation

In this section, I will use models introduced in the previous sections to simulate the current flowing situations in practical MgB_2 bulk samples. Five representative microstructural features are summarised and shown by corresponding schematic diagrams. For each type of microstructure, the contribution of current flowing on different length scales will be discussed. The main aim of this work is to figure out the conditions under which Bean's model can be successfully used and which kind of current density ($J_{c,macro}$ or $J_{c,cell}$) this model can give. In addition, the examples covered in this section will serve as a reference for the analysis of magnetization data in the experimental chapters.

Before going into details, it is necessary to list the parameters that will be used. All grains are assumed to be randomly oriented. Two subarrays of cells (A and B) are simulated and cells included in the subarrays are called Cell A and Cell B respectively. The subarray fractions are f_A and f_B. The connectivity (A_{con}) is from cell to cell within a subarray. p_{MgB_2} denotes the superconducting fraction of cells in the subarray. α is the interconnectivity between A and B. The upper critical field ($B_{c2}^{||ab}$) of grains in Cell A and Cell B are fixed as 10 T, and the anisotropy (γ) of both cells is fixed as 4. The percolation threshold (p_c) is set as 0.2. The sample radius is 1 mm but cell size (d) changes in different microstructures. Moreover, the grain size mentioned below refers to the data obtained by EBSD rather than the crystallite size measured by XRD.

4.2.6.1 Type I microstructures

As Figure 4.17 shows, this type of microstructure is characterised by dense structures where unconnected Cell B arrays are distributed in Subarray A that consists of smaller cells. Each cell in Subarray B includes many MgB_2 grains and is free of impurities ($p_{MgB_2} = 1$). In contrast, impurities with comparable size to MgB_2 grains present in Subarray A influence the superconducting fraction ($p_{MgB_2} < 1$). The connectivity problem within Cell A arises from small impurities at grain boundaries. The selected values of parameters are shown on the right side of the diagram.



Parameters	Subarray A	Subarray B
Fraction (f)	0.8	0.2
MgB_2 fraction (p_{MgB_2})	0.7	1
Cell size (d)	1 μm	10 μm
Connectivity (A_{con})	0.7	0

Figure 4.17 Schematic diagram of Type I microstructure that consists of Subarray A and Subarray B. The parameters used in the simulation are shown on the right table.

Results of simulation when interconnectivity (α) equals 0 and 1 are shown in Figure 4.18. There is little difference in both extreme cases, so α is not an important parameter here. The total ΔM curve almost overlaps the ΔM curve created by macro currents flowing in Subarray A, and the contribution of currents circulating within cells is neglectable.

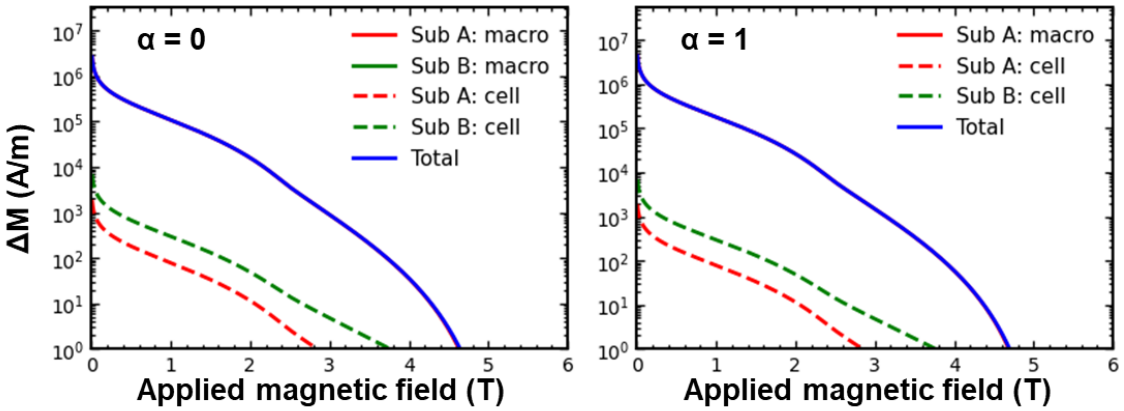
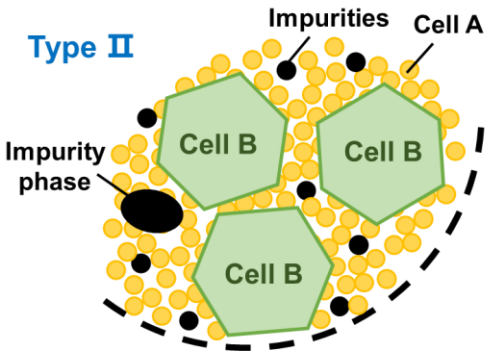


Figure 4.18 Theoretical ΔM curves of Type I microstructure as a function of B_{app} when α = 0 or α = 1.

4.2.6.2 Type II microstructures

The schematic diagram in Figure 4.19 presents Type II microstructure characterised by large impurity phases and porous structures in Subarray A. The connectivity is greatly impaired in this subarray, and the existence of pores/impurities additionally decreases the MgB_2 fraction. In comparison, Cell B with a much larger size does not contain impurities but also has no connectivity with each other. Different fractions of Subarray B have been tried, and the values are shown in the table.



Parameters	Subarray A	Subarray B
Fraction (f)	0.3	0.3/0.5
MgB_2 fraction (p_{MgB_2})	0.5	1.0
Cell size (d)	2 μm	30 μm
Connectivity (A_{con})	0.2	0

Figure 4.19 Schematic diagram of Type II microstructure that consists of Subarray A and Subarray B. The parameters used in the simulation are shown on the right table.

Figure 4.20a plot the ΔM curves under four interconnectivity conditions: α = 0, α = 1,

$\alpha = 0.3$ and $\alpha = 0.7$, and the fractions of Subarray B is fixed at 0.5. One can find that if there is no interconnectivity between Cell A and Cell B, the total ΔM curve exactly matches the ΔM curve generated by currents flowing within Cell B (green dotted line). However, under the fully-connected ($\alpha = 1$) condition, the total ΔM curve is first closely follows the ΔM curve generated by macro currents of Subarray A (red line) and then exactly follows the trend of the ΔM curve produced by cell B currents (green dotted line). If different types of cells are partially-connected, both ΔM values created by macro currents in Subarray A and cell B currents have a large contribution to the total ΔM shape in the low and medium field range. If $f_B = 0.3$, as shown in Figure 4.20b, when the interconnectivity increases from 0 to 1, the value of macroscopic J_c is greatly improved to dominate the total ΔM because strong currents in Cell B has opportunities to flow out of cell and form part of macro currents.

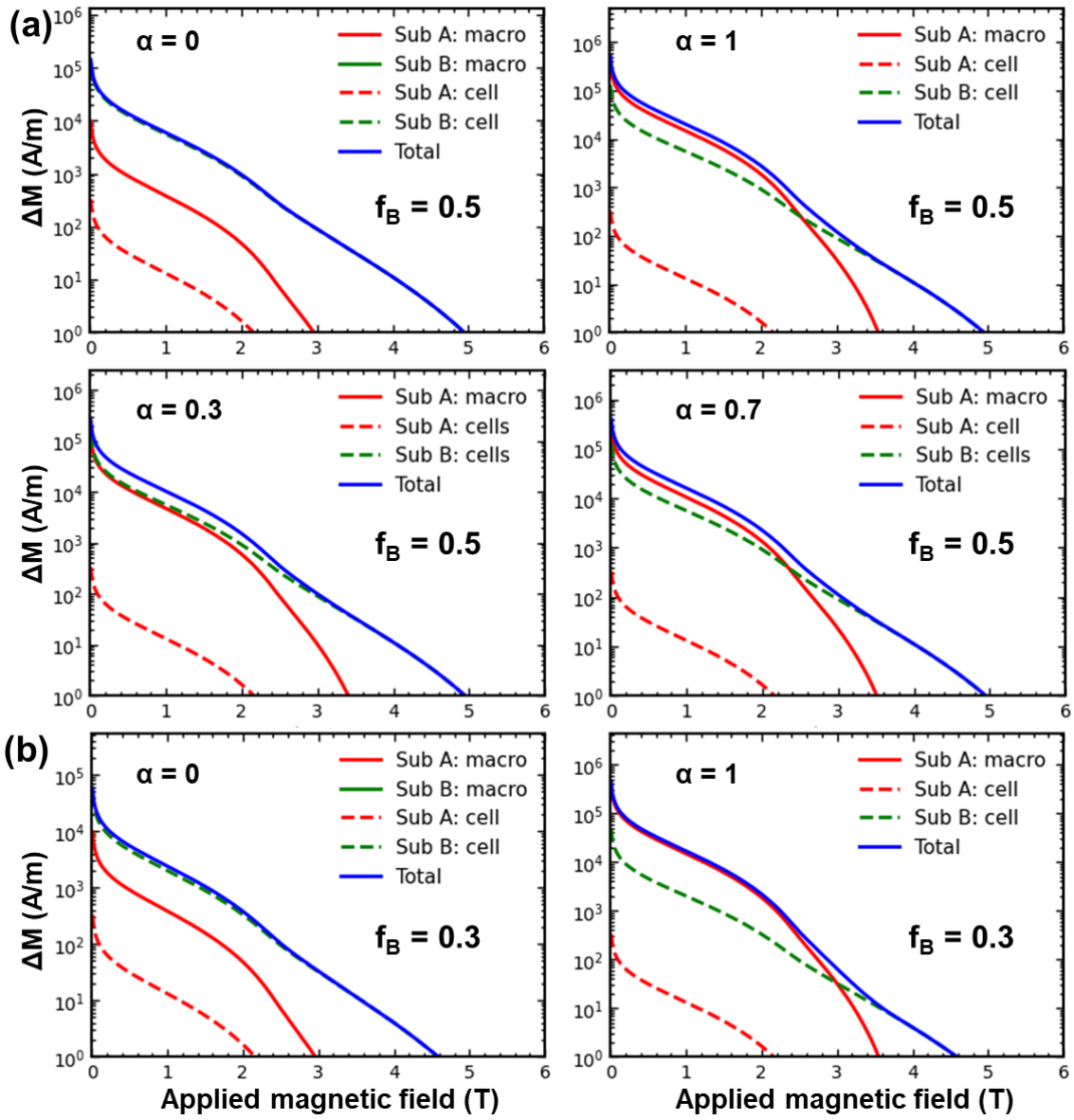
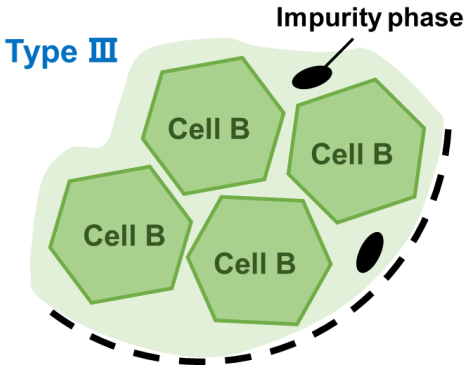


Figure 4.20 Theoretical ΔM curves of Type II microstructure as a function of B_{app} when (a) $f_B = 0.5$ and (b) $f_B = 0.3$ under different interconnectivity conditions.

4.2.6.3 Type III microstructures

In this type of microstructure, Cell B is large and close to each other, which means that the distance between two cells is much smaller than the cell size (Figure 4.21). Therefore, the duplex microstructure model can be simplified to Cell model D, but $J_{c,int}$ should be substituted by $J_{c,perc}$ calculated by the percolation theory. The fraction of

Subarray A is set as 0, so only cell B currents and macro currents exist. The area between different cells can be viewed as "cell boundaries" that have connectivity values smaller than 1. Due to the presence of some impurity phases, the fraction of Subarray B is below 1.



Parameters	Subarray A	Subarray B
Fraction (f)	0	0.9
MgB_2 fraction (p_{MgB_2})	--	1.0
Cell size (d)	--	40 μm
Connectivity (A_{con})	--	0.3/0.7

Figure 4.21 Schematic diagram of Type III microstructure that consists of Subarray A and Subarray B. The parameters used in the simulation are shown on the right table.

Figure 4.22 shows the simulation results of the total ΔM curves which exactly match the macro current flowing in the whole sample with the poor or good connectivity A_{con} (0.3 vs. 0.7). Therefore, changing connectivity only alters the magnitude of cell current but the total $\Delta M(B_{app})$ curve is still dominated by the macro currents in this case.

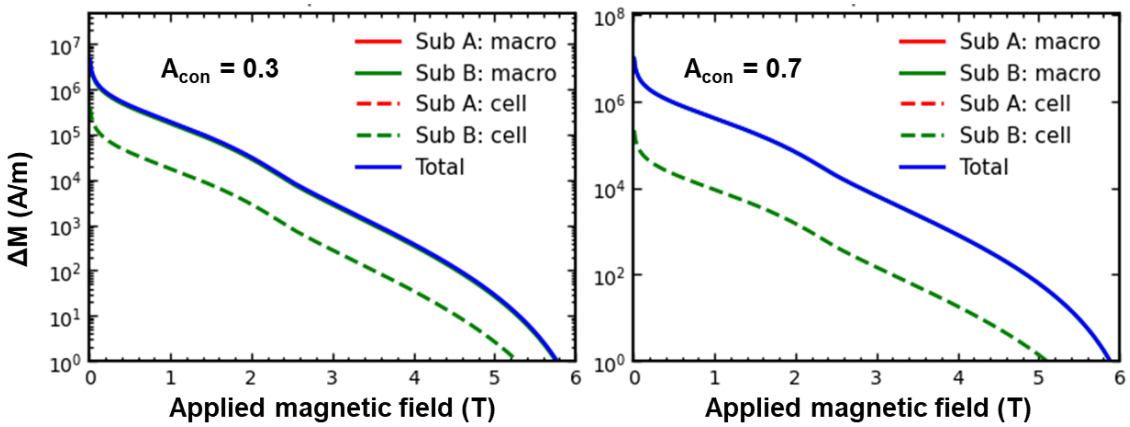


Figure 4.22 ΔM dependence of Type III microstructure on the B_{app}. The curves are simulated by Cell model D with J_c calculated by the percolation theory.

4.2.6.4 Type IV microstructures

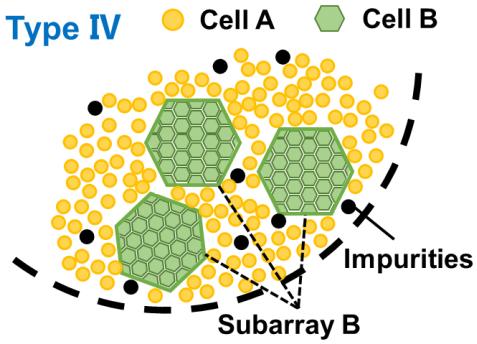
The main feature of this type of microstructure is the impaired grain connectivity in Subarray B and porous structures in Subarray A (Figure 4.23). Even though Cell B is viewed as single grains like Cell A with the size around 1 μm in this case, there is no contribution of Subarray B to the macroscopic current because regions in this Subarray are not connected to each other. Since $\alpha = 0$ and no non-superconducting grains with the size comparable to MgB_2 grains exist in Subarray B, Cell model C (Section 4.2.1.3) can be used to solve the grain connectivity problem ($A_b < 1$) with substituting $J_{c,int}$ by $J_{c,perc}$. For clarity, cell currents in B are called $J_{c,grain,B}$ while currents flowing within unconnected regions of Subarray B is represented $J_{c,micro,B}$. Two kinds of currents flow in the Subarray B regions are,

$$\begin{cases} J_{c,grain,B} = (1 - A_b) J_{c,perc,B} \\ J_{c,micro,B} = A_b J_{c,perc,B} \end{cases} \quad (4.36)$$

In comparison, the calculation of Cell A current and the macro current remain the same. Therefore,

$$\begin{aligned} \Delta M &= \Delta M_{macro,A} + \Delta M_{cell,A} + \Delta M_{grain,B} + \Delta M_{micro,B} \\ &= G\left[(J_{c,macro,A} D + f_B J_{c,micro,B} d_{micro} + (f_A J_{c,cell,A} + f_B J_{c,grain,B}) d_{cell}\right] \end{aligned} \quad (4.37)$$

A fraction around 0.2 is reserved for the presence of pores or non-superconducting impurities in the sample, and d_{micro} (each Subarray B region) is set as 10 μm.



Parameters	Subarray A	Subarray B
Fraction (f)	0.5/0.3	0.3/0.5
MgB_2 fraction (p_{MgB_2})	0.5	1
Cell size (d)	1 μm	1 μm
Connectivity (A_{con})	0.3	0.3/0.6

Figure 4.23 Schematic diagram of Type IV microstructure that consists of Subarray A and Subarray B. The parameters used in the simulation are shown on the right table.

The simulation results of $\Delta M(B_{app})$ curves with different cell fractions (f) and Cell B connectivity (A_b) are shown in Figure 4.24. If the interconnectivity between Cell A and Cell B is 0, it can be seen that A_b controls the relative magnitude of currents within grains (yellow dotted line) and isolated Subarray B regions (green dotted line). The fractions of subarrays determine the contribution of ΔM from Subarray B to the total ΔM values. When f_B = 0.3, the total ΔM are dominated by macro currents from Subarray A. Increasing f_B to 0.5, micro currents from Subarray B will have an unneglectable influence on the total ΔM, while the cell A and B currents (grain currents) contribute a little to the total $\Delta M(B_{app})$ curve in both magnitude and shape.

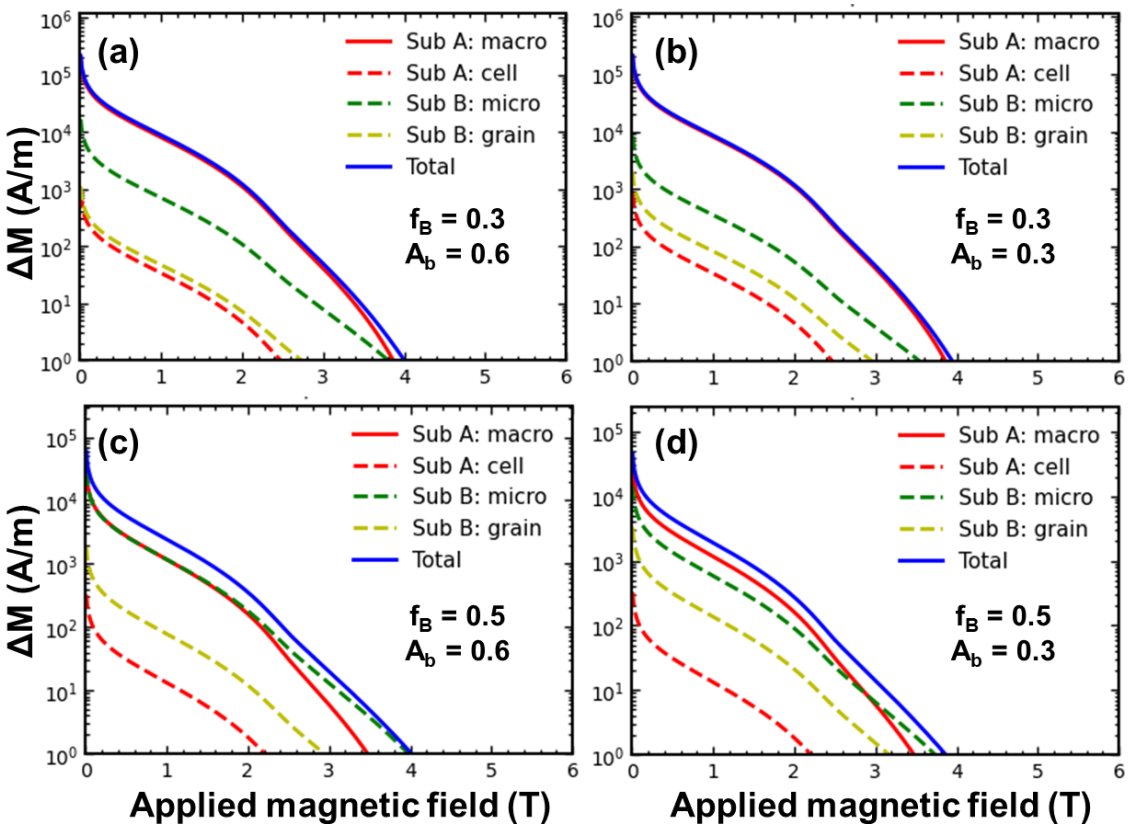
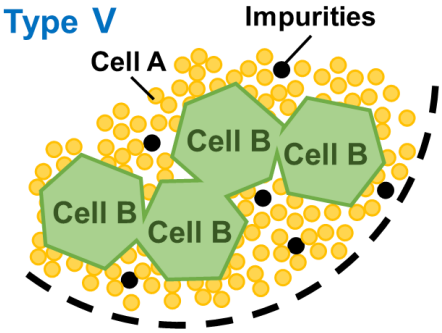


Figure 4.24 $\Delta M(B_{app})$ curves of Type IV microstructure when (a) $f_B = 0.3$ and $A_b = 0.6$, (b) $f_B = 0.3$ and $A_b = 0.3$, (c) $f_B = 0.5$ and $A_b = 0.6$ and (d) $f_B = 0.5$ and $A_b = 0.3$.

4.2.6.5 Type V microstructures

Figure 4.25 presents Type V microstructure characterised by the connection between Cell B that is made of many MgB_2 grains. 0.3 or 0.6 are selected representing the fraction of subarrays to simulate the condition of different porosity in the samples.



Parameters	Subarray A	Subarray B
Fraction (f)	0.3/0.6	0.3/0.6
MgB_2 fraction (p_{MgB_2})	0.6	0.8
Cell size (d)	1 μm	10 μm
Connectivity (A_{con})	0.5	0.2

Figure 4.25 Schematic diagram of Type V microstructure that consists of Subarray A and Subarray B. The parameters used in simulation are shown on the right table.

As shown in Figure 4.26a, in absence of interconnectivity ($\alpha = 0$), macro currents from both subarrays determine the total $\Delta M(B_{app})$ curve when the fractions of two subarrays are 0.3. As f_B increases to 0.6, the $\Delta M(B_{app})$ curve generated by macro currents in Subarray B overlaps the total $\Delta M(B_{app})$ curve (Figure 4.26b) compared to the total ΔM values dominated by macro currents in Subarray A if $f_A = 0.6$ (Figure 4.26c). If $\alpha = 1$, even though currents in Cell A and B will vary in magnitude, the total ΔM curves always match ΔM curves generated by macro currents, regardless of the fractions of Subarray A and B. Figure 4.26d is an example showing the dominant role of macro currents.

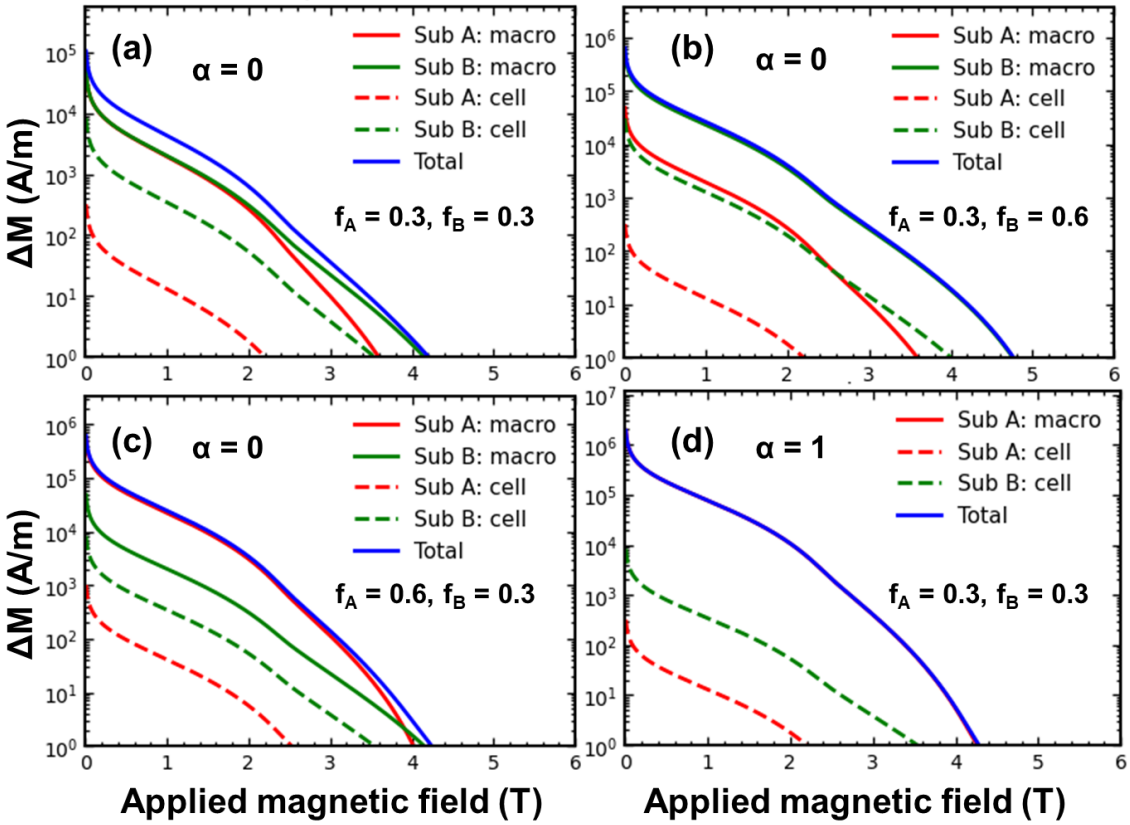


Figure 4.26 $\Delta M(B_{app})$ curves of Type IV microstructure when (a) $f_A = f_B = 0.3$, (b) $f_A = 0.3$ and $f_B = 0.6$, (c) $f_A = 0.6$ and $f_B = 0.3$ and (d) $f_A = f_B = 0.3$ ($\alpha = 1$).

4.3 Self-field corrections

The previous section stresses the significance of microstructural characterisation on determining the length scale of the currents that dominates the total ΔM. This section deals with another common problem when researchers plot pinning curves using $J_c(B_{app})$ curves extracted from Bean's critical model without data pre-processing. I will illustrate why the self-field correction is necessary and explain how to conduct it.

4.3.1 The origin of calculating pinning curves

For a given B, at J_c the pinning force balances the applied Lorentz force. Here B represents local magnetic field which is given by,

$$\mathbf{B}(r,z) = \mathbf{B}_{app} + \mathbf{B}_{self}(r,z) + \mu_0 \mathbf{M}_{rev} \quad (4.38)$$

$\mathbf{B}_{self}$ (r,z) is the self-field generated by local J_c with location expressed by cylindrical polar co-ordinates. $\mathbf{M}_{rev}$ refers to the reversible magnetization. The pinning force per unit volume value (F_p) can be calculated by,

$$-\mathbf{F}_p = \mathbf{J}_c \times \mathbf{B} \quad (4.39)$$

Besides, F_p values can be calculated by the required work (ΔW) that refers to moving a pinned flux line from the pinning centres to the nearest position where it is unpinned, as illustrated in [21],

$$F_p = -\frac{\eta L \Delta W}{x} \quad (4.40)$$

where η is an efficiency factor and L is the total length of pinned flux lines per unit

volume. x is the effective range of the pinning interaction. Dew-Hughes et al then used Eq. 4.40 to deduce a F_p formula based on the grain boundary pinning [21]:

$$F_p \propto \frac{B_{c2} h^{1/2} (1-h)^2}{\kappa^2} \quad (4.41)$$

Where $h = B/B_{c2}$ and κ is Ginsberg-Landau parameter. Combining Eq. 4.39 and Eq. 4.41, one can get Eq. 4.5 to calculate J_c under the grain boundary pinning condition. On the other hand, the method used in fitting J_c curves empirically is expressed as [184, 185],

$$J_c = J_{c0} \exp(-B/B_0)^a \quad (4.42)$$

where B_0 and a are the fitting parameters and J_{c0} corresponds to J_c values when B_{app} is zero. A large difference between two methods in obtaining J_c-B relationships can be observed in the shape and magnitude of J_c curve as B approaches 0. Eq. 4.42 gives a finite value (J_{c0}) while the value calculated from the pinning theory equation is infinite. This inconsistency arises from the effects of self-field. That is, when analysing pinning mechanisms, B instead of B_{app} should be used to plot to pinning curves to get a reasonable conclusion.

4.3.2 Methods of self-field corrections

The self-field influence can be evaluated roughly from the B_{peak} position. If B_{peak} is close to 0, it is reasonable to neglect corrections. According to [186], several assumptions have to make before corrections: (i) the reversible magnetization ($\mathbf{M}_{rev}$) is neglectable, (ii) samples are in a fully-penetrated state and the flux density gradient has

been totally reversed. (iii) Bean's critical state model can be used to obtain average J_c. The procedure is to transform $m(B_{app})$ to m(B) and then extract average J_c by Bean's model.

Due to infinite 'order of rotational symmetry', any site $P(r_p, z, \theta)$ can be simplified as $P(r_p, z, 0)$. As sketched in Figure 4.27, magnetic field at P point generated by a charged ring of radius r and height z_1 in a cylinder of radius r_a and height 2d can be calculated by complete elliptical integrals based on the Biot-Savart law:

$$B_{self,x} = \frac{\mu_0 r\bar{J}}{4\pi}\int_0^{2\pi} \frac{(z - z_1)\cos\beta}{\left[(r_p - r\cos\beta)^2 + (r\sin\beta)^2 + (z - z_1)^2\right]^{3/2}} d\beta \qquad (4.43)$$

$$B_{self,y} = \frac{\mu_0 r\bar{J}}{4\pi}\int_0^{2\pi} \frac{(z - z_1)\sin\beta}{\left[(r_p - r\cos\beta)^2 + (r\sin\beta)^2 + (z - z_1)^2\right]^{3/2}} d\beta \qquad (4.44)$$

$$B_{self,z} = \frac{\mu_0 r\bar{J}}{4\pi}\int_0^{2\pi} \frac{r - r_p\cos\beta}{\left[(r_p - r\cos\beta)^2 + (r\sin\beta)^2 + (z - z_1)^2\right]^{3/2}} d\beta \qquad (4.45)$$

$$B_{self,r} = {B_{self,x}}^2 + {B_{self,y}}^2 \qquad (4.46)$$

where $B_{self,r}$ and $B_{self,z}$ are axial and radial components. B_{self} in P site can be calculated by integrating field contributions of all current loops in the cylinder. Applying Bean's model,

$$\bar{J}_c = \frac{3m}{r_a V} \qquad (4.47)$$

Normalising the self-field over the samples volume V and defining D as an analogy to the demagnetizing factor used for homogenous magnetized samples,

$$\frac{1}{V}\int_{d}^{-d} B_{self}(\bar{J}_c, r, z)drdz = \mu_0(1-D)\frac{m}{V} \qquad (4.48)$$

The dependence of D values on the ratio r_a/d is plotted in Figure 4.27. Since D approaches 1 with an increasing ratio, self-field effects become severe in thin samples.

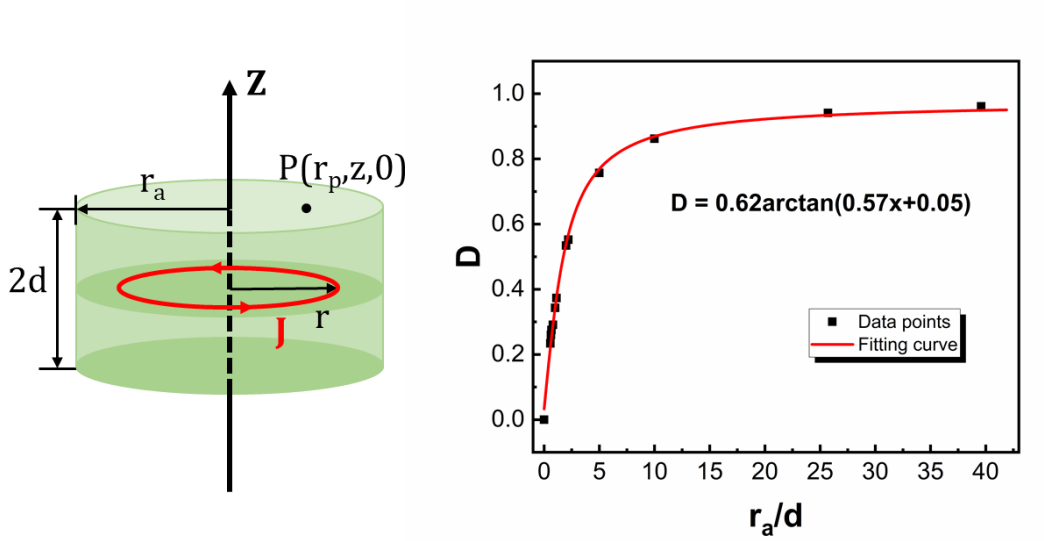


Figure 4.27 Sketch of a cylindrical sample in cylindrical polar co-ordinates. The right figure shows D values under various r_a/d and the fitting curve.

$\bar{J}_c$-independent axial and radial components $b_{self,z}$ and $b_{self,r}$ are defined by normalization,

$$b_{self,z} = B_{self,z}\frac{V}{(1-D)m\mu_0} \qquad (4.49)$$

$$b_{self,r} = B_{self,r}\frac{V}{(1-D)m\mu_0} \qquad (4.50)$$

For example, if $r_a/d = 0.57$, the distribution of $b_{self,z}$ and $b_{self,r}$ values is depicted in Figure 4.28. $b_{self,z}$ reaches maximum in the centre of the sample and minimum at the sample edge.

$$b_{self,z}^{max} = B_{self,z}(\bar{J}_c, 0, 0)\frac{V}{(1-D)m\mu_0} \qquad (4.51)$$

$$b_{self,z}^{min} = B_{self,z}(\bar{J}_c, r_a, 0)\frac{V}{(1-D)m\mu_0} \qquad (4.52)$$

Similarly, b_{app} can be defined,

$$b_{app}(r,z) = B_{app}\frac{V}{(1-D)m\mu_0} \tag{4.53}$$

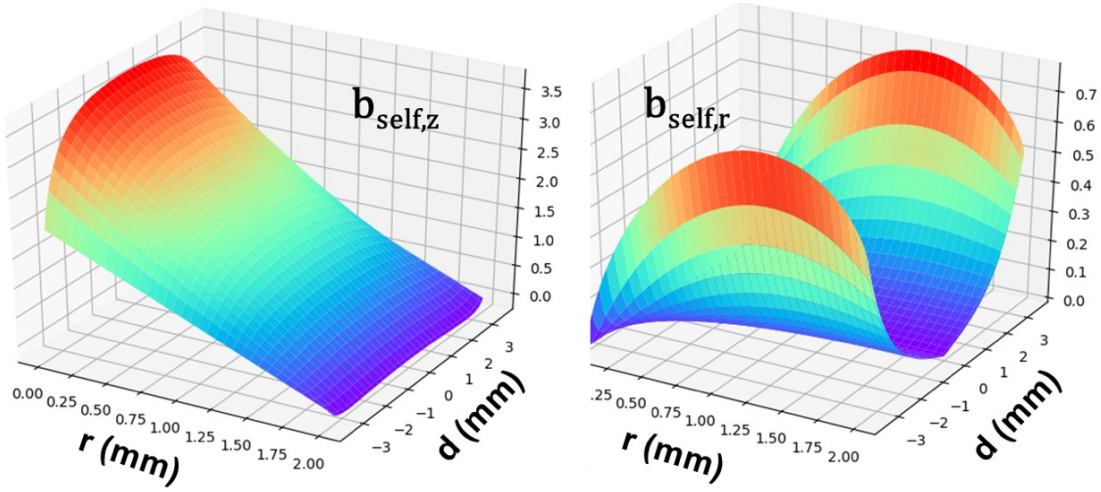


Figure 4.28 The distribution of normalised axial and radial self-field values ($b_{self,z}$ and $b_{self,r}$) in samples with $r_a/d = 0.57$.

Since,

$$b_{local} = \sqrt{\left(b_{app} + b_{self,z}\right)^2 + \left(b_{self,r}\right)^2} \tag{4.54}$$

Average b of the whole sample can be calculated from b_{local} analogous to $\bar{J}_c$ extracted from Bean's model,

$$b_{av} = \frac{\int_{-d}^{d}\int_{0}^{r_a} b_{local}\pi r^2 dr dz}{\int_{-d}^{d}\int_{0}^{r_a}\pi r^2 dr dz} = \frac{3}{r_a V}\int_{-d}^{d}\int_{0}^{r_a} b_{local}\pi r^2 dr dz \tag{4.55}$$

Defining the field correction function C_B:

$$C_B = b_{av} - |b_{app}| \tag{4.56}$$

The $m(B_{app})$ can be transformed to m(B) by,

$$B = |B_{app}| + C_B\frac{(1-D)\mu_0}{V}|m| \tag{4.57}$$

As Figure 4.29a shows, C_B represents the degree of deviation between the B_{app} and B and closely relates to the ratio r_a/d. $b_{self.z}^{max}$ and $b_{self.z}^{min}$ define the range that needs to be revised. b decides the line slope intersecting with moment curves in m-B_{app} plots, therefore dividing B_{app} into ranges with corresponding regimes in $C_B(b_{app})$ curves (Figure 4.29b and c). Details are summarized in Table 4.2. Since the flux density is not fully reversed in $B_3 < B_{app} < 0$, $m(B_{app})$ cannot be corrected in this range. An example of correction results is presented in Figure 4.29d. The inset figure shows that there is a gap around zero for which we have no data after self-field corrections, so the corrected J_c curve does not start from B = 0. From the trend of J_c curves, it can be speculated that $J_c \rightarrow \infty$ when B approaches 0, which is consistent with $J_c(B)$ formula calculated from pinning theories (Eq. 4.5).

Table 4.2 Summary of intervals of b_{app} and B_{app}. B_{self} and B_{app} are compared to determine the B_{av} direction.

Range in C_B (b_{app})	Range in $m(B_{app})$	State	B_{av} direction
$b_{min} < b_{app}$	$B_1 < B_{app}$	$B_{self} > 0$, $B_{app} > 0$, $B_{self} \gg B_{app}$	Positive
$0 < b_{app} < b_{min}$	$0 < B_{app} < B_1$	$B_{self} > 0$, $B_{app} > 0$, apparent B_{self} effects	Positive
$b_{peak} < b_{app} < 0$	$B_2 < B_{app} < 0$	$B_{self} > 0$, $B_{app} < 0$, $\lvert B_{app}\rvert < B_{self}$	Not fully reversed
$b_0 < b_{app} < b_{peak}$	$B_3 < B_{app} < B_2$	$B_{self} > 0$, $B_{app} < 0$, $\lvert B_{app}\rvert > B_{self}$	Not fully reversed
$b_{max} < b_{app} < b_0$	$B_4 < B_{app} < B_3$	$B_{self} < 0$, $B_{app} < 0$, apparent B_{self} effects	Negative
$b_{app} < b_{max}$	$B_{app} < B_4$	$B_{self} < 0$, $B_{app} < 0$, $\lvert B_{app}\rvert \gg B_{self}$	Negative

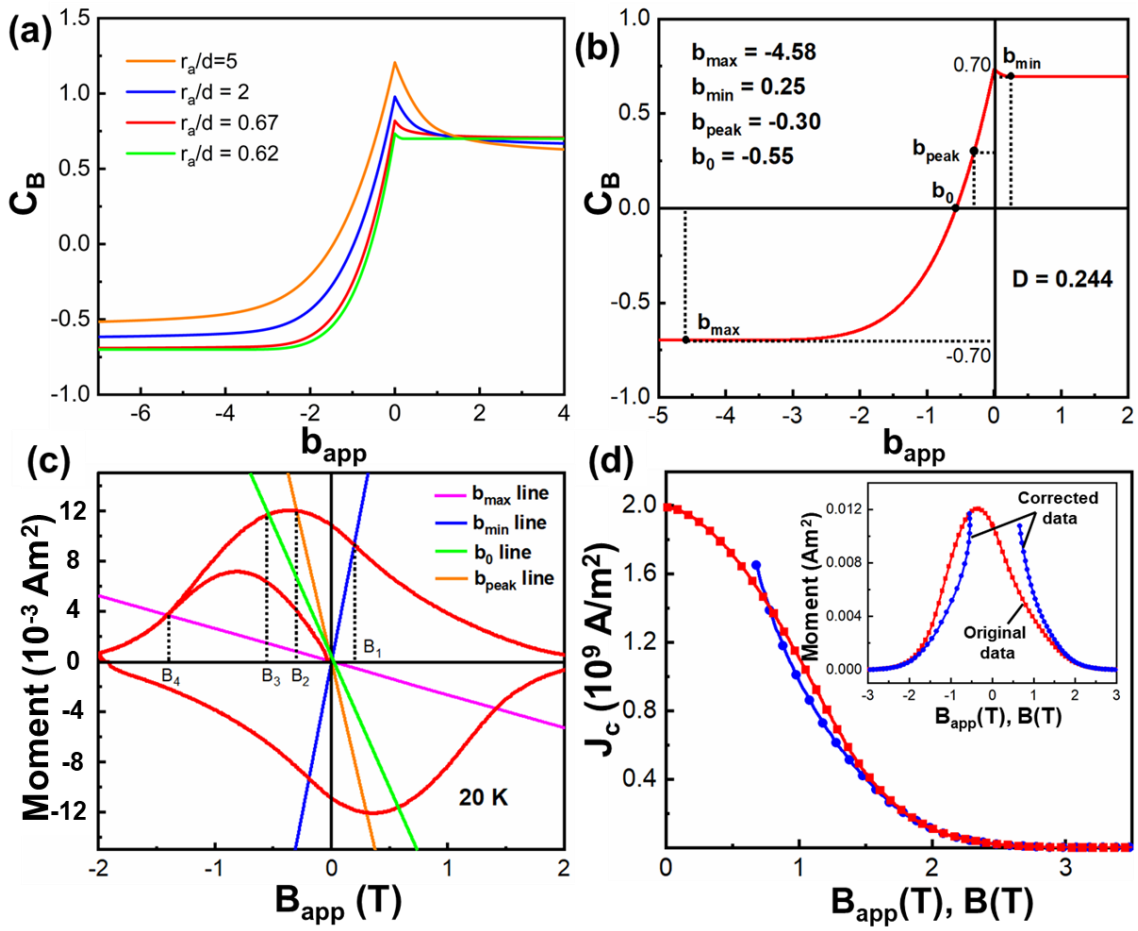


Figure 4.29 (a) shows field correction functions C_B for different r_a/d and important b values are labeled in (b). (c) depicts the B_{app} ranges divided by different lines of b. (d) presents the corrected moment and J_c curves.

4.4 Conclusions

This chapter solves two problems existing in the analysis of magnetization data.

i. The first one is the reliable extraction of J_c by Bean's critical state model. Cell model, percolation model and duplex microstructure model are discussed/established to calculate the total ΔM in the presence of different microstructural features. Practical simulation gives five schematic diagrams of typical microstructures based on which ΔM values from currents flowing

on different scales in samples are calculated to figure out their contribution to the total ΔM. This work stresses the importance of microstructural characterisation to explain the superconducting performance reasonably. Different microstructures are classified into five categories based on Section 4.2.6 followed by the estimation of $\Delta M(B_{app})$ performance and dominated J_c under different conditions.

ii. The second one is the self-field correction. Biot-Savart law is applied to calculate the local magnetic field in cylindrical samples with different dimensions. After transforming B_{app} to B, real $J_c(B)$ can be plotted and used to calculate pinning curves and analyse pinning mechanisms. I will introduce the influence of self-field corrections in Chapter 6 by experiments data to show its necessity.

Chapter 5 Microstructures and superconducting properties of MgB_2 bulk samples processed by ultra-high pressure-assisted sintering

5.1 Introduction

Some studies have used ultra-high pressure (2 GPa) to prepare in-situ or ex-situ MgB_2 bulk samples, and high boride (MgB_x, $x>4$) or Mg-B-O inclusions were supposed to be potential pinning centres in their conclusions [187, 188]. However, the causes of different performances in MgB_2 superconductors processed under various conditions have not been clearly explained. There are also other studies that applied ultra-high pressure to manufacture in-situ MgB_2 samples but lacked systematic microstructural characterization [64, 189]. Additionally, by investigating the role of extreme pressure (5 GPa) on processing other bulk samples such as alumina, it is found that plastic deformation of particles could aid the elimination of pores and enhance local atomic diffusion at grain boundaries, which helps achieve bulk densification in short process times [74]. In this chapter, I will report on the use of ultra-high pressure-assisted sintering to prepare MgB_2 bulk samples and examine the effects of temperature, pressure and time on microstructural evolution. This study linking microstructural evolution to corresponding changes in superconducting performance may have implications for designing superconductors by other processing methods.

5.2 Experimental Methods

The samples analysed in this chapter were prepared at Element Six. MgB_2 powder (purity: 99%, Alfa Aesar) was ground in an agate mortar before being pressed into cylindrical pellets. Cu/Ti was used as sheath materials and an additional Nb layer acts as a chemical barrier prohibiting the reaction between the outer sheath and the MgB_2 powder during heat treatment. An industrial-scale cubic press at Element Six was used to apply ultra-high pressures from 4.5 GPa to 7.5 GPa at temperatures ranging from 700 ^oC and 1100 ^oC. Different sintering times up to 20 min were studied to observe microstructural and phase evolution during the ultra-high pressure sintering process. Detailed processing conditions for all the samples are shown in Table 5.1.

Table 5.1 Processing conditions of MgB_2 samples

Samples		Time (min)	Temperature (^oC)	Pressure (GPa)
Time series	t5	5	800	5.5
	t10	10	800	5.5
	t15*	15	800	5.5
	t20	20	800	5.5
Temperature series	T700	15	700	5.5
	T800*	15	800	5.5
	T900	15	900	5
	T1100	15	1100	5
Pressure series	P4.5	15	800	4.5
	P5.5*	15	800	5.5
	P6.5	15	800	6.5
	P7.5	15	800	7.5

*t15, T800 and P5.5 refer to the same sample.

5.3 Effect of processing temperature on microstructure

The effect of temperature on microstructural development of a series of samples pressed

at 5/5.5 GPa for 15 min has been studied. The 0.5 GPa pressure difference between some of the samples is shown in section 5.3.2 to have little effect, so the differences in microstructure can most be attributed to the temperature variation.

5.3.1 Phase identification and quantitative analysis by Rietveld refinement

XRD patterns for bulk samples in the temperature series are presented in Figure 5.1. All samples show evidence of MgB_2 decomposition products, MgB_4 and MgO. As the processing temperature increases, one can observe increasing intensity and decreasing full-width at half-maximum (FWHM) of the MgB_2 peaks, indicating an improvement in crystallinity. The enlarged figure highlights the (002) and (110) peaks, the angular positions of which are related to c and a axis of the MgB_2 unit cell respectively. A clear shift of both peaks to lower angles with increasing sintering temperature from 700 ^oC to 900 ^oC corresponds to an increase in c and a axis. The peak splitting observed in T1100 is consistent with the expected Cu $K_{\alpha 1}$ and $K_{\alpha 2}$ X-ray contributions that are hidden by peak broadening from imperfect crystallinity in the samples processed at lower temperatures.

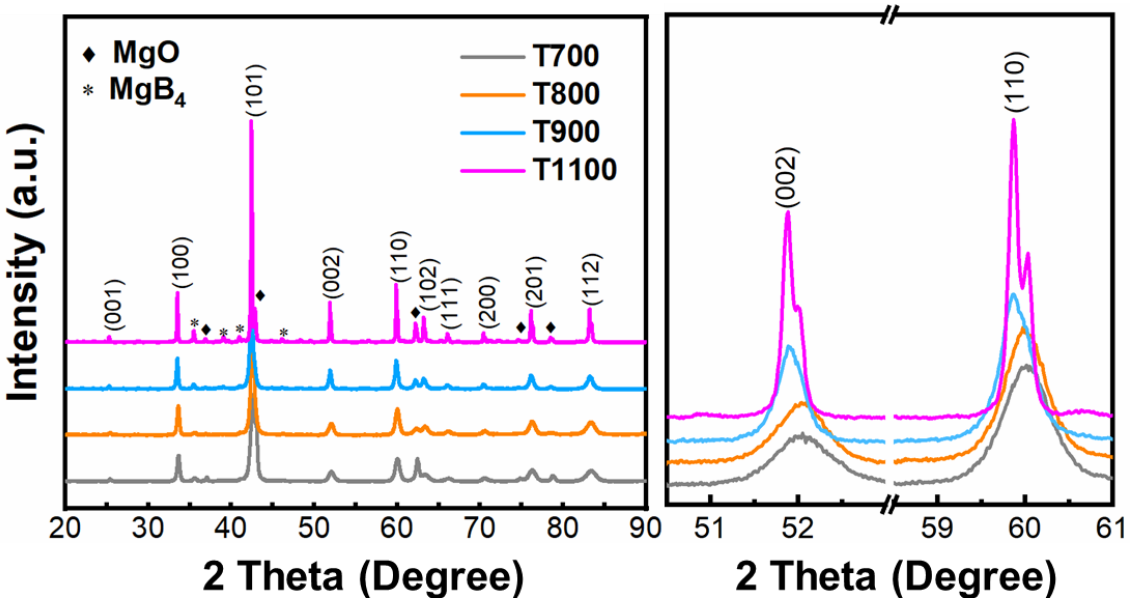


Figure 5.1 X-ray diffraction patterns (XRD) of MgB_2 samples processed at 700 °C, 800 °C, 900 °C and 1100 °C. The right figure shows an expanded region around the (002) and (110) peaks of MgB_2.

Table 5.2 summarises the results of quantitative analysis by the Rietveld method. The MgO content is found to increase by around 5 wt%, reaching 12 wt% at the highest processing temperature of 1100 °C. The reaction of Mg from extensive MgB_2 decomposition with adventitious oxygen is supposed to be responsible for the increasing MgO percentage at higher temperatures. An increase is also seen in MgB_4 content, from 6 wt% in T600 to 13 wt% in T1100. The Rietveld fitting methodology is the same as the previous work done by our group using the same software and procedure [67], so XRD results of MgB_2 bulk samples processed by field-assisted sintering at 900 °C and 1100 °C in their work are also listed in Table 5.2 for comparison. It can be seen that the c axis is apparently compressed in samples prepared under ultra-high pressure-assisted sintering process and MgB_4 formation from the decomposition of MgB_2 is effectively suppressed.

Table 5.2 The phase content, lattice parameters, crystallite size and strain are obtained by Rietveld refinement. Refinement results from FAST samples from [67] are presented as a comparison.

Sample	MgO (wt%)	MgB_4 (wt%)	MgB_2 a axis (Å)	MgB_2 c axis (Å)	Crystallite size (nm)	Microstrain (%)
T700	7	6	3.086	3.519	29	0.40
T800	8	6	3.086	3.519	30	0.37
T900	11	6	3.087	3.521	38	0.23
T1100	12	13	3.086	3.521	113	0.03
FAST900	7	11	3.085	3.525	120	0.12
FAST1100	8	16	3.084	3.527	140	0.13

Dramatic crystallite growth occurs when the temperature rises to 1100 ºC, below which there is only a modest increase in MgB_2 crystallite size (29 nm in T700 compared to 38 nm in T900). Even so, these values of crystallite size are still much smaller than those in samples prepared at the same nominal temperatures by FAST, a process in which only 50 MPa of pressure was applied for 5 min (Table 5.2). This demonstrates the advantage of ultra-high pressure in prohibiting crystallite growth during sintering. Micro-strain shows a steady drop from 0.4% in T700 to nearly zero in T1100, suggesting that crystal defects resulting from plastic deformation have been gradually eliminated at high processing temperatures.

5.3.2 Microstructural analysis

Backscattered electron (BSE) images of two typical microstructures are first shown in Figure 5.2. MgO grains appear brighter than the MgB_2 matrix and MgB_4 grains are darkest owing to atomic number contrast. The T1100 sample presented in Figure 5.2a shows MgB_2 regions ranging in size from a few microns to about tens of microns, surrounded by MgB_4 and MgO grains. The underlying, relatively uniform grain

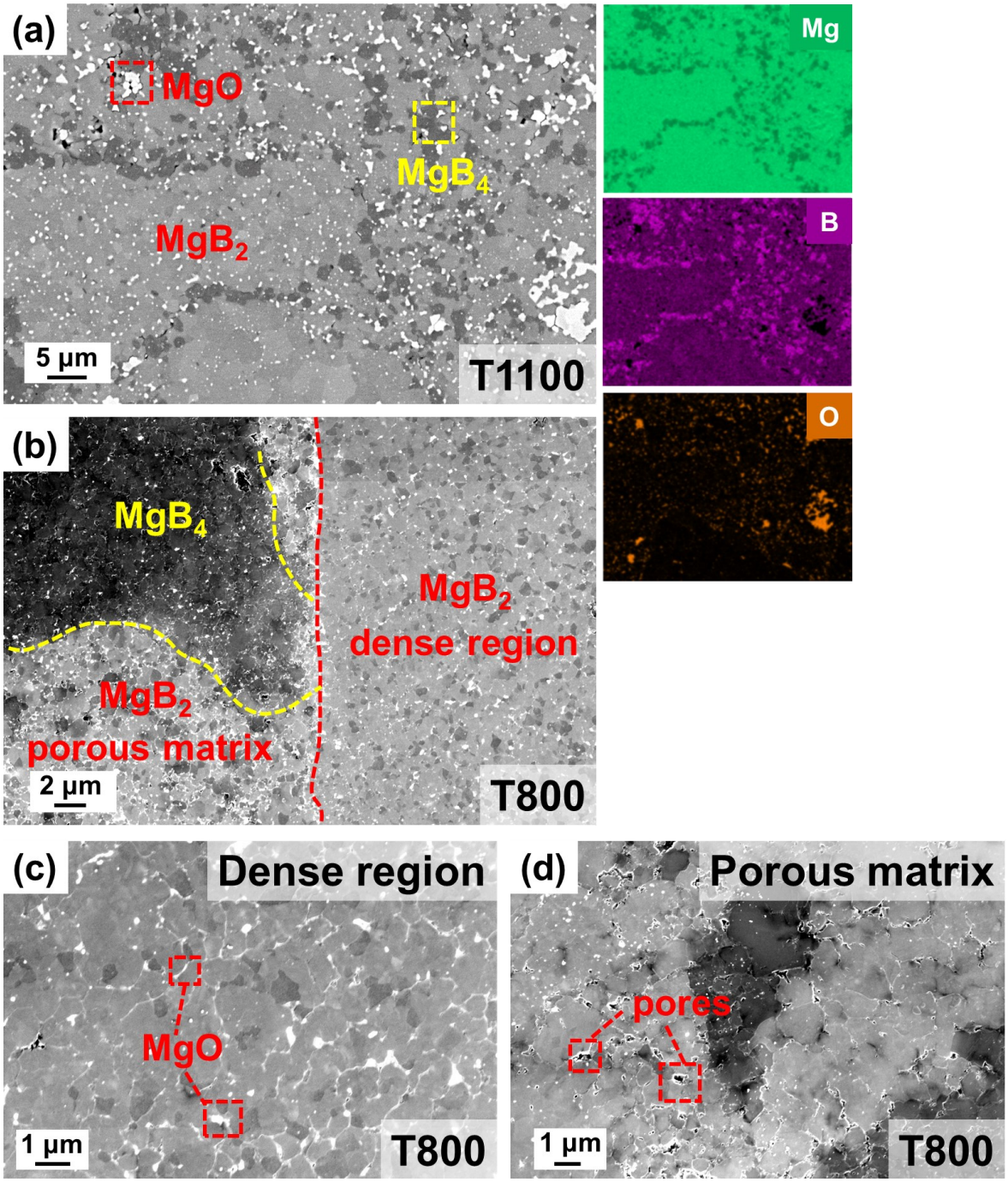


Figure 5.2 Backscattered electron (BSE) micrographs showing (a) different contrasts of MgB_2, MgO and MgB_4 (along with EDX maps of Mg, B and O elements) in the sample processed at 1100 ºC and 5 GPa for 15 min and (b) the existence of dense regions, porous matrix of MgB_2 and large MgB_4 phases in sample processed at 800 ºC and 5.5 GPa for 15 min. (c) and (d) present high magnification images of dense regions and porous matrix in T800.

structure can be seen owing to backscattered electron channeling effects. Figure 5.2b shows a lower temperature processed sample, T800, in which both dense MgB_2 and more porous MgB_2 regions can be observed, as well as large MgB_4 phases. Figure 5.2c is a high magnification image of a dense region in the T800 sample where the bright MgO impurities at grain boundaries can be observed. The porous matrix in Figure 5.2d contains a large number of partially-connected pores in the interfaces of MgB_2 particles, demonstrating the incomplete densification in the final stage of processing.

SEM images of polished T700, T800, T900 and T1100 samples at different magnifications (500× and 3000×) are presented in Figure 5.3. T700 has a high fraction of interconnected, non-uniform pores (Figure 5.3a and b). As the temperature is increased to 800 ºC, dense regions with sizes up to 50 μm form, surrounded by porous regions where large MgB_4 phases are situated (Figure 5.3c and d). The porous regions are fully eliminated in T900 and T1100 samples, as shown in Figure 5.3e and g, suggesting that complete densification can be achieved if the high-pressure sintering temperature is above 900 ºC. The higher magnification images in Figure 5.3f and h show that two different morphologies are present at higher temperatures. i.e., well-connected regions with coarse grains separated by transition zones characterised by fine grains. These transition zones are believed to be the final, and most difficult, regions to densify.

However, some prominent differences in microstructures distinguish the T1100 and T900 samples. First, higher temperatures (1100 ºC) lead to the formation of large MgB_9

particles around 4 μm in size (Figure 5.3g). Moreover, apart from large phases, more MgB_4 isolated grains can be observed in T1100. As Figure 5.2a shows, MgB_4 grains surrounding dense MgB_2 regions in T1100 form a partial barrier, separating dense MgB_2 colonies from each other and thus decreasing connectivity, which is expected to be detrimental to the transport of bulk currents. The apparent MgO-rich area in T1100, as a result of the severe decomposition of MgB_2, also indicates that 1100 ^oC is above the optimal processing temperature.

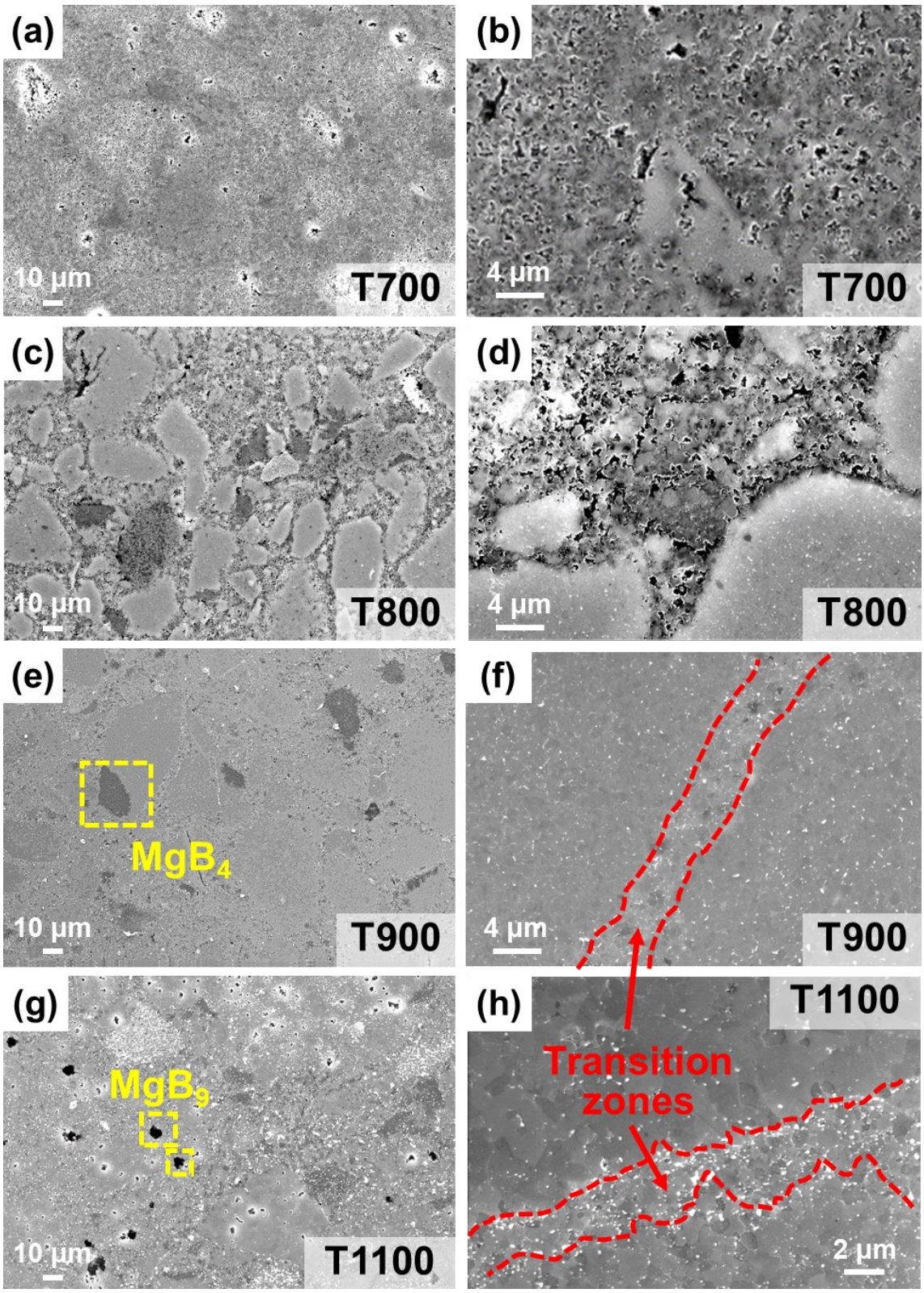


Figure 5.3 Scanning electron microscope (SEM) micrographs of samples processed at (a, b) 700 ºC, (c, d) 800 ºC, (e, f) 900 ºC and (g, h) 1100 ºC captured at 500× and 3000× magnifications respectively.

5.3.3 Detection of grain size and grain defects

EBSD mapping results of samples in the temperature series are shown in Figure 5.4. There is no apparent texture in the bulk samples, which may be explained because the pressure is applied by a cubic press rather than a uniaxial press. Figure 5.4a shows small grain sizes in T700, indicating the limited grain growth under such a low temperature. Black regions (unsolved pixels that arise from the poor diffraction patterns or the failure of fitting the diffraction patterns to the reference patterns generated by selected phases) mainly result from high porosity. With increasing temperature, the decreasing fraction of black regions suggests the elimination of pores so grains have better contact with each other (Figure 5.4b-d). However, inhomogeneous areas with different grain sizes are presented in Figure 5.4e, labelled as A and B, where the fine-grained matrix includes a higher amount of MgO impurities. The phase map obtained by Transmission Kikuchi Diffraction (TKD), as shown in Figure 5.4f, explains that black regions in Area B come from nanograins (MgO and MgB_4) beyond the resolution of traditional EBSD. The average grain size distribution plotted in Figure 5.4g shows a steady increase with sintering temperature. The broader grain size distribution in both T900 and T1100 is the consequence of the mixture of small grains in transition zones and larger grains within well-connected regions.

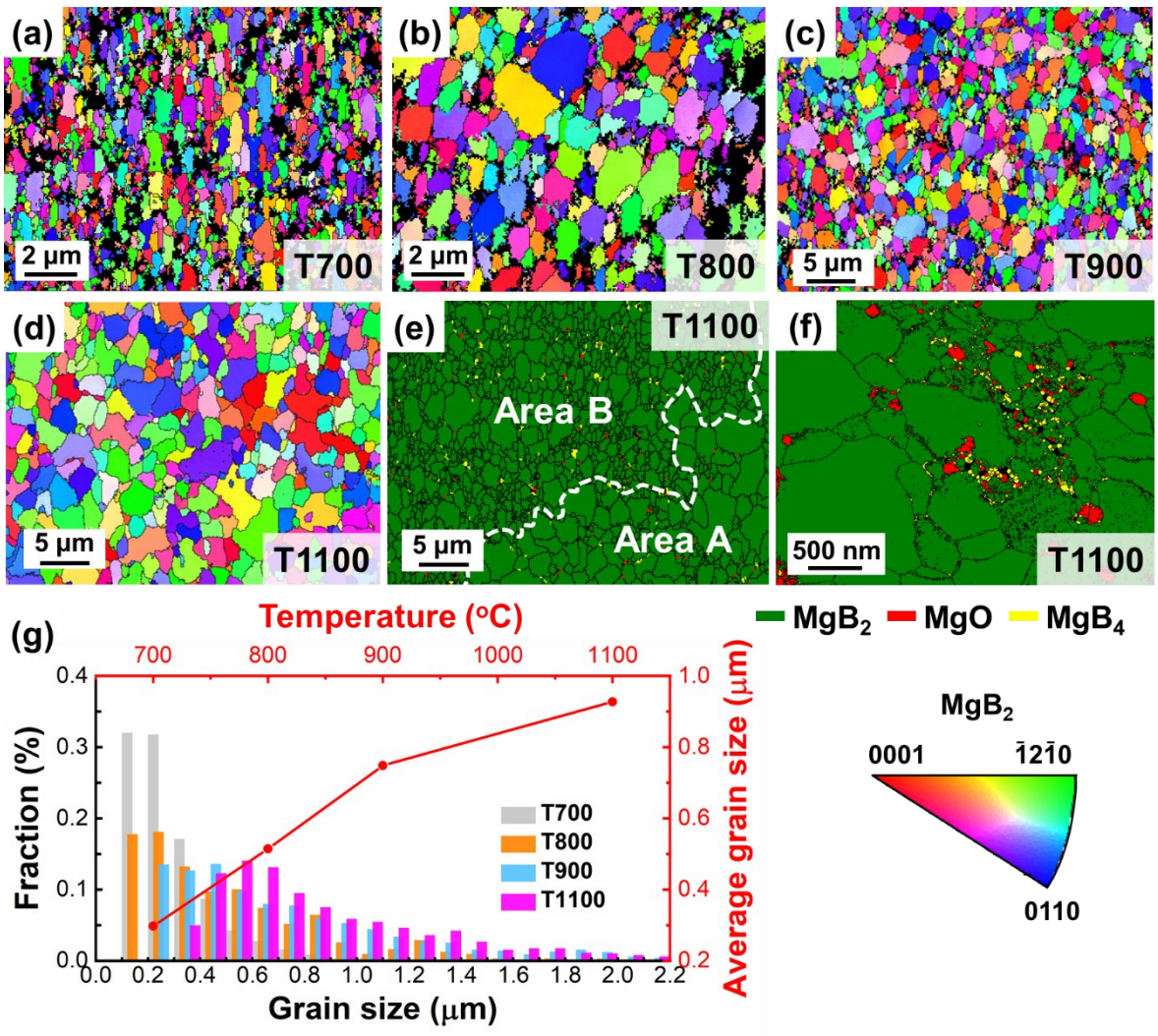


Figure 5.4 EBSD IPF maps from Z direction (IPFZ) of samples produced at (a) 700 ºC, (b) 800 ºC, (c) 900 ºC and (d) 1100 ºC. The black grain boundaries represent misorientations larger than 15°. (e) and (f) are phase maps of T1100 taken by traditional EBSD and by TKD. (g) shows the grain size distribution. Image (f) was captured by Dr. Sangeeta Santra.

As mentioned in Chapter 2, grain size is critical to the performance of MgB_2 superconductors to provide grain boundary pinning [190]. Additionally, grain defects such as dislocations may also introduce flux pinning centres to increase pinning strength [191]. Structural disorders within MgB_2 grains were investigated by Transmission electron microscopy (TEM), scanning TEM and High-resolution TEM

(Figure 5.5). Dislocation networks exist in T900 while the grain with regular geometry in T1100 is free of crystal defects. This observation is consistent with XRD results in Table 5.2, demonstrating that micro-strain is almost fully released in this higher temperature processed sample.

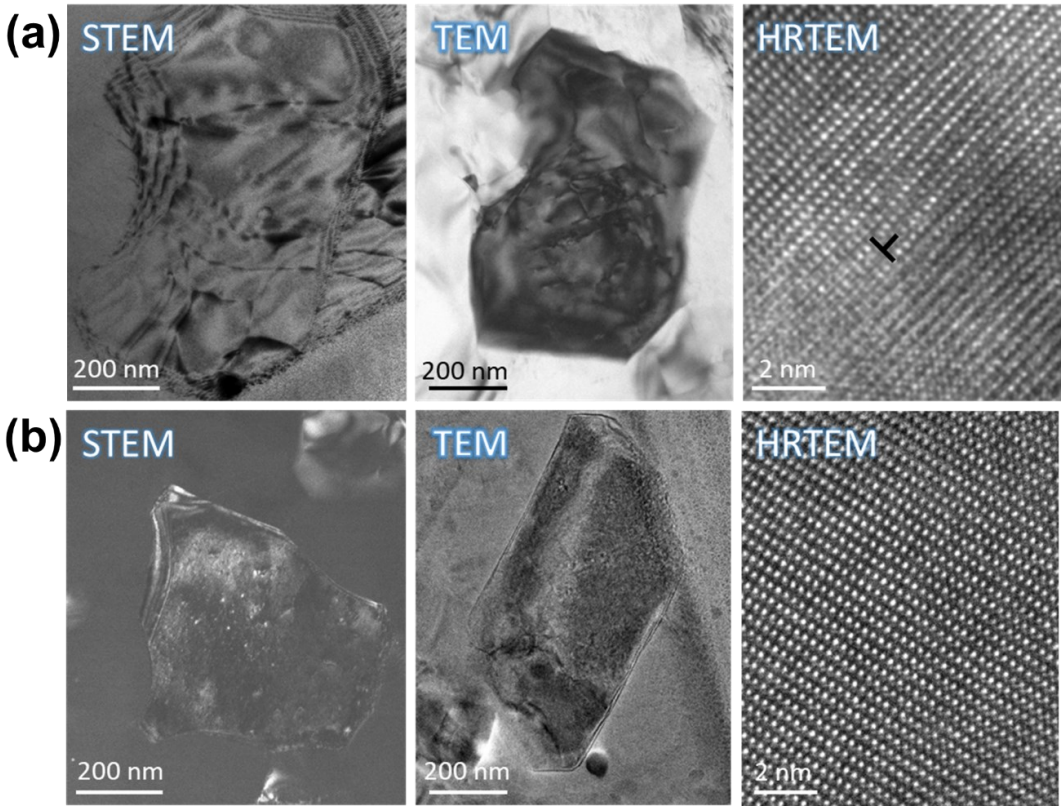


Figure 5.5 Transmission electron microscopy (TEM), scanning TEM and High-resolution TEM images of a single MgB_2 grain in (a) T900 and (b) T1100. All images were taken by Dr. Sajjad Amirkhanlou.

5.4 Effect of ultra-high pressure on microstructures

XRD patterns of MgB_2 bulk samples processed at different pressures at 800 ^oC are displayed in Figure 5.6. The peaks become slightly broader with increasing pressure, and the expanded region of XRD scans shows a modest shift of the (002) peak to higher angles but no change in the position of the (110) peak. Table 5.3 lists quantitative results

calculated by Rietveld refinement. The lattice parameter c drops slightly from 3.521 Å to 3.517 Å when the pressure increases to 7.5 GPa. This decrease in lattice parameters is consistent with the anisotropic compressibility of MgB_2 under ultra-high pressures studied by other authors [192-194]. There is no significant change in microstrain or crystallite size with pressure in this pressure regime. Microstrain beyond 0.4 in P7.5 indicates high levels of plastic deformation in this sample.

Table 5.3 The phase content, lattice parameters, crystallite size and strain extracted from XRD results by Rietveld refinement.

Sample	MgO (wt%)	MgB_4 (wt%)	MgB_2 a axis (Å)	MgB_2 c axis (Å)	Crystallite size (nm)	Microstrain (%)
P4.5	6	9	3.087	3.521	31	0.36
P5.5*	8	6	3.086	3.519	30	0.37
P6.5	9	5	3.087	3.519	27	0.35
P7.5	9	5	3.087	3.517	29	0.41

*t15, T800 and P5.5 refer to the same sample.

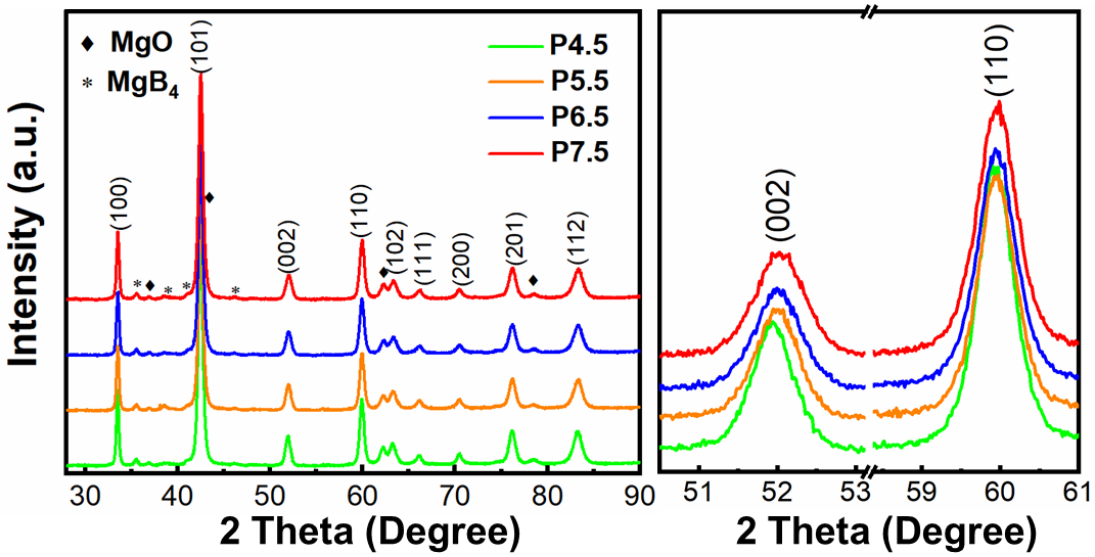


Figure 5.6 XRD diffraction patterns of P4.5, P5.5, P6.5 and P7.5 processed at 800 °C for 15 min. The right enlarged figure shows the (002) and (110) peaks of MgB_2.

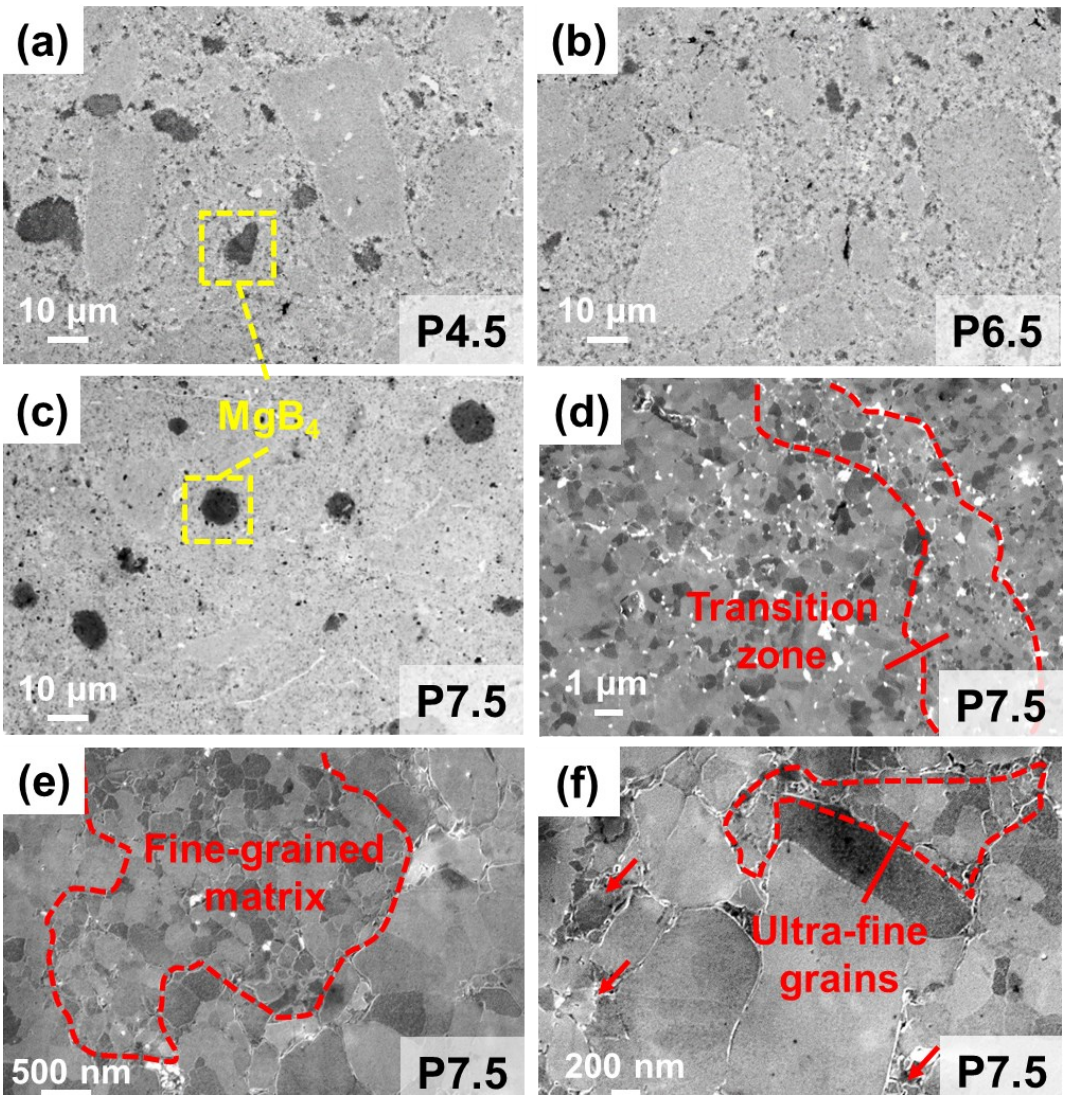


Figure 5.7 SEM images of samples processed under (a) 4.5 GPa, (b) 6.5 GPa, (c) 7.5 GPa at 800 ºC. (d) and (e) show the transition zone and fine-grained matrix in P7.5. (f) shows nanograins situated between large MgB_2 grains in P7.5.

A comparison of the microstructural features of samples is shown in Figure 5.7. P6.5 and P4.5 have quite similar structures with large MgB_2 dense regions distributed in the matrix but the sizes of MgB_4 phases are smaller in P6.5 (Figure 5.7a and b). Moreover, the area of porous regions is reduced with increasing applied pressure. Full densification is achieved in the sample processed at 7.5 GPa and 800 ºC within 15 min, which can be demonstrated by the transition zone linking well-connected MgB_2 regions

and the fine-grained matrix that is also free of pores (Figure 5.7d and e). Additionally, red arrows and areas within dashed lines in Figure 5.7f highlight the fine-grained area filling the space left between coarse grains.

Figure 5.8 shows EBSD maps obtained from P4.5 and P7.5. After removing outlying data points, the fraction of remaining unsolved pixels (black regions) increases from 12% to 36% at the higher pressure of 7.5 GPa (Figure 5.8a and b). These black regions in maps from P7.5 may consist of ultra-fine grains, as shown in Figure 5.7f. P4.5 and P7.5 samples are selected to examine dislocations accumulated within MgB_2 grains. The respective phase maps, as well as local misorientation maps (LAM) of three selected grains are shown on the right-hand side of Figure 5.8 within black dotted boxes. LAMs are obtained by comparing the misorientation of one pixel with its surrounding pixels (3 × 3 filter size) and assigning the mean value to this pixel, thereby highlighting areas of severe deformation. White lines in the phase maps represent low-angle grain boundaries (LAGB) (2^{o}~15^{o}). Under high applied stress, creep deformation accumulates, and cell walls due to dislocation entanglement are transformed into subgrains [195]. The obvious colour variation in two fragmented grains chosen from P7.5 corresponds to the formation and accumulation of LAGB within grains. The average grain size distribution in Figure 5.8c shows a decrease from about 750 nm to about 500 nm when the pressure increases to 7.5 GPa.

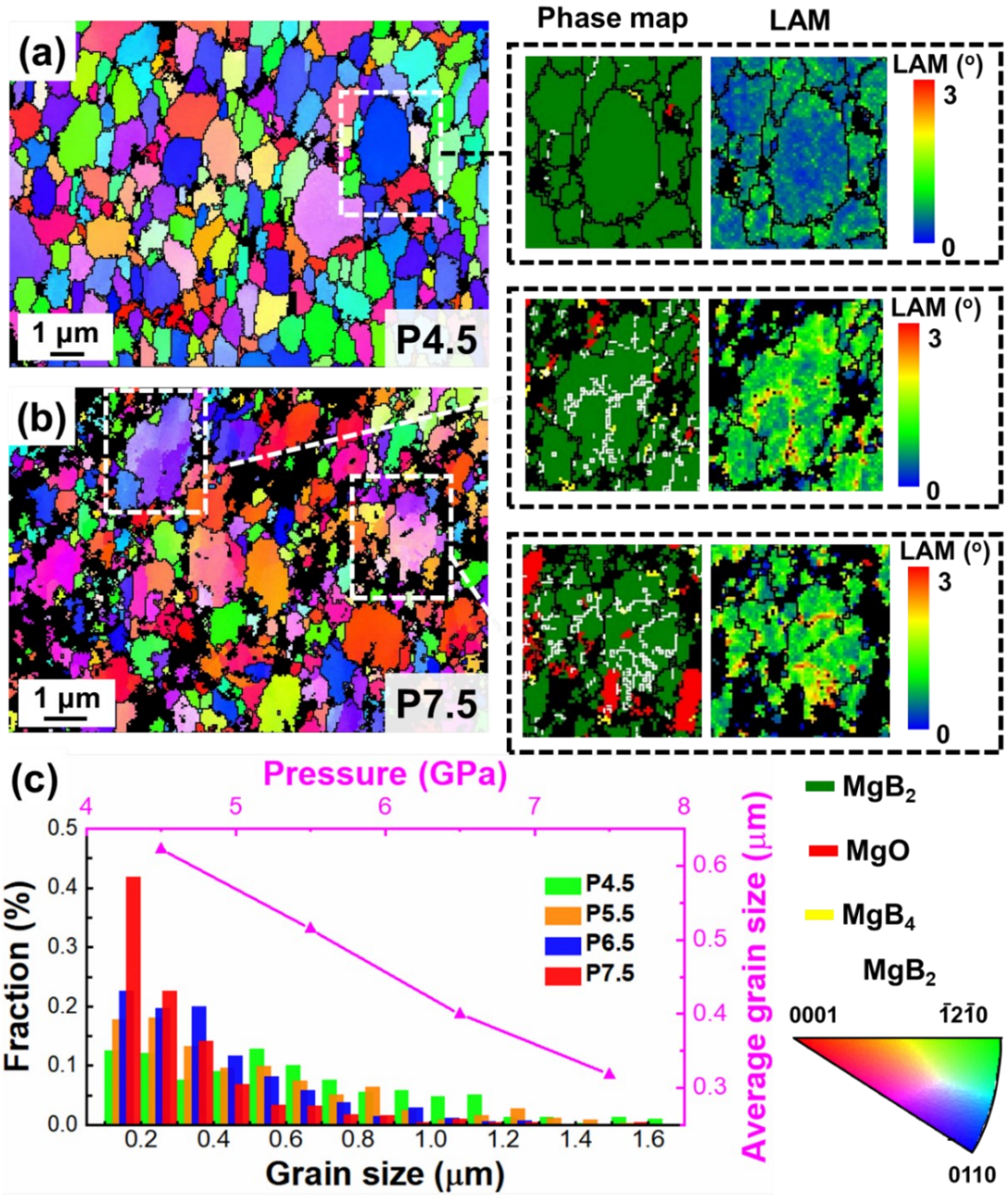


Figure 5.8 EBSD IPFZ maps of samples produced at (a) 4.5 GPa and (b) 7.5 GPa for 15 min at 800 °C. In the phase maps, black grain boundaries represent misorientations larger than 15°, while white lines inside the grains represent boundaries with misorientation angle between 2° to 15°. Local angular misorientation (LAM) maps of smaller areas identified in the IPFZ sections reveal the deformation substructures. (c) shows the grain size distribution histogram from EBSD analysis. The colour key of MgB_2 IPFZ maps is at the bottom-right corner.

5.5 Effect of time on microstructure

The evolution of morphologies of samples processed at 800 ºC, 5.5 GPa but different times is presented in Figure 5.9. The most obvious change is the growth of the MgB_4 particles as the time increases from 5 min to 20 min. At the beginning of processing (<5 min), there are a large number of pores in the samples, and dense regions can hardly be distinguished at this stage (Figure 5.9a). As the time is extended to 10 min, a duplex microstructure forms, with dense MgB_2 regions surrounded by a porous matrix (Figure 5.9c). At this relatively low temperature, even in the sample processed for 20 min, porous regions still exist (Figure 5.9e). A close inspection shows there are fewer pores in dense MgB_2 regions than in the matrix, with a size of around 0.5 μm in t5 (Figure 5.9b). These pores shrink and are almost completely eliminated in t10 and t20, accompanied by the formation of a larger amount of fine MgO generated at the MgB_2 triple grain junctions (Figure 5.9d and f).

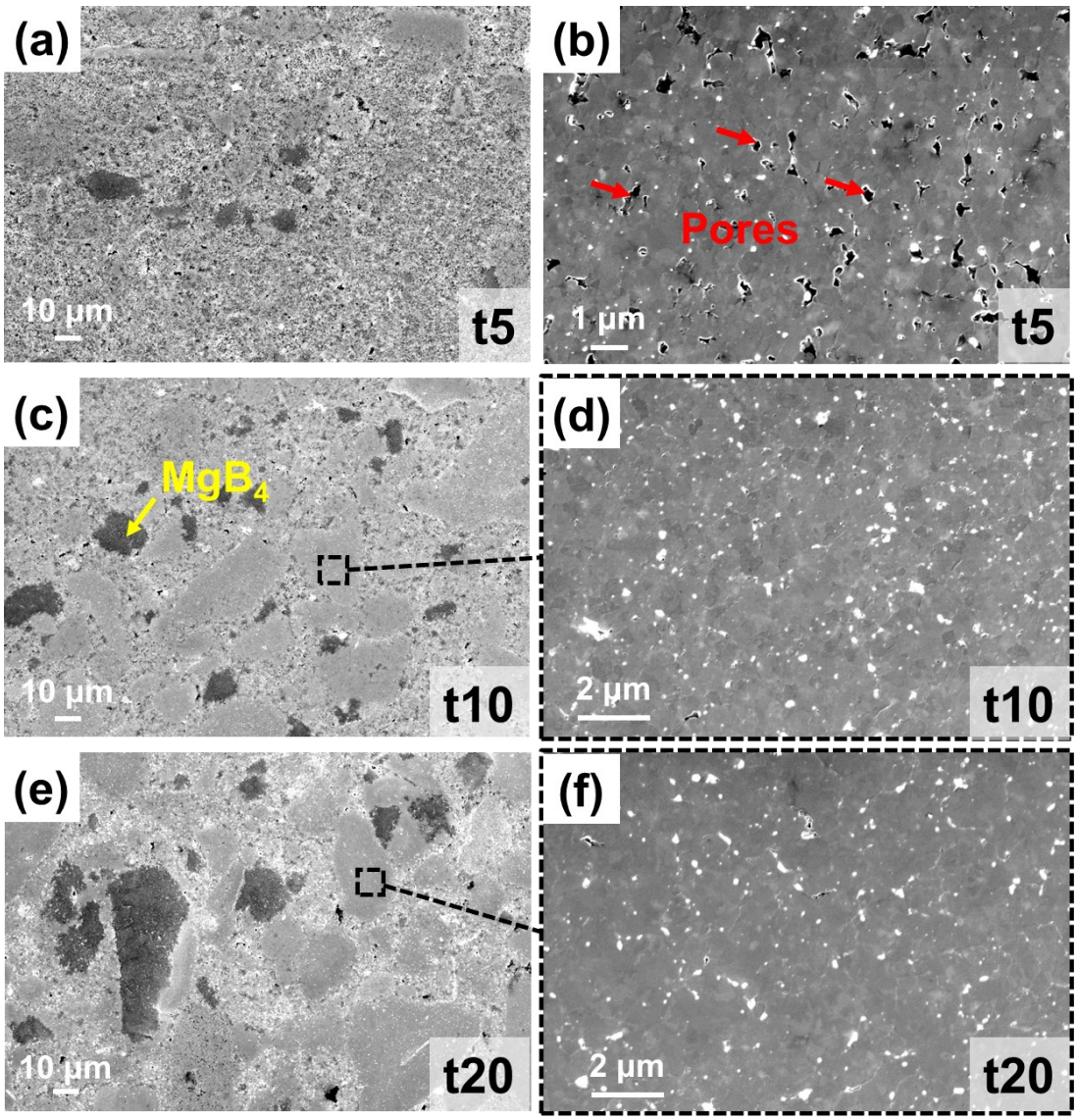


Figure 5.9 SEM images of (a) t5, (b) t10 and (c) t20. (d-f) are corresponding micrographs in dense MgB_2 regions at high magnification.

Figure 5.10 shows EBSD maps of these three samples and grain size distribution. As expected, the grain size increases with sintering time, from 370 nm in t5 to 580 nm in t20. With reference to EBSD maps and the grain size distribution, the decreasing fraction of small grains with time may indicate microstructural coarsening by Ostwald ripening.

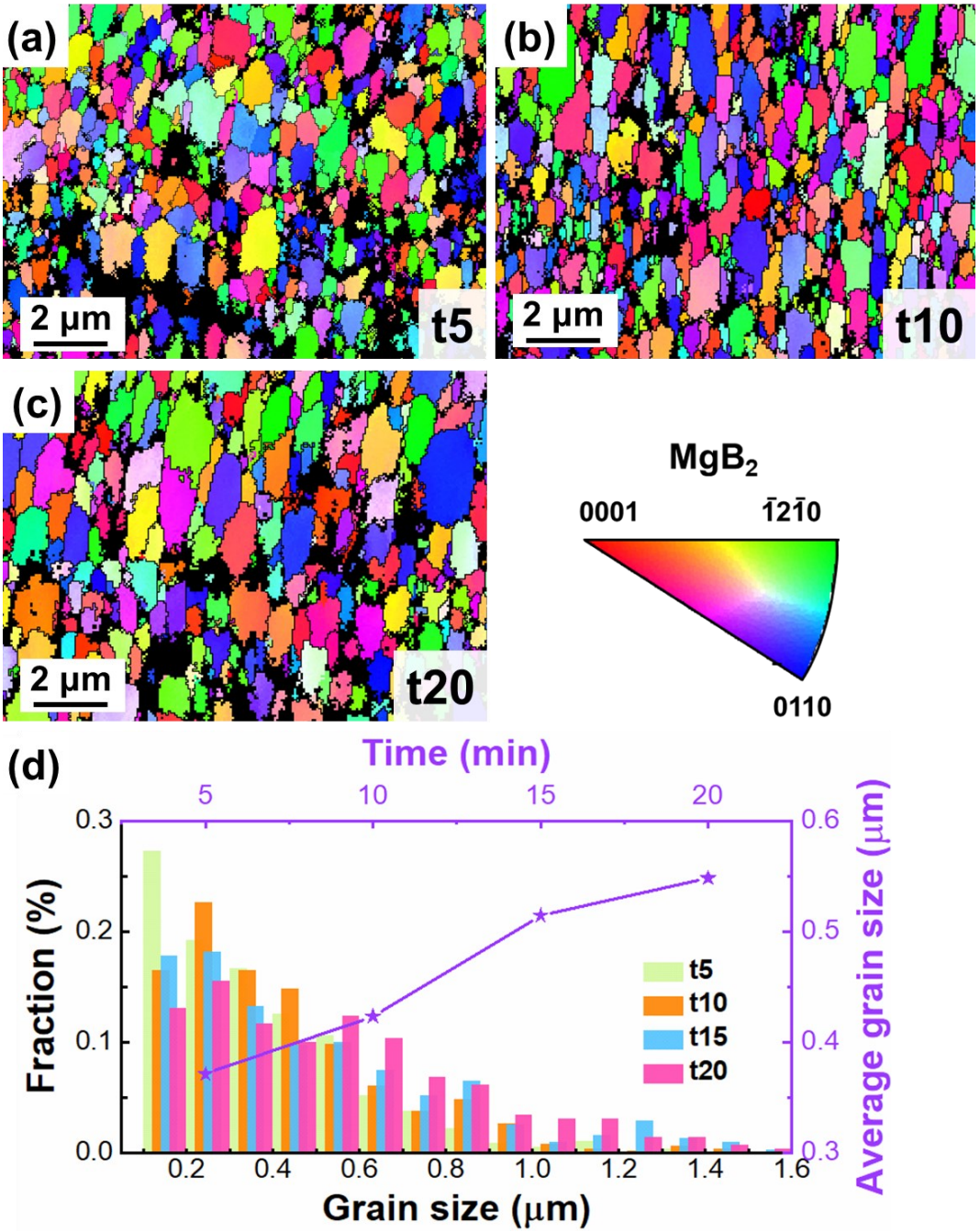


Figure 5.10 EBSD IPFZ maps of (a) t5, (b) t10 and (c) t20 processed at 800 °C and 5.5 GPa. The colour key of MgB_2 IPFZ maps is at the right hand. (d) is the gran size distribution histogram.

5.6 Discussion on microstructural evolution and mechanisms of densification

It is well known that the sintering in the hot pressing process can be divided into three

separate stages: (I) neck growth and grain boundary formation with minimal densification, (II) isolated pore creation with some grain growth and the majority of the densification process, and (III) pore shrinkage with grain growth and final densification [196]. Bulks processed from an initial powder with uniform particle size are expected to have homogenous microstructures. However, agglomeration in the precursor powders can change the sintering behavior and contribute to a hierarchical pore structure during consolidation, leading to different morphologies of bulk samples [197]. Figure 5.11 illustrates how I suggest the different types of microstructures observed in these MgB_2 samples form during high pressure processing from the green compact. Pore coordination number is defined as the average number of touching particles around each pore (R). Two types of pores exist in packed powders before sintering: (i) small pores with low coordination numbers (R_1) inside loose agglomerates, and (ii) large pores of higher pore coordination numbers (R_2) outside agglomerates where particles are loosely-packed. Generally, a critical coordination number R_c decides whether pores will disappear ($R < R_c$) or remain ($R > R_c$) after densification at the final stage of sintering. Lange et al illustrated that R_1 for intra-agglomerate pores is lower than R_2 for inter-agglomerate pores [198]. Therefore, in the initial stage of sintering under pressure, intra-agglomerate pores are prone to shrink and form dense regions [196, 197]. In short sintering times (<5 min), mass transport is inadequate so there is no obvious density inhomogeneity in the t5 sample. The slow diffusion rate at low temperature in T700 also limits the shrinkage of pores. This type of microstructure can be directly described

by Cell model D in Section 4.2.1.4 (Figure 5.3a and b).

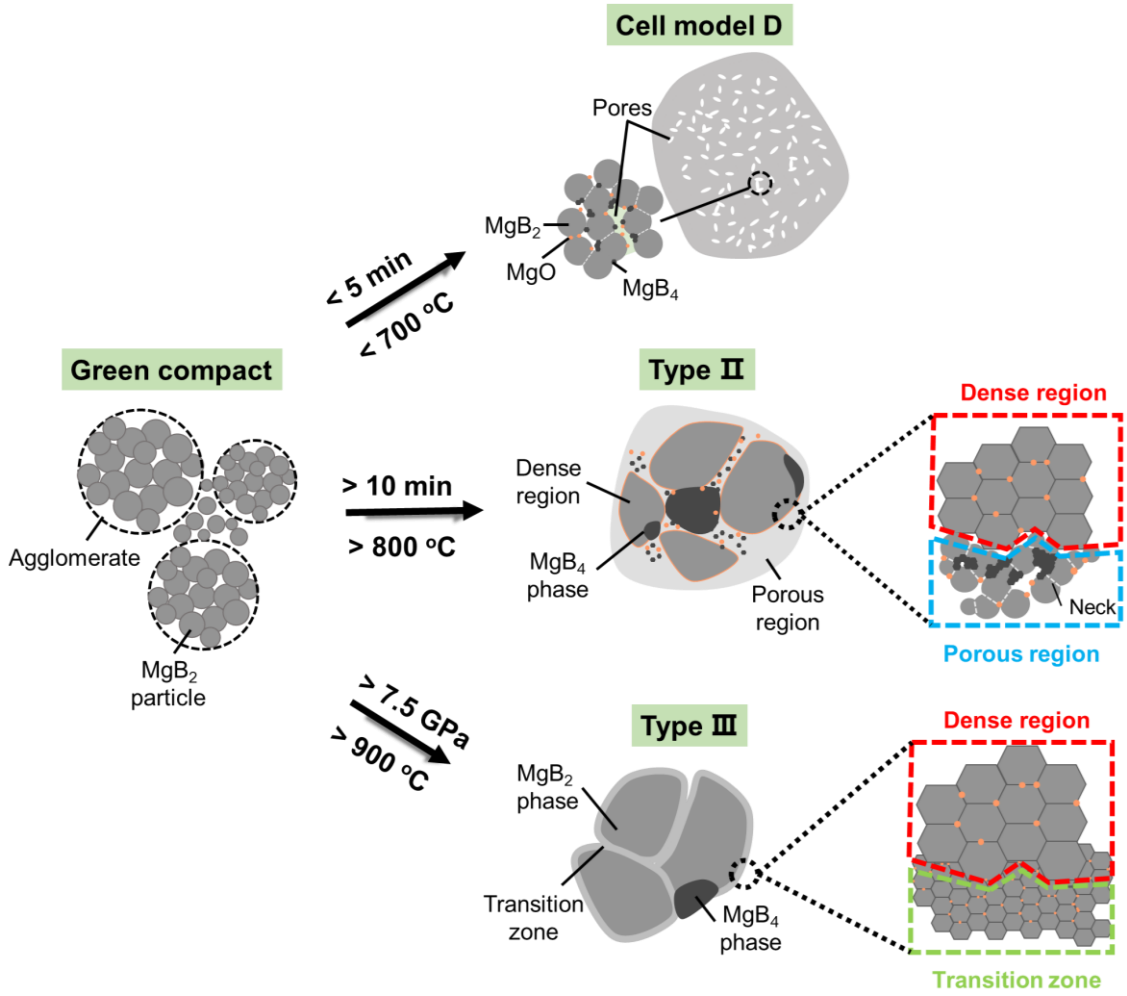


Figure 5.11 Schematic diagram of evolution from green compacts to three types of final microstructures in the MgB_2 bulk samples under different processing parameters.

When increasing temperature and time, the agglomerates are densified but the matrix remains porous. Additionally, residual oxygen trapped within pores in the matrix can react with Mg to form MgO, thus accelerating MgB_2 decomposition. This explains why large MgB_4 phases are always observed within the porous matrix (Figure 5.3). Zener pinning by fine second-phase particles or pores will slow down grain boundary movement in polycrystalline samples. Referring to the general form of Zener equation [199], the critical maximum grain radius (G_c) is expressed as:

$$G_c = k\frac{r_s}{f^m} \quad (5.1)$$

where k and m are constants, and m values usually lie in the range between 0.3 and 1, r_s and f are the radius and volume fraction of pinning particles, in this case, pores. Slower grain growth with the increasing fraction of porosity (or secondary phase particles) at the grain boundaries compared with that in denser regions may lead to heterogeneous Type II microstructures (Figure 5.3c and d).

Fully-dense samples, Type III, can be achieved either by increasing the processing temperature or external pressure, but densification mechanisms are different in the two cases. Faster mass transport at elevated processing temperature can promote rapid grain growth that reduces R_2 below R_c, so porous regions are able to densify within a short time. At the same time, grains in dense regions keep growing, resulting in a dramatic increase in the average grain size (Figure 5.4g). Increasing the applied pressure enhances densification via rearranging particles at the initial stage and increasing the driving force for sintering at the final stage. Fang concluded that the total driving force consists of two components, the intrinsic curvature-driven sintering stress and the external stress. When the applied pressure is beyond the intrinsic pressure, its effects on densification become obvious [200]. Even though atomic diffusion is limited at the low processing temperature (800 ^oC), P7.5 has been fully-densified, unlike P4.5. This proves that plastic deformation may act as the dominant densification mechanism under 7.5 GPa, and those nanograins observed in Figure 5.7 f come from the break-up of coarse grain under such high pressure.

5.7 Effect of temperatures and ultra-high pressure on superconducting properties

As explained in the introduction, processing conditions influence microstructures and superconducting properties. I have discussed the evolution of three typical microstructures with different processing parameters. The link between microstructures and superconducting performance will be examined in this section.

5.7.1 Critical transition temperatures and transition width

Figure 5.12a and b show DC susceptibility as a function of temperature of bulk samples in the pressure and temperature series. Onset T_c and transition widths (ΔT) are listed in Table 5.4. T_c fluctuates in a narrow range of 38 K~39 K, but ΔT becomes generally narrower with reducing applied pressure and increasing temperature. According to the percolation theory, if samples is homogeneous and free of defects like pores and impurities. ΔT_a values due to anisotropy should change linearly with the magnetic field, which can be expressed as [175]:

$$\Delta T_a = \frac{\sqrt{(\gamma^2 - 1){p_c}^2 + 1} - 1}{-\partial B_{c2}/\partial T} B \qquad 5.2$$

where γ represents the anisotropy. The percolation threshold p_c depends on the number of connections to neighboring grains [175]. Therefore, samples with higher γ and p_c will have broader ΔT. Besides, other reasons such as material inhomogeneity (lattice distortion, grain defects, or porosity) and thermal fluctuations can also lead to additional

width broadening [201]. More than one transition (grey arrows) and the broadest ΔT can be seen in the susceptibility curve of T700, which indicates the T_c inhomogeneity since the disorder has not been recovered at this low temperature. Similarly, additional transitions (green and blue arrows) and much broader ΔT can be seen in P6.5 and P7.5, and this may arise from inhomogeneity induced by the severe plastic deformation. It is not clear why ΔT in P4.5 is broader than in P5.5, but at least samples prepared at around 5 GPa and above 800 ºC all show the narrow transition (Figure 5.12a).

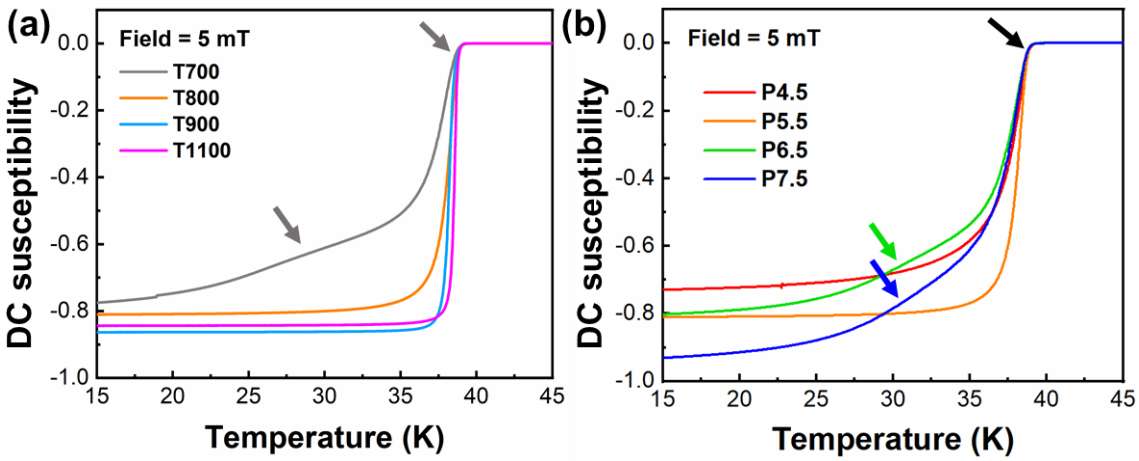


Figure 5.12 DC susceptibility curves of bulk samples in the (a) temperature series and (b) pressure series measured under 5 mT.

Table 5.4 The critical transition temperature (T_c) and transition width (ΔT) of samples in the temperature and pressure series

	T700	T800	T900	T1100	P4.5	P6.5	P7.5
T_c (K)	38.2	38.6	38.6	38.7	39.3	38.8	39.2
ΔT (K)	>15	1.9	0.8	0.8	~10	~15	~15

5.7.2 ΔM performance

ΔM values as a function of B_{app} at 4.2 K and 20 K are obtained from magnetisation loops (Figure 5.13a and b) [202]. T900, the sample processed at 900 ºC, performs best at both low and high magnetic fields. ΔM of T1100 at 0 T has a comparable value with

that of T900 but ΔM deteriorates much faster with the increasing magnetic field in T1100. The $\Delta M(B_{app})$ curve of T800 has an intersection with that of T1100 at around 4.5 T, above which T800 outperforms T1100. T700 has the lowest ΔM values over the entire field range.

From the aspect of microstructures, two reasons result in the best performance of T900. Firstly, the temperature is high enough for complete densification to occur, enabling the superconducting current to circulate throughout the whole sample (Figure 5.3f). Secondly, the temperature is low enough to ensure that MgB_2 decomposition is not too severe, preventing the formation of MgB_4 grains surrounding well-connected regions that partially inhibit the macroscopic current flow through different areas (Figure 5.2a). In addition, the intrinsic properties of MgB_2 may be improved because plastic deformation introduces extensive grain defects, and the processing temperature (900 ^oC) is not sufficiently high to fully anneal out defects like dislocations that are able to act as pinning centres. The high self-field value of T1100 is a result of the higher density compared with T800. However, the deterioration of performance with the increasing field may come from its lower intrinsic J_c because grain defects are fully annealed out and reduced grain-boundary pinning strength due to rapid grain growth (Figure 5.4 and Figure 5.5). The properties of T700 are limited by high porosity.

Moreover, the shape of experimental ΔM curves can be explained by simulation results in Section 4.2.4. For example, T800 at 4 K has a sharp ΔM curve at low fields, revealing the little effect of self-field. The curve of T1100 around 3 T is relatively flat before

quickly drops above 4 T where percolation may make a difference. However, the curve gradient becomes flat again when B_{app} > 7 T, corresponding to the flat tail in simulated results of Type II microstructures (Section 4.2.5.2) which reveals the dominant role of cell current at a high magnetic field regime. A clear inflexion between 1 T and 2 T can be seen in the ΔM curve of T1100 at 20 K, which is also similar to the simulation taking percolation into account, with the inflexion occurring at roughly $B_{c2}^{||c}$ (Type I microstructures in 4.2.6.1).

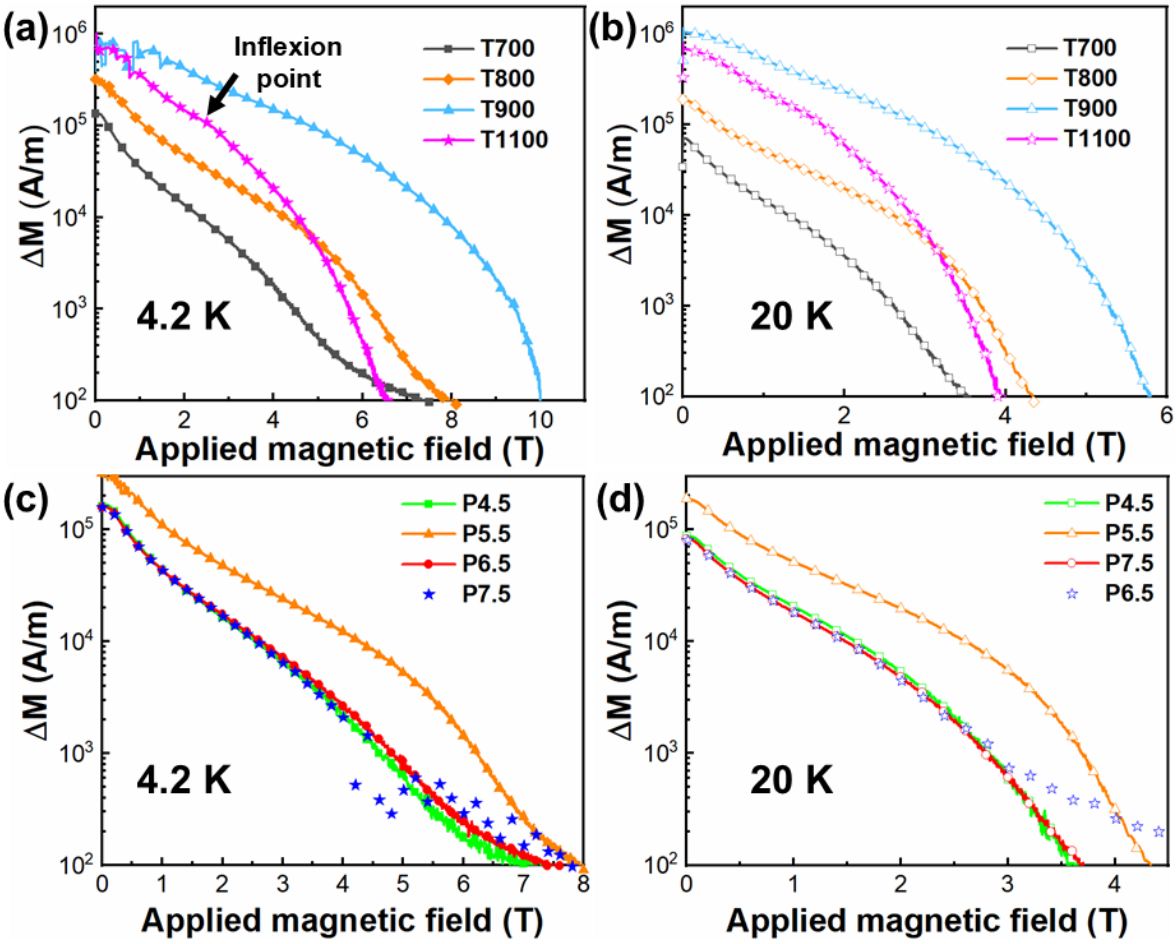


Figure 5.13 (a)(b) ΔM(B_{app}) curves of T700, T800, T900 and T1100 at 4.2 K and 20 K. (c)(d) ΔM(B_{app}) curves of P4.5, P5.5, P6.5 and P7.5 at 4.2 K and 20 K.

Figure 5.13c and d present the ΔM curves of samples at 4.2 K and 20 K in the pressure

series. P5.5 performs best at both 4 K and 20 K. All ΔM curves show a similar shape, with steep gradients at the low fields, indicating the low sample density. The experimental data of P6.5 has significant fluctuations when B_{app} is over 4 T at 4.2 K and 2.5 T at 20 K. The deterioration of P6.5 and P7.5 compared to P5.5 may come from the impaired grain connectivity, which can be linked to lots of unsolved pixels at grain boundaries where nanograins form due to severe structural disorder under plastic deformation (Figure 5.8b). However, it is unclear why P4.5 also has poorer performance. Cracks that are easily generated during the ultra-high pressure-assisted sintering process may be responsible for the deterioration.

5.8 Conclusions

Fully-dense nanostructured MgB_2 samples have been fabricated by ultra-high pressure-assisted sintering, and the effects of temperature, pressure and time have been systematically examined. According to the microstructural characterisation and the superconducting property measurements, the following conclusions can be drawn:

i. Ultra-high pressure is beneficial for shortening sintering time to 15 min (compared to several hours for hot pressing) and processing nanostructured, dense MgB_2 polycrystalline bulks. Complete densification can be achieved by enhancing either the sintering temperature to 900 ºC or the applied pressure to 7.5 GPa. High temperature mainly improves lattice and grain boundary diffusion while plastic deformation under extremely high pressure

also contributes to the sample consolidation.

ii. Ultra-high pressure can decrease the c axis of MgB_2 unit cells and introduce lots of grain defects, but these defects can be eliminated by increasing the sintering temperature. Besides, high temperature leads to rapid grain growth and a larger number of impurities due to the severe decomposition of MgB_2, which impairs the flux pinning and reduces the cross-section of critical current flow respectively. The optimum conditions I recommend are: around 5 GPa for the applying pressures, around 900 ^{o}C for the processing temperatures and 15 min for the processing time.

iii. T_c deteriorates with extremely high pressure and low sintering temperature because of the material inhomogeneity. The duplex morphology is inevitably formed due to the presence of agglomerates in precursors. This can have a significant effect on the current paths on different scales, especially when the matrix has a large fraction of pores such as T800 in this study.

Chapter 6 Effect of high-energy ball milling and Mg additions on MgB_2 bulk samples prepared by field-assisted sintering

6.1 Introduction

Previous studies on milling precursors before processing MgB_2 bulks can be categorized by different starting materials. In the in-situ method, large Mg particles with up to 250 μm and much finer B powders (~1 μm) are mixed [89, 203, 204]. As introduced in Section 3.1.1, this ductile-brittle system will experience fracturing, cold-welding and even mechanical alloying to form the MgB_2 phase. The effects of milling parameters like rotation speed and milling times on the eventual superconducting properties of MgB_2 bulk samples have been investigated in [89, 142, 143, 205]. Usually increasing milling time up to a critical value (t_c) can shift $J_c(B_{app})$ curves upwards at high magnetic fields due to the increase in the density of grain boundaries, but J_c performance in the low field range varies in different studies [28, 88, 143, 205]. This may arise from different degrees of grain connectivity resulting from various milling and sintering conditions. The saturation of grain refinement occurs when the milling time reaches t_c, beyond which a microporous grain network with increasing impurity content could rapidly degrade the J_c performance [206]. Another approach is directly milling commercial MgB_2 powders [65, 207-209]. Grain refinement and defect

introduction through plastic deformation have been found effective to enhance both the number and strength of pinning centers [92]. However, new reactive surfaces of small MgB_2 grains may promote the pick-up of oxygen contamination in the milling processes, which leads to a high MgO content in bulk samples [67]. Moreover, highly reactive MgB_2 grains are prone to decompose and form MgB_4 products [207]. All these disadvantages can lead to J_c deterioration if the milling process is not carefully controlled.

Additionally, the reaction of Mg and B powders in the in-situ method is favored for the strong inter-grain coupling, and excess Mg is often added to compensate for Mg loss during the reaction process [58]. However, the role of excess Mg additions in the ex-situ route is not yet fully understood. This chapter will deal with two series of bulk samples produced by the ex-situ method: ball-milled MgB_2 and ball-milled MgB_2 with Mg additions. First, microstructural characterisation is carried out to study the effects of milling time, Mg addition and processing temperatures on morphologies of bulk samples. The ΔM performance is then associated with corresponding microstructural features. Finally, revised J_c data by self-field corrections are used to analyse pinning mechanisms.

6.2 Experimental details

Commercially available MgB_2 powder (purity: 99%, Alfa Aesar) was used to prepare MgB_2 bulk samples. Ball milling conditions have been explained in Section 3.1.1.

About 0.5 g powder was taken out after 10 min, 0.5 h, 1 h, 3 h, 6 h, 12 h and 24 h of milling for phase analysis and microstructural characterisation. Powders (~3 g) after milling for 3 h, 6 h, 12 h and 24 h were pressed into disc-shaped pellets for field-assisted sintering. According to the previous study, excess Mg within 3 ~ 6 wt% can suppress MgB_2 decomposition without leaving residual Mg in bulk samples [210], so 5 wt% was chosen for preparing MgB_2 with the Mg addition in this study. Mg powder (purity: 99.8% purity, Alfa Aesar) was homogeneously mixed with ball-milled MgB_2 powders by hand under Ar atmosphere. Sintering was carried out at temperatures ranging from 1000 °C to 1200 °C in the FAST apparatus and the operational procedures have been described in Section 3.1.2. Table 6.1 summarises the parameters for processing these samples.

Table 6.1 Processing parameters for ball milling and field-assisted sintering

Sample	Milling time (h)	Sintering temperature (°C)	Dwell time (min)	Mg addition (wt%)
MgB_2	0	1200	5	-
MgB_2-3hM	3	1200	5	-
MgB_2-6hM	6	1200	5	-
MgB_2-12hM	12	1200	5	-
MgB_2-24hM	24	1200	5	-
MgB_2-5Mg	0	1200	5	5
MgB_2-5Mg-6hM*	6	1200	5	5
MgB_2-5Mg-12hM	12	1200	5	5
MgB_2-5Mg-900C	6	900	5	5
MgB_2-5Mg-1000C	6	1000	5	5
MgB_2-5Mg-1100C	6	1100	5	5

*This sample is also named MgB_2-5Mg-1200C when discussing the effect of sintering temperature.

6.3 Phase analysis and microstructural characterisation of MgB_2 powders prepared by high-energy ball milling

Figure 6.1 shows XRD patterns of MgB_2 powders milled for various lengths of time and highlights the evolution of (110) and (002) peaks. MgB_4 and MgO already exist in un-milled powders as impurities. As discussed in Chapter 5, broader FWHM and lower intensities of MgB_2 peaks reflect crystallite refinement and higher microstrain, while the consistent left shift of both (110) and (002) peaks indicate the increase in a and c lattice parameters with longer milling time. The shoulder on the right of the (110) peak arises from the $K_{\alpha 2}$ influence.

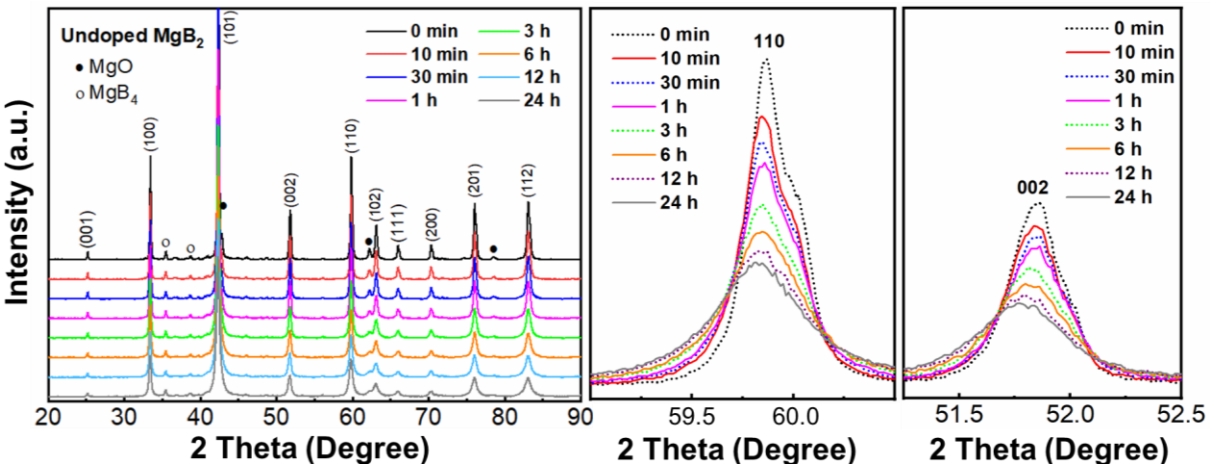


Figure 6.1 XRD patterns of MgB_2 powders after ball milling for 0 min, 10 min, 30 min, 1 h, 3 h, 6 h, 12 h and 24 h. The right two figures highlight (110) and (002) peaks corresponding to changes in the a and c axes.

Quantitative analysis was conducted by the Rietveld method, and results are summarised in Table 6.2. Both a and c axis are expanded by around 0.1% in 24 h-milled powders compared to the un-milled counterpart. In [88], the milling energy transferred per mass of powder sample is described as being proportional to the milling time, $E_p \propto$

$\beta\frac{(\omega_p r_p)^3}{r_v}t$, where β is the ball-to-powder ratio. ω_p and r_p are angular frequency and radius of the rotation stage of the planetary ball milling machine. r_v refers to the radius of milling vials. Therefore, a longer milling time means that more energy would be transferred to powders to refine crystallites. A dramatic decrease in crystallite size is seen within the initial 10 min of milling, from 76 nm to 63 nm, followed by a relatively steady drop until after 12 h of milling when the refinement reaches saturation. In contrast, the strain keeps increasing from 0.1% in un-milled powders to 0.28% in 24 h-milled powders, which means that lattice deformation becomes the dominant change in microstructure after 12 h of milling.

Table 6.2 Phase content, lattice parameters, crystallite size and strain calculated by Rietveld method in powders ball-milled for different times.

Milling time	a axis (Å)	c axis (Å)	Crystallite size (nm)	Strain (%)
0	3.086	3.524	77	0.10
10 min	3.087	3.524	63	0.12
30 min	3.087	3.524	63	0.13
1 h	3.087	3.524	61	0.15
3 h	3.087	3.525	56	0.19
6 h	3.088	3.526	48	0.21
12 h	3.088	3.527	40	0.24
24 h	3.089	3.528	39	0.28

BSE images and EDX maps of as-received powders are shown in Figure 6.2. MgB_2 particles, with a grey contrast lighter than the pre-existing MgB_4, exist in loosely-packed agglomerates varying in size from several microns to hundreds of microns. Images taken at higher magnification show the poor connectivity between MgB_2 grains due to a large number of pores and MgO impurities (brightest contrast). These agglomerates are prone to absorb impact energy and crack, decreasing in size quickly

at the beginning of milling.

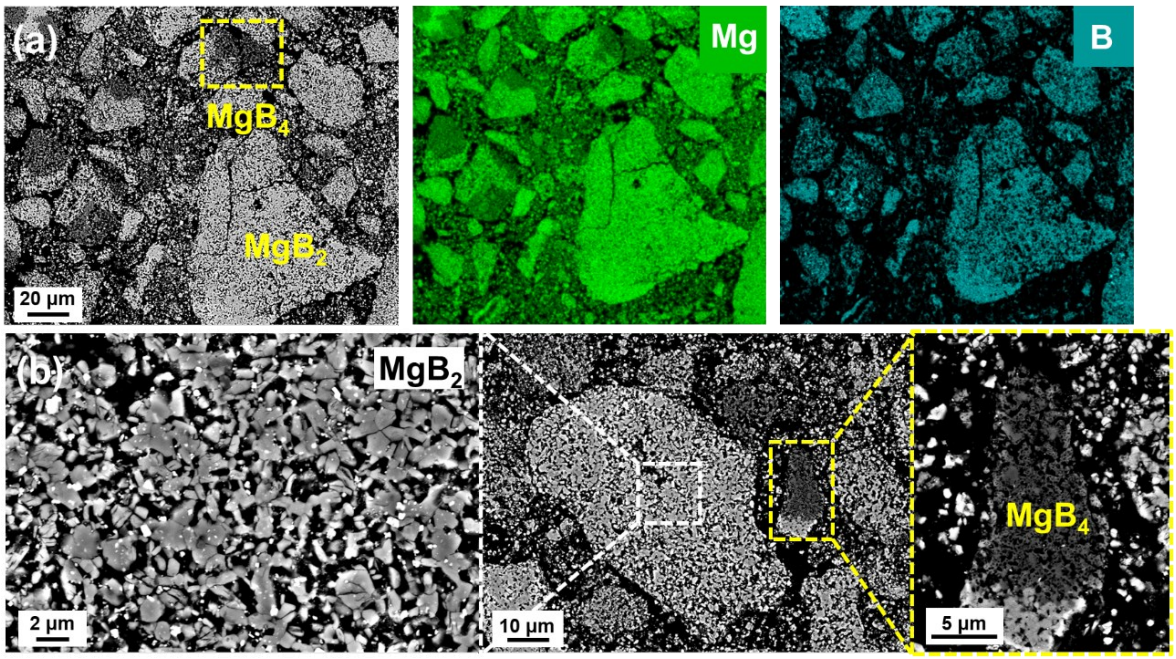


Figure 6.2 (a) BSE images (500×) and EDX maps of as-received MgB_2 powders. (b) BSE images taken at higher magnification showing the porosity in MgB_2 agglomerates and MgB_4 phases.

A comparison of morphologies of powders after different milling times is shown in Figure 6.3. During the first 10 minutes, most large MgB_2 agglomerates that show up bright in the images decrease in size rapidly to below 30 µm. After 3 h of milling, the angular shape of agglomerates changes to roughly equiaxed particles, and their size distribution becomes homogenous. Extension of the milling time to 24 h leads to a predominance of spherical particles but no noticeable decrease in the particle size.

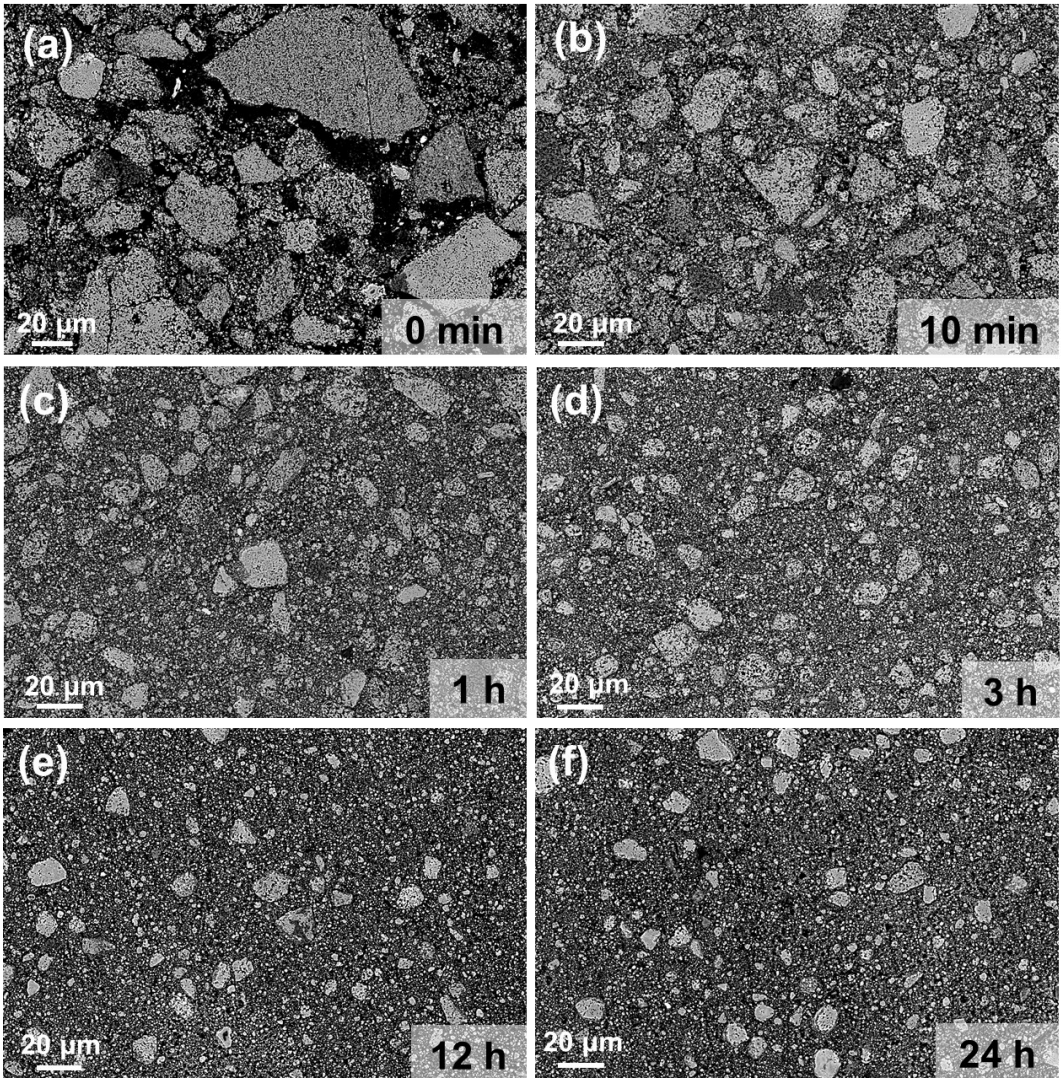


Figure 6.3 BSE images (500×) of MgB_2 powders after (a) 0 min; (b) 10 min; (c) 1 h; (d) 3 h; (e) 12 h and (f) 24 h of milling.

Figure 6.4 gives a further depiction of the microstructural evolution within the MgB_2 agglomerates at higher magnification as well as the background finer features that also have bright contrast in Figure 6.3. Poor inter-grain bonding can be observed in 10 min-milled powders as highlighted by red arrows, but small gaps between grains disappear as milling proceeds. With the ongoing fracturing caused by impact with milling balls, smaller volumes (a few microns) in the aggregates free of weakness (pores or brittle MgB_4 phases) are retained. It is clear from the images in Figure 6.4 that each of these

remaining aggregates consists of many MgB_2 grains below 1 μm. Dark contrast in the center of some of these refined particles suggests extra MgB_4 is generated in the milling process (Figure 6.4e and f). Additionally, one can observe that bright contrast in the background comes from small MgB_2 grains. This combination of dense polycrystalline aggregates and a matrix of finer powder particles is critical to the development of the bulk microstructures that will be discussed later.

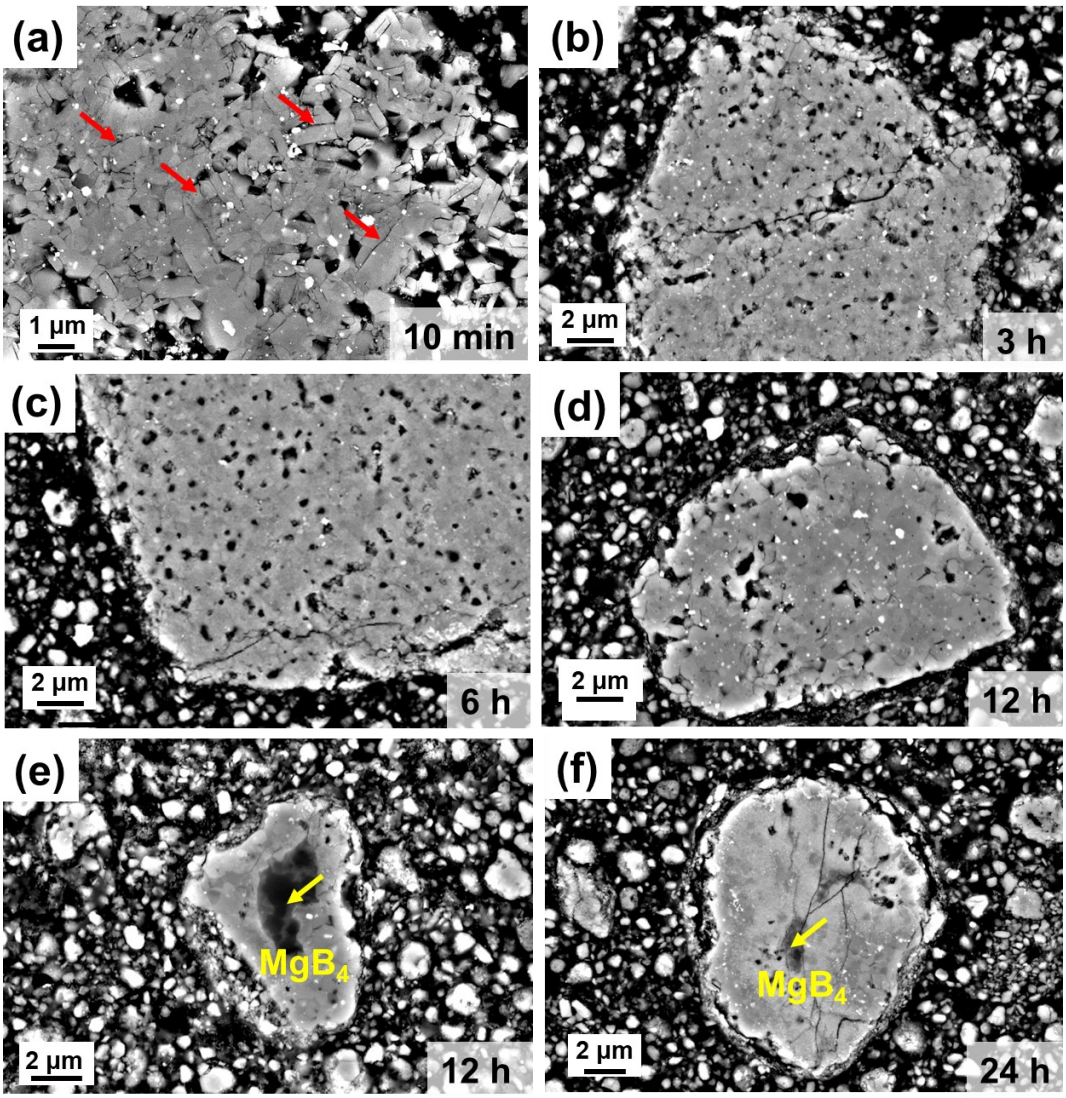


Figure 6.4 BSE images show microstructural evolution of MgB_2 powders after (a) 10 min; (b) 3 h; (c) 6 h and (d) 12 h of milling. (e) and (f) show newly-formed MgB_4 in powders milled for 12 h and 24 h.

6.4 Effect of milling time on phase evolution and microstructures of MgB_2 bulk samples

XRD patterns of bulk samples produced from powders milled for 0 h, 3 h, 6 h, 12 h and 24 h are shown in Figure 6.5a. The peaks from the un-milled MgB_2 are the sharpest in the sample set, and the increase in MgO peak intensity with longer milling time indicates a higher content of impurities. Figure 6.5b compares XRD scans of randomly-oriented powders and bulk samples. A stronger reflection from (002) can be observed in the patterns of bulk samples while (100) and (110) peaks do not show prominent changes in intensities compared with XRD scans of powers. Figure 6.5c shows the direction of applied pressure and zooms into the (002) and (110) peaks. Arrows highlight the intensity and peak position changes. Taking the (101) peak intensity (the strongest peak from MgB_2) as 1, the relative intensity of the (002) peak is found to increase from 0.17 (powders) to 0.25 (bulk samples). This reveals a weak preferred (002) orientation may form in bulk samples under the axial pressure. In addition, the prominent shift of the (110) peak to a higher 2θ value indicates that a axis of MgB_2 grains is shortened after sintering.

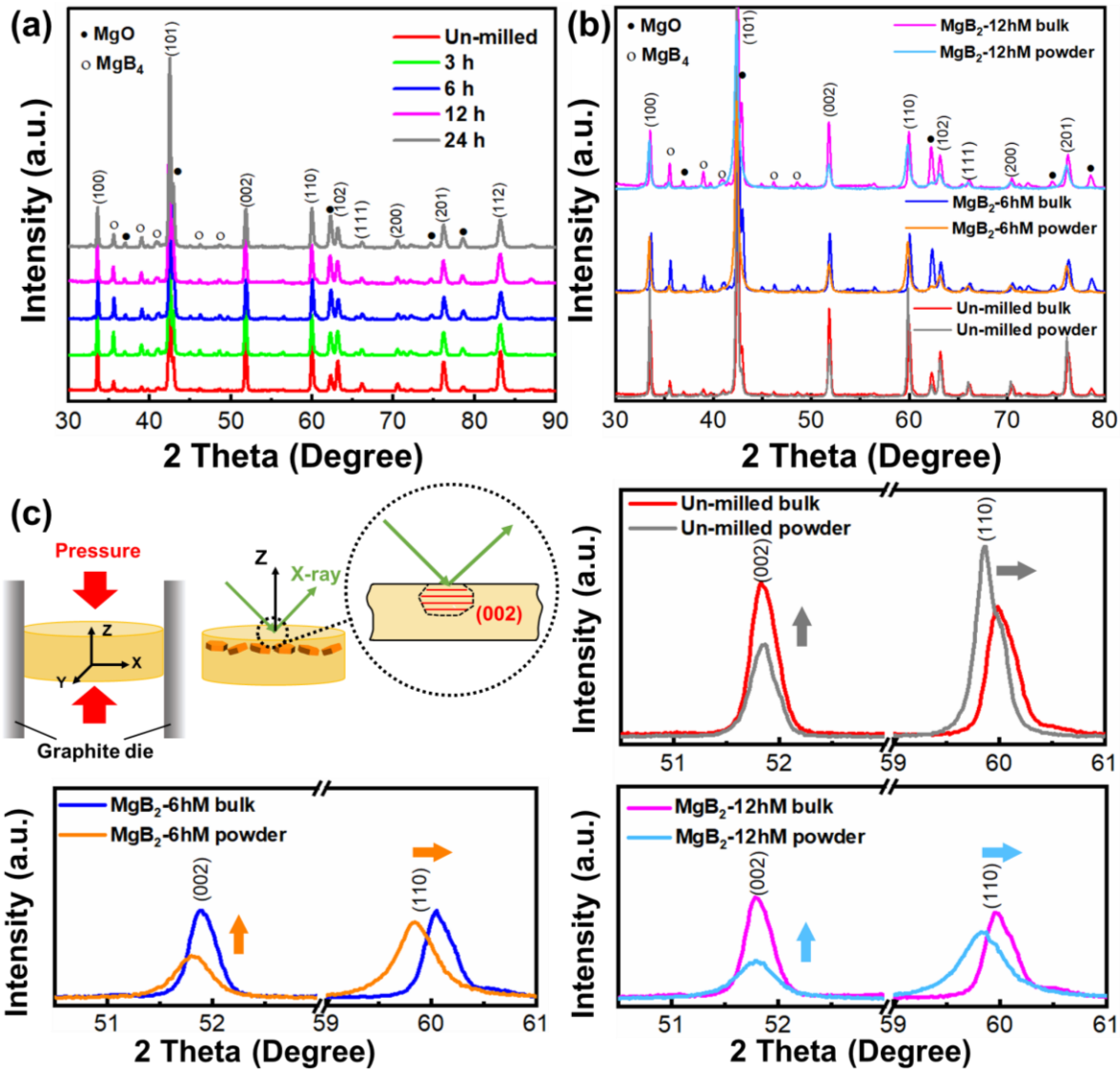


Figure 6.5 (a) XRD patterns of bulk samples processed by powders milled for various lengths of time and processed at 1200 ºC for 5 min. (b) compares XRD patterns of powders and bulk samples. (c) shows the pressure direction and the comparison of (002) and (110) peaks of powders and bulk samples.

The results of quantitative analysis are listed in Table 6.3. There is a subtle difference in a and c parameters between these bulk samples, but compared to the results from the powder samples (Table 6.2), lattice parameter a values decrease from around 3.088 Å to around 3.084 Å. Moreover, the crystallite size increases in the bulk samples compared with that of ball-milled powders, indicating grain growth at high processing

temperatures. Within the bulk sample series, specimens produced by powders milled for a longer time (up to 12 h) has relatively smaller crystallite sizes.

Table 6.3 Lattice parameters, crystallite size and strain of MgB_2 bulk samples produced by powders after different hours of milling. These results are calculated by the Rietveld method.

Milling time	a axis (Å)	c axis (Å)	Crystallite size (nm)	Strain (%)
0	3.084	3.528	100	0.10
3 h	3.083	3.529	75	0.16
6 h	3.083	3.526	62	0.17
12 h	3.084	3.527	52	0.15
24 h	3.084	3.527	54	0.16

SEM images shown in Figure 6.6 depict cross-sections of samples parallel to the pressing direction. Agglomerates with loosely-packed grains have changed in shape under the applied pressure and formed some alignment of phases separated by impurities such as MgO and MgB_4 (Figure 6.6a and b). In samples with powder milled for 3 h, MgB_4 still exists in the form of large, porous regions, but some well-connected MgB_2 regions become apparent gradually (Figure 6.6c and d). The matrix becomes denser overall at milling times of 6 h and above, and large MgB_4 phases have been transformed to separate, small grains distributed in the matrix (Figure 6.6e). The disappearance of porous MgB_4 large regions overall improves the sample density. The main difference between the circled region and the matrix is the content of the small MgO particles between the grains. Figure 6.6f shows that after 12 h milling the well-connected dense regions decrease in size below 10 μm. A careful comparison of the microstructure from many regions demonstrates that the sample prepared from powder milled for 24 h has a slightly higher percentage of MgB_4 impurities and porosity in the

fine-grained matrix than that milled for 12 h (Figure 6.6g and h).

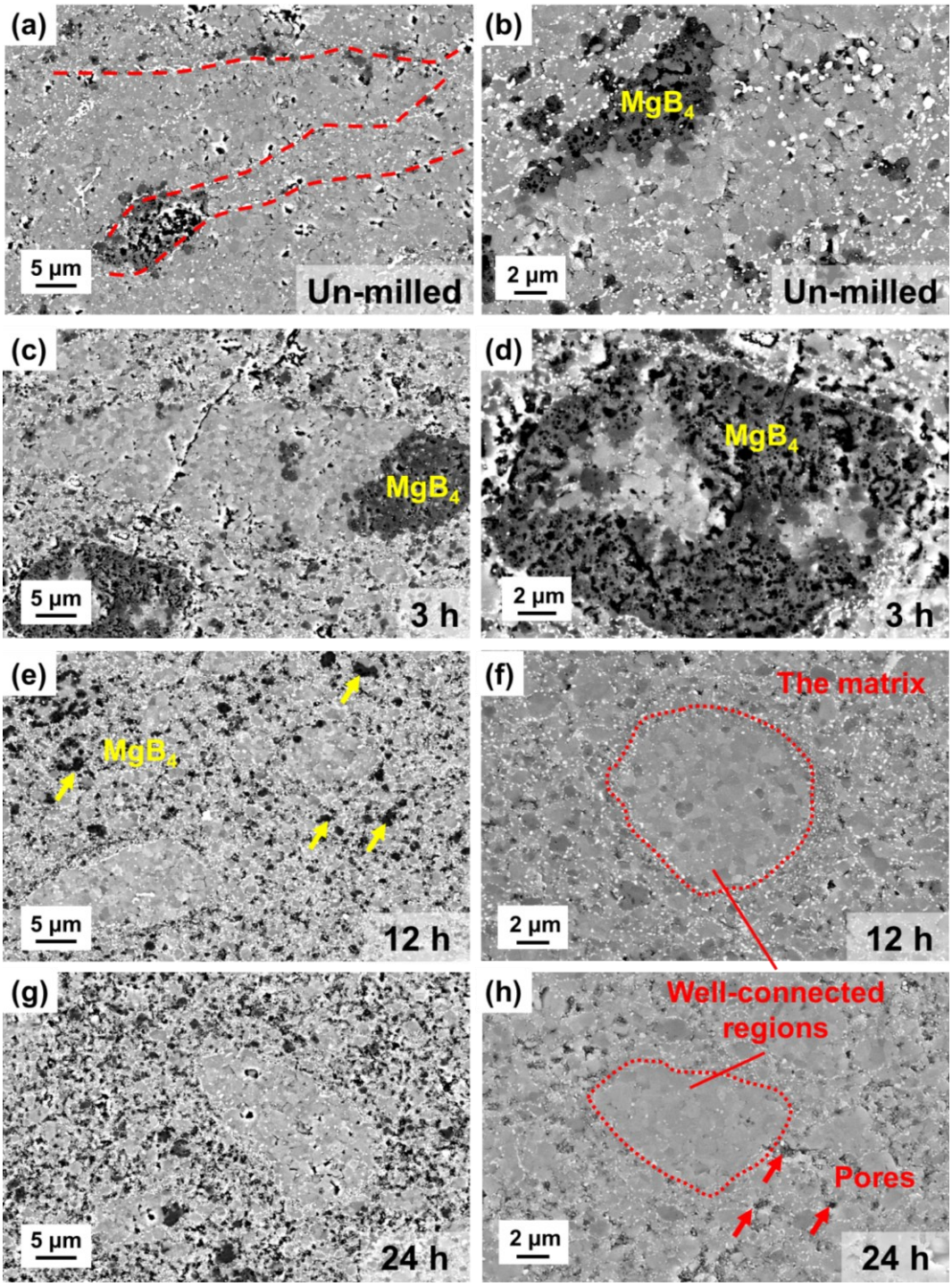


Figure 6.6 BSE images showing cross-sections of MgB_2 bulk samples along the direction parallel to the axial pressure. These samples processed at 1200 ºC for 5 min were prepared from precursors after (a)(b) 0 h, (c)(d) 3 h, (e) 12 h and (g) 24 h of milling. (f) and (h) SEM images highlight different matrix structures in samples produced from MgB_2 powder milled for 12 h and 24 h.

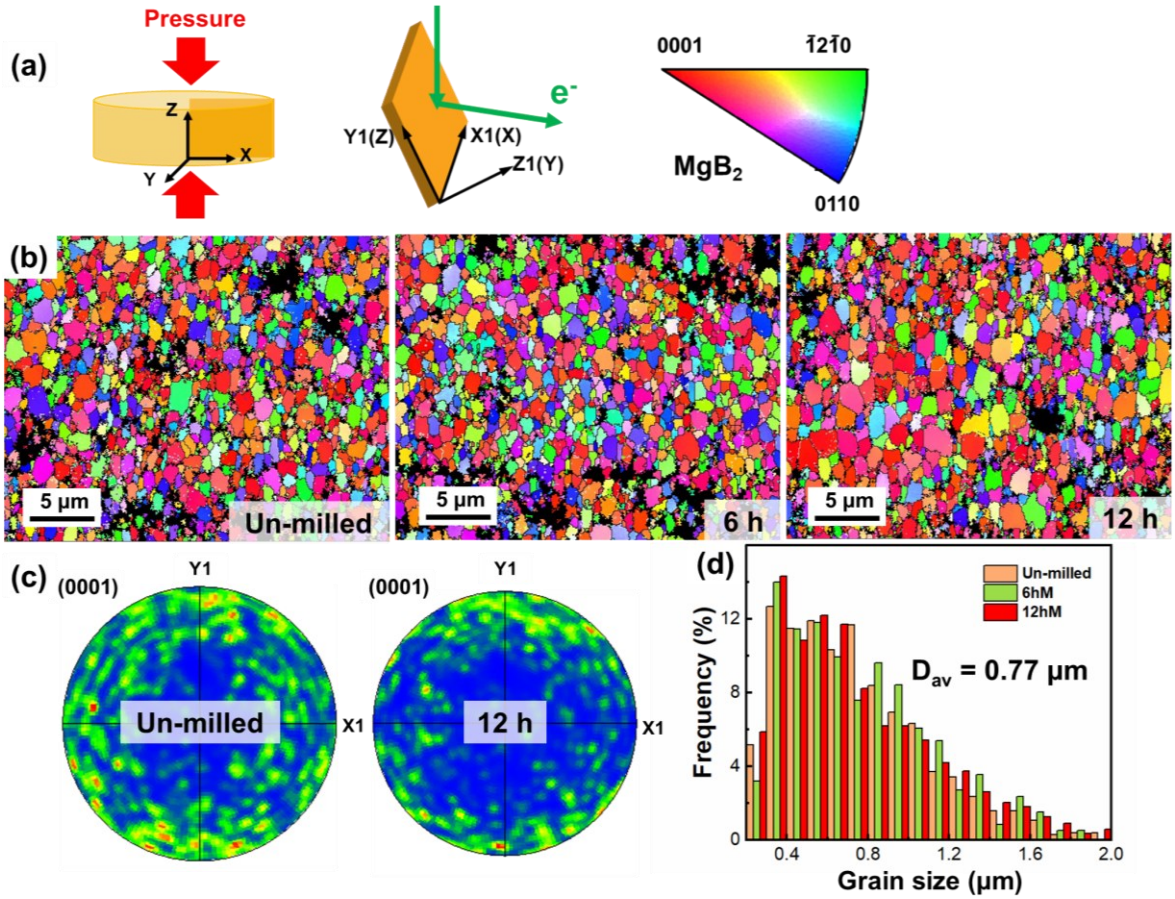


Figure 6.7 (a) Three-dimensional schematic of pressing direction and sample position in EBSD characterisation. (b) EBSD IPF Y1 maps of bulk samples with powder milled for 0 h, 6 h and 12 h processed at 1200 °C for 5min. (c) (0001) pole figures of MgB_2 grains in the un-milled and MgB_2-12hM samples. (d) shows the grain size distribution.

As shown in Figure 6.7, the grain morphologies were investigated by EBSD. It is noticeable that a proportion of grains align with (0001) in IPF Y1 images (red) which correspond to the Z direction in the pressing geometry. Pole figures shown in Figure 6.7c agree with the weak micro-texture of the preferential (002) orientation out of the surface observed in the XRD patterns (Figure 6.5). Grigoroscuta et al adopted slip casting under high magnetic fields to make green bodies and found the existence of weak texture in bulk samples [181]. From their results, around 10% of the MgB_2

crystallites with c axes aligned within 0-51° from the surface normal in partially-oriented MgB_2 bulks contribute little to the improvement of superconducting performance. This coincides with the simulation of texture effects discussed in Chapter 4 (Section 4.2.2.1). Therefore, only a strong texture can ameliorate percolation problems in MgB_2 polycrystalline samples if B_{app} is parallel to the ab plane. Figure 6.7d shows that there are no apparent changes in grain size in bulk samples with powder milled for different times, and the average value is around 0.77 μm.

6.5 Effect of Mg addition on phase evolution and microstructures of MgB_2 bulk samples

Mg with a low melting point (~650 °C) can activate the low-temperature reaction to form MgB_2 grains in in-situ processing, by which both the loss of Mg and the growth of MgB_2 grains can be effectively prevented. However, the sintering temperature in the ex-situ route needs to be much higher than 900 °C or high porosity and poor grain connectivity will influence the superconducting performance. As introduced in Section 6.1 , the addition of excess Mg here aims to prevent MgB_2 decomposition during sintering at high temperatures and improve the grain connectivity of bulk samples.

6.5.1 Effect of ball milling time on bulk samples with added Mg

XRD patterns of Mg added MgB_2 bulk samples and un-doped bulk samples processed at 1200 °C are plotted in Figure 6.8. No peaks corresponding to unreacted Mg are

detected. The main difference between the two sample sets lies in the content of MgB_4. When zooming into the range between 34° to 42°, details about the MgB_4 content in different samples can be extracted, as shown in the right-hand figure. MgB_4 peaks decrease dramatically in intensity in all 5 wt% Mg added samples.

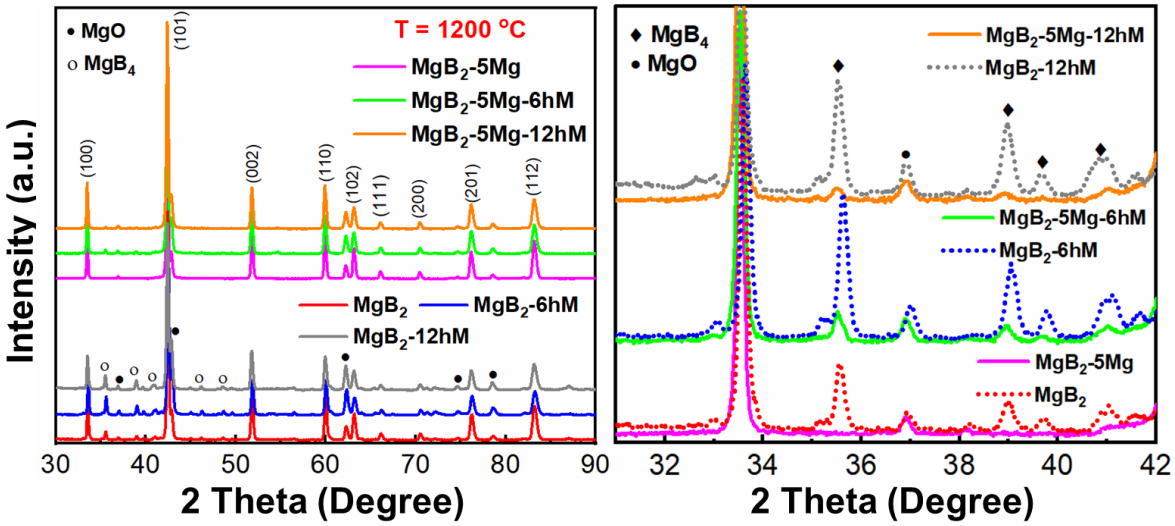


Figure 6.8 XRD patterns of MgB_2 bulk samples with the addition of 5 wt% Mg. 6 hM and 12 hM mean that MgB_2 powders were milled for 6 and 12 h before being processed at 1200 °C. The right figure compares the changes in MgB_4 peaks.

BSE images in Figure 6.9 show microstructures of bulk samples with and without Mg addition at different magnifications. Compared with un-doped MgB_2 samples, no large MgB_4 phases are observed in the Mg-added specimen, but a number of small pores can be seen (Figure 6.9a vs. e). Micrographs captured at a higher magnification reveal the grain boundaries are free of nano-MgO impurities (Figure 6.9c vs. g), and small MgB_4 grains are rarely found in MgB_2-5Mg samples. As mentioned above, if the precursors experience 6 h ball milling or longer, the microstructures of pure MgB_2 samples show a decreasing number of large MgB_4 phases and well-connected MgB_2 dense regions

become obvious. After adding Mg, the area between well-connected regions and the matrix which usually consists of a layer a few microns thick of smaller MgB_2 grains and MgO nanoparticles in un-doped MgB_2 samples disappears (Figure 6.9i vs. m). The presence of fewer insulating MgO and MgB_4 particles could increase the chance of supercurrents flowing macroscopically in the bulk sample.

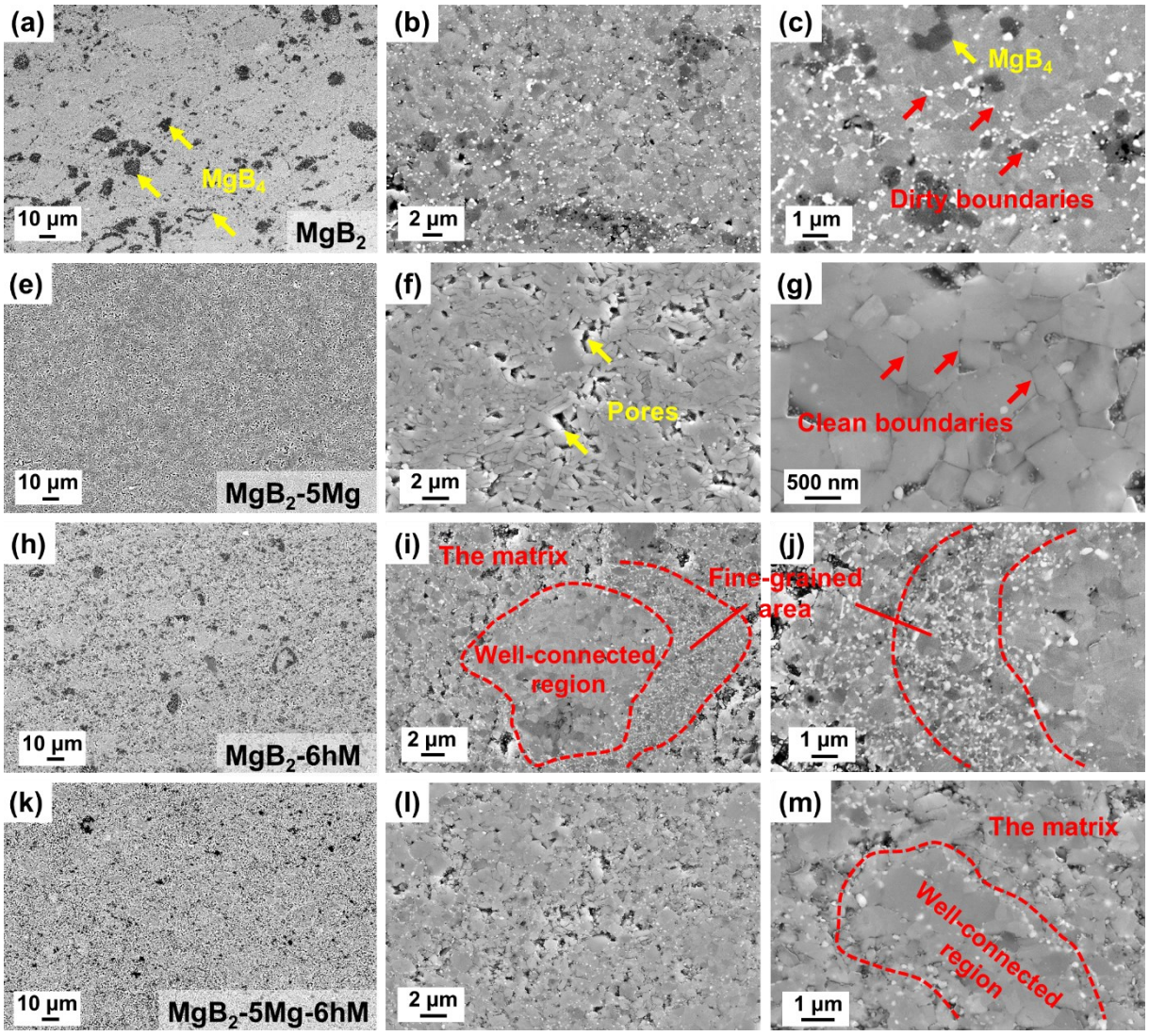


Figure 6.9 BSE images of (a-c) MgB_2, (e-g) MgB_2 + 5 wt% Mg, (h-j) 6 h ball-milled MgB_2 and (k-m) 6 h ball-milled MgB_2 + 5 wt% Mg samples processed at 1200 °C.

6.5.2 Effect of processing temperatures on Mg-added bulk samples

Figure 6.10 presents XRD scans of Mg-added bulk samples processed at different temperatures from 900 °C to 1200 °C. The apparent shift of the pattern in the MgB_2-5Mg-900C sample may be due to the uneven surface caused by the high porosity. The MgO peak next to the MgB_2 (102) peak has an increasing intensity with rising sintering temperatures. The right figure demonstrates the slightly higher content of MgB_4 in samples processed above 900 °C, but by comparison with the samples processed in the same way without added Mg, the addition of Mg effectively prevents the decomposition of MgB_2 to form MgB_4 impurities at high processing temperatures.

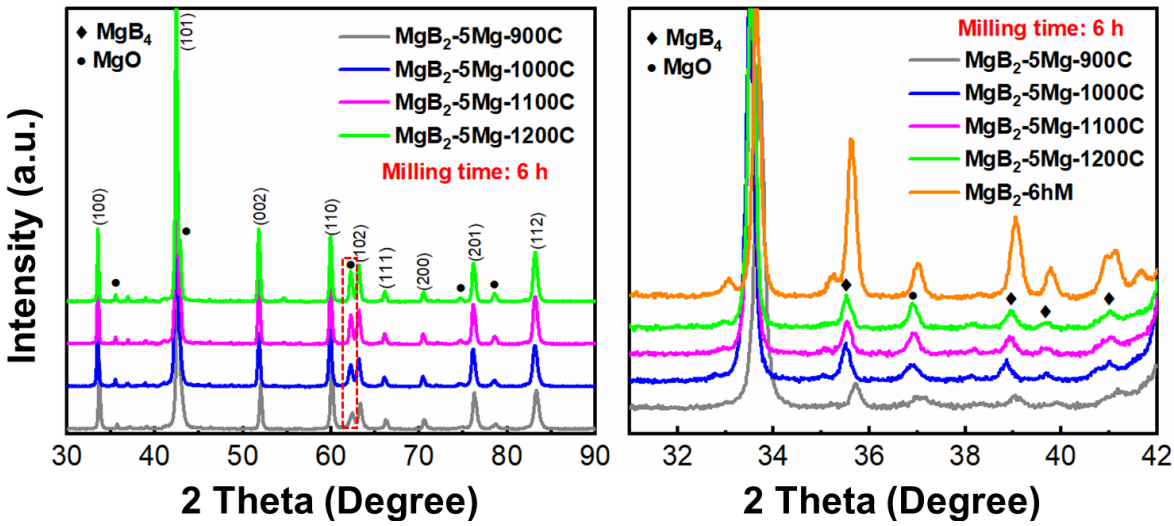


Figure 6.10 XRD patterns of Mg-added MgB_2 samples processed at temperatures from 900 °C to 1200 °C. The right figure highlights the change in the MgB_4 peaks.

The microstructural comparison of Mg-added and pure MgB_2 samples processed at 1000 °C with powder milled for 6 h is given in Figure 6.11. Large agglomerates from as-received powders remain in the MgB_2-1000C sample (Figure 6.11a), and pores still exist in these regions, indicating incomplete densification during sintering (Figure

6.11b). However, the combination of ball milling and Mg addition has changed the microstructure completely even though the sintering temperatures are the same. The agglomerates are reduced in size by milling as discussed above. Though small grains in the dense regions have relatively good contact with each other, there remains significant porosity in the intervening porous regions, indicating that 1000 °C is not high enough to make fully dense samples even with the assistance of Mg addition. Only by increasing the processing temperature can the porous matrix be densified without introducing a large amount of MgO impurities.

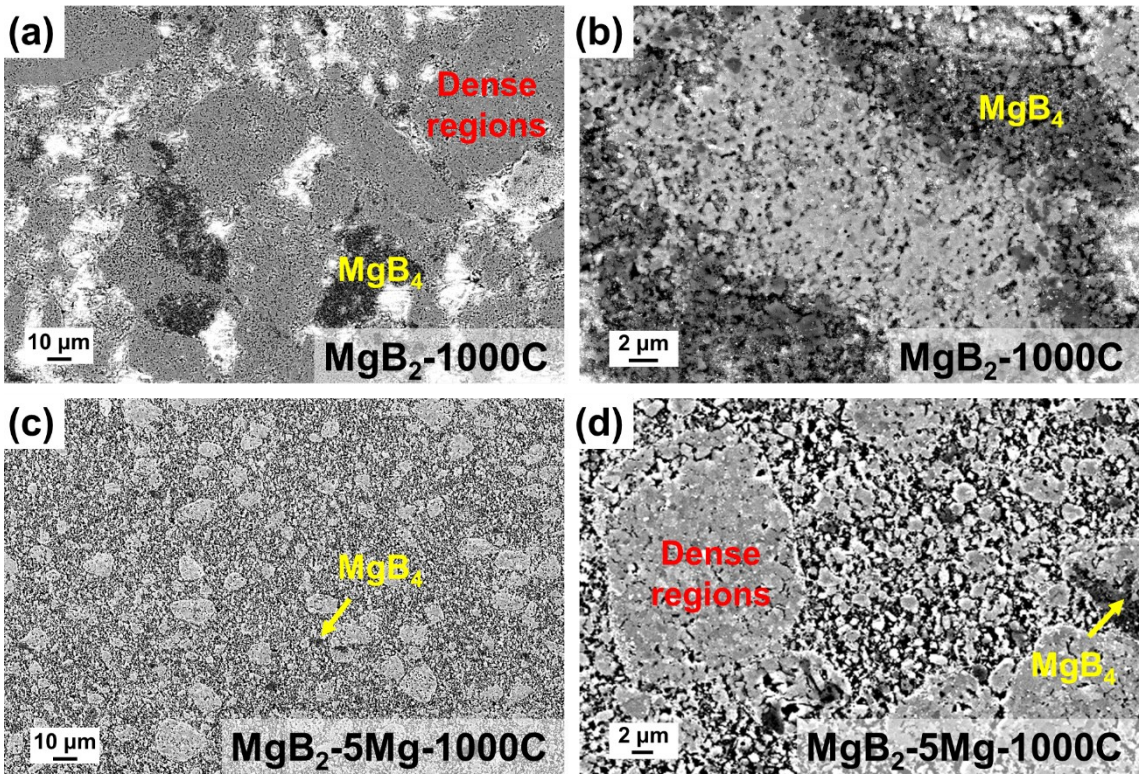


Figure 6.11 BSE images of (a)(b) un-milled MgB_2 and (c)(b) MgB_2 + 5 wt% Mg samples with powder milled for 6 h. Since porous areas are easily removed in the sample preparation, the uneven surface contributes to regions with the brightest contrast in (a).

6.6 Analysis of superconducting properties

Figure 6.12 depicts normalised susceptibility curves of pure and Mg-added MgB_2 samples made from precursor powders milled for various lengths of time and at different processing temperatures. T_c as an intrinsic property can be influenced by lattice distortion by atom substitution through doping or strain through plastic deformation, and ΔT is sensitive to microstructural homogeneities, impurities, etc. [177]. Ball milling for longer than 6 h degrades T_c by around 1 K, but the difference in the 12 h- and 24 h-milled samples is subtle (Figure 6.12a). With the addition of Mg, the decrease in T_c of the sample is only around 0.4 K, as shown in Figure 6.12b. Increasing the processing temperature significantly enhances T_c values, presumably because the lattice disorder introduced by ball milling can be partially recovered at high sintering temperatures (Figure 6.12c). As shown by the red arrows in Figure 6.12d, one can observe that by adding Mg, T_c is partially recovered, increasing by about 0.5 K. Mg addition also slightly narrows the transition width (ΔT) without affecting T_c. Due to the low melting point of Mg (~650 ^oC), the dominant solid phase reaction would transform to liquid phase sintering in 5 wt% Mg added MgB_2 samples at high processing temperatures. The accelerated mass transport makes samples macroscopically more homogenous.

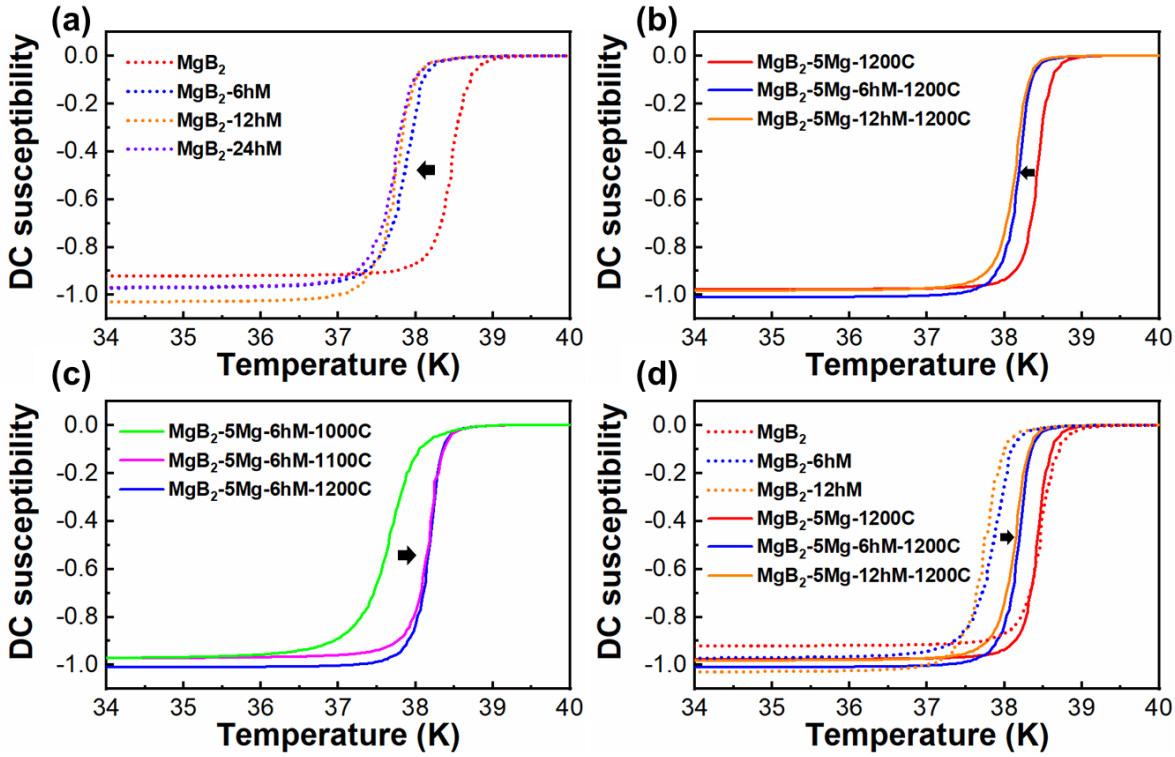


Figure 6.12 DC susceptibility curves of (a) MgB_2 samples, (b) Mg added MgB_2 samples made from powder milled for different times, (c) Mg added samples processed at different temperatures. (d) compares susceptibility curves of MgB_2 samples with/without Mg addition.

The results from microstructural analysis are compared with the simulation results in chapter 4 to identify the current flowing length scales likely to be dominating the magnetization signal. To avoid crossing references so much, SEM micrographs of three samples and the corresponding schematics are reproduced in Figure 6.13. Figure 6.13a shows that pure MgB_2 without milling has a Type III microstructure (Section 4.2.6.3), therefore the ΔM is likely to be dominated by macroscopic current loops. Samples with milling times below 12 h still have relatively dense structures but the duplex microstructures become gradually obvious (Figure 6.13b). These milled samples can be classified as Type I microstructures where macro currents dominate the total ΔM.

Figure 6.13c shows MgB_2-24hM sample has a porous matrix similar to Type II microstructure, so both currents flowing in dense regions and the whole sample determine the total $\Delta M(B_{app})$ curves. To summarise, macroscopic J_c values of all samples except MgB_2-24hM can be extracted reliably by Bean's model.

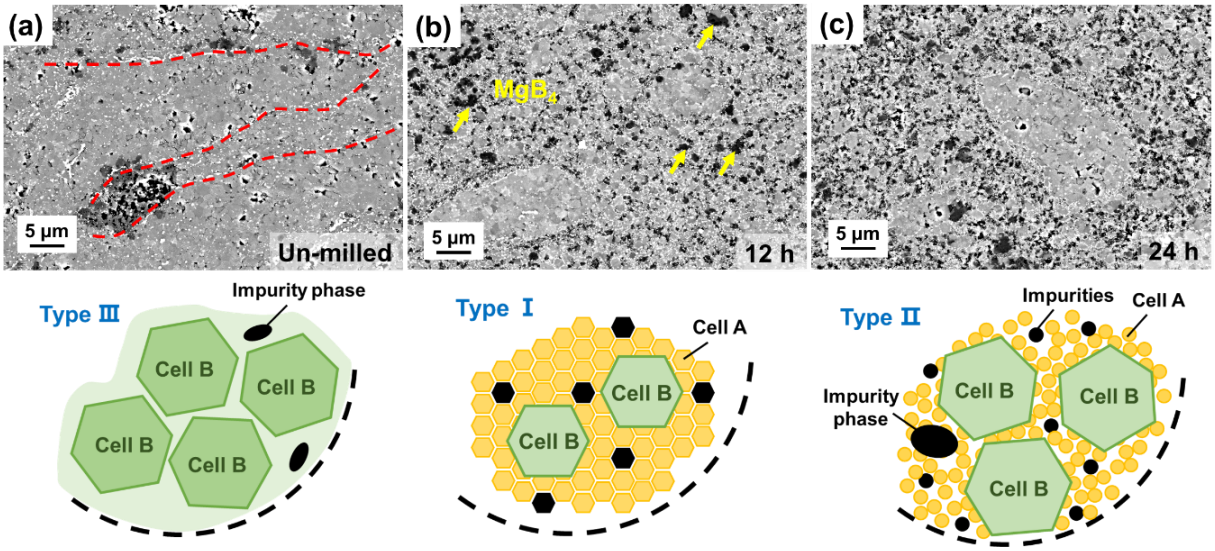


Figure 6.13 SEM micrographs of MgB_2 samples and the corresponding schematics (Chapter 4) to identify the currents flowing on different length scales.

The $\Delta M(B_{app})$ data measured at 4.2 K and 20 K of pure MgB_2 are plotted in Figure 6.14 a and b. Since ΔM curves measured at 4.2 K are influenced by flux jumps at low magnetic fields, only J_c measured at 20K is plotted as shown in Figure 6.14c. One can identify that milling time above 3 h improves macroscopic J_c values in the low and medium field range. MgB_2-6hM and MgB_2-12hM only have J_c values slightly higher than MgB_2-3hM. If referring back to ΔM curves, one can find that MgB_2-12hM performs best at both 4.2 K and 20 K. This may be because a longer milling time decreases the amount of large MgB_4 phases, which increases the fraction of superconducting regions. In addition, long milling times lead to small MgB_4 grains

distributed homogeneously in the matrix instead of larger agglomerates between the superconducting MgB_2 large cells, perhaps improving connectivity between large superconducting cells. However, excessive ball milling leads to a more porous matrix, which lowers the ΔM values compared with MgB_2-12hM.

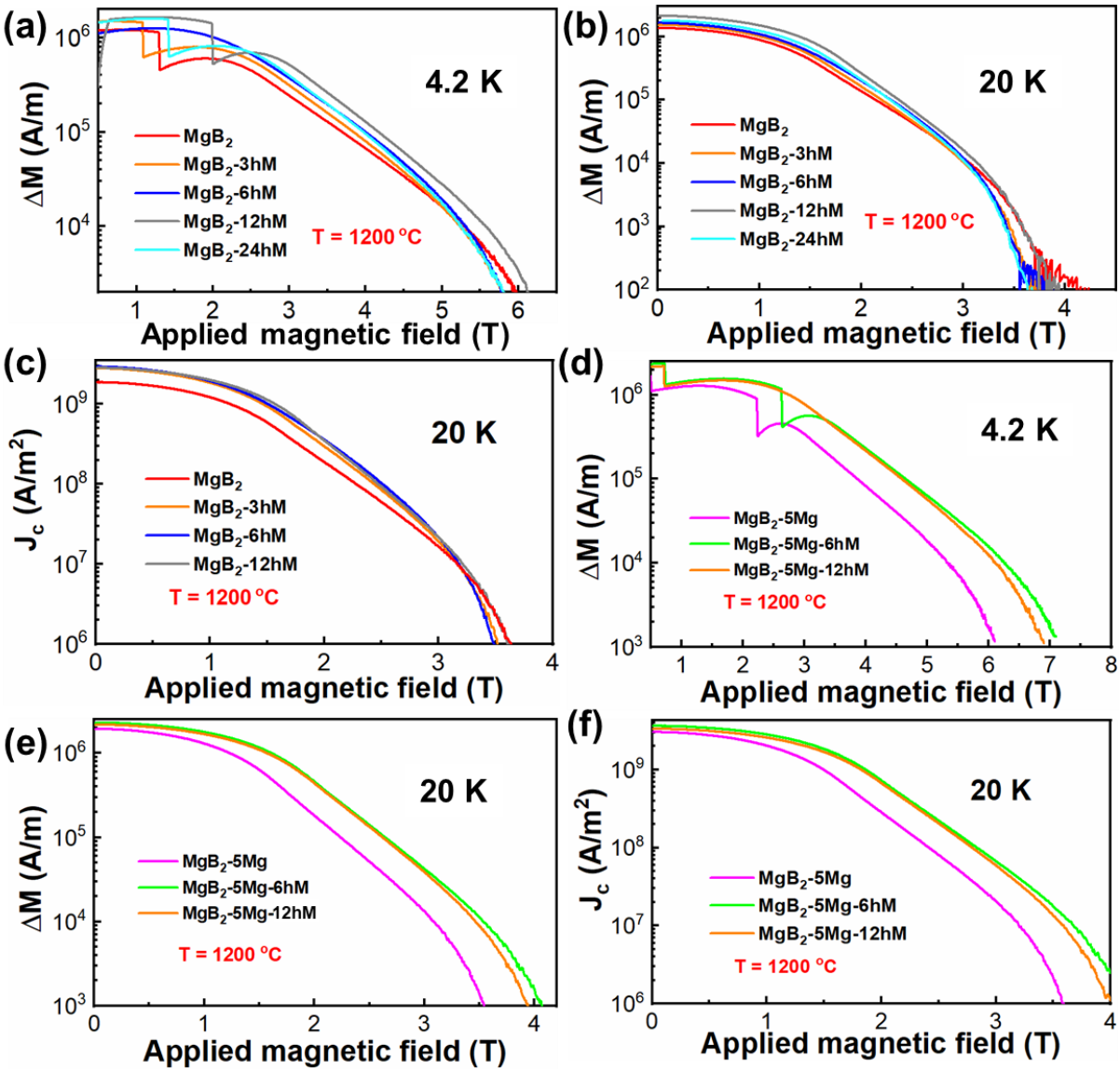


Figure 6.14 (a) and (b) show $\Delta M(B_{app})$ curves at 4.2 K and 20 K of pure MgB_2 samples. (c) presents J_c curves calculated by Bean's model. (d) and (e) show ΔM curves at 4.2 K and 20 K of MgB_2 + 5 wt% Mg samples with powder milled for various lengths of time. (f) presents $J_c(B)$ curves calculated by Bean's model.

The $\Delta M(B_{app})$ data measured at 4.2 K and 20 K of 5 wt% Mg added MgB_2 samples are

plotted in Figure 6.14d and e. The microstructure of MgB_2-5Mg is most closely reproduced by Cell model D (Section 4.2.1.4). Each grain can be viewed as a cell, and the cell currents are therefore much smaller than the macroscopic current. Mg-doped MgB_2 dense samples prepared from powders milled for 6 h and 12 h have microstructures similar to Type V (Section 4.2.6.5) but the model parameters should be revised[1]. The simulation results for this type of microstructure show that macroscopic currents dominate. Therefore, all J_c curves can be extracted with some confidence from Bean's model in this Mg-added MgB_2 sample series, with the J_c values calculated representing the macroscopic current density flowing through the sample. As Figure 6.14f shows, ball milling brings a significant improvement in J_c at medium and high magnetic fields.

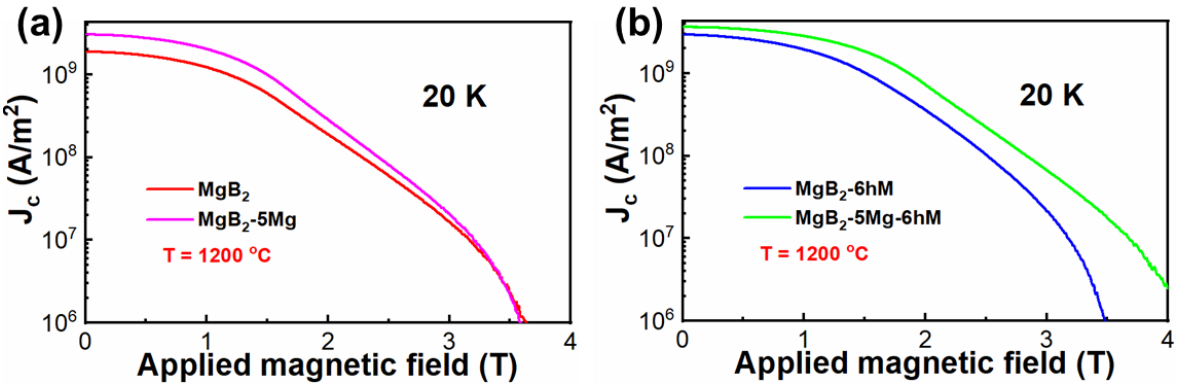


Figure 6.15 (a) and (b) compare J_c(B) curves at 20 K of MgB_2 samples with and without Mg addition.

A comparison of J_c(B) curves between pure and Mg added MgB_2 samples is presented in Figure 6.14a and b. Adding Mg without milling raises J_c values at lower fields,

[1] The revised input parameters are: f(Subarray A) = 0.3, f(Subarray B) = 0.6, A_{con}(Cell A) = 0.7, A_{con}(Cell B) = 0.3, p_{MgB2}(Subarray A) = 0.8, p_{MgB2}(Subarray B) = 1,d(cellA) = 10^{-6} m and d(cell B) = 10^{-5} m

presumably because grain boundaries are cleaner so better connectivity can be achieved (Figure 6.9g). In contrast, if the powder is milled for 6 h, Mg addition pushes the $J_c(B)$ curve upwards, especially in the moderate and high field regions. This probably comes from the better interconnectivity between dense regions and the matrix as well as a lower fraction of MgB_4 phases in Mg-added MgB_2 samples, so the percolation effects are weakened.

Different sintering temperatures also influence both T_c and J_c values. As Figure 6.16a shows, even though samples have similar onset T_c values, the sample processed at 1000 °C has the broadest transition ($\Delta T \approx 1.5$ K).

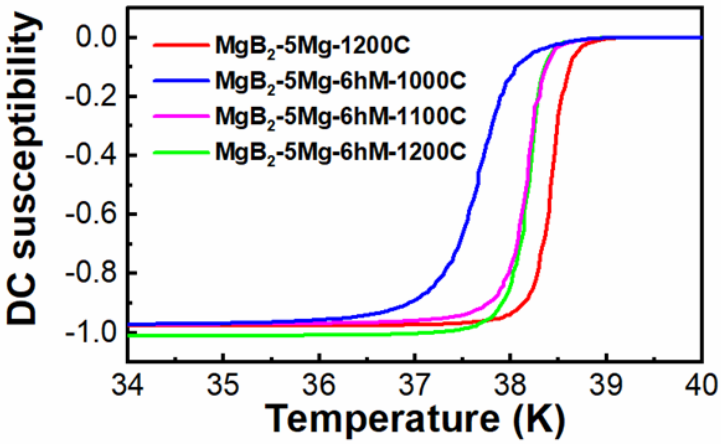


Figure 6.16 DC susceptibility curves of the MgB_2 + 5 wt% Mg bulk specimens processed at different temperatures.

From $\Delta M(B_{app})$ curves at 20 K in Figure 6.17a, one can observe that the superconducting performance of samples processed at 1000 °C is inferior to that of samples processed at higher temperatures, but with the increasing field, this difference becomes less clear. MgB_2-5Mg-6hM-1000C has Type II microstructure (Section 4.2.6.2). In view of poor connectivity between dense regions and the porous matrix,

interconnectivity between Subarray A and Subarray B was set to approach 0 in the simulation [2]. Results show that the total ΔM can be influenced by Cell B current. i.e., the current circulating within dense regions. Since we are interested in macro currents that are useful in practical conditions, only J_c values of the samples processed at temperatures over 1100 °C are calculated. As shown in Figure 6.17b, the small difference in $\Delta M(B_{app})$ curves of samples processed at 1100 °C and 1200 °C are eliminated in $J_c(B)$ curves, which indicates temperatures within 1100 ~ 1200 °C are most suitable for 5 wt% Mg added MgB_2 samples prepared by the ex-situ method.

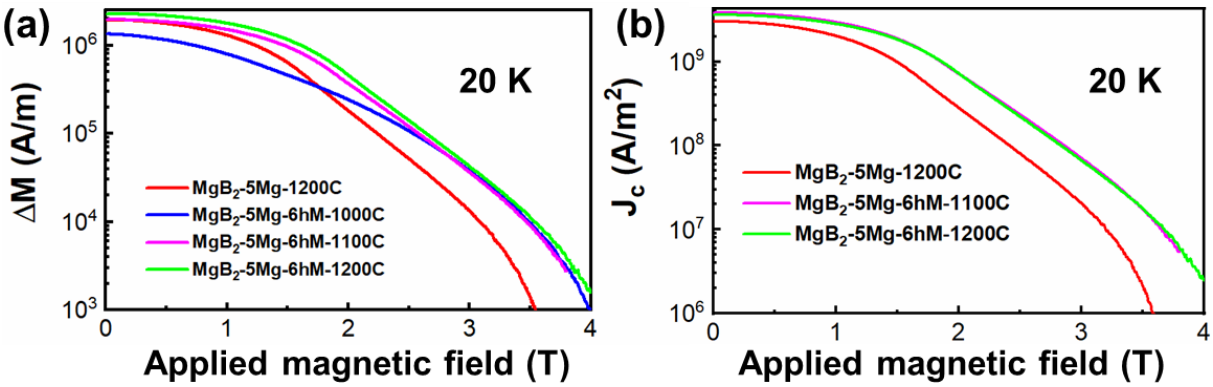


Figure 6.17 (a) and (b) are $\Delta M(B_{app})$ and $J_c(B_{app})$ curves at 20 K of MgB_2+5 wt% Mg samples processed at different temperatures.

6.7 Analysis of pinning mechanisms

The main aim of this section is to use experimental results to show that analysis of pinning curves without self-field corrections may lead to debatable conclusions. Using the method described in Section 4.3.2, the original J_c (B_{app}) and the self-field corrected

[2] The revised input parameters are: f(Subarray A) = 0.4, f(Subarray B) = 0.4, A_{con}(Cell A) = 0.3, A_{con}(Cell B) = 0, p_{MgB2}(Subarray A) = 0.5, p_{MgB2}(Subarray B) = 1,d(cellA) = 10^{-6} m and d(cell B) = 10^{-5} m.

$J_c(B)$ curves of MgB_2 samples with and without Mg addition are plotted in Figure 6.18a and b. $J_c(B)$ curves overlap with J_c (B_{app}) at high magnetic fields where the self-field effects are neglectable. The disparity between two curves becomes significant in the field range below around 2 T. As Section 2.3 introduces, the irreversibility field (B_{irr}) refers to the field above which thermal fluctuations become strong and flux lines begin to flow [66, 75]. There are two methods to obtain B_{irr} values. One is the linear extrapolation of $J^{0.5}B^{0.25}$ (B) curves (Kramer plots). The other is determined with a current density criterion (J_c = 100 A/cm^2) [211, 212]. There are three problems with Kramer plots: (i) B_{irr} estimation has high errors if Kramer plots at high field range are not linear; (ii) unmodified shear modulus, C66, will lead to a lower peak position of pinning curves [67], and (iii) Kramer plots are more appropriate for samples where the dominance of grain boundary pinning has been known. Therefore, the second method (J_c = 100 A/cm^2) is used here to estimate B_{irr}.

Pinning curves show the dependence of the normalized pinning force on the reduced field ($b = B/B_{irr}$) which are presented in Figure 6.18c and d. It can be seen that the peak positions (b_{peak}) of pinning curves calculated by corrected $J_c(B)$ data shift left and the peak of the un-milled MgB_2 (the pink one) locates around 0.2 compared with that calculated from the original $J_c(B)$ curves. This peak position of b = 0.2 is what is expected for the grain boundary pinning mechanism. In some previous studies, changes in b_{peak} are often viewed as a change in pinning mechanisms [66, 213]. However, my findings reveal that the b_{peak} change of pinning curves may also be influenced by self-

fields. Since no new elements or phases are introduced and ball milling is shown to lead to crystallite refinement in this study, it is reasonable to assume that grain boundary pinning is the dominant pinning mechanism. Moreover, the uncertainty in extracting B_{irr} value by different methods can also lead to a shift in the apparent peak position. Even after corrections, there is also a large deviation in the descending parts of the GB pinning curve and curves from experimental data. This phenomenon can be explained by the anisotropy (here $\gamma = B_{irr}/B_{c2}^{||ab}$) included in the percolation theory as explained in [67].

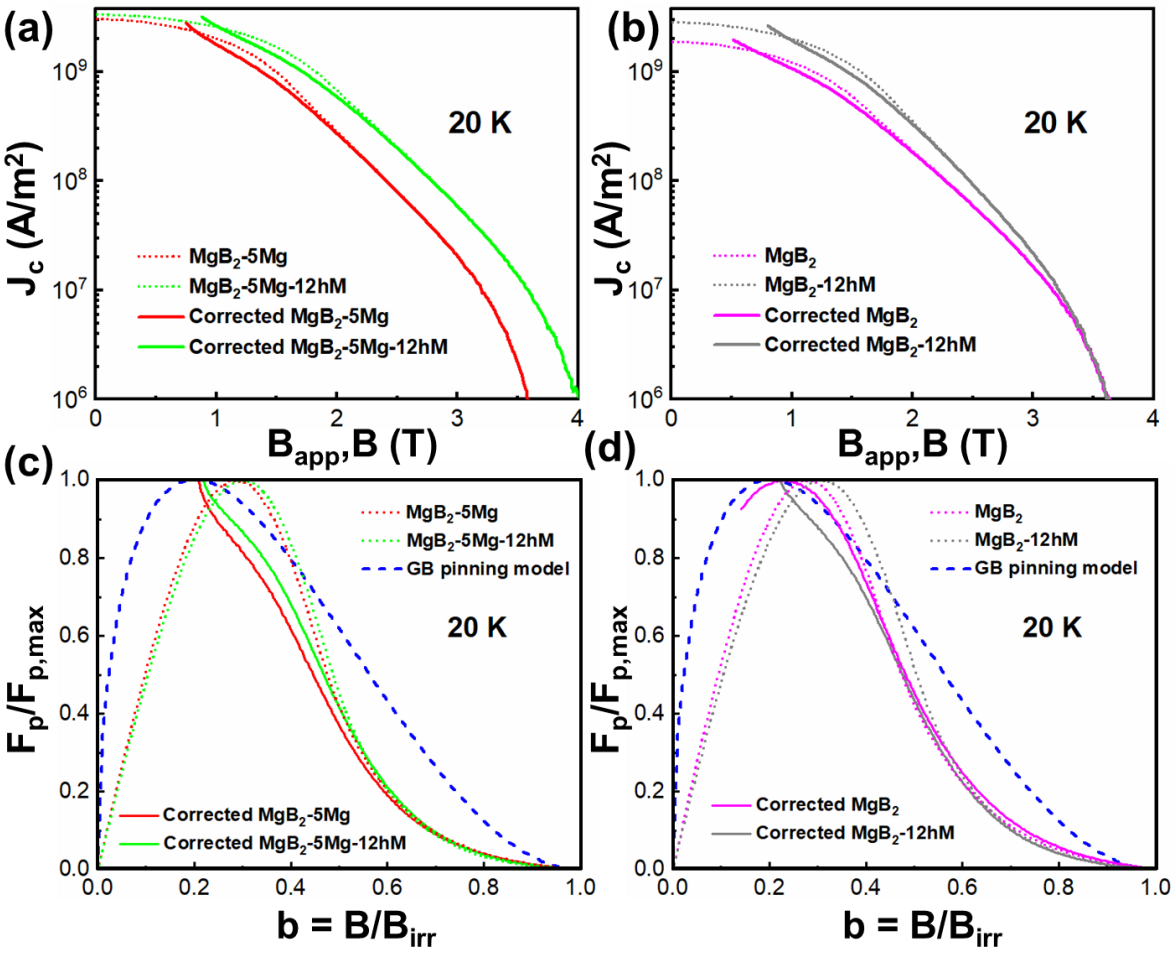


Figure 6.18 (a) and (b) show J_c curves at 20 K before and after self-field corrections. (c) and (d) show the comparison of pinning curves calculated from original and corrected J_c curves.

6.8 Conclusions

The present work studies the effect of ball milling and Mg addition on MgB_2 microstructures and superconducting performance. The following conclusions can be drawn：

i. There are two opposite effects on the J_c brought by high-energy ball milling. The positive effect arises from crystallite refinement and the introduction of grain defects. However, a longer milling time (24 h) also leads to the saturation of crystallite refinement. The oxygen accumulation on the surface of MgB_2 particles and the decomposition of MgB_2 due to the highly active surface of small particles/grains formed becomes more serious with the increasing milling time. These negative effects contribute to the formation of the porous matrix in bulk samples fabricated from powders subjected to long milling times, which impair the macro current flow.

ii. Mg addition can provide a liquid environment for sintering to improve the mass transfer rate. The grain boundaries free of impurities improve the grain boundary connectivity of Mg-added samples, which contributes to the better low-field J_c performance. If combined with ball milling, adding Mg can improve the connectivity between dense regions and the matrix, and the whole sample is more homogeneous with Mg addition. Moreover, the reduction in the density of dispersed MgB_4 grains in 5 wt% Mg+MgB_2

samples increases the effective cross-section for macroscopic currents, which improves the overall J_c performance.

iii. b_{peak} changes in pinning curves may come from the changes in the dominant pinning mechanism, B_{irr} uncertainty estimated by different methods, and the lack of self-field corrections. Higher anisotropy will lead to the increasing deviation of the curve shape compared to the grain boundary model in the high field range ($b > b_{peak}$).

Chapter 7 Microstructures and superconducting properties of cubic BN added MgB_2 bulk samples

7.1 Introduction

As introduced in Section 2.3.3, many papers have demonstrated that the improvement of MgB_2 superconducting performance by doping with carbon is mainly due to the substitution for B sites (Section 2.3.3). However, the role of another light element, N, has not been carefully checked yet. Only a few studies have tried N-containing dopants such as Si_3N_4 and cubic BN and concluded that high-field J_c performance of doped MgB_2 bulk samples can be enhanced. But, even so, their proposed mechanisms are quite different from each other and lack believable evidence from microstructural characterisation [214-216].

In this chapter, hard and brittle cBN particles were chosen to be co-milled with MgB_2 powder before being processed by field-assisted sintering. The effects of milling time, processing temperature and time on the microstructures of bulk samples will be systematically investigated. Results of superconducting properties are then presented and correlated to the corresponding microstructural features. Finally, different conclusions as to the effects of cBN additions will be made here, providing a new perspective of understanding the role of the N element in altering the superconducting performance of MgB_2.

I would like to thank Dr. Sangeeta Santra who co-prepared some samples with me.

7.2 Experimental methods

Commercially available MgB_2 powder (purity: 99%, Alfa Aesar) and cubic BN powder (~10 μm) were used to prepare MgB_2 bulk samples by an ex-situ method. x wt% cBN (x = 0, 0.5, 2, 5) was first mixed with MgB_2 powder in the glove box under Ar atmosphere. About 0.5 g powder was taken out after 10 min, 0.5 h, 1 h, 3 h, 6 h, 12 h and 24 h of ball milling for phase analysis and microstructural characterisation. Sintering was carried out in the FAST apparatus at temperatures ranging from 950 °C to 1200 °C with an applied uniaxial pressure of 50 MPa. All powders were sintered for 5 min, except one 5 wt% cBN doped sample that was sintered for 30 min.

Table 7.1 The processing conditions applied in the field-assisted sintering

Sample*	cBN fraction (wt%)	Milling time (h)	Sintering temperature (°C)	Dwell time (min)
0.5cBN-6hM	0.5	6	1200	5
0.5cBN-12hM	0.5	12	1200	5
0.5cBN-24hM	0.5	24	1200	5
2cBN-950C	2	24	950	5
2cBN-6hM	2	6	1200	5
2cBN-12hM	2	12	1200	5
2cBN-24hM	2	24	1200	5
5cBN-1050C	5	24	1050	5
5cBN-6hM	5	6	1200	5
5cBN-12hM	5	12	1200	5
5cBN-24hM	5	24	1200	5
5cBN-F30min	5	24	1200	30

*The sample name highlights the unique processing conditions.

7.3 Characterisation of ball-milled precursor powders

In this section, various percentages of cBN particles and MgB_2 powders were co-milled

for different lengths of time. Results of phase and microstructural analysis of the mixtures are listed and compared with those obtained from pure MgB_2 ball-milled powders (Chapter 6). Since few experiments have investigated the milling process and mechanisms in these kinds of ceramic systems, this work has implications for understanding the role of hard additives on MgB_2 crystallite refinement during the ball milling process.

7.3.1 Phase identification and quantitative analysis by Rietveld refinement

Figure 7.1a shows XRD patterns of 2 wt% and 5 wt% cBN added MgB_2 powder milled for selected times. Apart from the cBN peaks, no other N-containing phases are detected, suggesting that cBN did not react with MgB_2 during the milling process. With longer milling times, decreasing peak intensities and peak broadening indicate the reduction in MgB_2 crystallite size and the introduction of inhomogeneous strain. Quantitative analysis of the 5 wt% cBN added MgB_2 mixtures by Rietveld refinement is shown in Table 7.2. After 24 h of milling, the crystallite size decreases from 76 nm to 39 nm, and the strain increases from 0.10% to 0.28%.

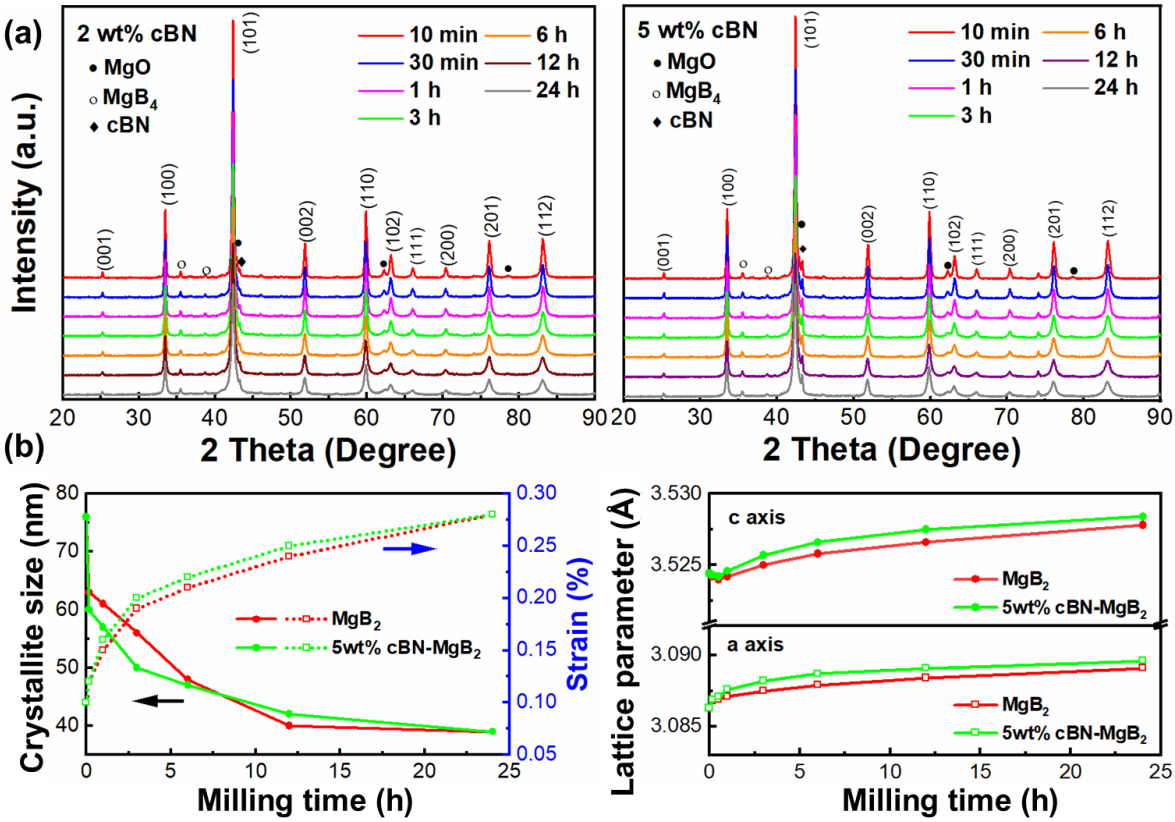


Figure 7.1 (a) XRD patterns of 2 wt% and 5 wt% cBN doped MgB_2 ball-milled powders. (b) the changes of MgB_2 lattice parameters, crystallite sizes and strain with the increasing milling time.

Table 7.2 Quantitative results of MgB_2 lattice parameters, crystallite size and strain of 5 wt% cBN added MgB_2 powders milled for selected times.

Milling time	a axis (Å)	c axis (Å)	Crystallite size (nm)	Strain (%)
0 min	3.086	3.524	76	0.10
10 min	3.087	3.524	60	0.12
1 h	3.087	3.524	57	0.16
3 h	3.088	3.525	50	0.20
6 h	3.088	3.526	43	0.24
12 h	3.089	3.527	42	0.25
24 h	3.089	3.528	39	0.28

The comparison of MgB_2 powders milled in the pure state and with 5 wt% cBN addition is shown in Figure 7.1b. A dramatic drop in crystallite size is seen in the initial 1 h of milling. Up to 6 h of milling, the cBN addition can assist in the refinement of crystallites, but after 24 h of milling, the refinement reaches saturation and there is no difference between the two powder sets. The increase of strain shows a similar trend, where the

increasing rate gradually slows down with the longer milling time, eventually approaching 0.3%. Additionally, both a and c axes show an increase, and cBN added MgB_2 powder has a slightly enlarged unit cell volume.

7.3.2 Characterisation of microstructures and chemical composition

BSE images of cBN powder are shown in Figure 7.2a. From element maps, the size of irregular cBN particles is estimated to be around 10 μm. SEM images of 5 wt% cBN added MgB_2 mixtures show the presence of MgB_2 aggregates (5 ~ 10 μm) among MgB_2 grains and cBN particles with the faceted structure after 12 h of milling (Figure 7.2b).

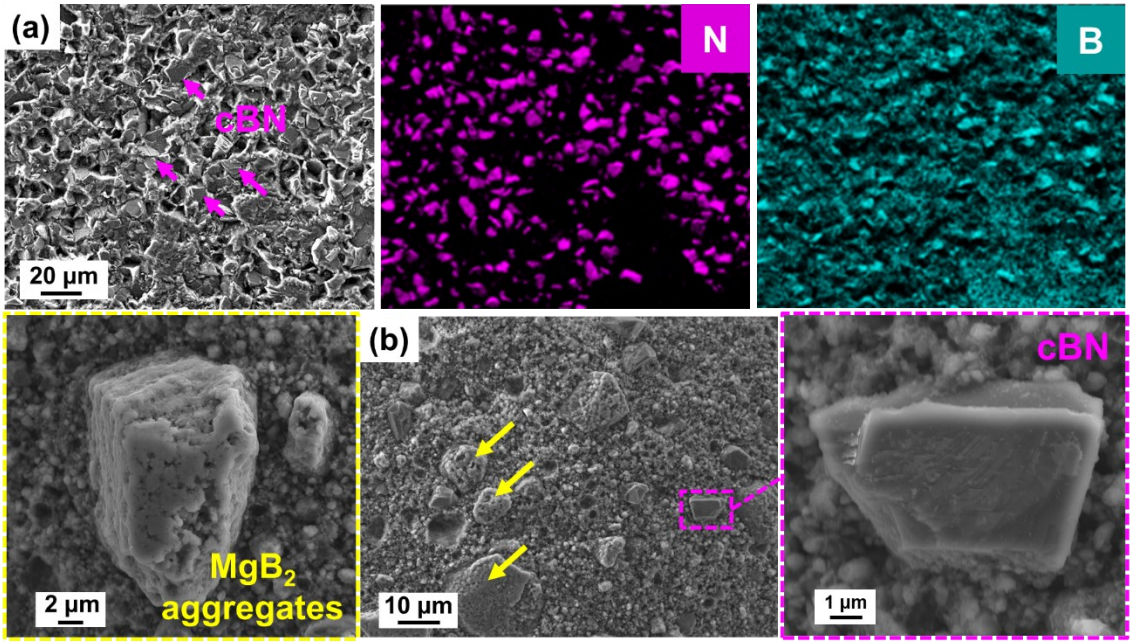


Figure 7.2 (a) BSE image along with elemental mapping of B and N of as-received cBN powders. (b) SEM images of 5 wt% cBN added MgB_2 precursor powders after 12 h of milling.

Figure 7.3 presents the microstructures of 5 wt% cBN doped MgB_2 powders after 10 min to 24 h of milling, where cBN particles with low average atomic mass give the darkest contrast. First of all, a significant decrease in the average size of cBN particles

after longer milling could be observed. Initial angular MgB_2 agglomerates were reduced in size rapidly in the first 10 min (Figure 7.3b). Continuing milling changes the morphology of MgB_2 particles into a round shape, while the extension of time to 24 h does not bring detectable further changes in particle size or shape (Figure 7.3e-g). The particle sizes of MgB_2 ball-milled powder with selected milling times were calculated by ImageJ (Figure 7.3h). A dramatic drop in particle size to 30 μm occurs in about 1 h of the milling process, followed by much slower changes in size and saturation after 24 h of milling. Adding cBN to MgB_2 powders is effective in reducing particle size initially but the final limiting values of particle sizes show little difference. By comparison with Figure 7.1b, one can find that crystalline refinement is also significant during the first hour of milling. However, for milling times between 1 h and 12 h, the decrease in crystallite size is much more noticeable. This different behaviour arises from the separate mechanisms of particle size and crystallite size reduction. The decrease in the brittle particle size correlates to fracture due to the impact introduced by milling balls while the refinement of crystallite originates from creating a network of dislocations to accommodate severe plastic deformation. A simple model proposed by Li et al uses the expression $D = Kt^b$ to describe the dependence of particle/grain size D on the milling time t [217]. K is a constant while b values describe the decreasing rate determined by the relationship between yield stress/lattice friction stress and grain/particle stress. $b = -2/3$ for grain size variation and -1 for particle size reduction were estimated in their study, indicating particle size would reduce faster than grain size. This trend is

consistent with the experimental results here.

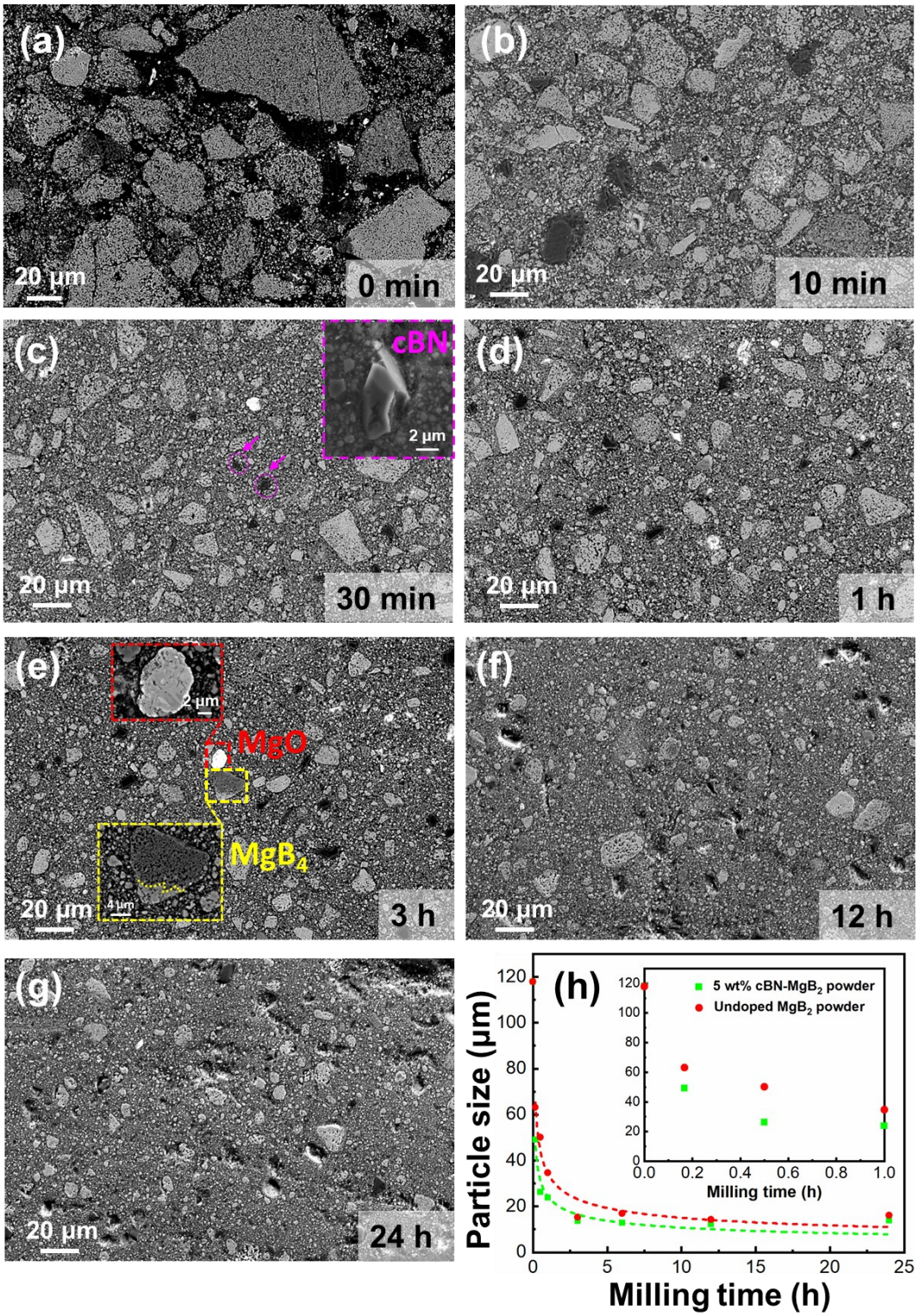


Figure 7.3 BSE images of (a) as-received powder and 5 wt% cBN doped MgB_2 powder after (b) 10 min, (c) 30 min, (d) 1 h, (e) 3 h, (f) 12 h and (g) 24 h of milling. (h) shows the particle size vs. milling time for the two powder sets.

Another finding in this study is a different role of harder additives on softer powders. Zamora et al found the presence of harder SiC (~0.55 μm) slowed down the refinement kinetics of ZrB_2 single-crystal particles (~2 μm) and attributed it to the friction sliding brought by nano-SiC particles that lower compressive stresses on ZrB_2 particles [218]. By contrast, cBN particles are harder than MgB_2 but in my results can accelerate the refinement of MgB_2 particles. The opposed results are ascribed to the relative sizes of original particles and their difference in brittleness. In my study, cBN particles (~10 μm) are much larger than MgB_2 (<1 μm) grains, so can be viewed as an increase in the ball-to-powder ratio, which can benefit the reduction in particle size. The limiting value of particle size after 24 h of milling results from the fracture strength inversely increasing with smaller particle sizes.

7.4 Investigation of cBN addition on phase and microstructural evolution of MgB_2 bulk samples

The following sections classify sample sets by three different percentages of cBN and discuss the influence of milling time, processing temperature and processing time on MgB_2 bulk samples.

7.4.1 Characterisation of MgB_2 bulk samples with 0.5 wt% cBN addition

XRD patterns of 0.5 wt% cBN added MgB_2 samples processed at 1200 °C for 5 min are shown in Figure 7.4. Apart from MgO and MgB_4, no other impurity phases could

be detected. The height of the MgB_2 peaks shows a noticeable decrease in the 0.5cBN-24hM sample, and the strongest MgB_4 peak at around 35.6° indicates that the longer milling process of powders leads to a larger volume fraction of decomposition products in bulk samples after sintering.

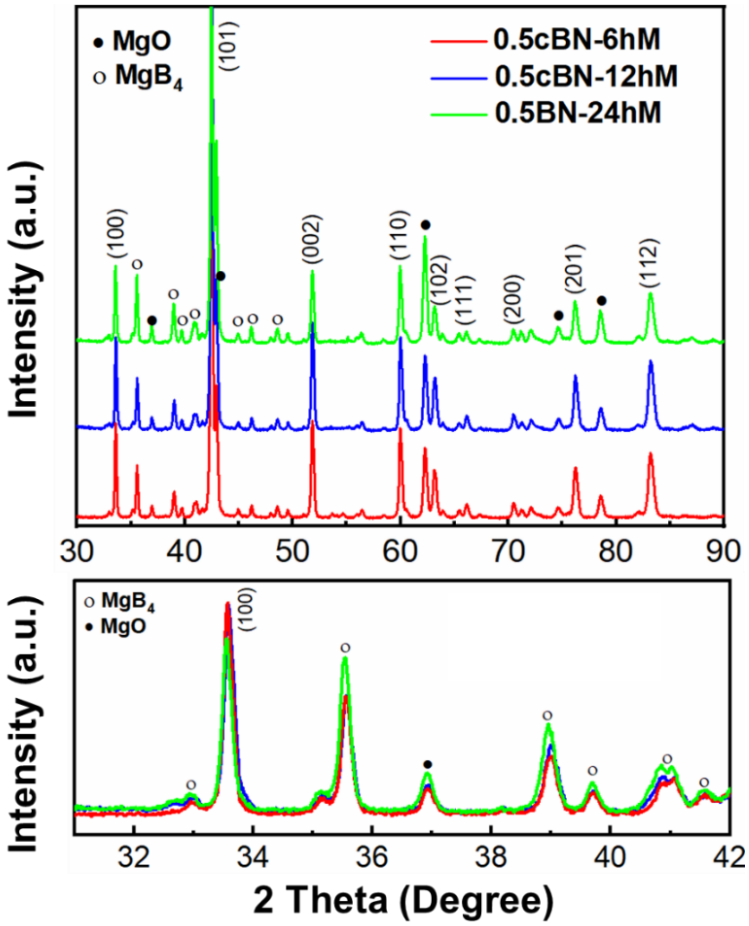


Figure 7.4 XRD patterns of 0.5 wt% cBN added MgB_2 bulk samples with powder milled for selected times and then processed at 1200 °C for 5 min. The lower figure highlights the phase evolution of MgB_4 and MgO after different milling times.

Figure 7.5 presents morphologies of 0.5 wt% cBN added MgB_2 samples produced from powder milled for 12 h and 24 h. 0.5cBN-12hM has dense and relatively homogenous structures (Figure 7.5a). Only a small fraction of large MgB_4 phases (medium-dark contrast) and cBN particles with 5 μm in size (darkest contrast) highlighted by arrows

can be observed. Figure 7.5b taken at higher magnification shows MgB_4 grains with comparable sizes to MgB_2 grains dispersed homogeneously in the matrix. The well-connected area that contains fewer MgO impurities (yellow lines) arises from strong aggregates in the milled powder (Figure 7.2b). The contrast variation in Figure 7.5c indicates the obvious inhomogeneity of the 0.5cBN-24hM sample where dense MgB_2 regions become distinctive as well as a higher fraction of newly-formed MgB_4 phases. When zooming in, one can find higher porosity in the matrix compared to 0.5cBN-12hM, and MgB_2 decomposition initiated in the interior of dense regions results in the formation and growth of large MgB_4 phases (Figure 7.5d).

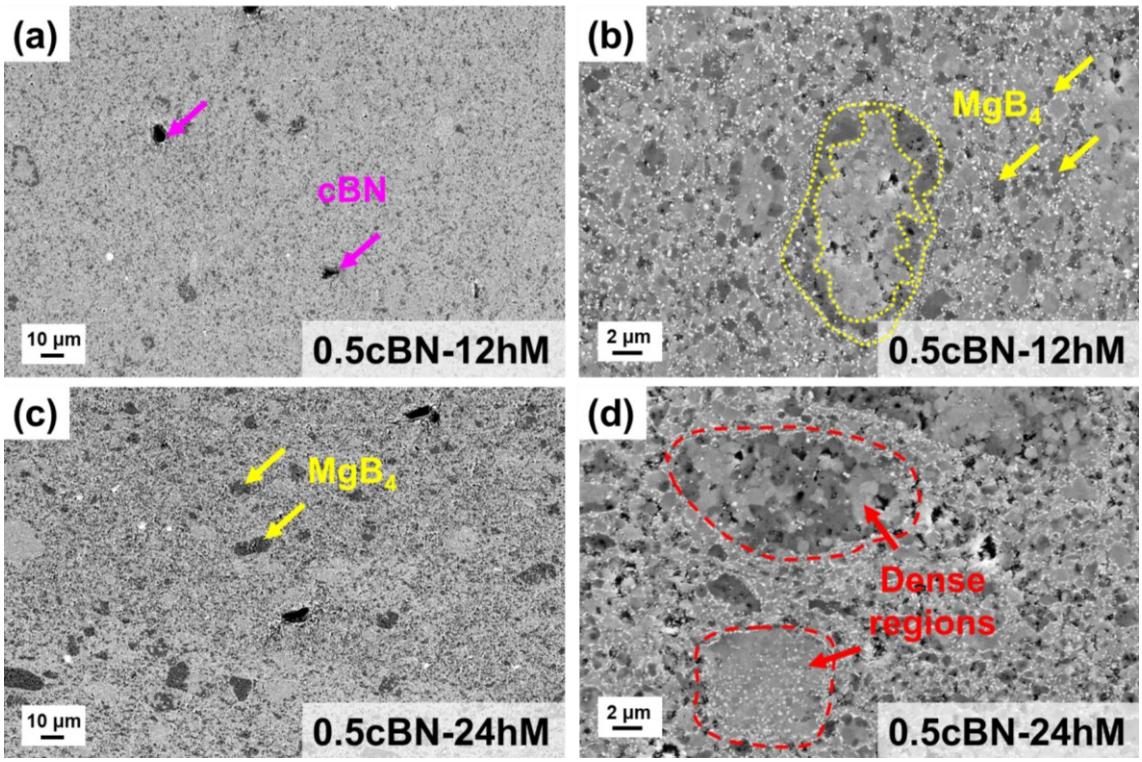


Figure 7.5 BSE micrographs of 0.5 wt% cBN added MgB_2 samples with powder milled for (a)(b) 12 h and (c)(d) 24 h and then processed at 1200 ºC for 5 min.

The chemical composition of 0.5cBN-12hM investigated by EDX is shown in Figure

7.6. Line scan results indicate the existence of N-containing phases in the same regions where the B counts are also high. However, element maps show smaller area with weak N signals compared with area with strong B-rich signals. This may be explained by the small number and size of N-containing impurities in 0.5 cBN wt% added samples so the individual small particles are difficult to be detected.

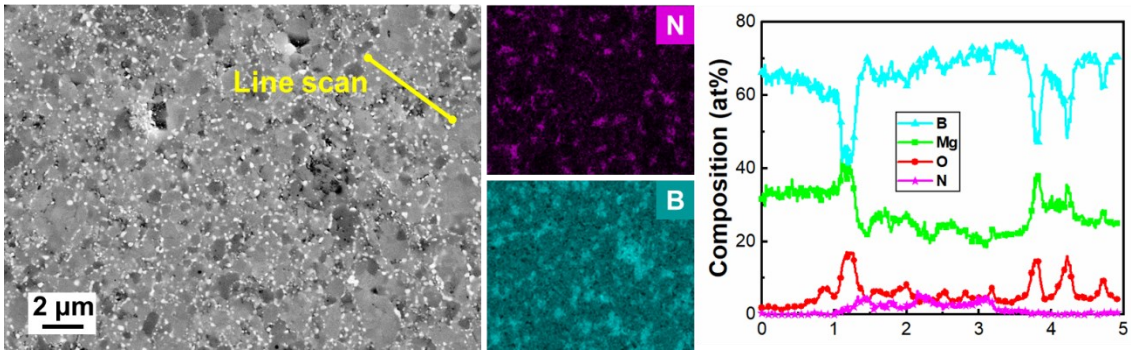


Figure 7.6 EDX results of 0.5cBN-12hM processed at 1200 ºC for 5 min.

7.4.2 Characterisation of MgB_2 bulk samples with 2 wt% cBN addition

Figure 7.7a presents the phase evolution of 2 wt% cBN added MgB_2 bulk samples with various milling times processed at 1200 ºC (or 950 ºC). Due to the increased cBN percentage, the strongest peak of cBN with 2θ at 43.3º can be detected in this sample. MgB_2 peaks are sharper with higher processing temperatures (1200 ºC) due to better crystallinity. With the prolongation of milling time, the lowest MgB_2 peak intensity occurs in the pattern of the 2cBN-12hM sample, as shown by pink dashed lines. Moreover, a significant change in the pattern of 2cBN-24hM compared to 2cBN-12hM is the great reduction in the number of MgB_4 peaks. An expanded view between 31º to 42º is shown in the right-hand figures to examine these differences carefully. As Figure 7.7b shows, the MgB_4 content increases in the 2cBN-12hM sample, which is attributed

to the higher active surface area after a longer milling process. However, a surprisingly dramatic decrease in MgB_4 peak intensity is seen in the sample milled for 24 h, indicating the transformation of MgB_4 to other phases in the presence of cBN additives, which requires further investigation. When fixing the milling time (24 h) but lowering the processing temperature to 950 °C (Figure 7.7c), MgB_4 has not been transformed to other impurities so is the most dominant impurity phase, which suggests that as well as the milling time the processing temperature is another critical factor to induce the MgB_4 transformation.

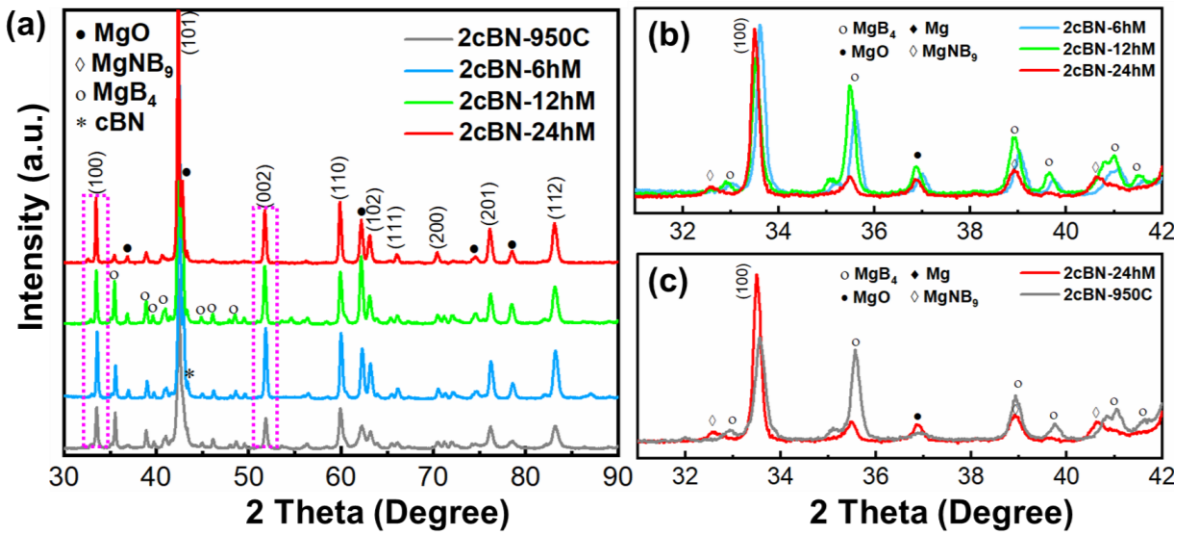


Figure 7.7 (a) XRD patterns of 2 wt% cBN added MgB_2 samples with powder processed at selected milling times or at different temperatures. (b) and (c) highlight the phase evolution of MgB_4 impurities.

Figure 7.8 depicts morphologies of the 2 wt% cBN added MgB_2 sample set. Consistent with the XRD results, the fraction of large MgB_4 phases is high in 2cBN-6hM and 2cBN-12hM, but both samples have relatively dense structures (Figure 7.8a and b). Sample inhomogeneities are obvious in 2cBN-24hM and 2cBN-950C, indicated by the

strong contrast difference between dense regions and porous matrix (Figure 7.8c and d).

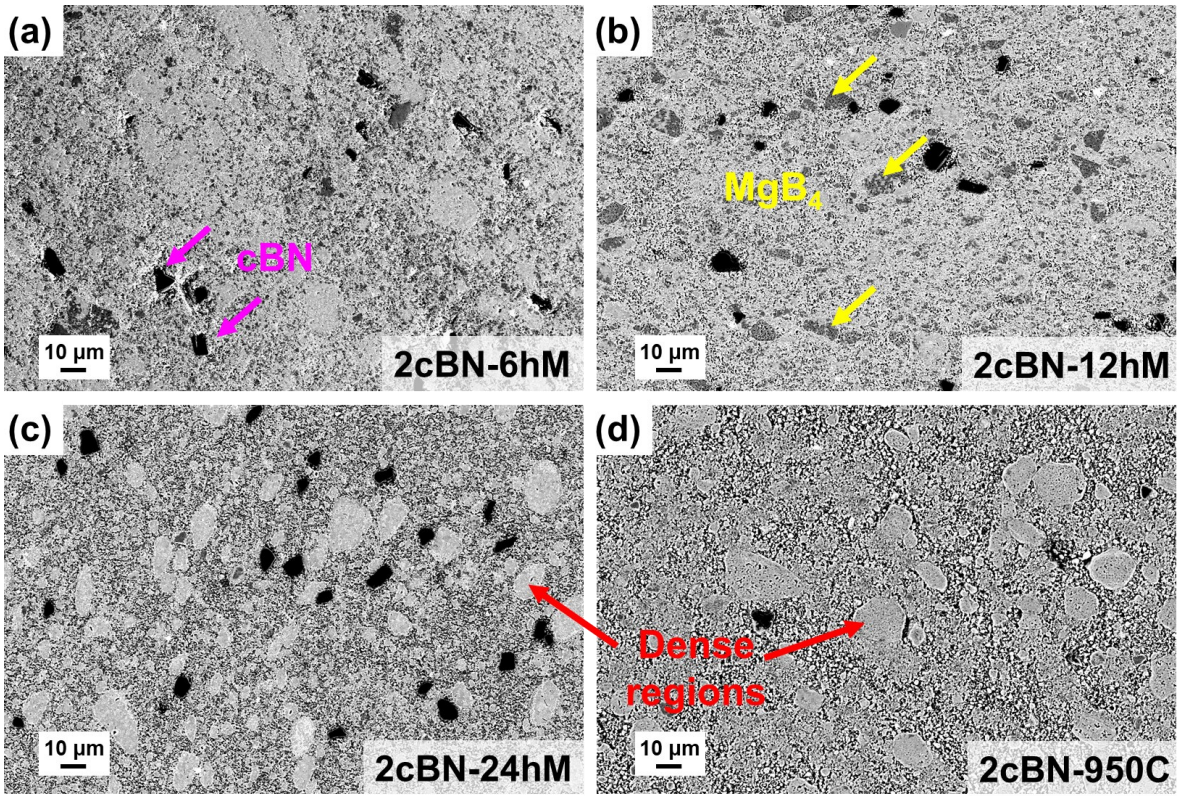


Figure 7.8 BSE micrographs of 2 wt% cBN added MgB_2 samples with powder milled for (a) 6 h, (b) 12 h, (c) 24 h before processed at 1200 ºC for 5 min and (d) 24 h before processed at 950 ºC for 5 min.

BSE images taken at higher magnification, Figure 7.9, show more details about connectivity between different regions and grains. As shown in Figure 7.9a, grains within dense regions have good connectivity unlike those surrounded by fine MgO impurities in the matrix. Additionally, Figure 7.9b reveals that pores accompanied by MgB_4 grains are present in the matrix in 2cBN-12hM. The structure of the sample with powder milled for 24 h has a strongly deteriorated matrix that has a high porosity (Figure 7.9c). As shown in Figure 7.9d, pores are along grain boundaries and

interconnect with each other.

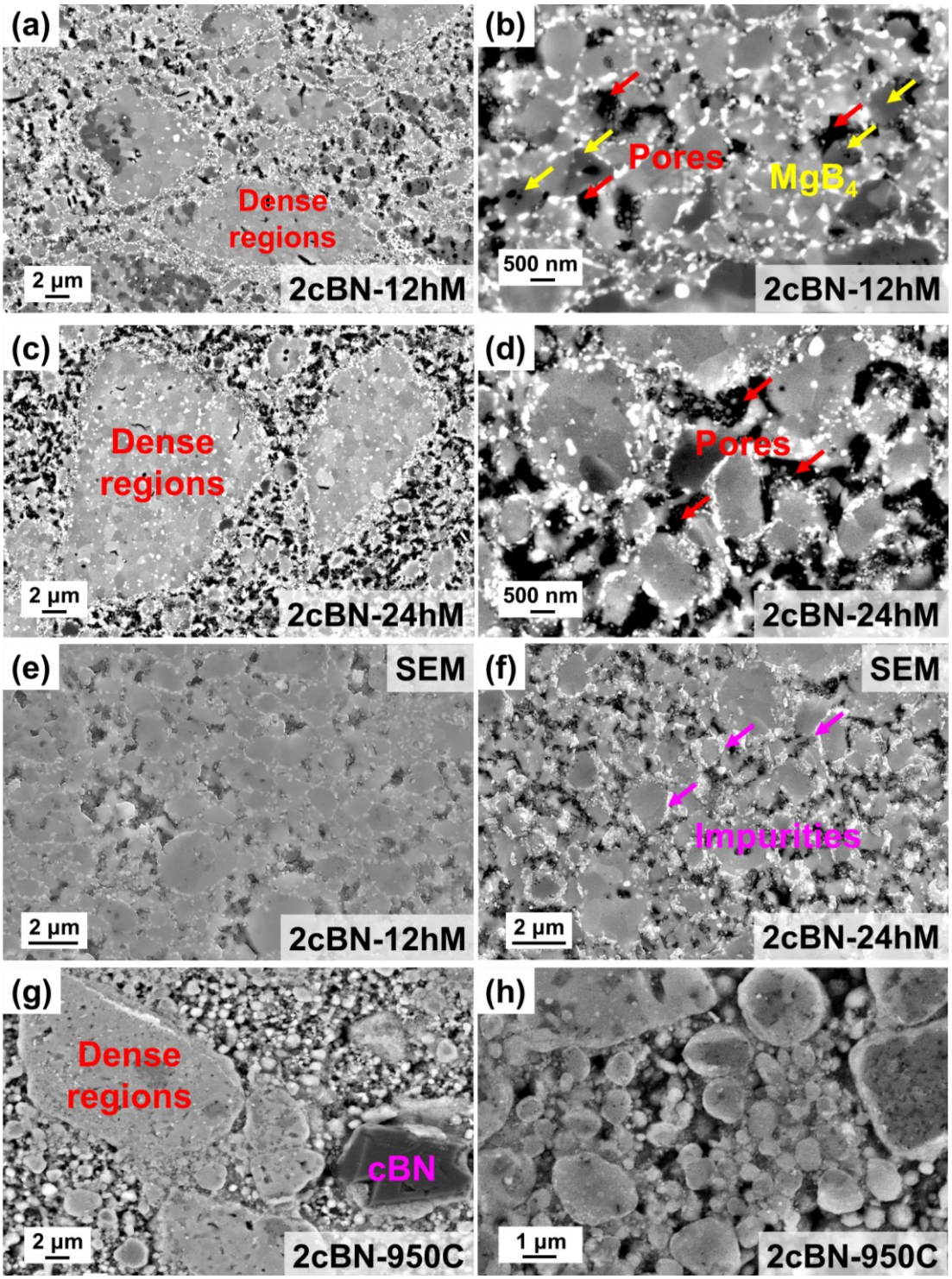


Figure 7.9 BSE images of 2 wt% cBN added MgB_2 samples with powder milled for (a)(b) 12 h, (c)(d) 24 h and then processed at 1200 °C for 5 min. (e) and (f) are SEM micrographs of the matrix. (g) and (h) shows morphologies of 2 wt% cBN doped MgB_2 samples with powder milled for 24 h and then processed at 950 °C for 5 min.

Since the atomic number contrast in BSE images is not sensitive to surface topography, I also compare SE micrographs to confirm the blackest contrast is indeed from the presence of pores (Figure 7.9e and f). Moreover, as shown in Figure 7.9f, it can be seen that grain boundaries in the 2cBN-24hM sample are decorated with many small particles with the brightest contrast compared with those in 2cBN-12hM. These grain boundary decorations may resist sample densification, limit grain growth and lead to the higher porosity of the matrix. Figure 7.9g and h show small particles/grains in the porous matrix are almost fully isolated from each other, and even sintering necks have not formed yet in 2cBN-950C.

EDX results in Figure 7.10 demonstrate the presence of N-containing phases in 2cBN-1200C. Figure 7.10a shows that large cBN particles (>5 μm) retain the stoichiometric ratio of B/N ≈1. Small cBN grains with sizes below 1 μm distribute within the matrix (Figure 7.10b). However, by checking the grain boundaries, one can find that the B/N ratio of some N-containing phases deviates from 1 with the percentage of B slightly above 50 at% while the N percentage decreases from 50 at% to 30 at% as the arrow in Figure 7.10c highlights. This indicates a reaction between cBN and MgB_2 that produces Mg(N,B) phases.

Benefiting from the improved resolution, the partially-transformed cBN particle shown in Figure 7.10d is analysed in a thin foil prepared from 2cBN-24hM. A line scan was conducted across the interface of cBN and MgB_2 grains, from which several layers could be determined: (i) Layer I is N-rich with the proportion gradually increasing from

50 at% to 60 at%; (ii) Mg shows a dramatic decrease from 60% to 20% opposed to the increase of B content to 70% in Layer II; (iii) Layer III is N-containing phases where the concentration of Mg increases while the composition of B reduces; (iv) Mg and B have relatively stable distribution with the ratio of 2:3 in Layer IV, and there is no N detected. Table 7.3 reports elemental compositions at different sites (S1-S6). Table 3.2 has shown the ideal atomic Mg:B ratio within the MgB_2 grains obtained in EDX results is 1:2. Layers I and IV originate from cBN and MgB_2 respectively, and the deviation of stoichiometric ratio may come from aggressive liquid Mg during the sintering process, transforming cBN to Mg(N,B) phases (Layer II & III). Comprehensively considering the content and changes of the elements in Figure 7.10c and d, it is possible that the transformation of cBN and the stoichiometry of Mg(N,B) phases are closely related to the amount of Mg liquid phase during the sintering process. This conclusion can explain why there is a dramatic decrease in MgB_4 peak intensity but no characteristic peaks from other impurities can be observed in the XRD spectrum of 2cBN-24hM where the stable stoichiometry has not been established (Figure 7.7b). The proposed mechanism is explained in detail in Section 7.5 .

Table 7.3 Chemical composition results from point analysis by EDX in Figure 7.10.

	I		II	IV		
	S1	S2	S3	S4	S5	S6
B (at%)	46	34	62	60	70	57
Mg (at%)	-	6	25	40	30	30
N (at%)	54	56	5	-	-	5

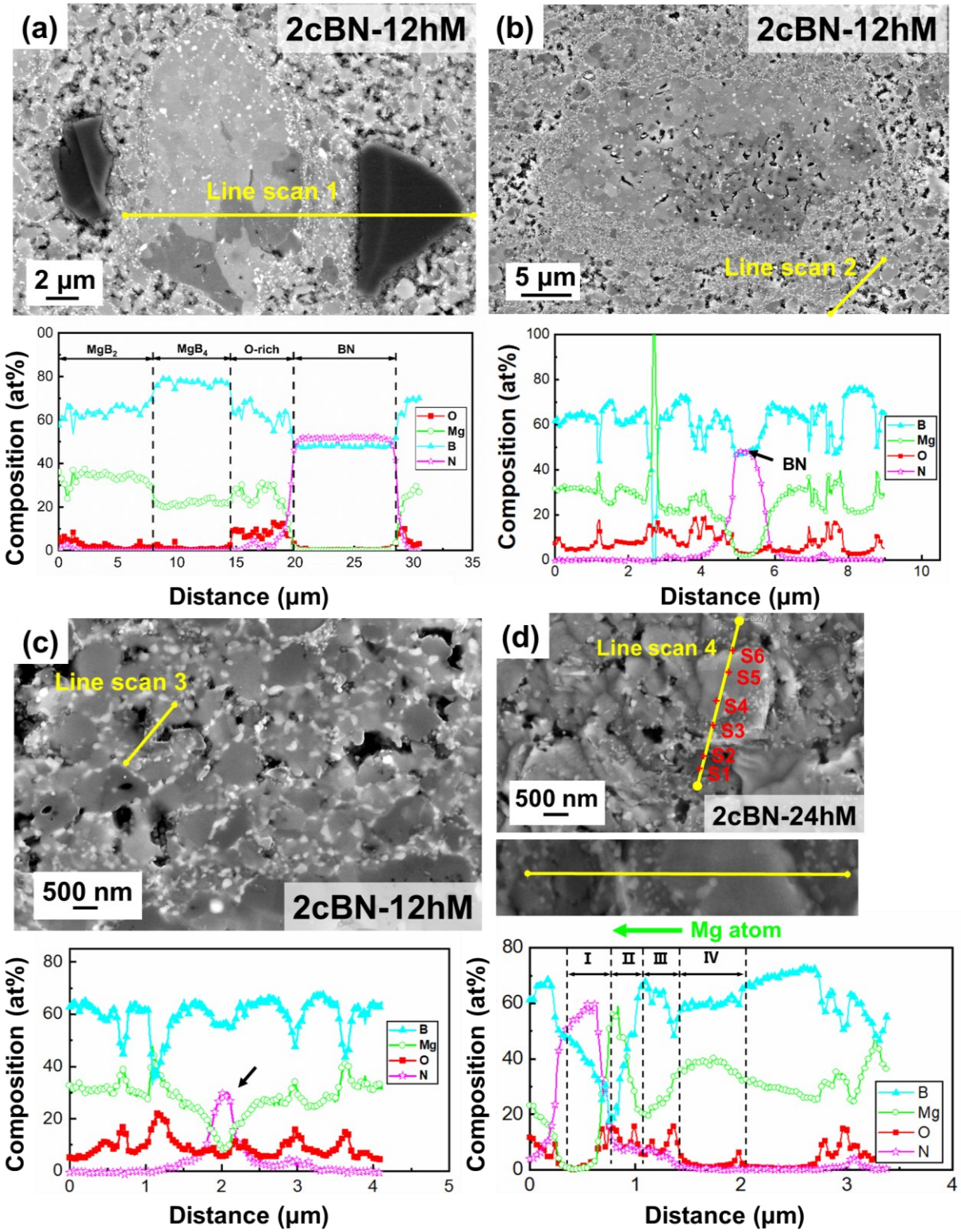


Figure 7.10 Chemical composition analysis of (a-c) 2cBN-12hM (bulk samples) showing the existence of N-containing phases and (d) 2cBN-24hM (thin foils) showing the reaction layers at the cBN/MgB_2 interface.

7.4.3 Characterisation of MgB_2 bulk samples with 5 wt% cBN addition

The characterisation of this sample set is divided into two sections: bulk samples and thin foils. The greatly-enhanced spatial resolution in the thin foils enables the chemical and phase analysis of tiny impurities grains by scanning TEM and TKD.

7.4.3.1 Phase and microstructural characterisation of bulk samples

XRD patterns of 5 wt% cBN added MgB_2 bulk samples with powder milled for various time and processed at different temperatures/times are shown in Figure 7.11a. The most significant feature of this sample set is the presence of $MgNB_9$ and Mg peaks, detected in the 5cBN-24hM and 5cBN-F30min samples. As Figure 7.11b shows, the MgB_4 peak intensity of bulk samples slightly decreases as the milling time rises from 6 h to 12 h, while a sudden drop occurs in the 5cBN-24hM sample along with the appearance of the small $MgNB_9$ peak at 32.6° and Mg peak at 36.6°. Fixing the milling time at 24 h and lowering the processing temperature to 1050 °C, the high intensity of MgB_4 peaks indicates it is the main impurity in this sample (Figure 7.11c). Prolonging the processing time from 5 min to 30 min, the $MgNB_9$ and Mg peaks are sharper and no MgB_4 peaks can be detected (Figure 7.9d). The MgB_2 (110) peak has been distorted heavily both in intensity and shape towards higher angles as highlighted in Figure 7.11d. Considering that there is no peak between 33° to 34° in the reference pattern of $MgNB_9$, the possible overlap of MgB_2 peaks and $MgNB_9$ peaks can be ruled out. If the peak distortion comes from the decomposition, the MgB_4 peaks should be obvious which is not the case in the

XRD patterns of the 5cBN-F30min sample. Also, one can observe that (110) peak changes in shape while (002) does not, as the green rings in Figure 7.11a highlight. I speculate that boron layers of remaining MgB_2 grains may be distorted by substitutional N atoms in this sample processed for 30 min.

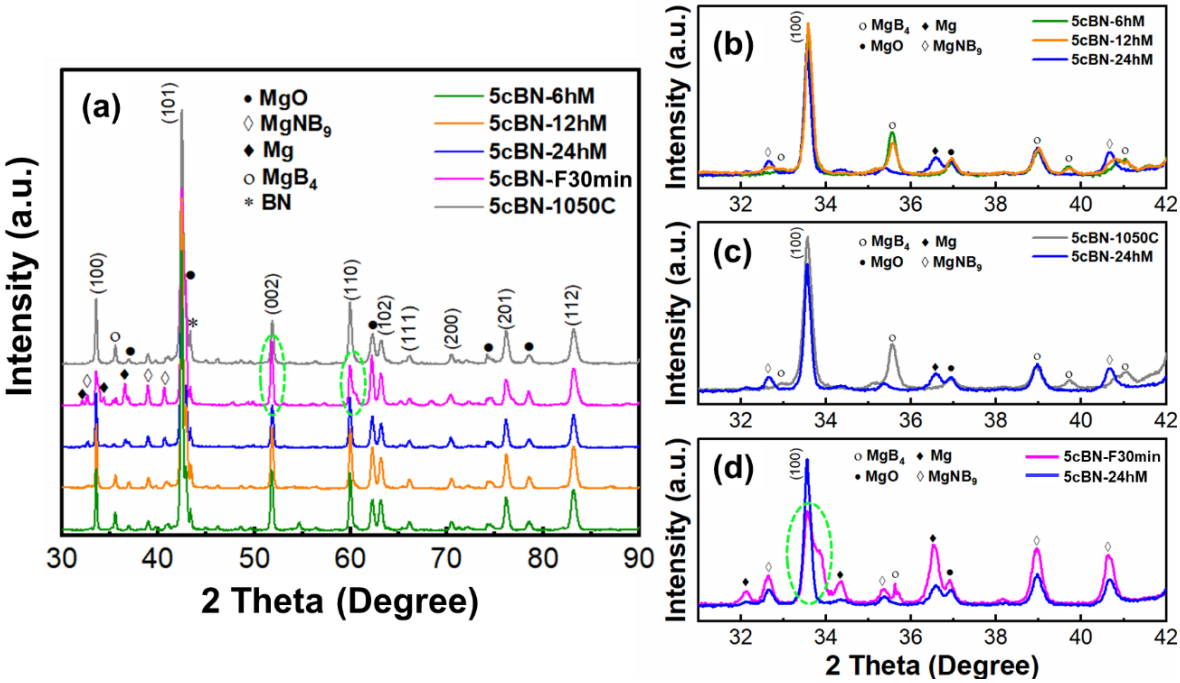


Figure 7.11 (a) XRD patterns of 5 wt% cBN added MgB_2 bulk samples with powder milled for various times and processed at different processing conditions. The processing temperature is 1200 ºC unless labelled and the processing time is 5 min unless labelled. (b-d) the phase evolution of MgB_4, $MgNB_9$ and Mg impurities under various processing conditions.

BSE images depict microstructural features of four selected 5 wt% cBN-added bulk samples in Figure 7.12. Similar to the 2cBN-6hM sample, 5cBN-6hM still has a high density and retains some large MgB_4 phases (Figure 7.8a and Figure 7.12a). The inhomogeneity of samples is reflected by Figure 7.12b and c, with distinct dense MgB_2 regions similar to the microstructures of 2cBN-24hM (Figure 7.8c). The contrast variation within dense regions and the porous matrix in Figure 7.12c requires further

analysis. Additionally, the number of dense MgB_2 regions in 5cBN-1050C is much lower than the other two samples processed at 1200 ºC (Figure 7.12d). Compared with a higher density of 2 wt% cBN added MgB_2 samples processed at 950 ºC (Figure 7.8d), it can be seen that excessive cBN addition prohibits sample densification.

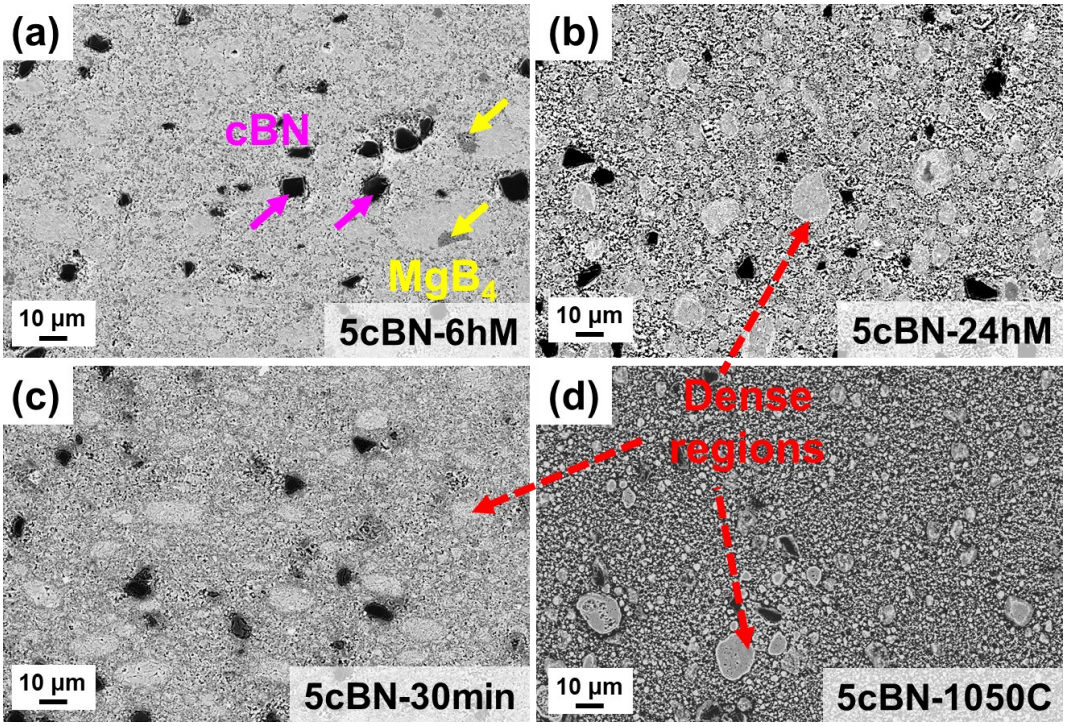


Figure 7.12 BSE micrographs of 5 wt% cBN added MgB_2 bulk sample with powder milled for (a) 6 h and (b) 24 h and then processed at 1200 ºC for 5 min. BSE images of 5 wt% cBN added MgB_2 bulk sample with powder milled for 24 h and then processed at (c) 1200 ºC for 30 min and (d) 1050 ºC for 5 min.

The morphologies of dense regions and the matrix are examined by micrographs taken at higher magnification (Figure 7.13). Figure 7.13a and b show grains in the dense regions are well-connected but a small number of pores exist in the matrix of the 5cBN-6hM. This reveals that a higher percentage of cBN is responsible for the high porosity in the matrix of samples made from powders milled for a shorter time. Figure 7.13c and d show that grain connectivity in the matrix is severely reduced, and grain contact in

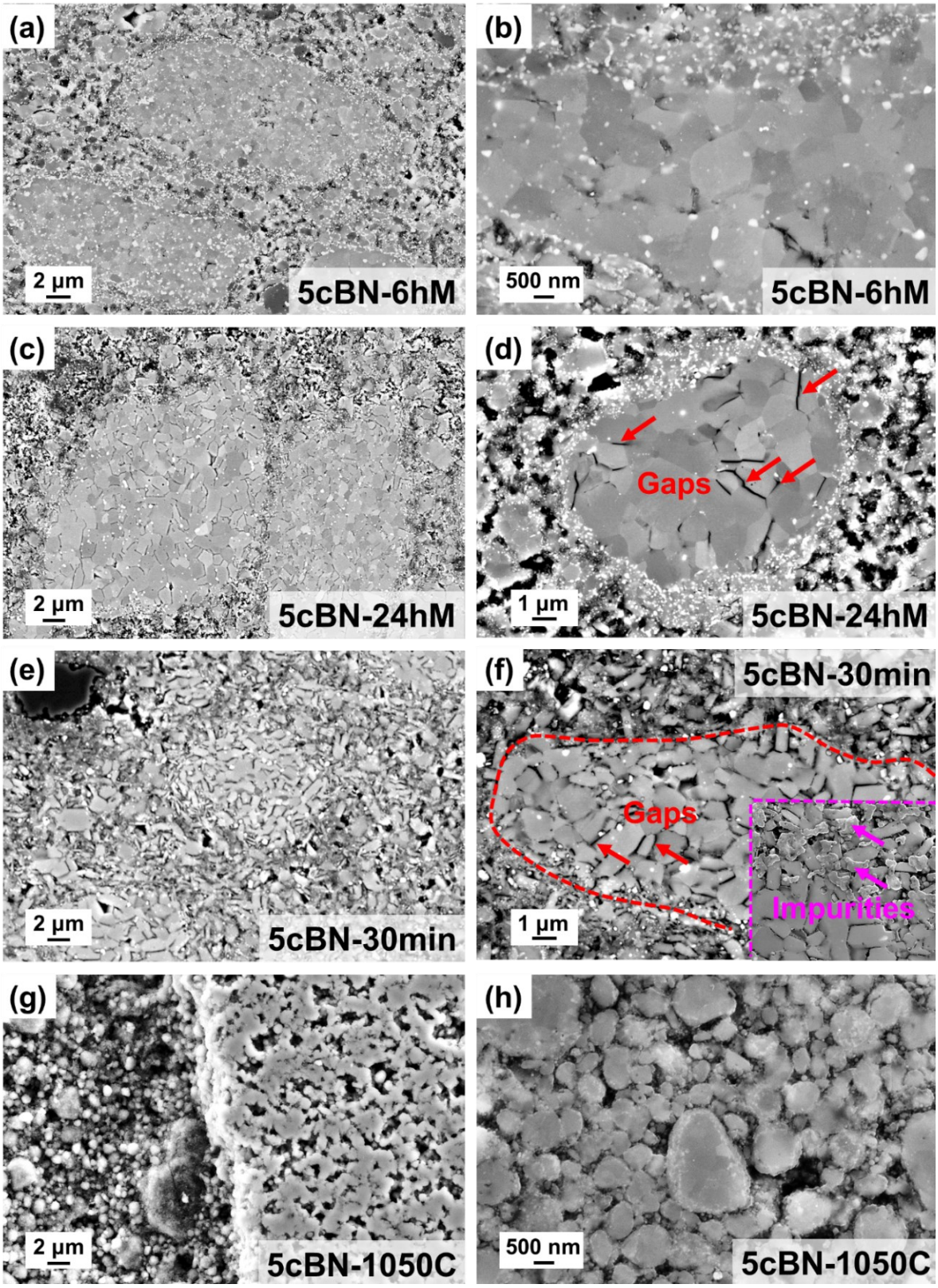


Figure 7.13 BSE images of dense regions and the matrix in (a)(b) 5cBN-6hM, (c)(d) 5cBN-24hM, (e)(f) 5cBN-30 min and (g)(h) 5cBN-1050C.

dense regions is partially influenced in 5 wt% cBN added MgB_2 bulk samples prepared from powders milled over 24 h. The impairment of connectivity in the matrix is attributed to the increasing number of pores, but the weakening of contact in dense regions is reflected by gaps between MgB_2 grains highlighted by arrows in Figure 7.13d. The prolongation of processing time to 30 min aggravates the deterioration (Figure 7.13e). The contrast difference between dense regions and the matrix is less apparent because of the increasing number of gaps that result in MgB_2 grains in dense regions almost being separated from each other (Figure 7.13f). The inset figure shows a surface-sensitive SEM image showing the impurities decorating grain boundaries which contribute to the contrast variation in BSE images. Figure 7.13g and h show the highly-porous nature of agglomerates and round particles retained in the sample due to incomplete densification at 1050 ^{o}C.

Figure 7.14 presents EDX results at the gaps between MgB_2 grains in dense regions observed in the microstructural analysis of the 5cBN-F30min sample. Arrows in the Mg element map highlight the Mg-rich gaps, the same with the rising composition of Mg in line scan results. Moreover, point analysis shows that Site 1 at the gap area consists of 57 at% B and 37 at% Mg and 6 at% O. Guillaume et al found the presence of residual Mg nanograins (<100 nm) at grain boundaries in their 10 wt% Mg-MgB_2 samples by STEM analysis, which is supposed to be left by the liquid phase formed in the sintering process [210]. By referring back to the Mg peaks in the XRD pattern, it is reasonable to speculate that these gaps may contain ultra-fine Mg-rich phases.

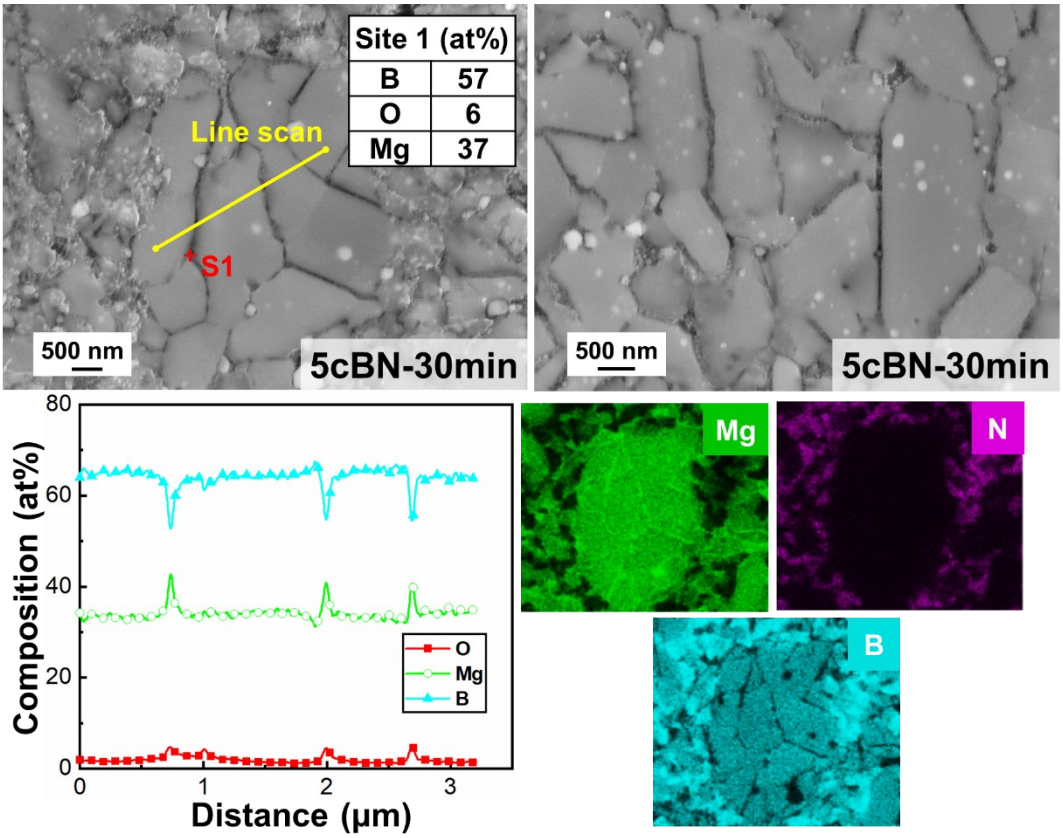


Figure 7.14 SEM images and EDX analysis of gaps between MgB_2 grains in dense regions of 5cBN-F30min with powder milled for 24 h and then processed at 1200 °C for 30 min.

7.4.3.2 Microstructural characterisation of thin foils

Figure 7.15 shows results on the electron-transparent thin foils of 5cBN-F30min and 5cBN-24hM. As presented in Figure 7.15a, darker grains dispersed in Region A between dense regions, and Region B (the matrix) can be distinguished by the different extents of porosity. Images taken at higher magnification show the details of Region A and B. Element maps reveal that scattered darker grains with sizes below 200 nm are rich in boron and nitrogen (Figure 7.15c). In Region B, N-containing impurities connect, grow along the MgB_2 grain boundaries and form a network surrounding MgB_2 area (Figure 7.15e). Element maps show that the boron and nitrogen-rich areas overlap,

indicating the disappearance of MgB_4. As for the 5cBN-24hM sample, Region A between dense MgB_2 regions presented in Figure 7.15d has a similar morphology as Region A in the 5cBN-F30min foil. However, the distribution of N-containing grains remains scattered in Region B (Figure 7.15f). Line scan analysis in Figure 7.15h indicates the concentration of N is lower in 5cBN-24hM processed for 5 min compared with 5cBN-F30min. Point analysis of selected sites is summarized in Table 7.4, from which one can confirm that the interior area of MgB_2 grains is free of N, such as S2 and Q1. The N, Mg and B concentration of Mg(N,B) impurities fluctuates at around 8 at%, 15 at% and 72 at% in 5cBN-F30min, in contrast to larger fluctuations in N content in 5cBN-24hM. This means N concentration will approach stability after a long time sintering process, revealing that the formation of Mg(N,B) phases is not simple precipitation in the liquid Mg environment.

Table 7.4 Chemical composition of different sites in the 5cBN-F30min and 5cBN-24hM samples by point analysis. The sites are labelled in Figure 7.14.

	S1	S2	S3	S4	S5	S6	S7	Q1	Q2	Q3	Q4	Q5	Q6
B (at%)	65	67	-	70	70	77	70	68	73	68	67	63	65
Mg (at%)	22	33	53	15	30	12	30	32	15	20	28	23	22
N (at%)	6	-	-	7	-	9	-	-	8	6	2	5	5
O (at%)	7	0	47	8	0	2	0	0	4	6	3	9	8

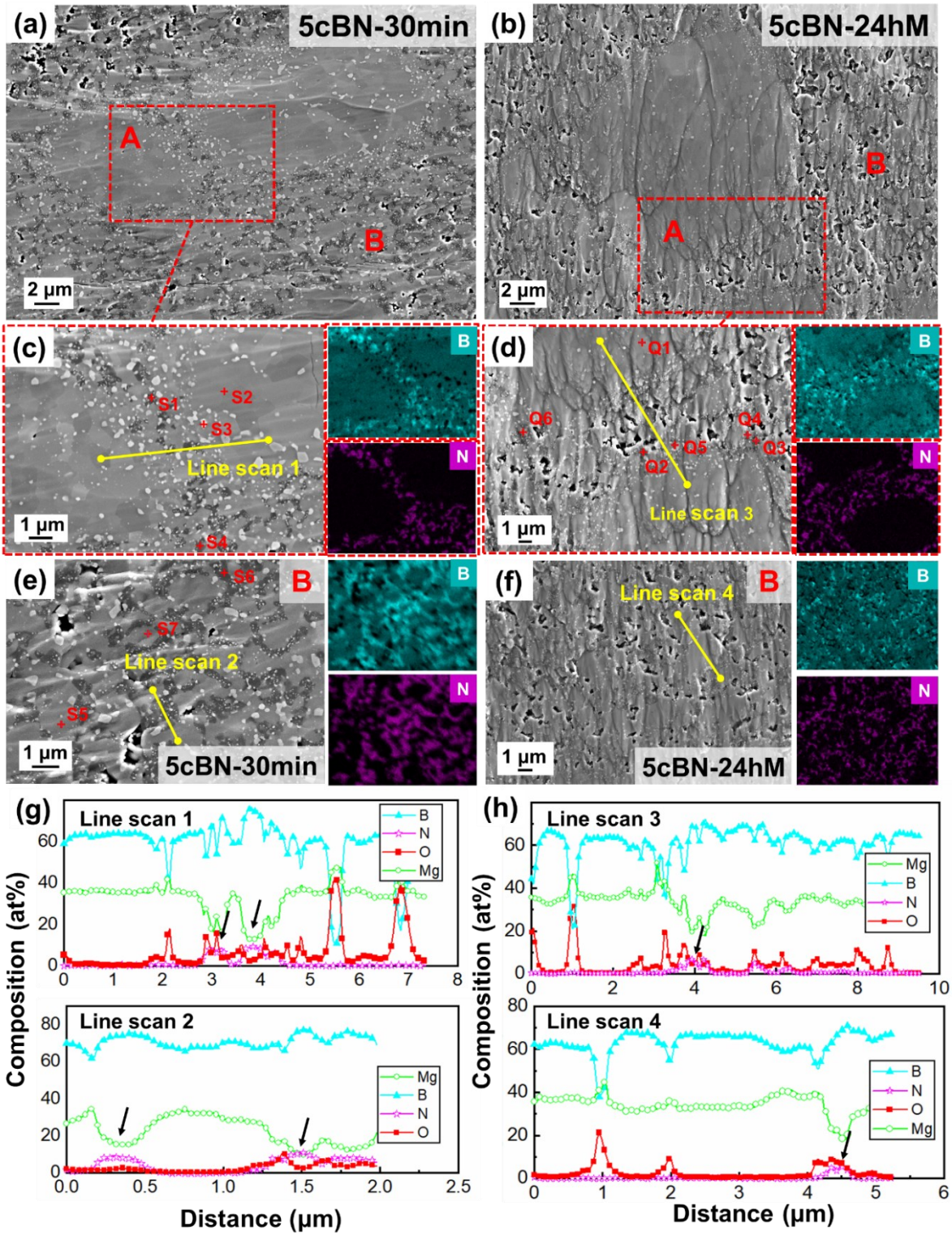


Figure 7.15 SEM images and EDX analysis of (a)(c)(e) 5cBN-F30min and (b)(d)(f) 5cBN-24hM. (g) and (h) show the corresponding line scan data. The only difference in the processing conditions of two samples is the sintering time (5 and 30 min).

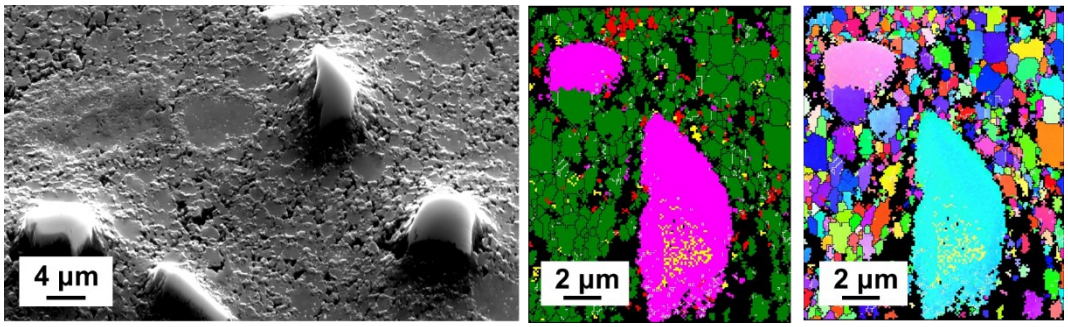


Figure 7.16 SEM image, phase map and IPFZ map taken by typical bulk EBSD. The colour key is the same as Figure 7.17.

Traditional EBSD results show the protrusions of hard cBN grains from the surface (Figure 7.16). Though small cBN single micro-crystals can be easily detected, it is difficult to investigate Mg(N,B) grains and the possible presence of cBN nanograins. Therefore, two image groups are captured in two sites of the 5cBN-F30min thin foils by TKD. No nanosized cBN grains can be found, and some small $MgNB_9$ grains can be indexed. As arrows and areas within the yellow dashed line show, the low pattern quality in these regions arises from porosity, ultra-fine grains and imperfect crystal structures of impurities. Additionally, some areas within MgB_2 grains also cannot be indexed because of the lattice distortion brought by the reaction with cBN (Figure 7.17e and f). Low angle grain boundaries in MgB_2 grains, Figure 7.17f, are ascribed to the plastic deformation created in the milling process.

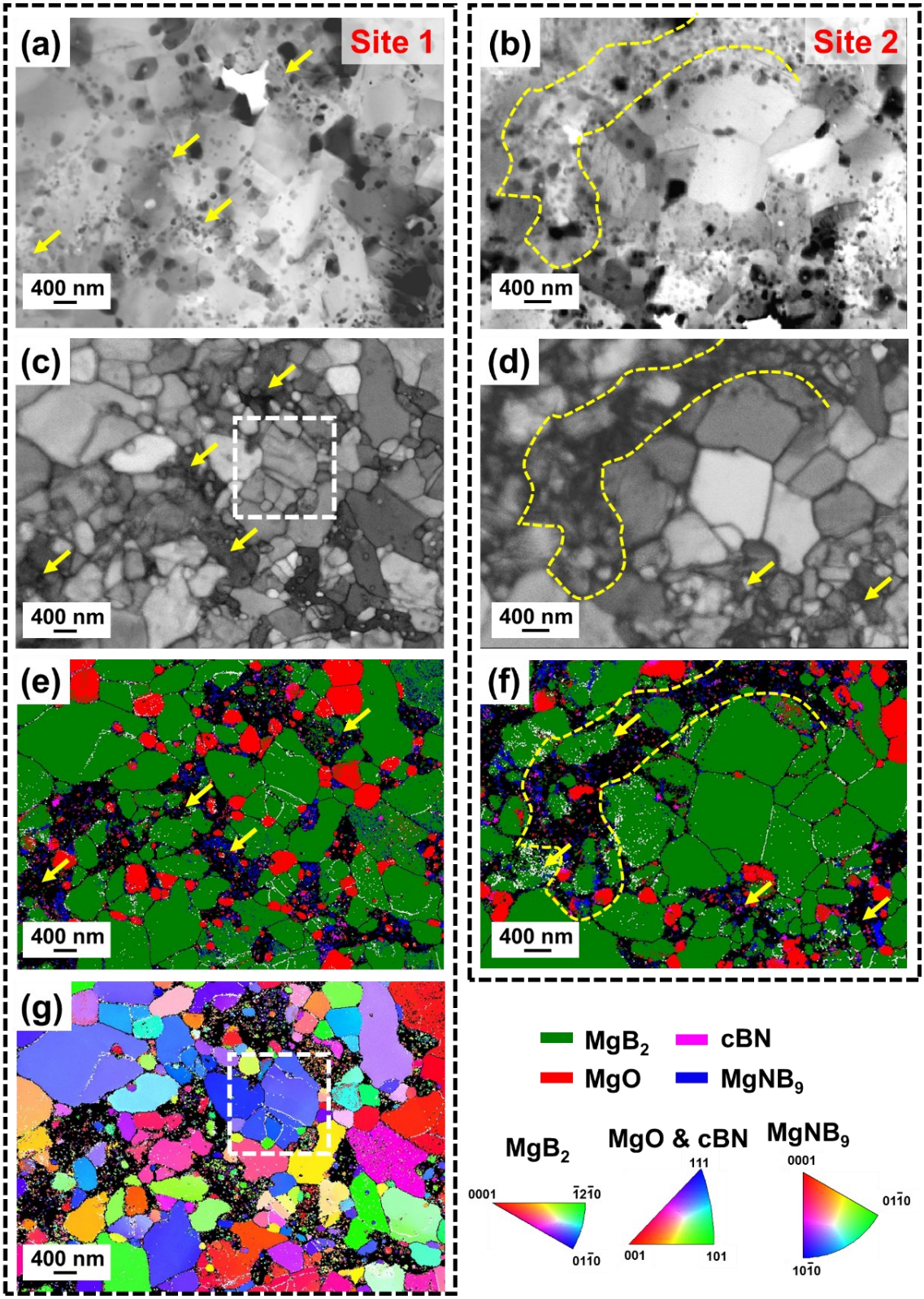


Figure 7.17 Two TKD image sets of two sites in TEM foils of 5cBN-F30min, showing (a)(b) bright-field, (c)(d) band contrast, (e)(f) phase maps and (g) IPFZ images.

7.5 The formation and growth mechanisms of $MgNB_9$ impurities

Although MgB_2 is a simple binary compound, its phase diagram is complicated because the intermediate phases of the Mg-B system depend on the reaction temperature, pressure, stoichiometric ratio and vapor pressure of Mg (Figure 7.18a). In the ex-situ method, MgB_2 begins to decompose at about 600 °C under atmospheric pressure. Due to the volatilization of Mg, the boron-rich phases will be left and form MgB_4, MgB_7 or even higher boron-rich phases under higher processing temperatures [219]. If N-containing compounds are added in MgB_2, the stable Mg-B-N ternary phase system needs to be considered [220].

Since long hours of milling (24 h) and a higher amount of cBN addition contribute to the increasing number of smaller cBN grains with highly active surfaces, the reaction of cBN and MgB_2 with the assistance of liquid Mg becomes obvious, which can explain the switch from MgB_4 to $MgNB_9$ as the main impurities in samples with 5 wt% cBN addition processed at 1200 °C for more than 5 min (Figure 7.18). Karpinski et al put Mg and B in the BN crucible before applying temperatures up to 2200 °C and pressure ranging in 10 ~ 30 kbar. Figure 7.18b, the P-T phase diagram, shows the intermediate nitride $MgNB_9$ is stable under lower pressures [220]. Similarly, Singah et al used $Mg_3B_2N_4$ as a catalyst-solvent to convert amorphous BN into cBN and found the dissociation of Mg and N to form MgB_x compounds at temperatures higher than 1300 °C and 40 kbar pressure [221]. Zhigadlo tried to grow hBN from Mg flakes, B and

amorphous BN powers and pointed out that the formation of $MgNB_9$ is from the ternary Mg-B-N solvent [222]. All these studies demonstrate that the eutectic liquid Mg-B-N forms in the reaction where $MgBN_9$ can be produced in low-pressure and low-temperature processing.

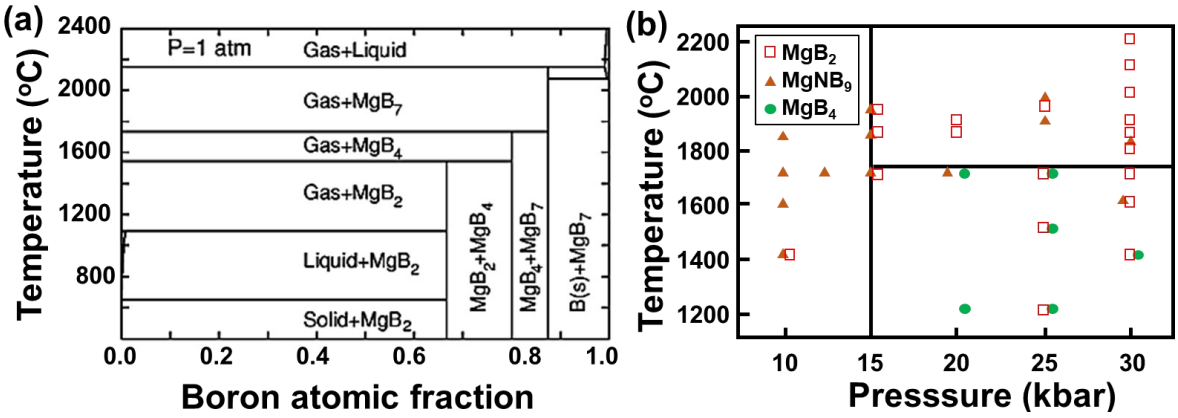


Figure 7.18 (a) The phase diagram of the binary Mg-B system under the pressure of 1 atm (Reproduced figure from [219] with permission from AIP Publishing). (b) P-T phase diagram of ternary Mg-B-N system (Reproduced figure from [220] with permission from Elsevier).

In my study, Layer II and Layer III in Figure 7.10d are from the Mg-B-N solvent, and the composition variation of the remaining cBN (Layer I) indicates the incomplete mass transport within 5 min. The network of $MgNB_9$ impurities in Figure 7.15e provides further evidence of the liquid formation, which results from the liquid flowing in the gaps between the remaining MgB_2 grains in the matrix [214, 220].

$$4MgB_2 + cBN \rightarrow 4Mg + 8B + cBN \rightarrow MgNB_9 + 3Mg\ (l,g)$$

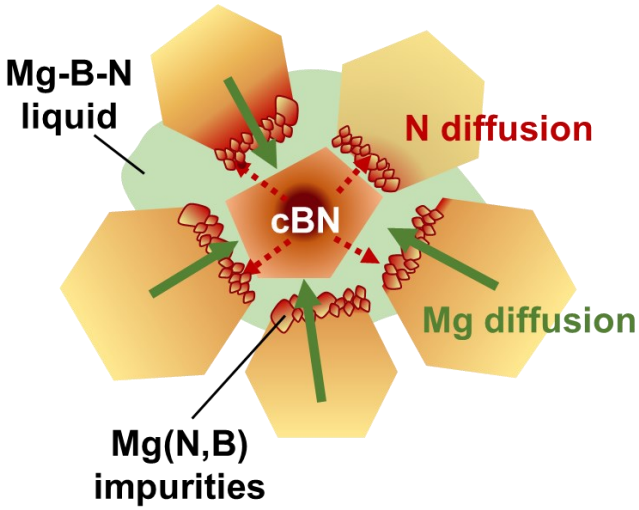


Figure 7.19 Schematic of the possible reaction between MgB_2 and cBN during high temperature sintering process.

7.6 Analysis of superconducting properties

The DC susceptibility of bulk samples as a function of temperature is shown in Figure 7.20. In the 0.5 wt% cBN doped MgB_2 sample series, T_c values of all samples with additions are about 1 K lower than that of pristine MgB_2. The T_c of 2BN-24hM is the lowest, reaching 37.2 K compared with 38.1 K and 37.8 K of 2BN-6hM and 2BN-12hM samples. As to the 5 wt% cBN doped MgB_2 sample set, 24 h of milling reduces the onset T_c from around 38.5 K to 37.8 K compared with 6h and 12 h of milling. The T_c curve of 5cBN-1050C shows double transition stages, and ΔT is much broader than that of samples sintered at 1200 °C because of high inhomogeneity. Increasing the processing time to 30 min leads to an additional decrease in T_c by 0.5 K compared with 5cBN-24hM, which can be explained by the lattice distortion of MgB_2 unit cells of 5cBN-30Fmin (Figure 7.11). The comparison of samples with different percentages of

cBN addition is shown in Figure 7.18d. The onset T_c values do not show much difference but 2cBN-12hM has the broadest ΔT. The reason is unclear but may relate to the higher amount of MgB_4 phases within MgB_2 dense regions, which exacerbates inhomogeneity (Figure 7.5a and Figure 7.8b).

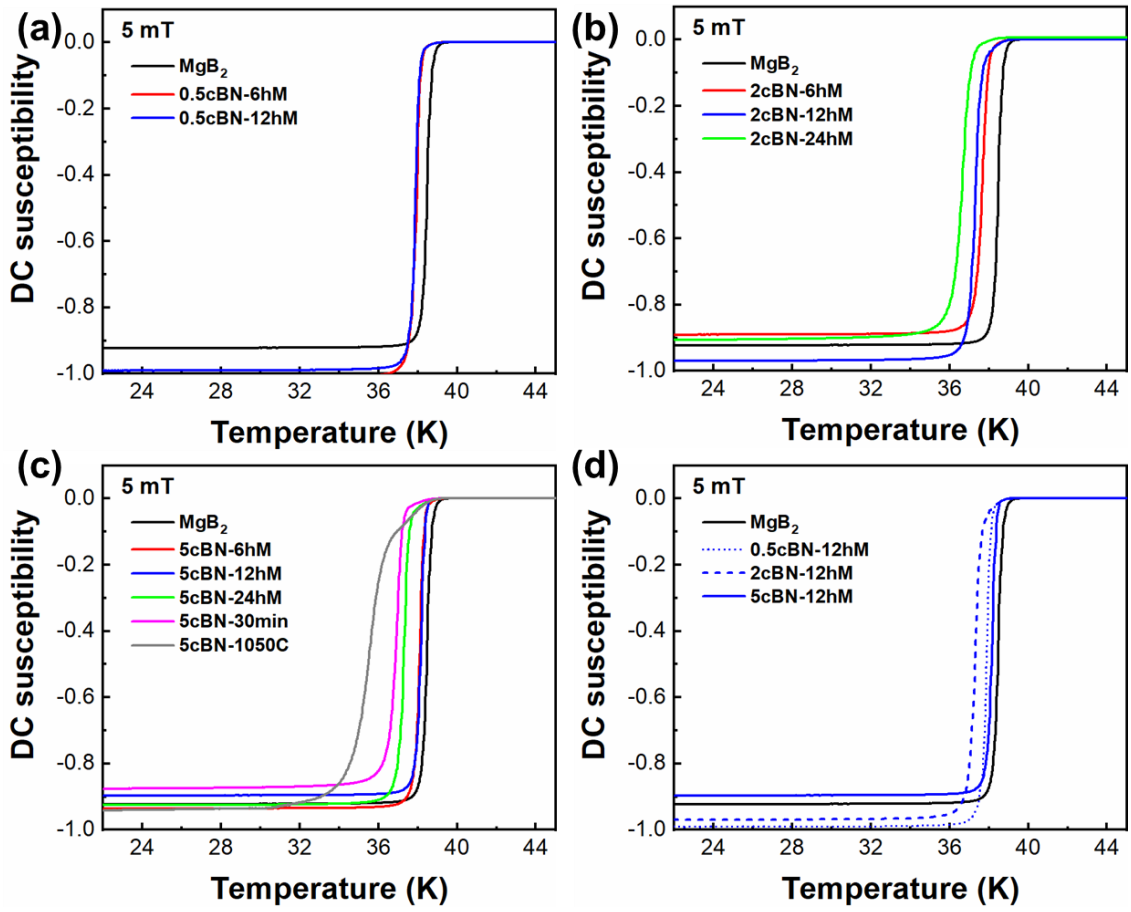


Figure 7.20 DC susceptibility under 5 mT as a function of temperature in (a) 0.5 wt% cBN, (b) 2 wt% cBN and (c) 5 wt% cBN added MgB_2 bulk sample series. (d) compares T_c of samples with different cBN percentages.

As Figure 7.21 shows, 0.5 wt% cBN added MgB_2 samples have dense microstructures so can be simulated by simple Cell model D or Type I microstructure model. Considering the distinction between the porous matrix and dense MgB_2 regions in 2cBN-24hM, I classify it as a Type II microstructure. Gap features appear in 5cBN-

24hM and 5cBN-F30min so they can be classified into the Type IV group.

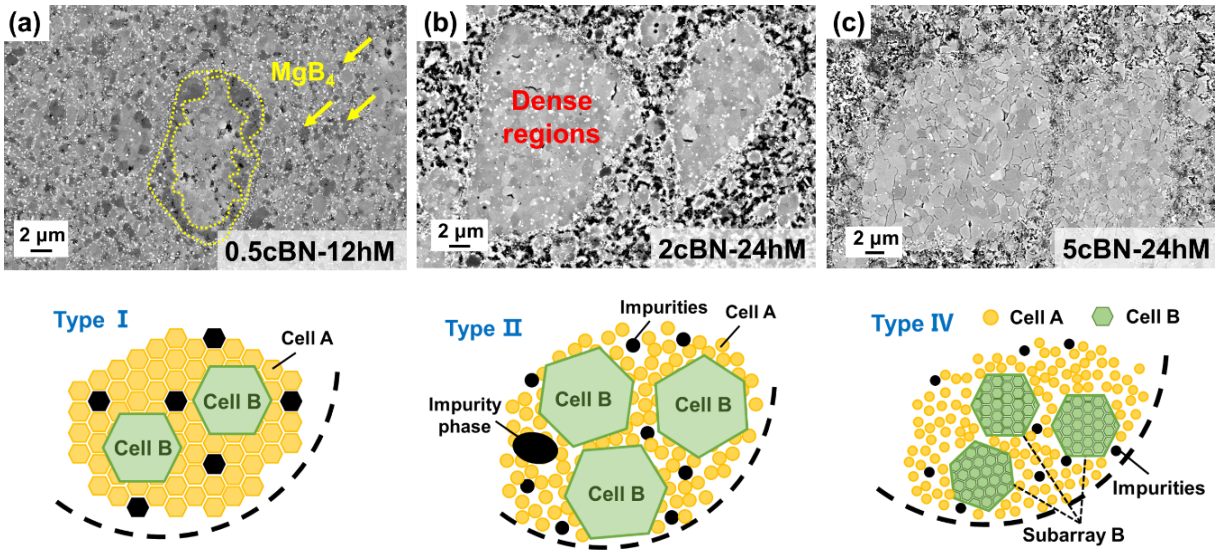


Figure 7.21 SEM micrographs of cBN added MgB_2 and the corresponding schematics (Chapter 4) to identify the currents flowing on different length scales.

$\Delta M(B_{app})$ curves of cBN added MgB_2 samples at 20 K are shown in Figure 7.22a-c. Samples with 0.5 wt% cBN addition show a small increase in the low and medium magnetic field range, and 0.5cBN-12hM outperforms 0.5cBN-6hM (Figure 7.22a). As presented in Figure 7.22b, the improvement of 2 wt% cBN added MgB_2 samples is limited. Even though the sample prepared from powders milled for 12 h has slightly better ΔM than that prepared from powders milled for 6h, the longest milling time (24 h) leads to deterioration of superconducting performance. This may be due to the surface contamination in the long milling process that can form MgO impurities to resist densification during the FAST process. Figure 7.22c shows that the differences in the $\Delta M(B_{app})$ performance of the 5 wt% cBN added MgB_2 samples are more varied. Samples prepared from powders milled within 12 h perform best, but milling powders for 24 h brings a significant decrease in ΔM values at high magnetic fields. The ΔM

performance of 5cBN-1050C at the low magnetic field regime is highly suppressed, but its high-field performance is comparable to pure MgB_2. Increasing the processing time to 30 min leads to an overall drop in ΔM values. The reason for ΔM deterioration with increasing milling time is similar to the 2 wt% cBN added sample series, but the obvious drop may come from the gaps in most dense regions in 5cBN-24hM which partially impair the connectivity of superconducting grains. High porosity leads to the poorest performance of 5cBN-1050C, but it outperforms 5cBN-24hM in the high magnetic field range, which may arise from better intrinsic properties such as smaller grains within dense regions that can control the ΔM curve tails. The overall suppressed performance of 5cBN-30Fmin arises from the $MgNB_9$ networks that nearly cut off macro current paths in the matrix, so currents can only circulate within cells with the size comparable to the size of a group of MgB_2 grains (Figure 7.15e and Figure 7.17). Besides, impaired grain connectivity in dense regions exaggerates the deterioration in this sample.

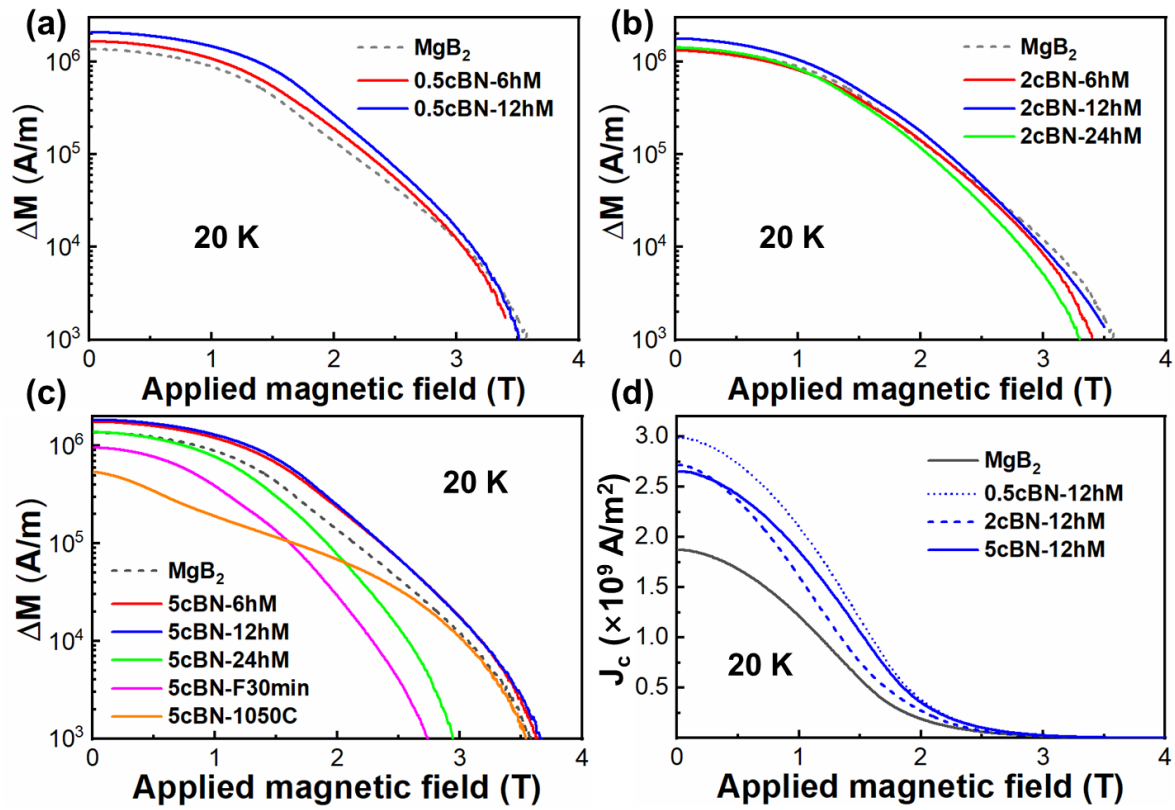


Figure 7.22 $\Delta M(B_{app})$ curves on the log-log scale of (a) 0.5 wt% cBN, (b) 2 wt% cBN and (c) 5 wt% cBN added MgB_2 sample series processed at 1050/1200 ºC for 5/30 min. (d) $J_c(B_{app})$ curves of MgB_2 samples added different percentages of cBN.

According to the classification of microstructures above, cBN added samples prepared from powders milled for 12 h were chosen to calculate macro J_c by Bean's critical model (Figure 7.22d). A critical reason for the best low-field performance of 0.5cBN-12hM is probably due to the higher effective cross-section for current flow because much fewer large cBN particles are present in samples (Figure 7.5a). In contrast, higher grain defects introduced in the milling process and a smaller number of large MgB_4 phases in 5cBN-12hM may lead to better performance in the medium-field range compared with 2cBN-12hM (Figure 7.12a vs. Figure 7.8b).

7.7 Conclusions

The brittle-brittle milling system (cBN and MgB_2) and the role of hard cBN particles on MgB_2 microstructures and superconducting performance were systematically studied in the present work. The following conclusions can be drawn:

i. Ball milling results of the brittle-brittle system depend on relative sizes of original particles and their difference in brittleness. Since cBN has much larger particle sizes than MgB_2 grains, it can assist the crystallite refinement and size reduction of MgB_2 agglomerates. Even though both processes will reach saturation after 24 h of milling, their efficiencies at the early stage of milling are different. The faster decrease in brittle particle size correlates to fracture due to the impact introduced by milling balls while the refinement of crystallite originates from the creation of dislocations brought by severe plastic deformation.

ii. The superconducting performance of cBN added MgB_2 samples can be enhanced in samples prepared from powders milled lower than 12 h. The long milling process promotes the formation of duplex microstructures. The porous matrix occurs in samples prepared from powders milled for 24 h, which influences the contribution of macro currents to the total ΔM.

iii. The prolongation of milling time combined with higher cBN addition can lead to the formation of N-containing impurities in samples processed at 1200 ^{o}C,

and the dominant impurity will change from MgB_4 to Mg(N,B) impurities. The stoichiometry of Mg(N,B) phases is closely related to the amount of liquid phase generated during the sintering process. With a long processing time, $MgNB_9$ can exist stably and be detected in XRD and TKD. $MgNB_9$ network as a consequence of excess Mg-N-B ternary solvent produced in the FAST process can cut the macroscopic current paths and therefore lower the overall $\Delta M(B_{app})$ curves significantly.

Chapter 8 Microstructures and superconducting properties of hexagonal BN added MgB_2 bulk samples

8.1 Introduction

Chapter 7 discussed the effects of adding hard cBN particles on MgB_2 powder and bulk samples, which inspired me to consider its much softer allotrope in the hexagonal form, hBN. The comparison of these two different forms of BN is shown in Table 8.1. Some reports have demonstrated that thin layers like hBN and graphene can be generated by mechanical exfoliation, and ball milling is one of the effective methods for preparing nanosheets, owing to the strong shear forces and high-energy collisions in the process [223-225]. It is supposed that these nanosheets could potentially lead to improvements in flux pinning and hence the intrinsic J_c of the material [226].

Table 8.1 Structural and physical properties of cubic BN and hexagonal BN [227] (Copyright © (2017) by John Wiley & Sons, Inc. Used with permission).

	Space group	Lattice parameter (Å)	Density (g/cm^3)	Hardness (Mohs scale)	Bulk modulus (GPa)
cBN	cubic, $F\bar{4}3m$	a = 3.6169	3.5	9.5	369 ~ 400
hBN	hexagonal, $P6_3/mmc$	a = 2.5043 b = 6.6562	2.2	1.5	36.5

In this chapter, hBN nanoparticles are chosen as additives in MgB_2. For comparison, graphene with a similar hexagonal lattice structure is also investigated. The role of hBN/graphene additions on the microstructural evolution and superconducting performance has been studied. These results provide a guide for choosing impurity

additions and improving our understanding of how superconducting properties will be influenced by changes in microstructure. The graphene nanosheets used in this study were kindly provided by Kailing Huang.

8.2 Experimental methods

Commercially available MgB_2 powder (purity: 99%, Alfa Aesar) and hexagonal BN nanoparticles (average particle size <150 nm, Sigma-Aldrich) were used to prepare MgB_2 bulk samples by an ex-situ method. x wt% hBN (x = 0.5, 1, 2) were first mixed with MgB_2 powder manually in the glove box under an Ar atmosphere. The ball milling process was carried out using the methodology explained in Chapter 3. About 0.5 g powder was taken out after 6 h and 12 h of milling for phase analysis and microstructural characterisation. MgB_2 powders with the addition of 0.5 wt% graphene sheets for comparison were ball-milled for 12 h. All mixtures were sintered for 5 min in the FAST apparatus, and the applied axial pressure was gradually increased to 50 MPa as the temperature approached 1200 °C.

Table 8.2 Processing conditions applied in high-energy ball milling and field-assisted sintering process

Sample	hBN/graphene addition (wt%)	Milling time (h)	Sintering temperature (°C)	Sintering time (min)
0.5graphene-12hM	0.5	12	1200	5
0.5hBN-6hM	0.5	6	1200	5
0.5hBN-12hM	0.5	12	1200	5
1hBN-6hM	1	6	1200	5
1hBN-12hM	1	12	1200	5
2hBN-6hM	2	6	1200	5
2hBN-12hM	2	12	1200	5

8.3 Investigation on phase evolution and morphologies of milled powders

XRD patterns of hBN doped MgB_2 powders milled for 6 h and 12 h are shown in Figure 8.1. Unlike 2 wt% cBN+MgB_2 mixtures, no hBN peaks can be observed, and the addition of hBN/graphene does not influence the amount of MgB_4 and MgO phase present in the sample. Figure 8.1c shows the comparison of (002) and (110) peaks of MgB_2 powder added hBN, cBN or graphene. After 6 h of milling, both peaks show a decreasing intensity with higher percentages of hBN addition. cBN is more effective than hBN in assisting crystallite refinement indicated by peak broadening. As the milling time is prolonged to 12 h, there is little difference in the (002) and (110) peaks of <1 wt% hBN added MgB_2 powders, and the intensity of both peaks are higher than 2 wt% cBN added counterparts. Surprisingly, the 0.5 wt% graphene and 2 wt% hBN added MgB_2 powders have higher peak intensity than others. There is a study showing doping graphite (2 wt%) can lubricate the contact between powders themselves as well as between powder and milling balls so slow down the crystallite refinement of ZrB_2 [228]. Previous literature has demonstrated that graphene or graphene oxide nanolayers in MgB_2 can improve the connectivity of MgB_2 grains [226, 229]. Moreover, hBN and graphene with sheet structures can be applied as solid lubricants to reduce friction [230], but more than 10 h milling time is required to exfoliate thin BN layers [223]. Considering that the hBN nano precursors used here are in the form of particles before

ball milling, unlike the graphene nanosheets used in 0.5graphene-12hM, adequate hBN addition (2 wt%) and enough milling time (12 h) are required to generate hBN thin layers mixed with MgB_2 powders. Therefore, it is speculated that these 2D sheets covering MgB_2 particles may assist to reduce the impact energy by sliding powder particles, so plastic deformation and the crystallite refinement of MgB_2 grains can be weakened (Figure 8.1b).

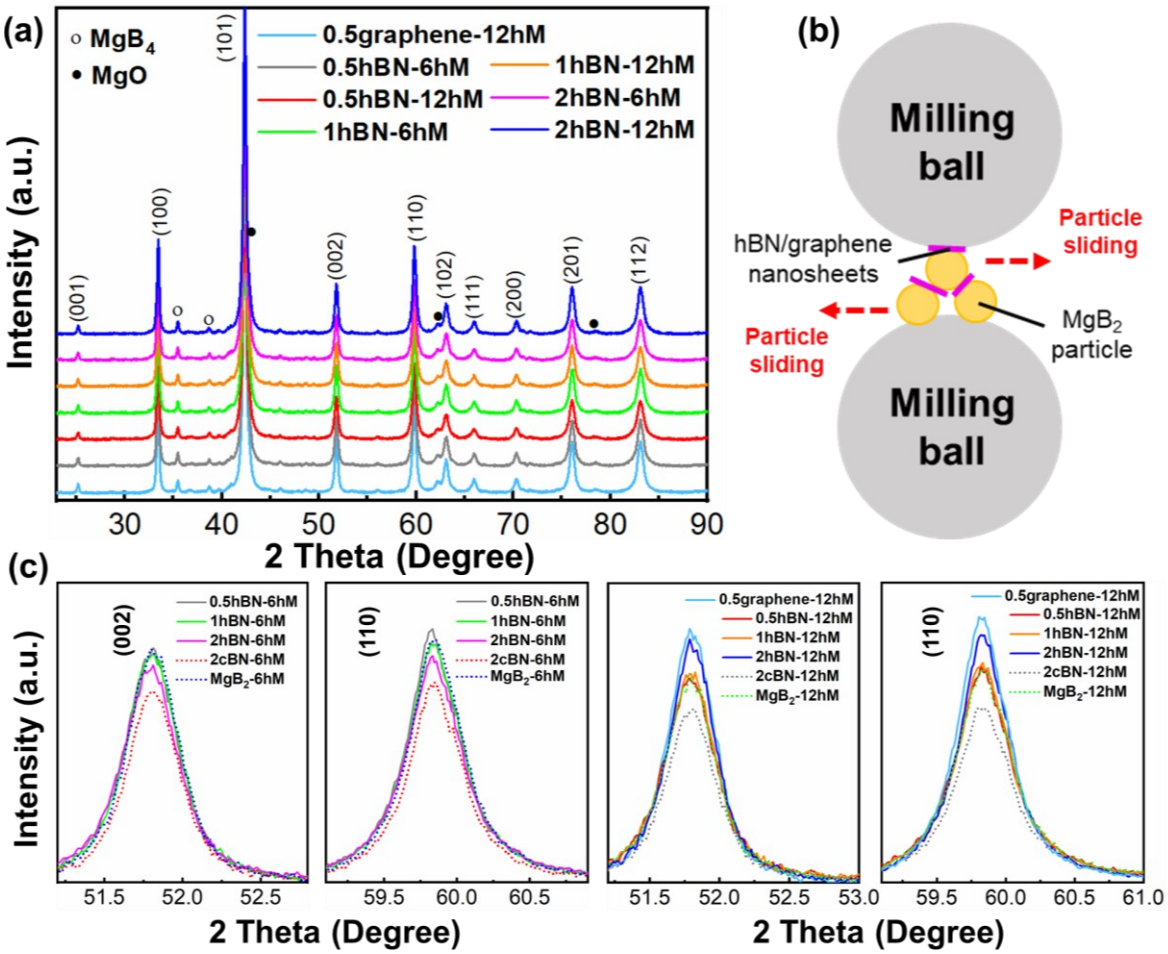


Figure 8.1 (a) XRD scans of x wt% hBN+MgB_2 (x = 0.5, 1 and 2) powder milled for 6 and 12 h and 0.5 wt% graphene+MgB_2 powders milled for 12 h. (b) schematic diagram showing the role of hBN/graphene layers on MgB_2 powders during the ball milling process. (c) compares the (002) and (110) peaks of undoped MgB_2 and MgB_2 powders with hBN, graphene and cBN addition.

Figure 8.2 shows BSE images of 0.5 wt% hBN and 2 wt% cBN doped powder particles

after 12 h of milling, and the contrast variation within particles reflects the porosity instead of impurities. Milled powders with cBN addition have more small dense particles than those with hBN addition, indicating the addition of cBN is beneficial to particle size reduction, apart from crystallite refinement shown in XRD results above. The influence of hBN nanoparticles on the behaviour of the mixtures after milling will be discussed in Section 8.6.

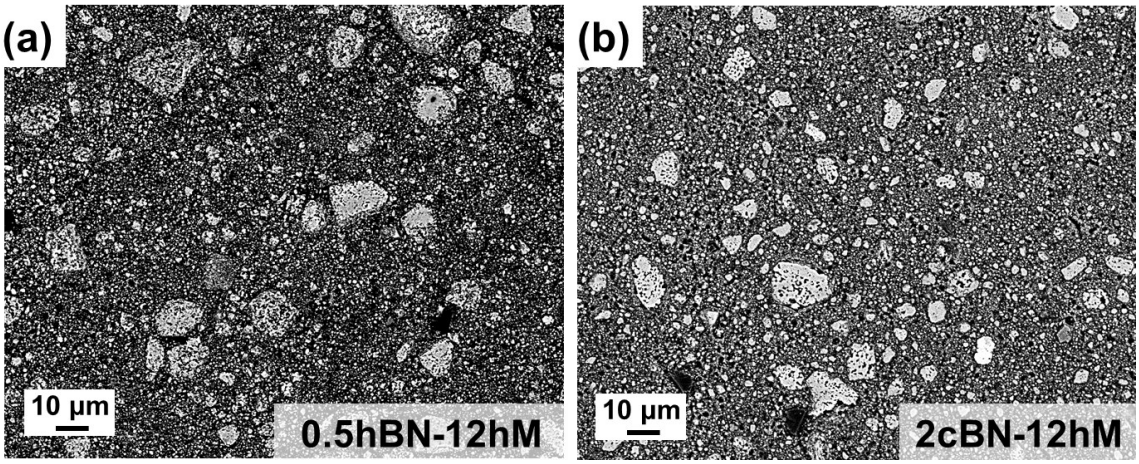


Figure 8.2 BSE images of (a) 0.5 wt% hBN and (b) 2 wt% cBN added MgB_2 powders after 12 h of milling.

8.4 Investigation on phase evolution, morphology and chemical composition of hBN added bulk samples

Figure 8.3 shows XRD patterns of MgB_2 bulk samples with hBN/graphene addition processed at 1200 °C for 5 min. The significant increase in MgO peak intensity at $2\theta = 62^{o}$ compared with the XRD scans of the milled powders indicates oxidation during sintering, as shown in Figure 8.3a. There is also a transformation in the impurity phase from MgB_4 to $MgNB_9$ + Mg with the addition of hBN nanoparticles, but the standards

of distinguishing the dominant impurity become necessary in this chapter but can also be supplementary to the phase analysis in Chapter 7. Since the complicated crystal structure of B-rich compounds makes it difficult to distinguish peaks of different impurities, the three strongest peaks of MgB_4, $MgNB_9$ and Mg phases selected from the standard PDF cards are listed in Table 8.3. As the table shows, the second strongest peak of MgB_4 and the strongest peak of $MgNB_9$ overlap at around 38.8°, while the third strongest peak of MgB_4 and the second strongest peak of $MgNB_9$ overlap between 40.6° and 41°. Therefore, critical factors to tell these two phases apart are the appearance of the strongest peak of MgB_4 at 35.4° and the relative intensity of peaks located at 38.8° and 40.6°. i.e., comparable high intensities of peaks at 38.8° and 40.6° indicate the dominance of $MgNB_9$.

Table 8.3 The crystallographic parameters and three strongest peaks of MgB_2 and $MgNB_9$ from the standard PDF cards in the ICSD database: MgB_4 PDF 00-015-0299; Mg PDF 01-089-4894; $MgNB_9$ PDF 96-201-2797. The percentages in parentheses refer to the relative peak intensities.

Compound	Structure	Space group	Lattice parameters (Å)	Peak location 2θ (°)		
				1st	2nd	3rd
MgB_4	orthorhombic	Pnma	a = 5.464 b = 7.472 c = 4.428	35.4 (100%)	38.8 (42%)	41.0 (26%)
$MgNB_9$	trigonal	$R\bar{3}m$	a = 5.496 b = 20.087	38.8 (100%)	40.6 (75%)	32.5 (58%)
Mg	hexagonal	$P6_3/mmc$	a = 3.209 b = 5.210	36.6 (100%)	34.4 (27%)	32.2 (25%)

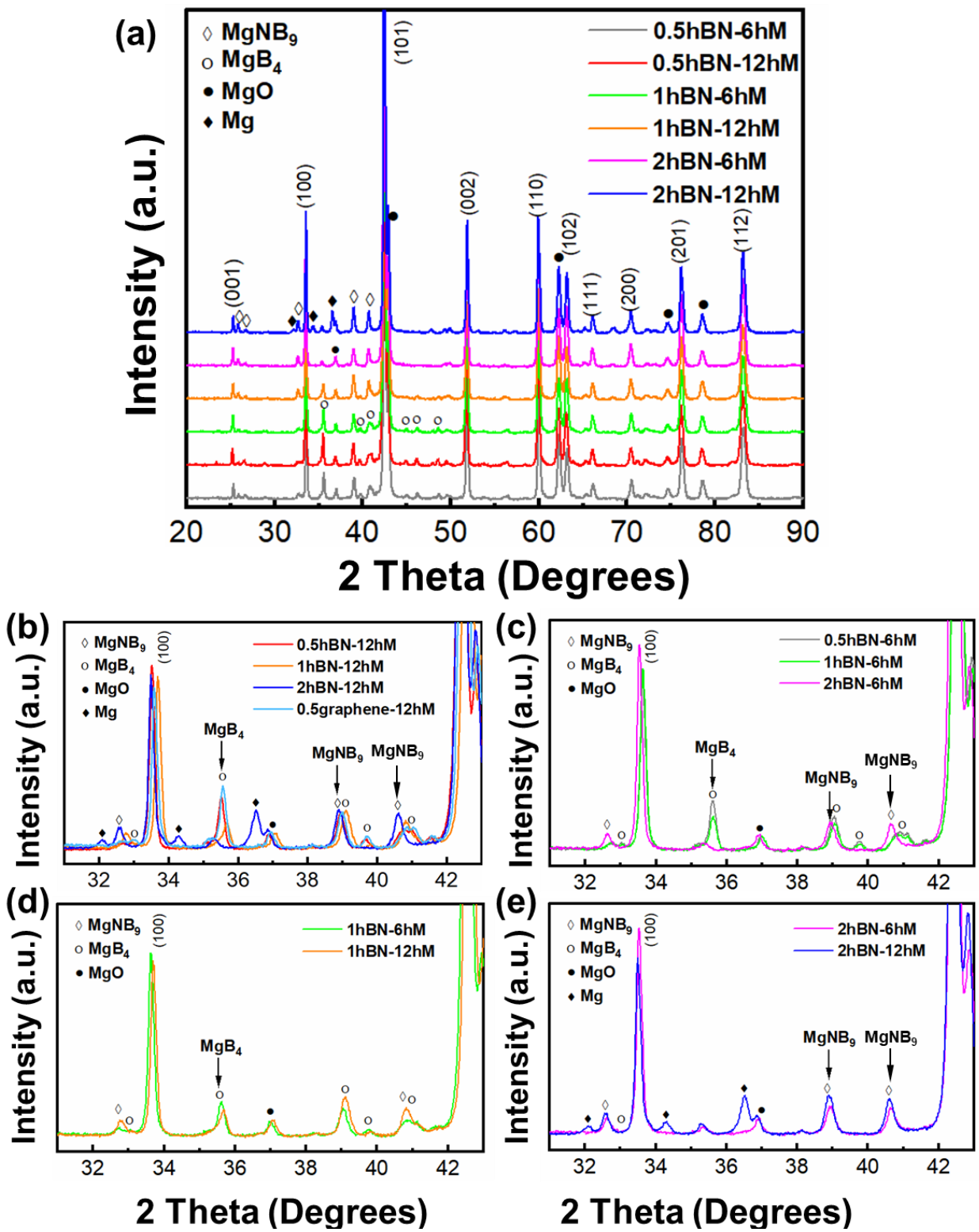


Figure 8.3 (a) XRD patterns of x wt% hBN + MgB_2 (x = 0.5, 1 and 2) and 0.5graphene-12hM bulk samples with powder milled for 6 or 12 h and processed at 1200 °C for 5 min. (b-e) show the dominant impurity in different samples.

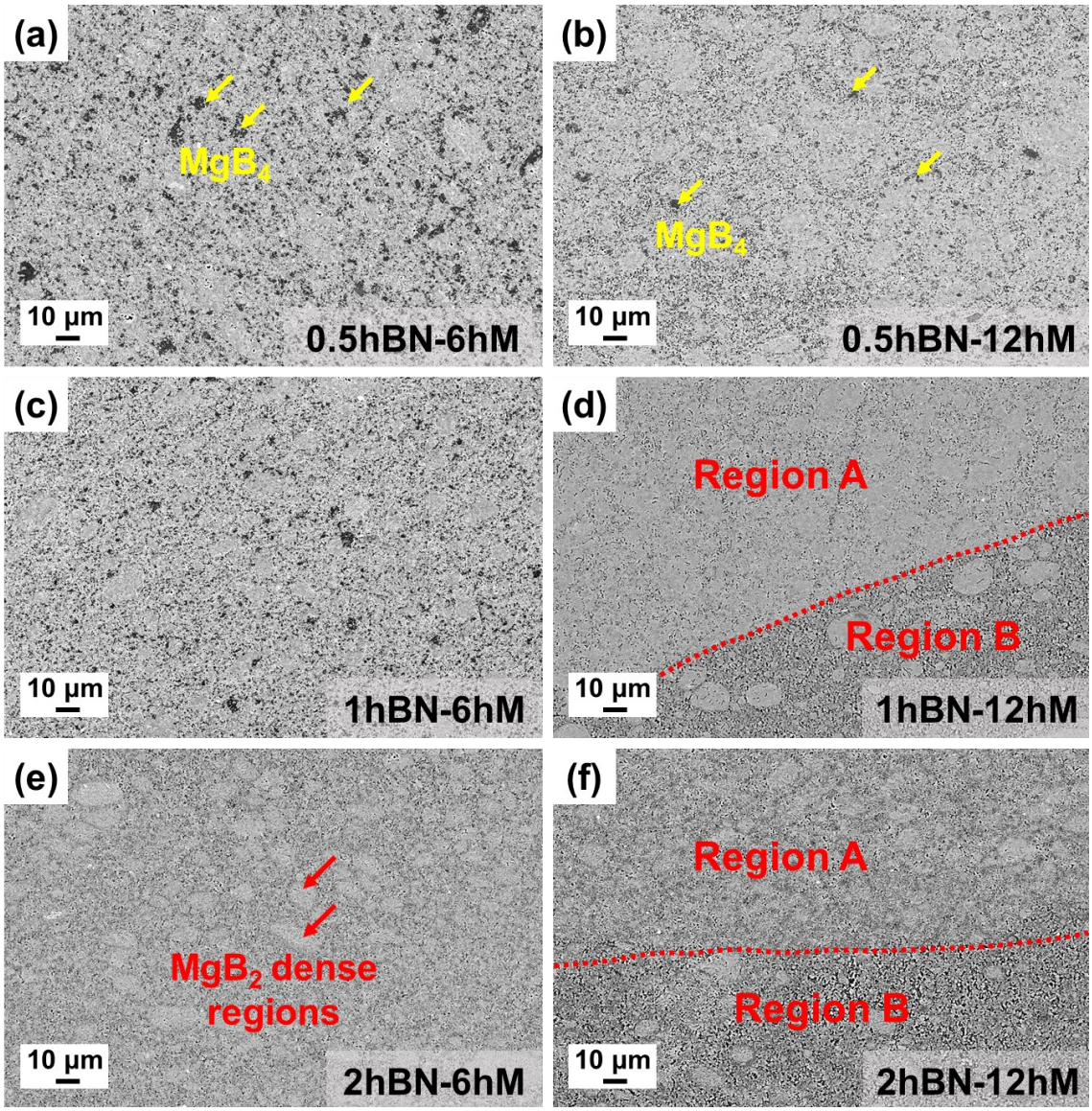


Figure 8.4 BSE micrographs of x wt% hBN added MgB_2 samples (x = 0.5, 1 and 2) produced from mixtures milled for 6 h and 12 h.

Figure 8.4 shows the morphologies of hBN added MgB_2 bulk samples processed at 1200 °C for 5 min. The 0.5hBN-6hM sample features small MgB_4 phases distributed homogeneously as shown in Figure 8.4a. With increasing the hBN percentage to 2 wt%, the contrast difference between dense regions and the matrix becomes distinct, indicating the increasing porosity of the matrix in bulk samples (Figure 8.4c and e). Microstructural evolution under a longer milling time (12 h) shows a similar trend. But

two regions showing quite different morphologies and distinct interfaces, labelled A and B in Figure 8.4d and f, form in the 1hBN-12hM and 2hBN-12hM samples. Region A consists of a higher number of dense regions (aggregates formed after milling) and extends over distances of several millimeters. This unique morphology has not been observed in pure and cBN added samples milled for the same time, and its formation mechanism will be discussed in Section 8.6 .

8.4.1 Characterisation of bulk samples with 0.5 wt% hBN addition

Detailed investigation of dense regions and the matrix of 0.5 wt% hBN/graphene added MgB_2 samples processed at 1200 ºC for 5 min is shown in Figure 8.5. The 0.5hBN-6hM sample contains dense structures with MgB_4 grains dispersed in the matrix (Figure 8.5a and b). 12 h of milling leads to the distinct dense regions with the narrow intermediate zone free of pores between them as shown in Figure 8.5c. However, Figure 8.5d reveals a slightly higher porosity in most regions of the matrix, partially impairing the grain connectivity. Similarly, with 0.5 wt% graphene addition, clear interfaces between dense regions and the matrix can be observed (Figure 8.5e). Pores in dense regions are also highlighted in Figure 8.5f.

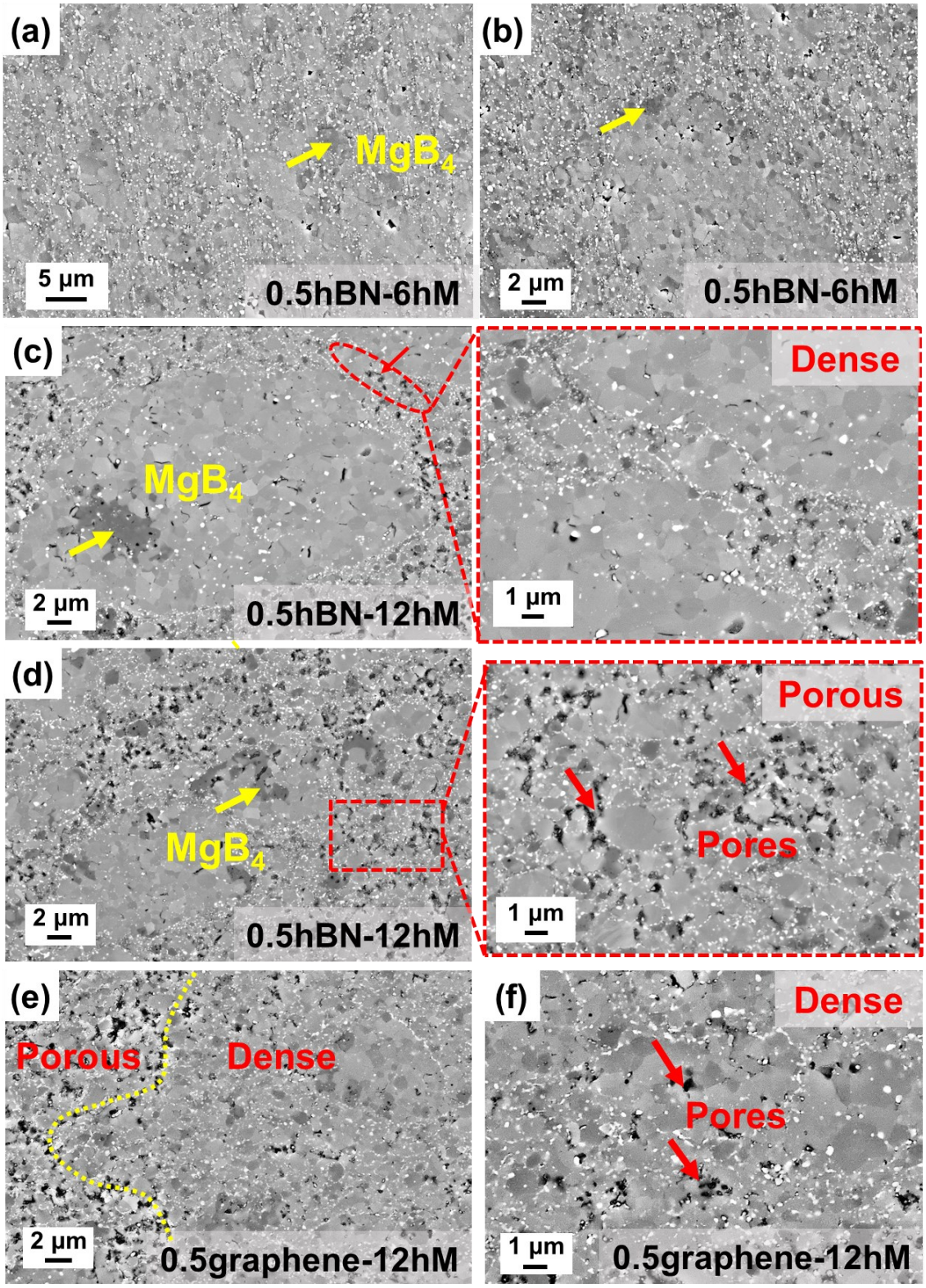


Figure 8.5 BSE images of 0.5 wt% hBN added MgB_2 bulk samples produced by powders milled for (a)(b) 6 h and (c)(d) 12 h. (e)(f) 0.5 wt% graphene added MgB_2 samples produced by powders milled for 12 h and processed at 1200 °C for 5 min.

EDX analysis was carried out to explore the reasons for pore formation and contrast variations in the matrix, and the results are presented in Figure 8.6. The N element map of 0.5hBN-6hM shows weak signals in contrast to the B element map that reveals the B-rich area (Figure 8.6a) is N-free. The MgB_4 and possible Mg(N,B) impurities are labelled in the composition plots. From the distances over which the N composition varies, one can see that the N-containing impurities are much smaller than MgB_4 grains, so the darker contrast in this sample mainly comes from MgB_4. Composition results from sites in Figure 8.6b are summarised in Table 8.4, where S1 and S2 are MgB_4 grains and S3-S5 are identified as Mg(N,B) phases, and they are all located at the MgB_2/MgB_2 grain boundaries. The problems with EDX quantification of light elements have been discussed in Chapter 3. The precise detection of N in the 0.5 wt% hBN sample is difficult due to the low N content and the small size of the N-containing additions.

Table 8.4 Chemical composition analysis of 0.5hBN-6hM. The corresponding sites are labelled in Figure 8.5b.

Element	S1	S2	S3	S4	S5
B (at%)	75	74	74	75	65
Mg (at%)	24	24	16	17	26
O (at%)	1	2	1	5	5
N (at%)	-	-	7	3	4

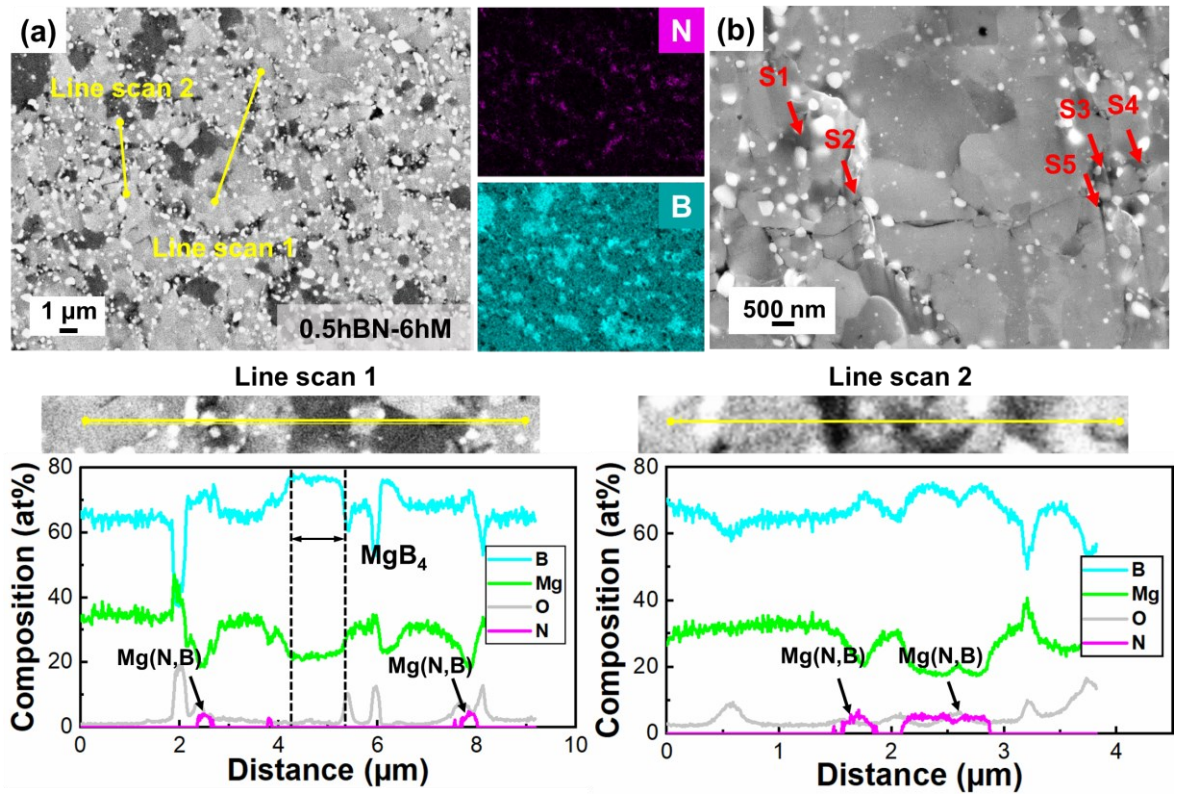


Figure 8.6 BSE images and EDX analysis of 0.5hBN-6hM. (a) shows the line scan analysis across MgB_4 and Mg(N,B) impurities.

8.4.2 Characterisation of bulk samples with 1 wt% hBN addition

Morphologies of dense regions and the matrix in 1 wt% hBN added MgB_2 samples with precursors milled for 6 h and 12 h are shown in Figure 8.7. In 1hBN-6hM, pores with sizes smaller than MgB_2 grains in the matrix partially impair grain connectivity, but dense regions and the matrix show good connectivity without too many pores or impurity particles decorating the interface (Figure 8.7a and b). In contrast, a large number of pores can be observed in both samples with powder milled for 12 h. For Region A, pores are distributed between dense regions (Figure 8.7c) while Region B possesses a few small dense agglomerates in a poorly connected matrix (Figure 8.7d).

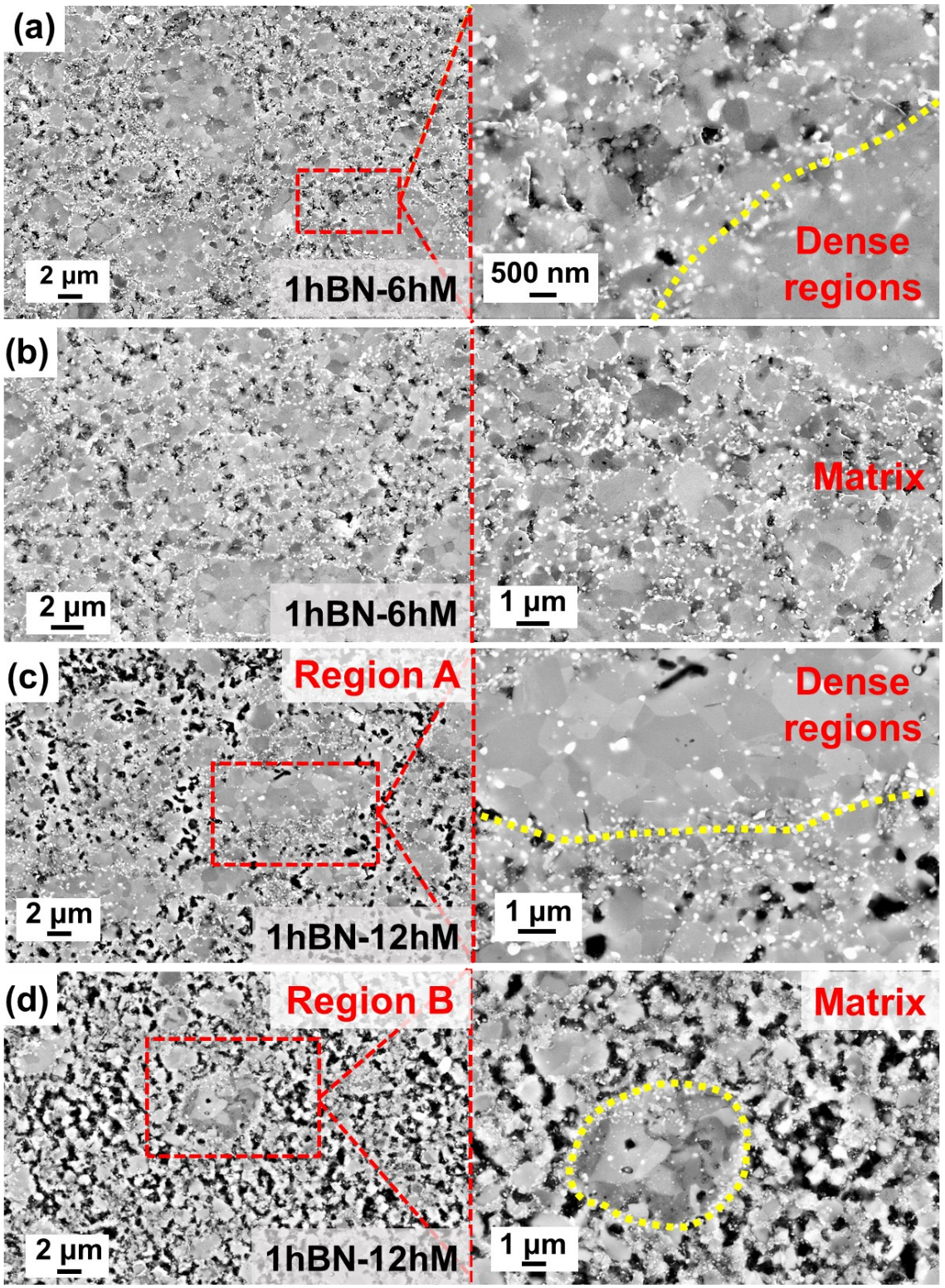


Figure 8.7 SEM images of dense regions and the matrix in 1 wt% hBN doped MgB_2 samples with powder milled for (a, b) 6 h and (c, d)12 h and processed at 1200 ºC for 5 min.

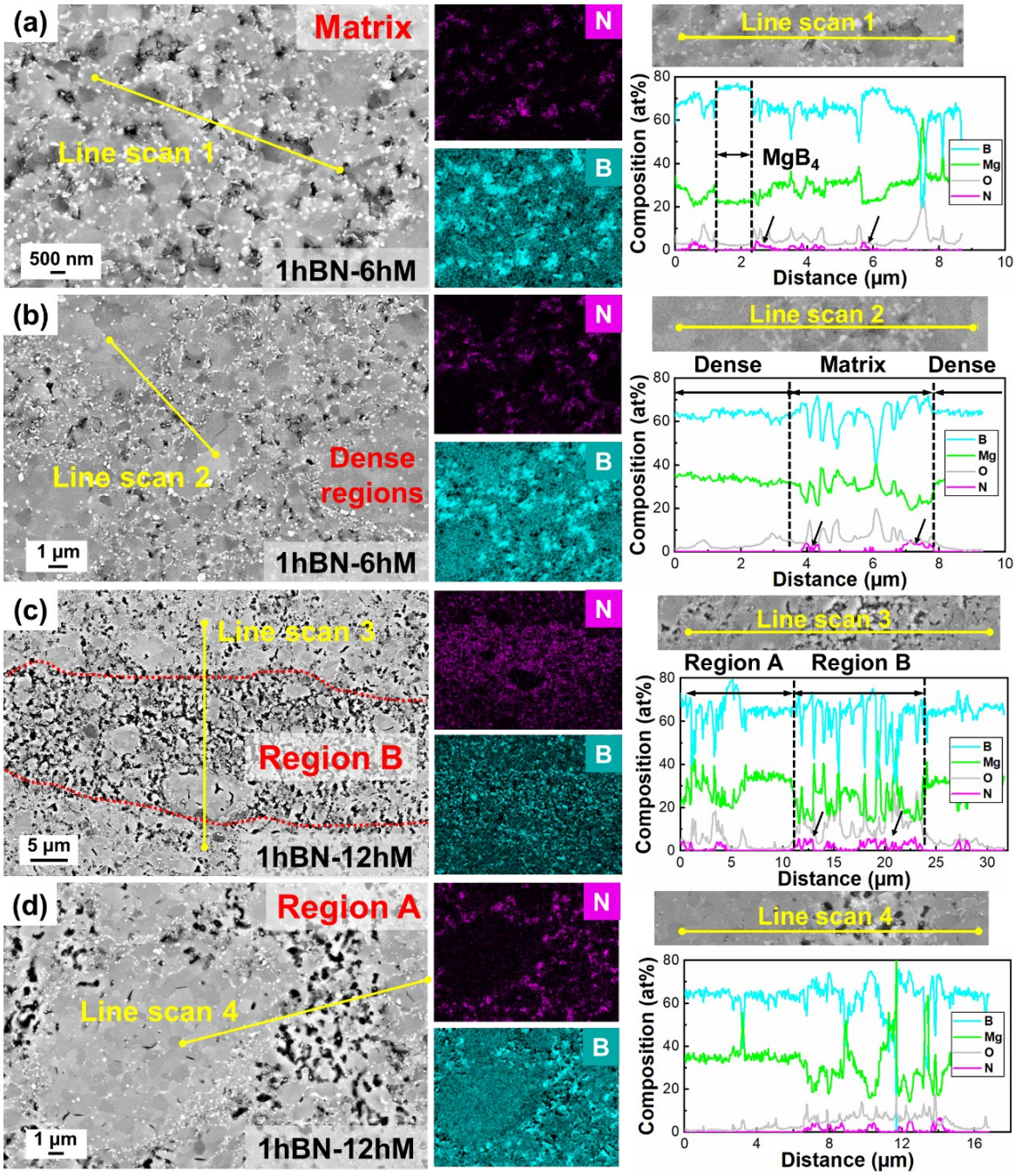


Figure 8.8 EDX analysis of 1 wt% hBN added MgB_2 samples processed at 1200 °C for 5min. (a, b) show N and B element maps from porous matrix and dense regions and line scans in the 1hBN-6hM sample. (c, d) show equivalent data from Region A and Region B in the 1hBN-12hM sample.

Figure 8.8 depicts the distribution of different elements in MgB_2 samples by EDX analysis. As presented in Figure 8.8a and b, the B-rich area is much larger than the N-rich regions, and line scan results show the co-existence of large MgB_4 grains (~1 μm)

and smaller N-containing phases (<100 nm). No isolated grains or impurities can be found within dense regions, which means the connectivity of the grains is not affected within dense regions. This observation is critical to choosing parameters in the simulation model when discussing superconducting performance. Under longer milling times, Mg(N,B) phases are distributed uniformly in Regions A and B of the matrix, Figure 8.8c and d. The abrupt changes of B and Mg content shown in the line scans originate from the pores and MgO impurities. It can be observed that N- and B-rich regions nearly overlap, and the peaks in the N line scans match with peaks in the B line scans, indicating the dominance of Mg(N,B) phases in 1hBN-12hM after the FAST process.

8.4.3 Characterisation of bulk samples with 2 wt% hBN addition

Microstructures of 2 wt% hBN doped MgB_2 samples are shown in Figure 8.9. Dark features between MgB_2 grains within dense regions are obvious in the 2hBN-6hM sample, similar to the microstructures of 5 wt% cBN added MgB_2 samples with powder milled for 12 h and then processed at 1200 ^oC for 30 min (Figure 7.13e). Figure 8.9b zooms into the matrix where darker contrast appears at the MgB_2/MgB_2 grain boundaries together with extremely tiny bright MgO grains, both of which presumably inhibit the contact between MgB_2 grains. As shown in Figure 8.9c and d, Region A is as porous as Region B and the size of dense regions decreases accompanied by a larger fraction of dark features between grains (Figure 8.9e). Pores in the matrix are around 1

μm in size, comparable to the MgB_2 grain size (Figure 8.9f).

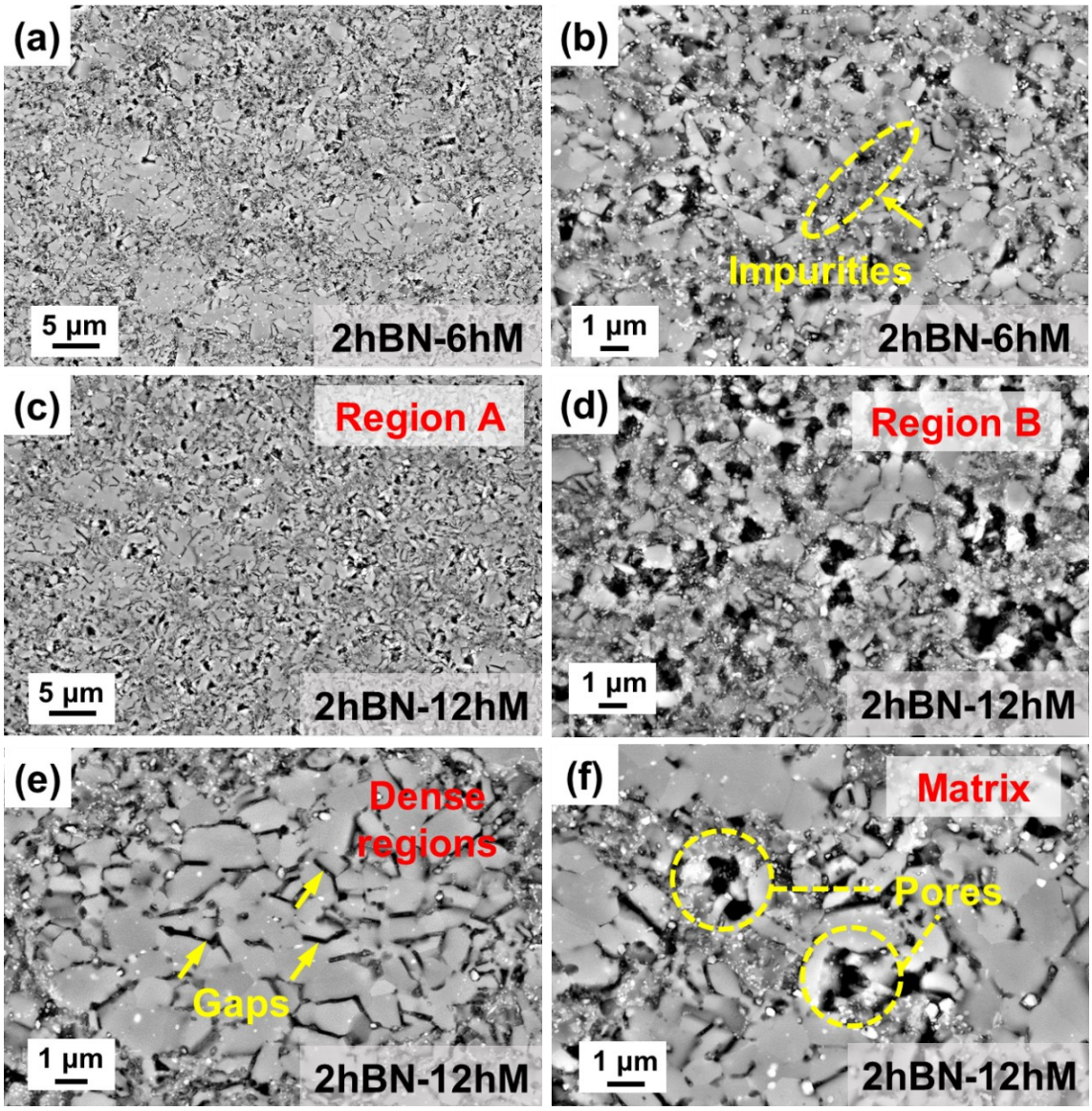


Figure 8.9 BSE images of 2 wt% hBN added MgB_2 samples with powder milled for (a)(b) 6 h and (c-f)12 h before processed at 1200 ºC for 5 min.

EDX analysis of both samples is presented in Figure 8.10. The SEM image in Figure 8.10b shows that MgB_2 grains in the porous matrix lose their regular morphologies with the edges apparently transformed to nanoscale Mg(N,B) impurities highlighted by lines and arrows. Figure 8.11 shows volatile composition change across dark features in line scan results in dense regions of the 2hBN-12hM sample, which is highly related to the

formation of liquid phase at grain boundaries during the sintering process, similar to the effects of cBN addition (Chapter 7). Strong evidence will be shown in Chapter 9 where hBN and Mg are co-added in MgB_2 samples.

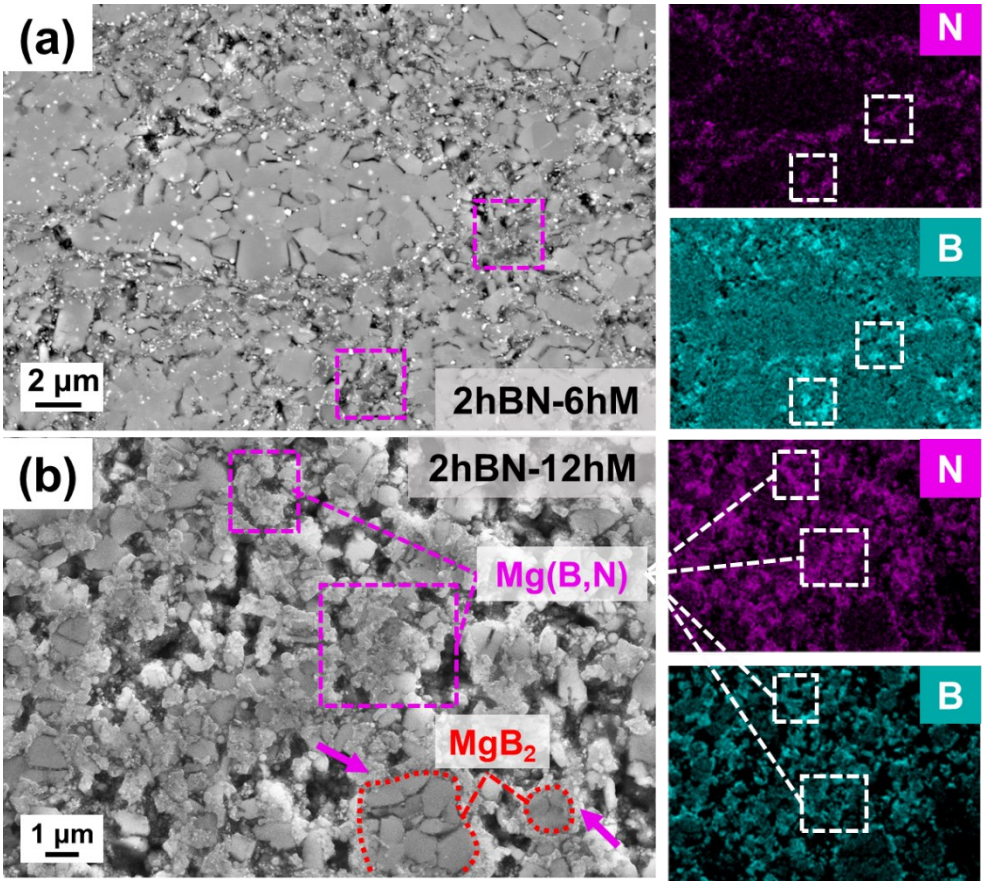


Figure 8.10 (a) BSE image and EDX analysis of 2hBN-6hM. (b) SEM image and EDX analysis of porous regions in 2hBN-12hM.

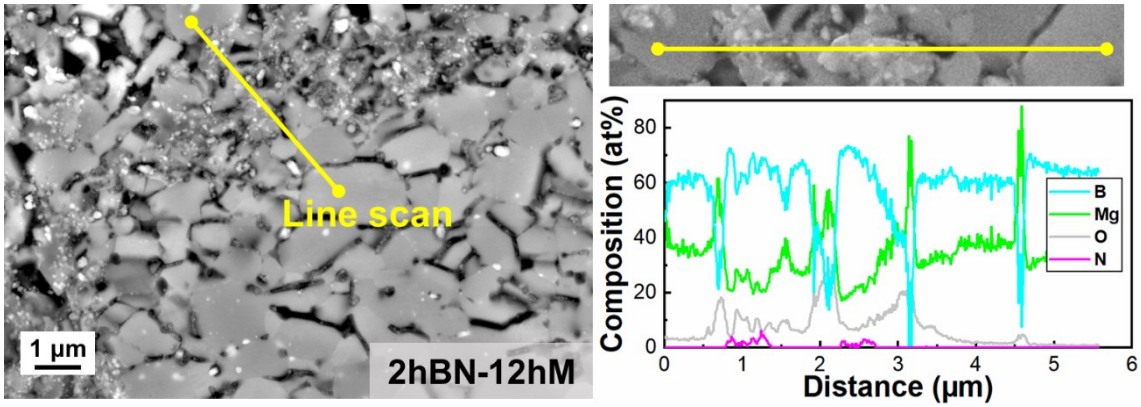


Figure 8.11 BSE image and line scan results of 2hBN-12hM.

8.5 Investigation of effect of hBN addition on grain sizes and phase transformations

EBSD analysis has been performed on these samples to explore the effect of processing conditions on microstructures. Inverse pole figure maps of four MgB_2 samples processed at 1200 ^oC for 5 min with different hBN percentages are shown in Figure 8.12a-d. Average grain sizes (D_{av}) of 0.5 wt% and 1 wt% hBN doped samples are estimated to be around 0.80 ± 0.36 μm in contrast to 0.97 ± 0.47 μm in 2hBN-12hM. D_{av} of grains in 2hBN-6hM is in between (0.86 ± 0.42 μm). These results indicate that the liquid phases created by hBN addition may promote MgB_2 grain growth. This can also be demonstrated from the histogram of grain size distribution where samples with higher hBN additions have more large grains over 1 μm (Figure 8.12e).

TKD results of the 1hBN-6hM thin foils are presented in Figure 8.13a and b. The area circled by dashed lines are N-rich phases observed by EDX and is indexed as $MgNB_9$ in TKD. The size of $MgNB_9$ grains can be tens of nanometers or larger, but have low pattern quality compared with MgB_2 grains. The Kikuchi patterns have been checked in the very dark areas shown by arrows and reveal that indexing failure comes from pores or extremely thin layers where only diffraction spots can be obtained.

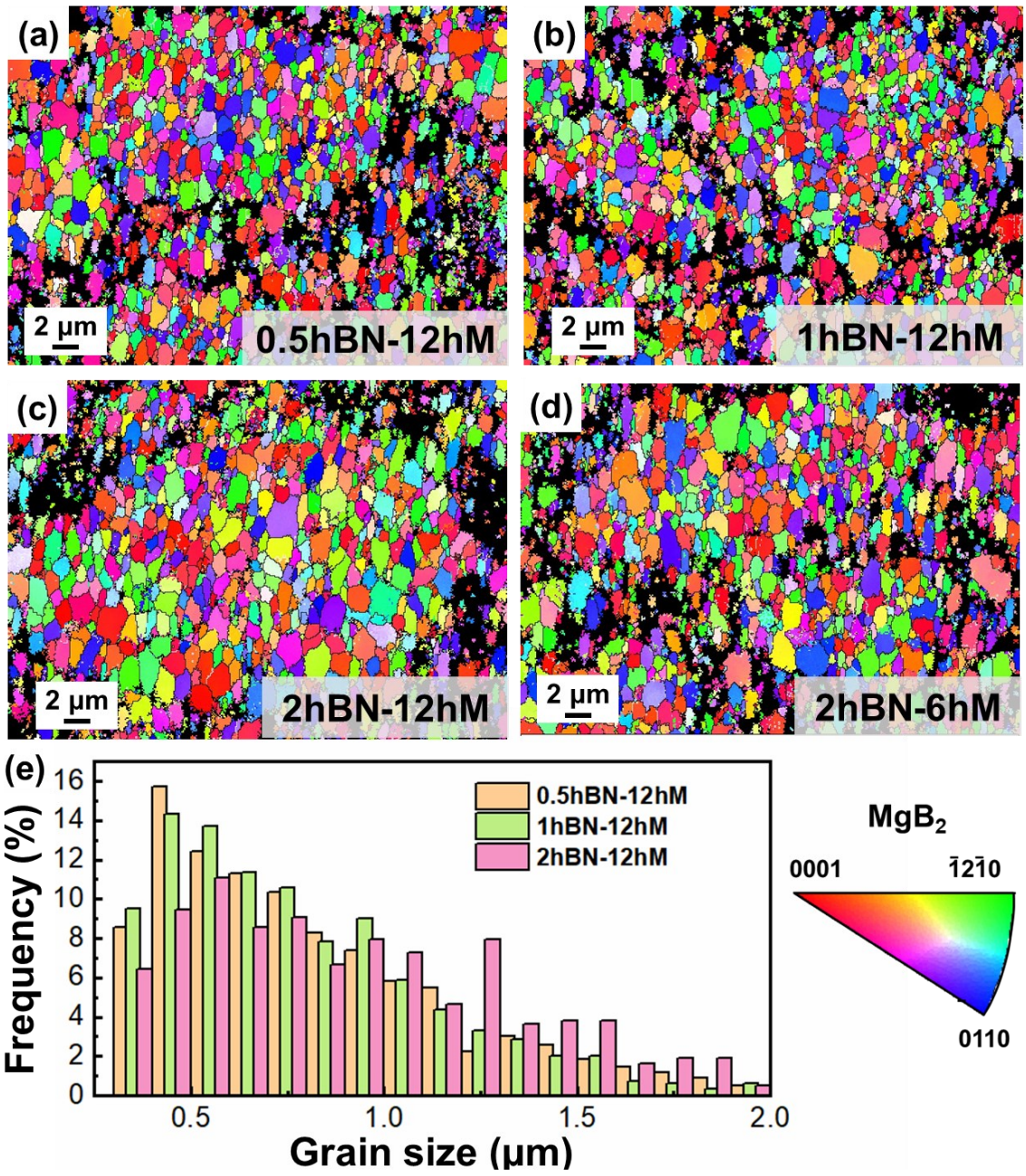


Figure 8.12 EBSD inverse pole figure maps from Y-direction (IPFY) of (a) 0.5hBN-12hM, (b) 1hBN-12hM, (c) 2hBN-12hM and (d) 2hBN-6hM. The black grain boundaries represent misorientations larger than 15°. (e) presents the grain size distribution.

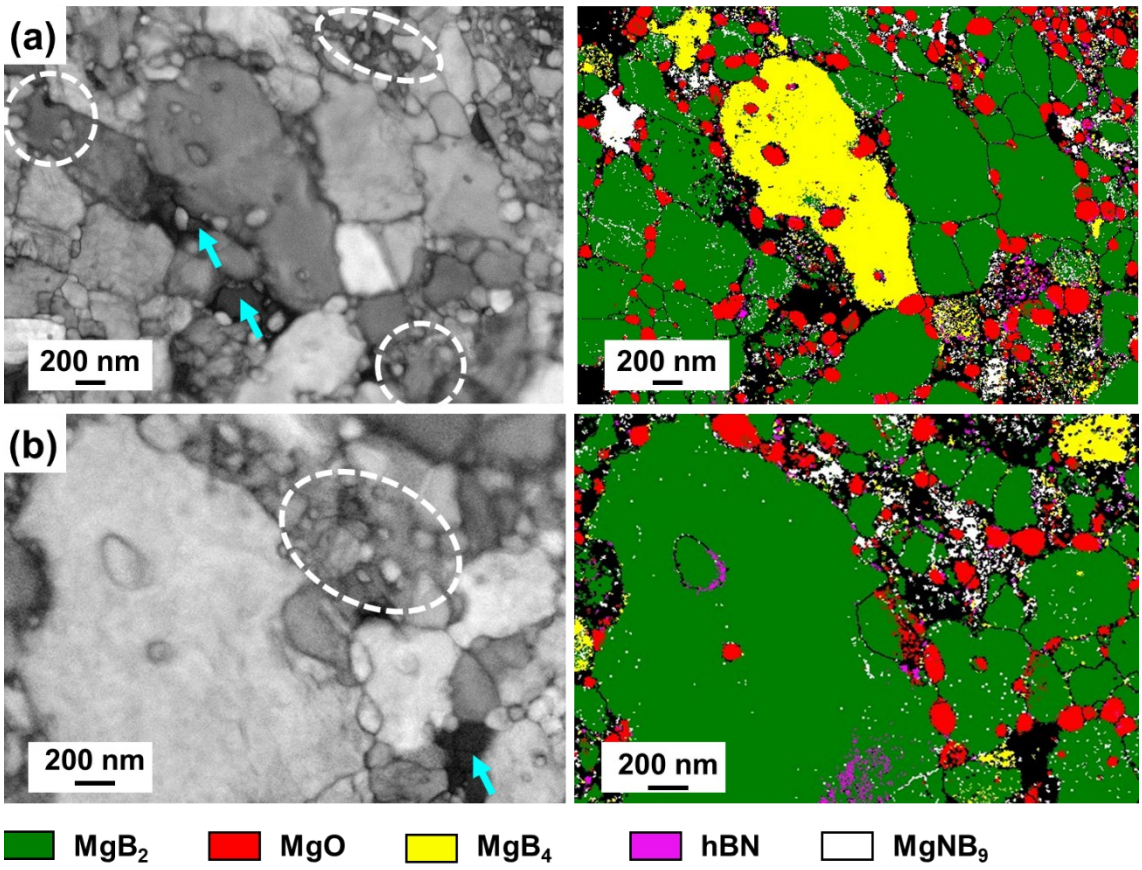


Figure 8.13 (a) and (b) show band contrast and phase maps of different regions in 1hBN-6hM thin foils.

8.6 The influence of hBN addition on milled powders and green compacts

The effects of powder additions can be discussed from two perspectives: (i) the size reduction and surface modification of MgB_2 particles after ball milling and (ii) the particle arrangement in green compacts. Since microstructures are critical to the superconducting performance and powder processing affects microstructural features of processed samples, it is necessary to investigate the impacts of hBN addition and compare it with the cBN addition discussed in Chapter 7.

8.6.1 The influence of hBN addition on milled powders

As mentioned in Section 8.3, milling MgB_2 particles with soft hBN much smaller than MgB_2 particles can first lessen the impact from the milling balls, so the efficiency of particle size reduction, as well as crystallite refinement, is expected to be reduced. Moreover, grains in the loosely-packed agglomerates have more opportunities to rearrange themselves under the external force and therefore the shape of agglomerates will also be changed easily. Besides, hBN nanoparticles or thin layers generated after long milling times can adhere to the particle surface and modify the MgB_2 particle surface (Figure 8.14a). These decorations are easier to react with MgB_2 once the processing temperature rises to 1200 ^oC. In contrast, large cBN particles (~10 μm) act as a grinding aid, accelerating the milling process and generating a larger fraction of round MgB_2 aggregates than agglomerates (Figure 8.2). The sizes of cBN fragments after milling can vary greatly in size from 1 to 10 μm, which is comparable to MgB_2 grains or particle size. Therefore, these hard additives are mixed with MgB_2 grains or particles rather than modifying MgB_2 grains/particle surface (Figure 8.14a).

8.6.2 The influence of hBN addition on green compacts

Two types of MgB_2 particles, large agglomerates or aggregates and fine grains (~1 μm) are co-present in the milled mixtures. Particle segregation is unavoidable in the handling process, which is influenced by the size, density, surface state, fraction and shape of particles [231]. Since the prepared powders were transferred by lab weighing

paper, three kinds of segregation may occur in this process. The first one is fluidization segregation. MgB_2 agglomerates fall faster than finer particles because their gravity is much greater than air resistance. Percolation segregation happens when finer particles infiltrate through gaps formed by MgB_2 agglomerates that serve as sieves. Due to the angle of repose when pouring powders, heavier agglomerates will fall away from the top of the conical pile in contrast to finer particles, which is known as trajectory segregation. Although I changed the pouring sites manually above the die and shorten the time of pouring powders, this problem cannot be completely avoided. The consequence of segregation is that agglomerates have greater chances to stay together in certain regions of the sample as well as fine particles cluster (Figure 8.14a).

When preparing green compacts by uniaxial pressing, the loosely packed agglomerates with irregular shapes are easier to deform, interconnect and interlock by the grain re-arrangement, prohibiting the further movement of super-agglomerates. Thus, super-elongated agglomerates form in the green compact with the long axis perpendicular to the pressure direction (Figure 8.14c). In comparison, harder aggregates with smaller sizes than the agglomerates are less prone to be deformed. Additionally, round shapes assist their higher mobility so they can be distributed more uniformly with the assistance of the rearrangement of surrounding finer particles under the applied pressure (Figure 8.14d).

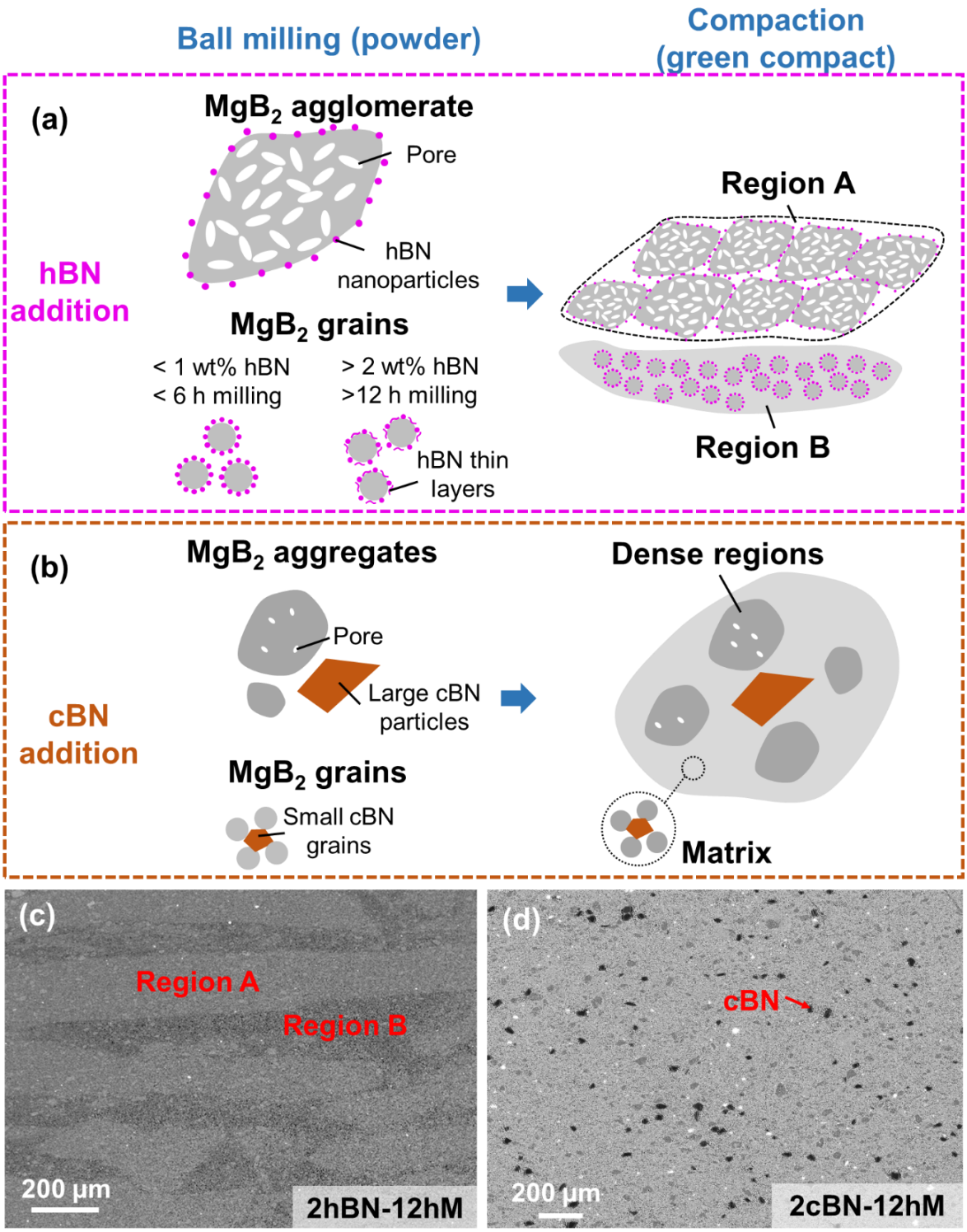


Figure 8.14 Schematic diagrams comparing role of (a) soft, small hBN nanoparticles and (b) hard, large cBN particles on ball-milled mixture powder and green compacts. (c) and (d) BSE images of 2hBN-12hM and 2cBN-12hM showing the microstructures of processed samples with hBN/cBN addition.

From the discussion above, it is easy to understand why Region A and B formed in >1

wt% hBN added MgB_2 samples prepared by powders milled for 12 h. With the same mass fraction, a higher number of hBN nanoparticles will be introduced compared with cBN particles (10 ~ 20 μm). hBN thin layers after long hours of milling are much helpful to impede the particle hardening and lead to the formation of many agglomerates. All these reasons cause obvious segregation.

8.7 The influence of hBN addition on MgB_2 bulk samples

The addition of hBN in MgB_2 powders can also alter sintering behaviour in the FAST process and form $MgNB_9$ impurities. Chapter 7 has discussed how $MgNB_9$ forms in the matrix of cBN added MgB_2 samples. Though the addition in this Chapter changes to hBN, the chemical reaction is similar,

$$4MgB_2 + hBN \rightarrow 4Mg + 8B + hBN \rightarrow MgNB_9 + 3Mg\ (l,g)$$

In 2 wt% hBN added samples processed for 5 min, even dense regions show signs of separating into individual grains, which is also observed in 5cBN-F30min (Figure 7.13e). This can be explained by a large amount of Mg liquid from MgB_2 decomposition during the FAST process in these samples which leads to the formation of Mg-B-N eutectic liquid infiltrating into agglomerates along grain boundaries. These impurities inhibit the further densification of dense regions, therefore leaving the “gap” features between MgB_2 grains shown in Figure 8.15.

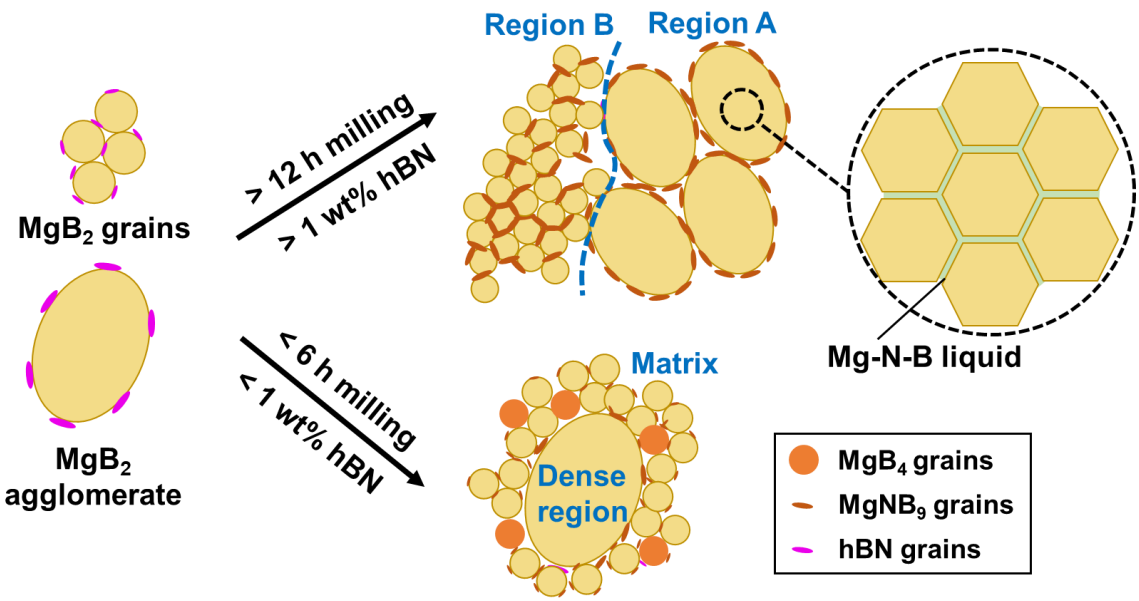


Figure 8.15 Schematic diagrams showing the role of hBN nanoparticles on microstructures of MgB_2 bulk samples. The enlarged figure shows that the Mg-N-B liquid phase exists in the sintering process.

8.8 Analysis of superconducting properties

Figure 8.16 shows the DC susceptibility of hBN/graphene added MgB_2 bulk samples as a function of temperature. 0.5graphene-12hM and 0.5hBN-12hM have similar transition widths (ΔT) around 0.7 K, but the graphene added MgB_2 sample has a lower onset T_c at 38.0 K compared with 38.5 K of the hBN added one. The suppressed T_c of 0.5graphene-12hM may result from carbon atoms released from graphene substituting for B atoms, as has also been found in [226]. In the 1 wt% hBN added sample series, the onset T_c of samples prepared from powders after 6 and 12 h of milling is the same but 1hBN-12hM shows a slightly broader ΔT than 1hBN-6hM (Figure 8.16b). As Figure 8.16c presents, there is an obvious variation between 2hBN-6hM and 2hBN-12hM. The onset T_c of the latter one decreases to 38.2 K, and ΔT increases to around

1.4 K due to the higher lattice disorder introduced by ball milling. The comparison of samples with different percentages of hBN addition is shown in Figure 8.16d. With the increasing hBN percentage, the ΔT increases, especially from 1 wt% to 2 wt%. The much broader transition in the 2 wt% hBN added sample series indicates that higher percentages of hBN exaggerate sample inhomogeneity due to the severe reaction between hBN and MgB_2.

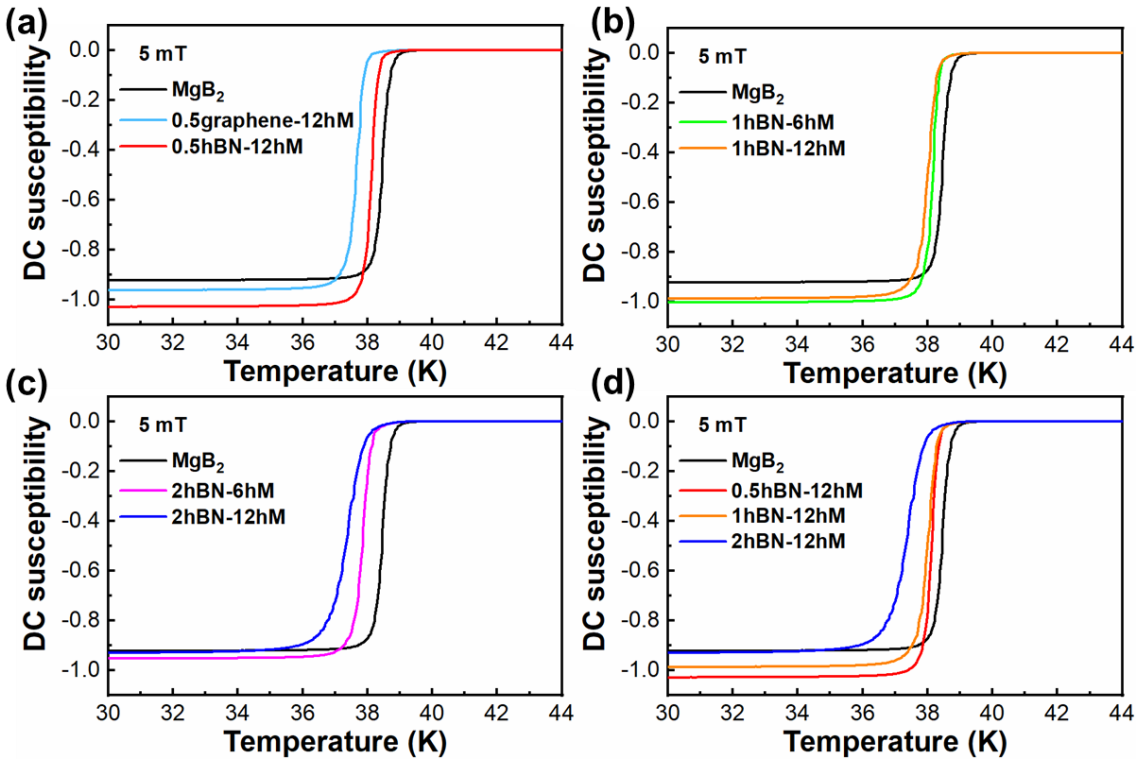


Figure 8.16 DC susceptibility curves under 5 mT in (a) 0.5 wt% hBN/graphene, (b) 1 wt% hBN and (c) 2 wt% hBN added MgB_2 bulk samples processed at 1200 °C for 5 min. (d) compares the T_c of samples with different percentages of hBN addition.

0.5 hBN/graphene doped samples have Type I-like microstructures (Section 4.2.5.1). The microstructural influence of the increasing percentage of hBN is balanced by a short time of milling in 1hBN-6hM, so the sample still has relatively dense structures. This sample microstructure is characterised by smaller MgB_4 grains distributed in the

matrix instead of large MgB_4 phases (Figure 8.7a and b), so can also be described by the Type I microstructure model. The occurrence of Region A and B make the situation complicated in 1hBN-12hM (Figure 8.4, Figure 8.7c and d). For simplicity, it can be approximately simulated by modified Type II microstructures where Subarray B represents denser Region A (hundreds of microns) and the superconducting fraction in Subarray B is set below 1[3]. Simulation results indicate micro current within Subarray B have a great contribution to the total ΔM. 2hBN-6hM has Type IV microstructure with the presence of gaps between MgB_2 grains in relatively dense regions.

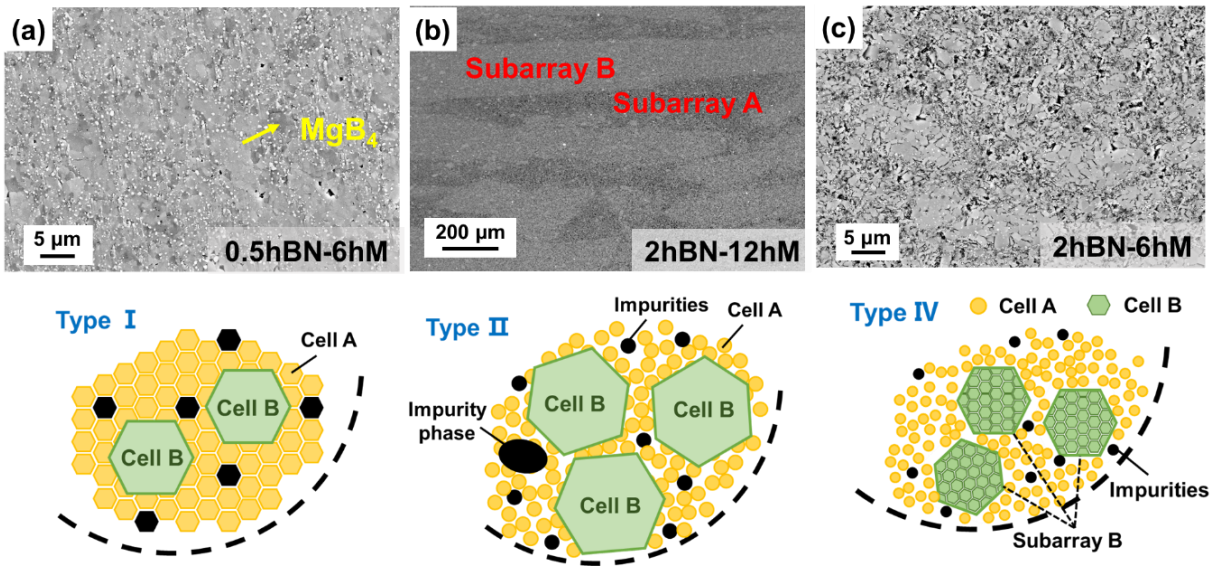


Figure 8.17 SEM micrographs and the corresponding schematics (Chapter 4) to identify the currents flowing on different length scales.

The $\Delta M(B_{app})$ curves of hBN/graphene added MgB_2 samples at 20 K are shown in Figure 8.18a-c. A significant overall ΔM improvement can be seen in both 0.5 wt% graphene and hBN added MgB_2 samples, and the specimen with graphene addition

[3] The revised input parameters are: f(Subarray A) = 0.2, f(Subarray B) = 0.6, A_{con}(Cell A) = 0.5, A_{con}(Cell B) = 0, p_s(Subarray A) = 0.5, p_s(Subarray B) = 0.7, d(cellA) = 10^{-6} m and d(cell B) = 5×10^{-4} m

outperforms the hBN added one as the field exceeds 3 T (Figure 8.18a). De Silva et al thought the transition temperature fluctuation induced pinning (δT_c pinning) is critical in graphene-doped MgB_2 samples [232]. Moreover, Li et al pointed out that the effective 2D flux pinning centres (graphene thin layers) and improved grain connectivity contribute to the good superconducting performance of graphene doped MgB_2, apart from the C substitution for B sites [226]. Increased pinning sites may also be applicable to explain the enhanced performance of 0.5hBN-12hM by tiny $MgNB_9$ grains or 2D thin layers, and the lack of high-field ΔM improvement is presumably from the lack of atom substitution that C-containing materials can generate. 1hBN-6hM shows superior superconducting performance in the whole range of fields while 1hBN-12h has slightly higher low-field ΔM values than un-doped MgB_2 samples but its ΔM value drops quicker at the high-field regime, as shown in Figure 8.18b. The high porosity and weak connectivity of dense regions in Region A intensify the anisotropy effects of this sample so it has a faster decrease in the high-field regime (Figure 8.7c). In the 2 wt% hBN added sample series, there is a dramatic decrease in the $\Delta M(B_{app})$ curve of 2hBN-6hM and severe deterioration of superconducting performance of 2hBN-12hM. The presence of gaps in 2hBN-6hM between MgB_2 grains in relatively dense regions is responsible for its poor performance at high fields. ΔM values of 2hBN-12hM are even lower than that of 5cBN-F30min (Figure 7.22), indicating the high activity of nanoparticles can exacerbate reactions at interfaces, therefore blocking supercurrent. According to simulation results, Figure 8.18d shows J_c (B) curves of

specimens where macro currents are dominated. One can observe that less than 1 wt% hBN added MgB_2 samples prepared from powders milled up to 12 h have much higher macro J_c values in the low and medium range.

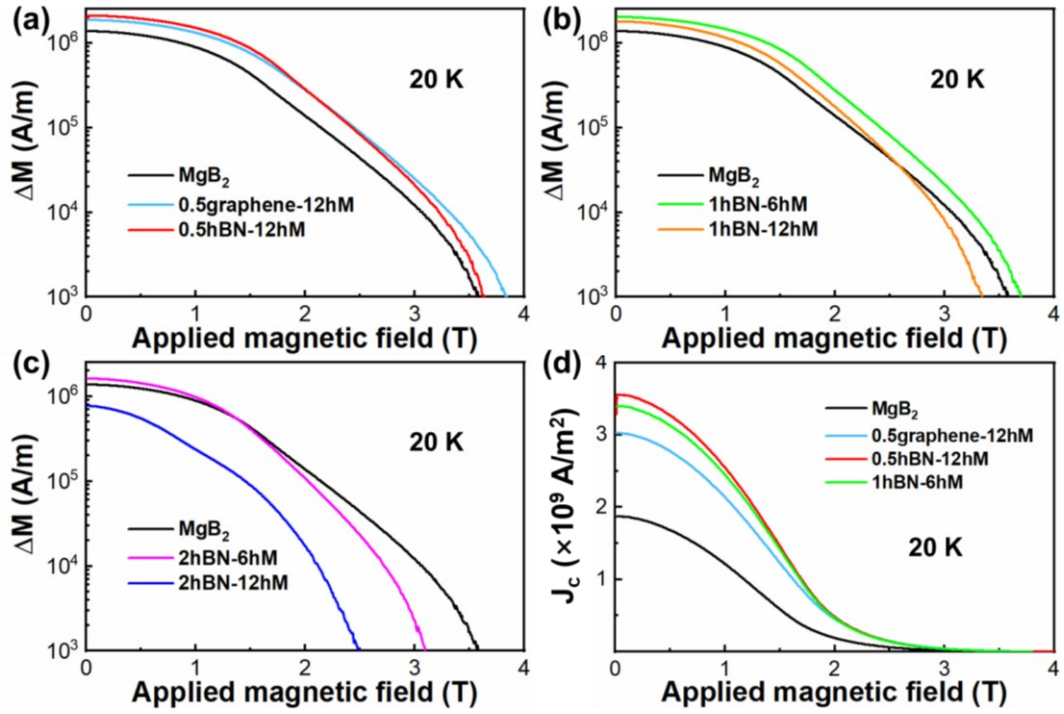


Figure 8.18 $\Delta M(B_{app})$ curves on the log-log scale of (a) 0.5 wt% hBN/graphene, (b) 1 wt% hBN and (c) 2 wt% hBN added MgB_2 sample series. All samples are processed at 1200 °C for 5 min. (d) compares $J_c(B)$ curves of selective MgB_2 samples.

8.9 Conclusions

The present work studied the ductile-brittle milling system (hBN/graphene and MgB_2) and the effects of soft hBN/graphene nanoparticles on MgB_2 microstructures as well as superconducting performance. The following conclusions can be drawn：

i. The relative size, brittleness and hardness are critical to the milling results and should be carefully considered when choosing additions in MgB_2 powders. Soft nanoparticles/thin layers can promote particle sliding and

adhere to the active surface of MgB_2 grains in milling, therefore consuming the impact energy from milling balls and slowing down the particle reduction progress. The segregation problem should be paid additional attention to when choosing the additions, which may intensify inhomogeneous microstructures.

ii. The control of liquid content formed in the sintering process by the milling time and the percentage of hBN adjustment is critical to the distribution and the amount of Mg(N,B) impurities. The reaction between hBN/cBN additions and MgB_2 grains in the sintering process (1200 ^{o}C) is similar, but much smaller hBN additions have higher activity and specific surface area, so are prone to react with MgB_2. Long milling time with hBN addition increases material inhomogeneity and destroys connectivity between MgB_2 grains. The optimal processing conditions are 0.5 wt% hBN addition and 12 h of milling or 1 wt% hBN addition and 6 h of milling.

iii. Tiny Mg(N,B) impurities may increase flux pinning centres, and the appropriate amount of liquid Mg phase formed during the sintering process can improve connectivity and prevent the formation of large MgB_4 phases. The superconducting performance of hBN doped MgB_2 samples has been overall improved over the whole range of fields and is even better than the graphene-doped MgB_2 one in the low-field regime.

Chapter 9 Microstructures and superconducting properties of Metal (Mg/Cu) and BN (hBN/cBN) co-doped MgB_2 bulk samples

9.1 Introduction

The addition of Mg, Cu and other metals to MgB_2 tapes and bulk samples has been investigated before. Even though the superconducting properties vary widely in different studies, the results of the metal atoms can be summarised as follows:

i. Providing a liquid phase sintering environment by adding metals with low melting points like Ag and Cu [112, 233-235]. However, low melting eutectics such as Mg_2Cu and $MgCu_2$ generated during sintering may lead to the impairment of grain contact.

ii. decreasing the fraction of MgB_4 such as the addition of Mg (Section 6.5), so MgB_2 grain connectivity can be improved [236, 237].

iii. Generating small alloy impurities by reacting with MgB_2 that can act as pinning centres [238].

Co-doping with other additives such as C-containing compounds or rare earth oxides can improve the overall performance of MgB_2 bulk samples by increasing the upper critical field or introducing artificial pinning centres [229, 239, 240]. In this chapter, Mg and Cu are chosen as metal additions in order to improve the J_c performance at low

fields by improving particle connectivity. At the same time, hBN and cBN are selected as co-dopants in MgB_2 bulk samples prepared by ex-situ routes. Two kinds of combinations, Mg + hBN and Cu + cBN, have been tried, and the results of phase analysis and microstructures of both two sample sets are presented. This work explores the co-doping effects of metal and N-containing additions on MgB_2 superconducting performance by linking to microstructural features.

9.2 Experimental details

Commercially MgB_2 powder (purity: 99%, Alfa Aesar), Mg powder (purity: 99.8%, Alfa Aesar) and hexagonal BN nanoparticles (average particle size <150 nm, Sigma-Aldrich) were used to prepare bulk samples by an ex-situ method. x wt% hBN (x = 1, 2) was first mixed with MgB_2 powder manually in the glove box under an Ar atmosphere. After 6 h or 12 h of milling, powders were transferred to a glass jar in the glove box. Next, 5 wt% Mg was added to the hBN + MgB_2 mixtures and thoroughly mixed by hand for 5 min before being uniaxially pressed into pellets. The consolidated pellets were then subjected to field-assisted sintering for 5 min in vacuum. The temperature is set as 1100/1200 ^oC with the applied axial pressure gradually increasing to 50 MPa. For the preparation of Cu and cBN co-added MgB_2 bulks, MgB_2 powders were mixed with 2 wt% cBN powders and milled for 10 h. Next, 5 wt% Cu powders (Max. Particle size: 5 μm, 99.8% purity, Goodfellow) were added to the mixtures, after which the powders were subject to an extra 2 h of milling. Consolidated pellets of these

precursors were processed by field-assisted sintering at temperatures from 900 ºC to 1100 ºC for 5/15 min.

Table 9.1 Processing conditions applied in the FAST apparatus

Sample	hBN/cBN addition (wt%)	Mg/Cu addition (wt%)	Milling time (h)	Temperature (ºC)	Dwell time (min)
1hBN-5Mg-6hM-1100C	1	5	6	1100	5
1hBN-5Mg-6hM-1200C	1	5	6	1200	5
1hBN-5Mg-12hM-1200C	1	5	12	1200	5
2hBN-5Mg-6hM-1200C	2	5	6	1200	5
2cBN-5Cu-900C-F15min	2	5	12	900	15
2cBN-5Cu-1000C-F5min	2	5	12	1000	5
2cBN-5Cu-1100C -F5min	2	5	12	1100	5

9.3 On the role of Mg and hBN addition on microstructural evolution of MgB_2 bulk samples

XRD scans of hBN and Mg co-doped MgB_2 samples are shown in Figure 9.1. All samples processed at 1200 ºC for 5 min have prominent $MgNB_9$ and Mg phases regardless of milling time and hBN percentage (>1 wt%). In contrast, only the 2 wt% hBN added sample (i.e., without additional Mg) with powder milled for 6 h has distinct $MgNB_9$ and Mg peaks under the same processing temperature and time in Chapter 8. This reveals that the addition of Mg promotes the reaction of hBN and MgB_2, and the formation of $MgNB_9$.

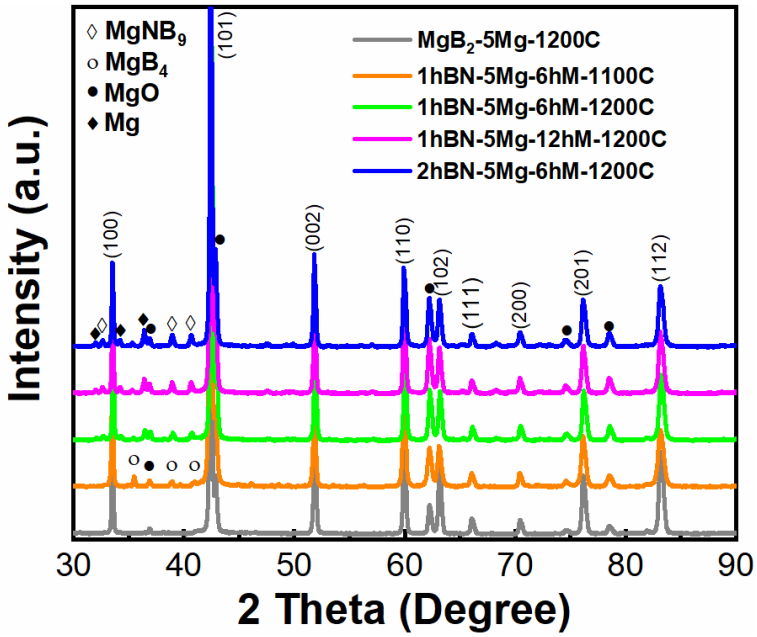


Figure 9.1 XRD patterns of hBN and Mg co-doped bulk samples processed from powder milled for 6 h (or 12 h) and processed at 1200 °C (or 1100 °C) for 5 min.

The comparison of impurity contents is presented in Figure 9.2. Mg-only added MgB_2 bulk sample is purer and no impurity peaks can be observed. In contrast, $MgNB_9$ becomes the dominant impurity in the 1 wt% hBN + 5 wt% Mg added samples processed at 1200 °C, replacing the dominant MgB_4 phase in the one prepared at 1100 °C (Figure 9.2a and b). The longer milling time (12 h) aggravates the reaction between hBN and MgB_2 due to the creation of much more active surfaces on the fractured milled powders (Figure 9.2c). Also, Figure 9.2d reveals that a higher hBN percentage leads to an increasing fraction of $MgNB_9$ impurities because more reactions sites are created after ball milling.

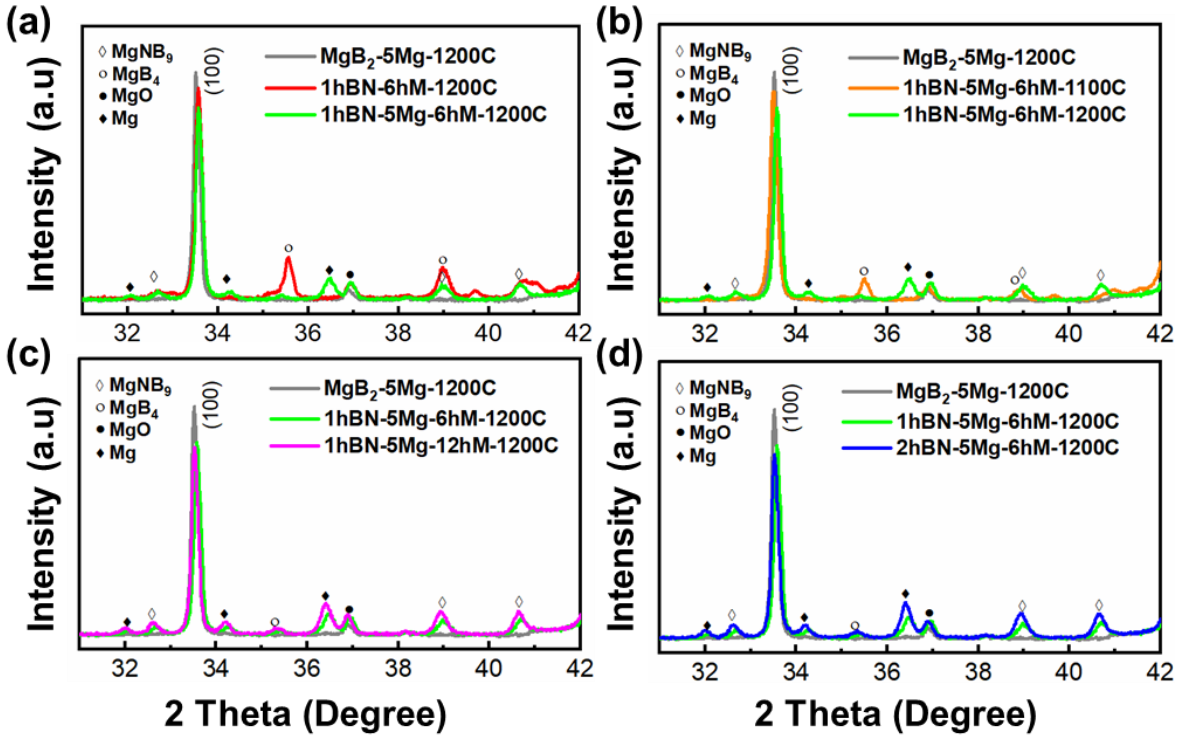


Figure 9.2 XRD results showing the impurity contents of samples under different processing conditions.

These samples show quite different microstructural features, as depicted in Figure 9.3. Inhomogeneities in the sample processed at 1100 ºC feature dense regions, porous matrix and small MgB_4 phases (<5 μm) as shown in Figure 9.3a. However, Figure 9.3b illustrates that in samples processed at 1200 ºC, large MgB_2 regions with sizes up to hundreds of microns (circled by red dashed lines) are separated by impurities with darker contrast. Instead of forming large particles like MgB_4, these finely dispersed impurities are mixed with MgB_2 grains. The prolongation of milling time to 12 h reduces the size of large MgB_2 regions (Figure 9.3c). With increasing the hBN percentage to 2 wt%, the uniformly distributed impurities have grown to form large phases (~5 μm), as the size of MgB_2 regions shrinks and the microstructure becomes homogenous (Figure 9.3d).

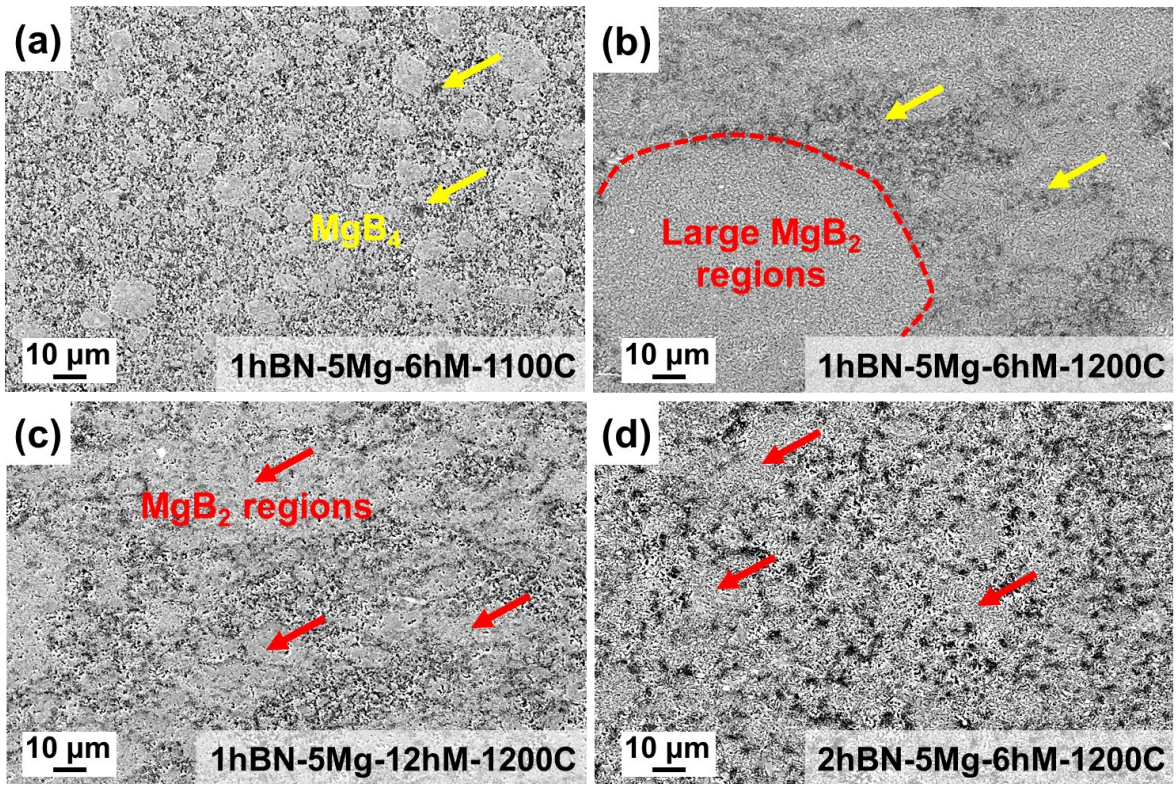


Figure 9.3 BSE images showing the morphologies of Mg and hBN co-doped samples.

Higher magnification views of these microstructures are presented in Figure 9.4. Dense regions in the 1hBN-5Mg-6hM-1100C sample have good grain connectivity and a clear interface with the porous matrix (Figure 9.4a). The grain connectivity in large MgB_2 regions as shown in Figure 9.4b, is heavily impaired. Clusters of Mg(N,B) impurities mixed with tiny MgO grains partition the matrix into smaller regions with sizes below 5 μm.

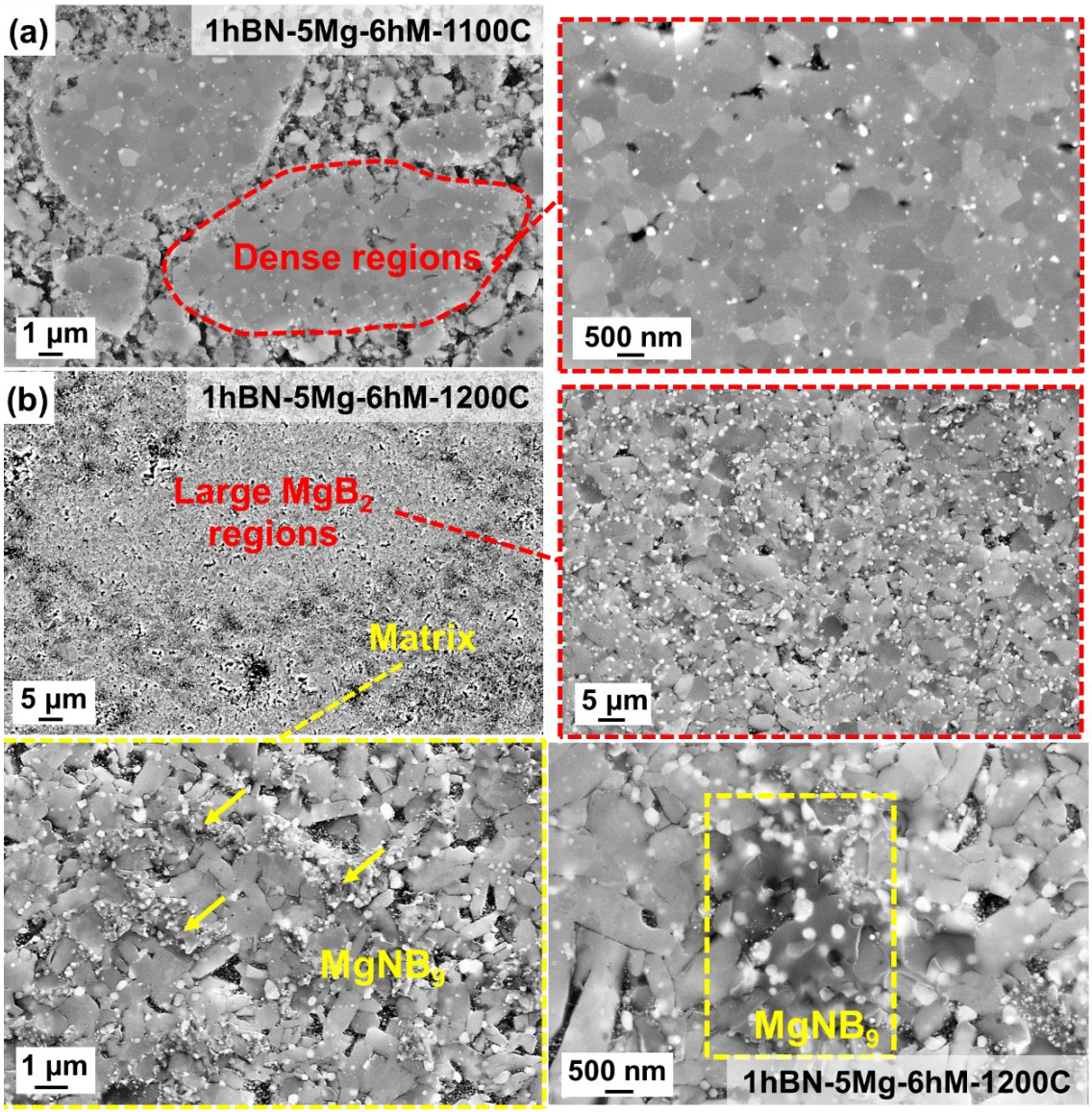


Figure 9.4 SEM images showing microstructures of hBN and Mg co-doped MgB_2 bulk samples at higher magnification.

The distribution of N and B in co-doped samples is shown in Figure 9.5. Weak N signals in B-rich areas in Figure 9.5a demonstrated the presence of MgB_4 while Figure 9.5b shows the dominance of Mg(N,B) phases. The line scan in 2hBN-5Mg-6hM-1200C shows the Mg(N,B) phases grow between large MgB_2 regions in a layer around 2 μm thick (Figure 9.5c).

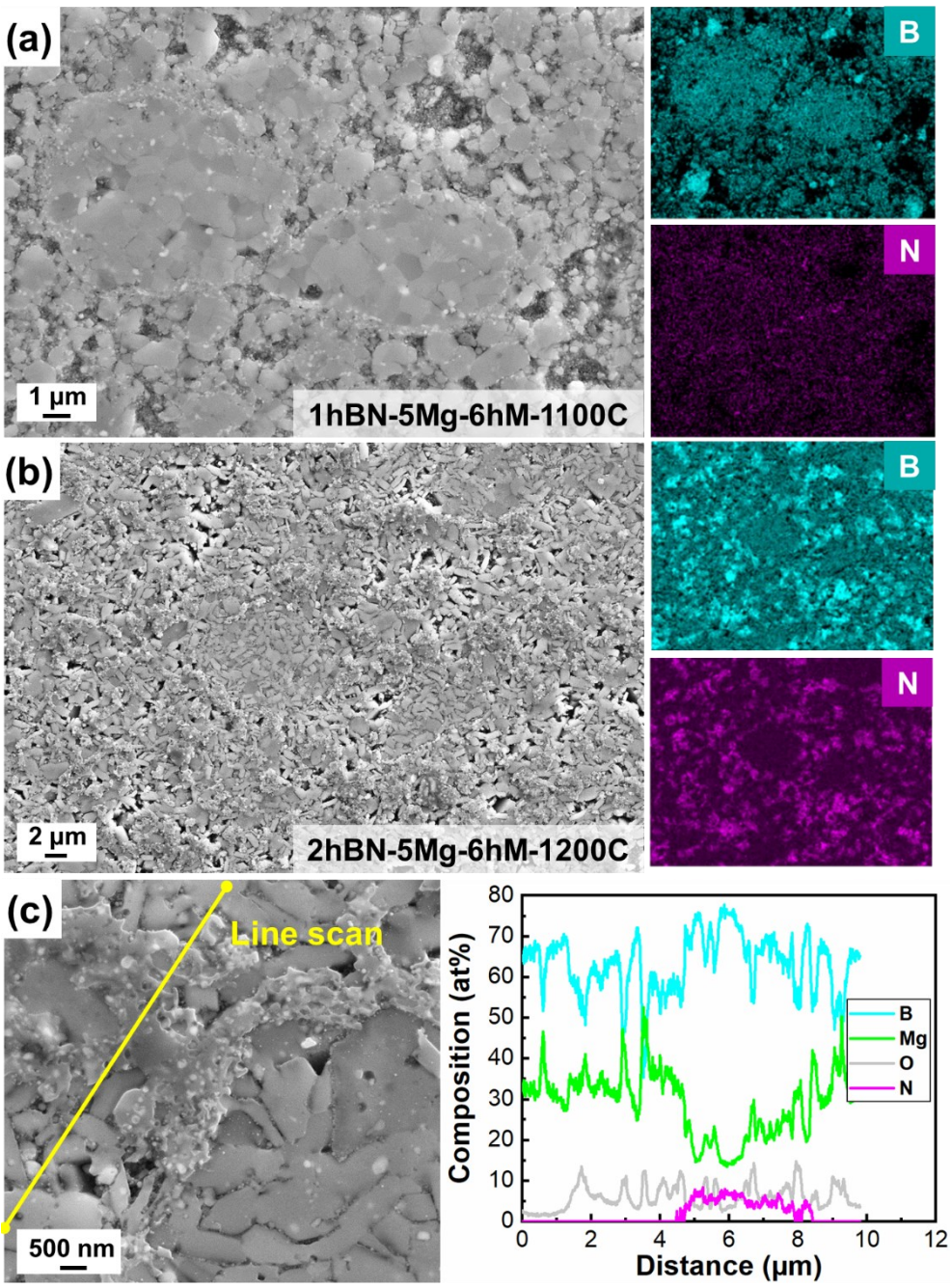


Figure 9.5 SEM image and elemental mapping of (a) 1hBN-6hM-1100C and (b) 2hBN-5Mg-6hM-1200C. (c) shows the line scan data of 2hBN-5Mg-6hM-1200C.

EBSD characterisation of three hBN and Mg co-doped samples is depicted in Figure 9.6. Under the 5 wt% Mg addition, some small impurity grains such as MgB_4 and $MgNB_9$ are detected at MgB_2 grain boundaries, but MgB_2 grains still keep good contact in the sample processed at 1100 ºC (Figure 9.6a and b). At 1200 ºC, the amount of

MgB_4, $MgNB_9$ and MgO increases, forming narrow barriers between adjacent MgB_2 grains in the dense regions and inhibiting the densification (white dashed circles in Figure 9.6c and d). Figure 9.6e shows the phase map of this sample at a higher magnification, and white lines represent low-angle grain boundaries (2 ~ 15º). One can find that the grain shapes are destroyed as more MgB_4 and $MgNB_9$ impurities form. Moreover, the density of low grain boundaries increases. The band contrast map of samples with 2 wt% hBN addition shows a high percentage of nanograins distributed between grains with normal size (Figure 9.6g). The unindexed pixels in the phase map may be due to these nanograins or lattice distortion brought by elemental variations due to B and Mg diffusion as discussed in Chapter 7.

The explanation of an impurity layer in dense regions can provide evidence for the mechanism of "gap" formation in 5cBN-F30min and 2hBN-12hM explained by liquid infiltration in the previous two chapters. As we know, liquid Mg can activate the sintering at low temperatures. In the presence of BN, the formation of excessive Mg-N-B liquid accelerates MgB_2 decomposition. The volume change due to the decomposition promotes liquid infiltration into MgB_2 regions, which leaves the impurity layers along grain boundaries. The impurity nanolayers resist densification and leave the apparent "gaps" between grains.

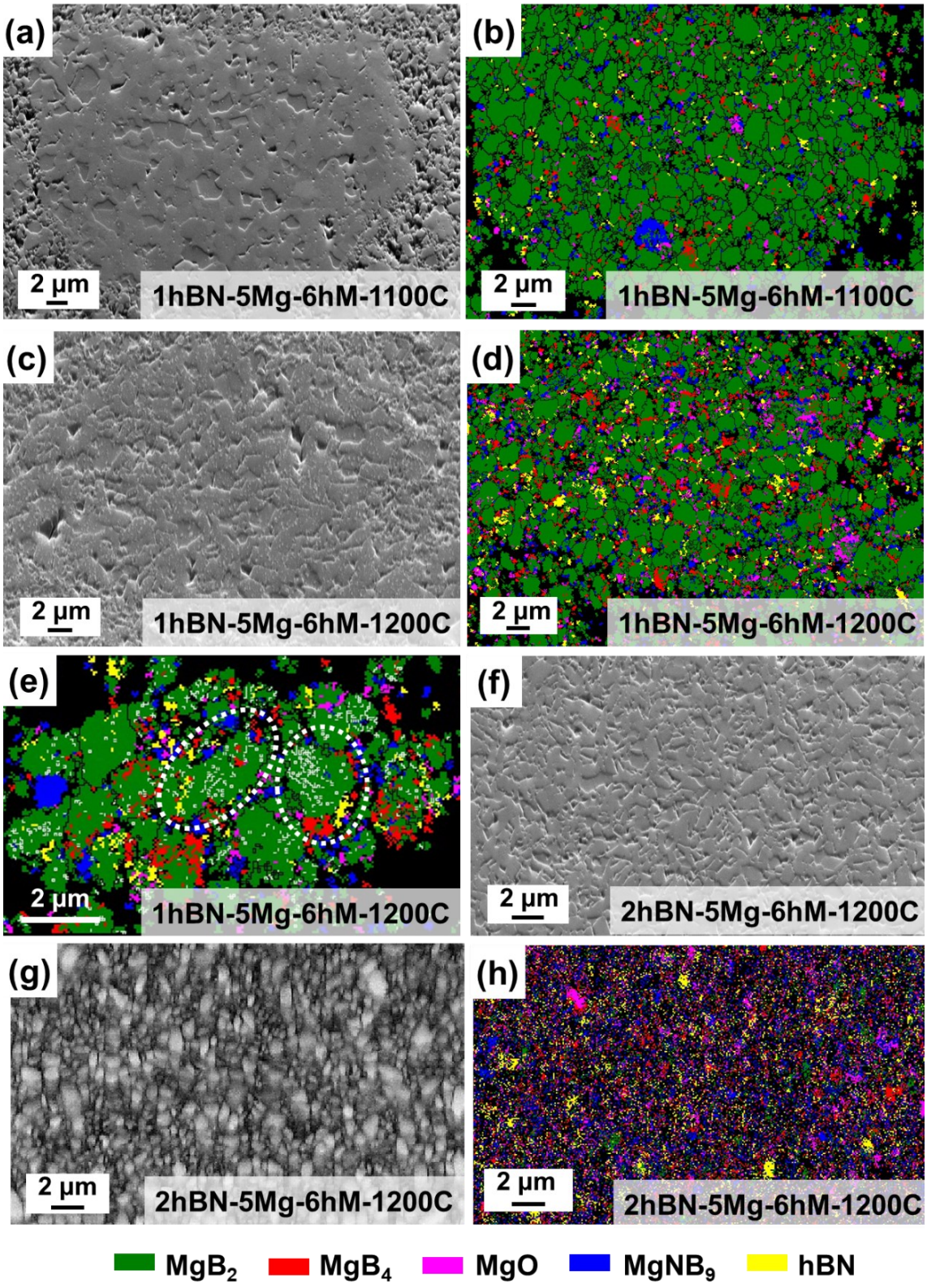


Figure 9.6 SEM images and phase maps of 1 wt% hBN + 5 wt% Mg co-doped MgB_2 bulk samples processed at (a)(b)1100 °C and (c)(d)1200 °C. (e) highlights impurities situated between MgB_2 grains in dense regions. (f-h) shows SEM, band contrast and IPFZ images of 2hBN-5Mh-6hM-1200C.

9.4 On the role of Cu and cBN additions on the microstructural evolution of MgB_2 bulk samples

XRD scans of MgB_2 powder and bulk samples with the addition of 2 wt% cBN + 5 wt% Cu are shown in Figure 9.7a. Prominent Cu peaks, as well as small MgB_4 peaks, can be detected in the pattern from the milled powder. In contrast, Cu peaks disappear and MgB_4 peaks show a dramatic increase in intensity in bulk samples. Cu-Mg alloy (Cu_2Mg) forms after processing as shown in Figure 9.7a. The phase diagram in Figure 9.7b shows that two intermetallic phases, $CuMg_2$ and Cu_2Mg, in the Cu-Mg system, which melt at 588 ºC and 797 ºC respectively can form at ambient pressure [241]. Ma et al used in-situ methods to investigate Cu-doped MgB_2 samples processed at different temperatures. They found Mg_2Cu is dominant at a lower reaction temperature (575 ºC) before the reaction of Mg and B occurs, and this phase would be transformed to $MgCu_2$ when processed at 850 ºC by the reaction $2Mg_2Cu + 6B = 3MgB_2 + MgCu_2$ [233]. In my ex-situ method, Cu (5 wt%) has a higher percentage than Mg produced by MgB_2 decomposition originally during processing at 1200 ºC, which may be another reason why Cu would exist in the form of $MgCu_2$. The Mg-Cu liquid is also expected to accelerate the decomposition of MgB_2 as indicated by the larger amount of MgB_4 impurities in my samples.

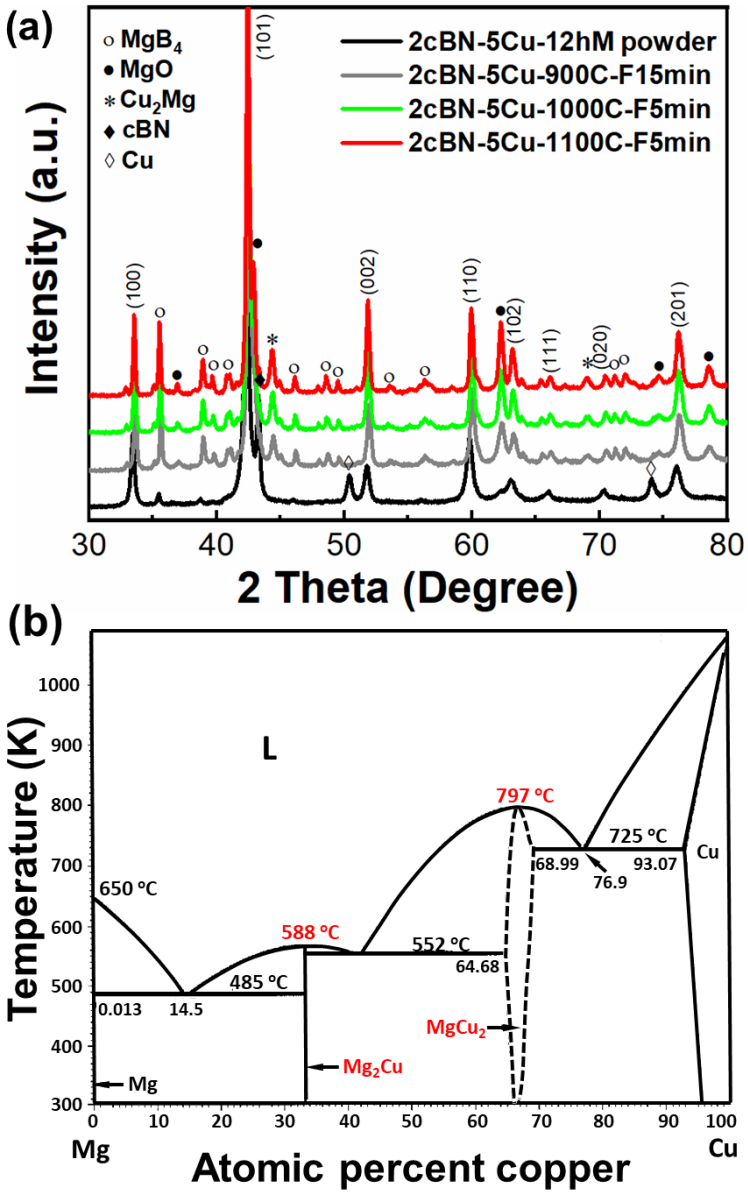


Figure 9.7 (a) XRD patterns of cBN and Cu co-doped powder milled for 12 h and bulk samples processed at different temperatures for 5/15 min. (b) binary phase diagram for Cu-Mg the system (Reproduced from [241] with permission from Springer nature).

Microstructures of these samples are shown in Figure 9.8. The darkest contrast comes from cBN and the less dark phases are MgB_4, while the Mg-Cu alloy impurities have the brightest contrast. The matrix in samples processed at 1000 °C has a number of pores, and the porosity is reduced by increasing the sintering temperature to 1100 °C

(Figure 9.8a and d). Since the formation of Cu-Mg liquid promotes MgB_2 decomposition and accelerates the mass transport, MgB_4 regions are denser than those in pure MgB_2 samples (Figure 9.8e vs. Figure 6.6). Large MgO impurities around 1μm form in MgB_2 dense regions, different from boundaries free of impurities in Mg added samples. As highlighted in Figure 9.8e and f, residual Cu-Mg phases are commonly seen at the interface between dense regions and the matrix and at MgB_2 grain boundaries, varying in size from 1 μm to below 100 nm, with angular shapes.

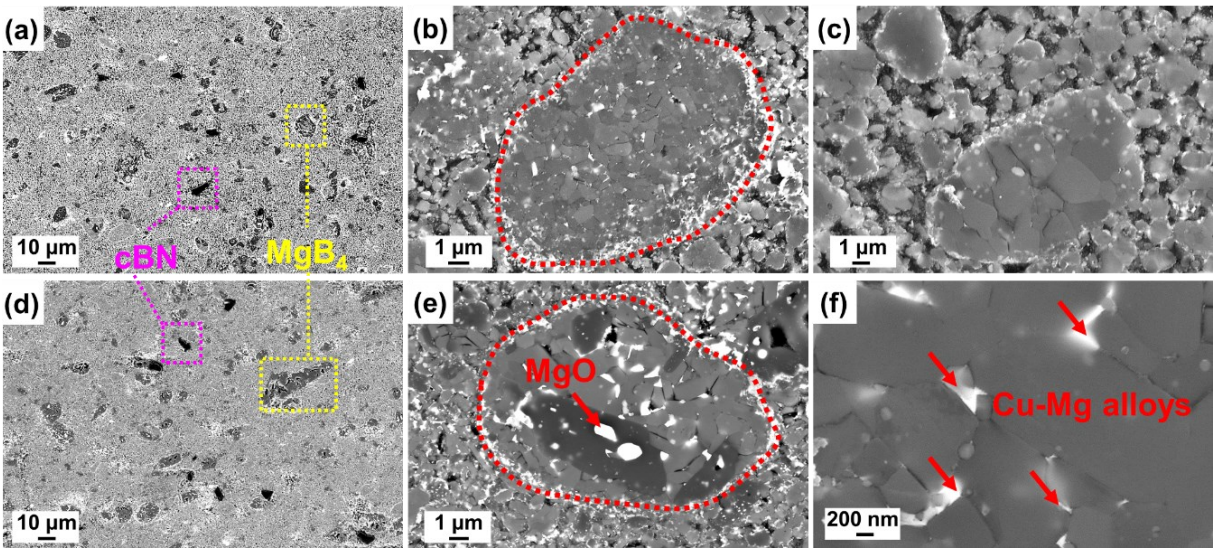


Figure 9.8 BSE images showing the microstructures of cBN and Cu co-doped MgB_2 bulk samples processed at (a-c) 1000 °C and (d-f) 1100 °C.

Figure 9.9 presents EDX results of 2cBN-5Cu-12hM-1100C. Element maps reveal that N-containing impurities are much smaller and less numerous than the Cu-Mg phases. Line scan results show the infiltration of Cu-Mg liquid into the voids between MgB_2 grains, which may impair the MgB_2 grain connectivity after this ex-situ processing.

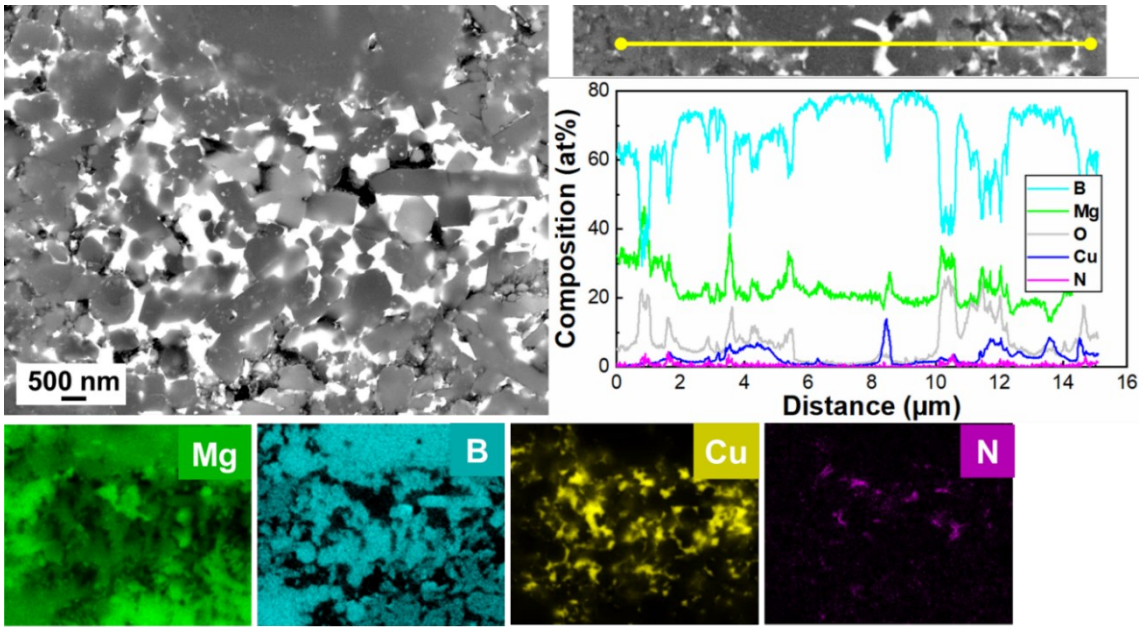


Figure 9.9 BSE image and EDX results from 2cBN-5Cu-12hM-1100C with line scan data and element maps.

9.5 Superconducting properties of Mg and hBN co-doped MgB_2 bulk samples

The DC susceptibility curves of Mg and hBN co-doped MgB_2 samples are shown in Figure 9.10. Both 1 wt% hBN doped samples have comparable onset T_c values that are around 0.4 K lower than the pure MgB_2 sample. The behaviour of 1hBN-5Mg-12hM-1200C and 2hBN-5Mg-6hM-1200C are similar, and onset values of both are around 38 K. The extent of decrease in T_c indicates MgB_2 lattice distortion.

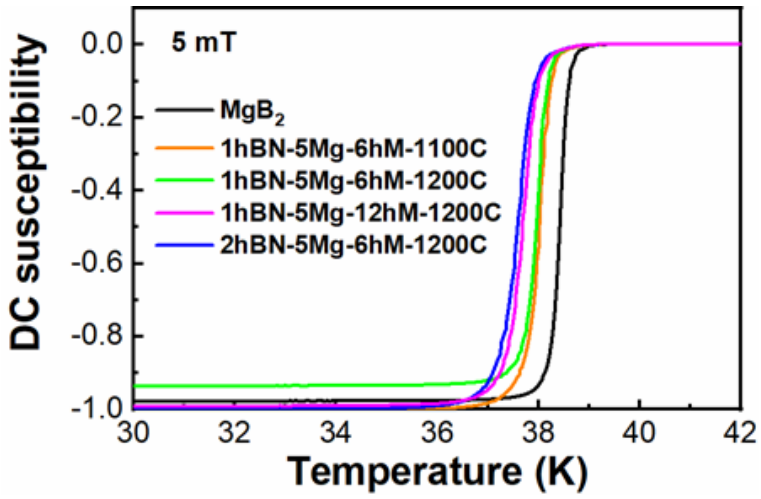


Figure 9.10 DC susceptibility under 5 mT as a function of temperature in hBN and Mg co-doped MgB_2 samples processed at 1100 ºC or 1200 ºC for 5 min.

Figure 9.11 shows the $\Delta M(B_{app})$ curves of MgB_2 with Mg and hBN additions on a log scale and a linear scale. The log scale presents a full range of information at different magnetic fields, and from Figure 9.11a, one can see that the 1 wt% hBN and 5 wt% Mg co-doped sample processed at 1100 ºC has an overall ΔM enhancement while ΔM of the one processed at 1200 ºC drops fast in the high-field range. This can be explained by the decreasing micro current flowing in dense regions due to impaired grain connectivity, which dominated the tail of ΔM curves. Since the addition of excess Mg can create the liquid phase environment, a lower sintering temperature is required to avoid the fast reaction between MgB_2 and hBN nanoparticles and prevent the gap generation within dense regions due to the quick liquid infiltration. The deterioration of 1hBN-5Mg-12hM-1200C and 2hBN-5Mg-6hM-1200C also arise from this reason. The linear scale shows the ΔM values in the low and medium field ranges, where 1hBN-5Mg-6hM samples have higher self-field than the un-doped MgB_2. This may be

ascribed to better macroscopic connectivity due to improved interconnectivity between subarrays of cells (i.e., the interface is free of MgO barrier layers).

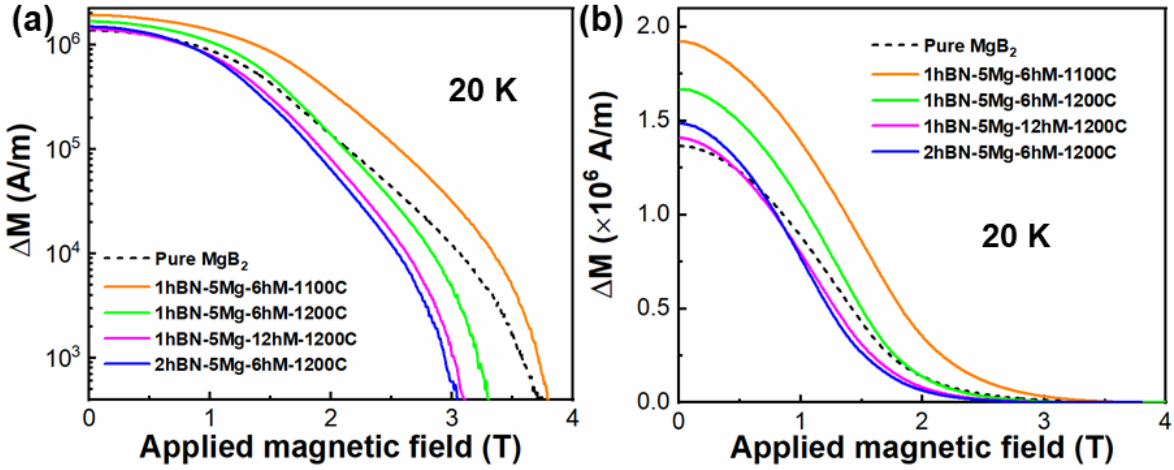


Figure 9.11 $\Delta M(B_{app})$ curves of MgB_2 samples with Mg and hBN additions processed at 1200 °C for 5 min on (a) a log-log scale and (b) a linear scale.

9.6 Superconducting properties of Cu and cBN co-doped MgB_2 bulk samples

Figure 9.12 shows susceptibility curves in Cu and cBN co-doped MgB_2 bulk samples. A slight decrease in T_c values can be observed in the sample processed at 900 °C for 15 min but the onset T_c of 2cBN-5Cu-1000C-F5min is reduced by around 1 K compared with pure MgB_2. The possible reason is the less recovery of the ball-milled disorder under the lower processing temperature and the short processing time.

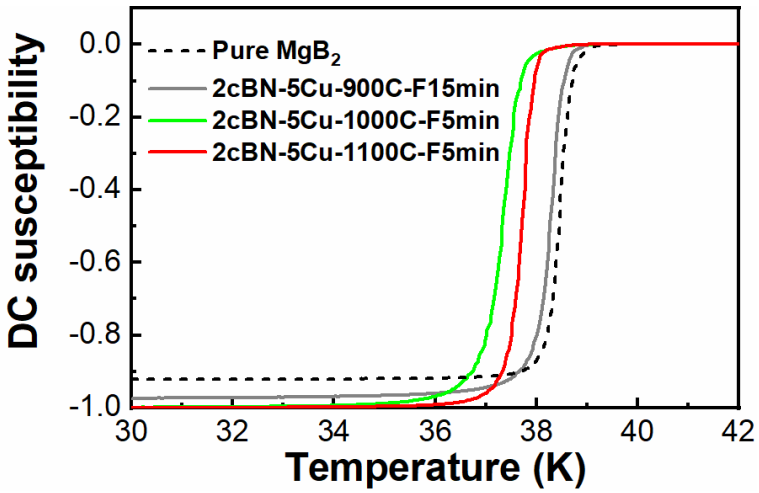


Figure 9.12 DC susceptibility curves under 5 mT in Cu and MgB_2 co-doped MgB_2 samples processed at different processing conditions.

The $\Delta M(B_{app})$ curves of samples are shown in Figure 9.13 on a log scale and a linear scale. The log-log plot indicates that this co-doping combination deteriorates the high-field performance. One possible reason is the fast grain growth in the liquid sintering process reduces the grain boundary pinning strength. Besides, the microstructures of these samples can be classified as Type II (Figure 9.8 and Figure 4.20). Section 4.2.6.2 has shown that the influence of microscopic currents will become prominent at high magnetic fields. Since the $MgCu_2$ impurities in the dense regions impair the grain connectivity, ΔM values drop faster. The improvement of ΔM by increasing processing temperatures is more obvious than prolonging the processing time. However, if compared to the improved low-field performance by the cBN addition (Figure 7.22 vs. Figure 9.13b), even for the best one in this sample series, 2cBN-5Cu-1100C-F5min, the low-field ΔM values do not see an increase. This finding reveals that the Cu addition cannot improve the grain connectivity of MgB_2 samples prepared by the ex-situ method,

which is different from the conclusion of some studies using a similar percentage of Cu addition but the in-situ route [112, 233]. Besides, one can see $MgCu_2$ impurities in these samples have detrimental effects on the superconducting performance rather than acting as pinning centres as the literature concluded [233].

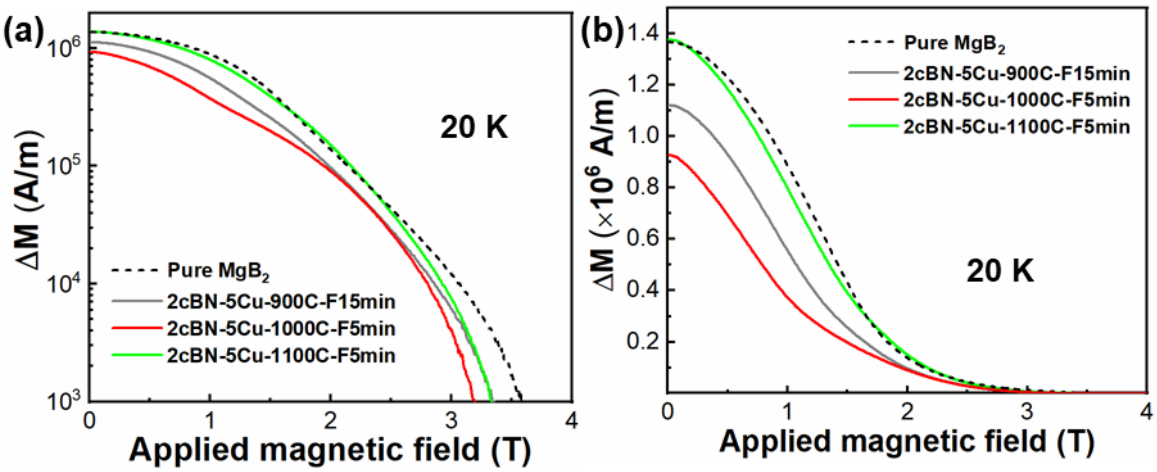


Figure 9.13 $\Delta M(B_{app})$ curves of MgB_2 samples with Cu and cBN additions processed at 1200 °C for 5 min on (a) a log-log scale and (b) a linear scale.

9.7 Conclusions

Two combinations of metal and N-containing dopants have been tried in this experimental work. The effects of hBN & Mg and cBN & Cu on the phase content, microstructures and superconducting performance of bulk samples are investigated and the following conclusions can be summarised:

i. Mg addition assists the formation of the Mg-N-B liquid phase so the processing temperature, as well as the percentage of hBN additions, should be reduced to avoid a fast and intensive reaction between the additions and MgB_2. Under the optimal processing conditions, Mg and hBN can have a synergistic effect on

MgB_2 performance. Mg can clean grain boundaries by preventing MgB_2 decomposition and decreasing the MgB_4 content, and the introduction of hBN can lead to the formation of tiny Mg(N,B) impurities. Therefore, an overall enhancement of ΔM is observed.

ii. Cu addition can help form Mg-Cu liquid but lowering the processing temperature does not lead to ΔM improvement. Instead, it results in a large amount of $MgCu_2$ impurities in grain boundaries, severely affecting the grain connectivity. Cu and cBN cannot produce a combined effect on MgB_2 performance. The enhancement of low-field performance of MgB_2 by adding cBN is eliminated by Cu addition, and large impurities formed during the sintering process are not efficient pinning centres and so do not offset the degradation caused by reduced connectivity.

Chapter 10 Conclusions and future work

The main aim of this project is to explore effective ways to improve the macro current density of MgB_2 bulk samples as well as investigate the link between different microstructure features and the corresponding superconducting performance. The conclusions from each chapter and suggestions for future work are summarised in this chapter.

10.1 Conclusions

Chapter 4 has shown that two primary problems exist in analysing data from moment measurements in many previous studies. One is the improper explanation of Jc calculated by Bean's critical model as currents flowing through the whole superconductor without considering microstructures. The other is the exploration of flux pinning mechanisms in superconducting materials using the applied magnetic field instead of the actual magnetic field to plot pinning curves. The duplex microstructural model takes homogeneity, anisotropy and connectivity into consideration, simulating the contribution of macro currents and cell currents under different conditions by changing corresponding parameters. This simulation method has not been systematically explored before, so also provides useful instruction in the superconducting analysis of studying other superconductors. The self-field corrections are often neglected when analysing pinning mechanisms but have strong effects on the

peak position of pinning curves. Since the peak position is an important reference to figure out the dominant pinning mechanism in superconductors. It is necessary to revise $J_c(B_{app})$ curves to $J_c(B)$ curves by instructions described in Section 4.3.2.

In the experimental work, high-energy ball milling was used to refine particle size and crystallite size. Two processing methods, ultra-high pressure-assisted sintering and field-assisted sintering, were applied to prepare MgB_2 bulk samples. Three main kinds of dopants (Mg, cBN and hBN) have been added in MgB_2 samples to explore the effects these additions could make.

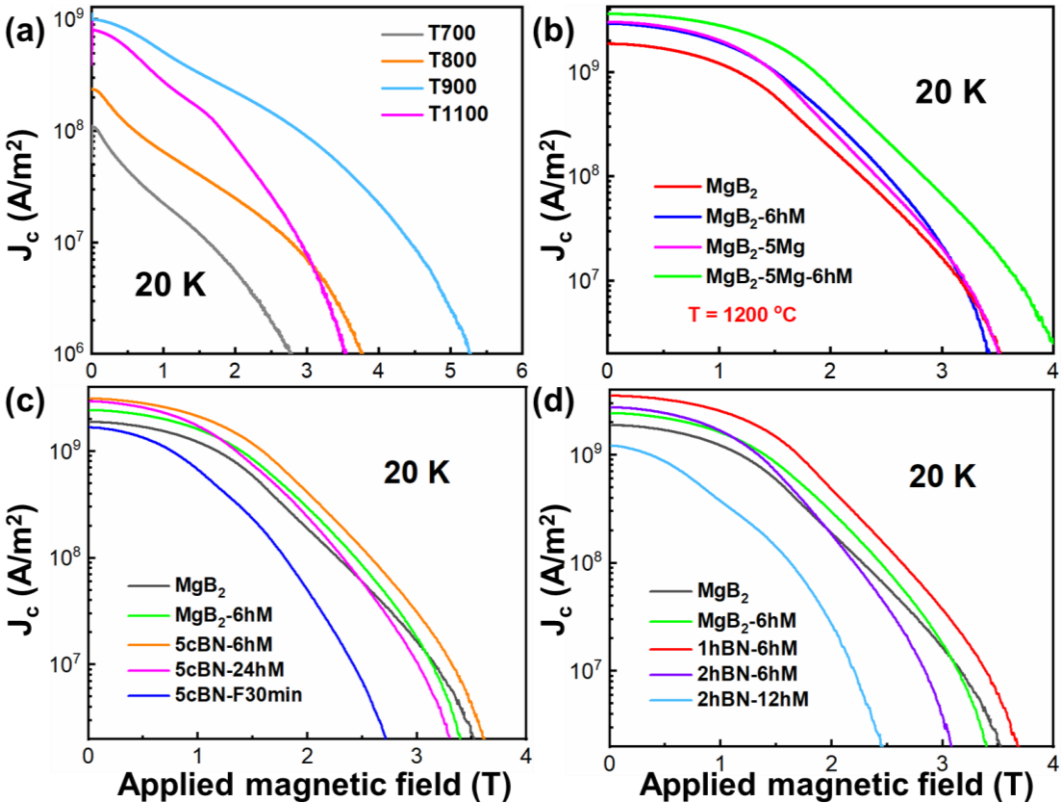


Figure 10.1 $J_c(B_{app})$ curves measured at 20 K and calculated by Bean's critical model of (a) MgB_2 samples processed under ultra-high pressure sintering, (b) 5wt% Mg+MgB_2 and unmodified samples prepared from milled powders, (c) 5 wt% cBN+MgB_2 samples processed under different conditions and (d) MgB_2 samples with 1 or 2 wt% hBN addition with powder milled for 6 h or 12 h.

Even though applying Bean's model to obtain J_c in MgB_2 bulk samples may not be reliable on some occasions, for easy comparison with other work, $J_c(B)$ curves of selected samples are calculated and presented in Figure 10.1. The following conclusions can be drawn:

i. Ultra-high pressure can shorten sintering time to 15 min (compared to several hours for hot pressing) and process nanostructured, dense MgB_2 polycrystalline bulks. High strain by the application of ultra-high pressure decreases the c axis of MgB_2 unit cells significantly and introduces grain defects, but it can be eliminated by increasing the sintering temperature. Complete densification is achieved by enhancing either the sintering temperature to 900 ºC or the applied pressure to 7.5 GPa. T_c deteriorates with extremely high pressure and low sintering temperature because of the lattice disorder. The overall enhancement of $J_c(B)$ curves, especially at high magnetic fields is achieved in T900 (Figure 10.1a), so the optimum conditions I recommend are: around 5 GPa for the applying pressures, around 900 ºC for the processing temperatures.

ii. Two opposite effects on J_c are brought by high-energy ball milling. The positive effect arises from crystallite refinement and the introduction of grain defects. However, a longer milling time (>24 h) leads to the saturation of crystallite refinement and oxygen contamination. Mg addition can provide a liquid environment for sintering to improve the mass transfer rate

and clean grain boundaries by preventing the formation of MgO, which contributes to the better low-field J_c performance. If combined with ball milling, the overall J_c performance of samples can be enhanced (Figure 10.1b).

iii. In brittle-brittle systems (cBN and MgB_2), cBN with larger particle sizes cab assist the crystallite refinement and size reduction of MgB_2 agglomerates. In ductile-brittle systems (hBN and MgB_2), soft and small nanoparticles/thin layers may slow down the efficiency of particle/crystallite refinement and cause the segregation problem of milled powders, which changes the sintering behaviour and increases sample inhomogeneity. With 6 h of milling and suitable percentages of BN (5 wt% for cBN and < 1 wt% for hBN), the improved pinning strength due to nano impurities and the presence of excess Mg help with fusing between particles during sintering and thus improves connectivity. Both factors lead to the enhancement of J_c curves in the entire range of fields, as shown in Figure 10.1c and d. 24 h milling combined with 5 wt% cBN or 2 wt% hBN addition can lead to excessive Mg-N-B impurities accumulated at grain boundaries, which has a negative effect, resulting in a severe percolation problem or even completely blocking currents between different regions. A compromise between the introduction of secondary phase particles to act as pinning centres to enhance intrinsic J_c and the adverse influence on grain connectivity should

be considered when deciding on the best dopant percentage.

iv. Mg and hBN can have a synergistic effect on MgB_2 performance in 1 wt% hBN and 5 wt% Mg co-doped samples processed at 1100 °C by the introduction of tiny Mg-N-B impurities and cleaner boundaries. In contrast, the enhancement of low-field performance of MgB_2 by adding cBN is eliminated by Cu addition, and large impurities formed during the sintering process do little to the pinning centres.

10.2 Future work

This research is not the end of the investigation on the ways to improve the superconducting performance of MgB_2. Instead, some experimental work needs to be carried out later to figure out answers to some problems proposed as follows:

i. This work mainly discusses the extrinsic factors influencing the microstructures to figure out the length scale that current can flow. The improvement of MgB_2 superconducting performance by introducing effective pinning centres with coherence length comparable to MgB_2 is less studied. Since impurities in grain boundaries will impair grain connectivity, nano defects inside the MgB_2 grains are expected to enhance J_c without impeding current flow across different grains. It would be interesting to find a dopant and design a processing route to create intra-grain pinning sites.

ii. The presence of agglomerates/aggregates will significantly influence the

sintering behaviour, so how to avoid agglomeration is a challenge for preparing MgB_2 powders by high-energy ball milling. One possible solution is to adopt wet ball milling by adding proper agents. The other is to use measures to break up agglomerates such as ultrasonication, finer mesh sieves, sedimentation, etc.

iii. Even though the trapped magnetic field (B_{trap}) can be somehow reflected by the J_c performance of bulk samples if samples are inhomogeneous, there are errors when using Bean's model to extract J_c and therefore obtain a reliable estimation of B_{trap}. The theoretical model proposed in this study can only estimate if macro currents are dominant in samples with different microstructural features. The accurate results of B_{trap} should be obtained by scanning hall probe microscopy.

iv. Other techniques, such as resistivity measurements that reflect the grain connectivity, should be carried out later to be supplementary to observation from microstructural characterisation. Moreover, TEM is supposed to be applied in order to observe nano defects.

References

[1] D. van Delft, P. Kes, The discovery of superconductivity. Physics Today, 2010. 63(9): p. 38-43.
[2] C. Buzea, T. Yamashita, Review of the superconducting properties of MgB_2. Superconductor Science and Technology, 2001. 14(11): p. R115-R146.
[3] B.T. Matthias, T.H. Geballe, R.H. Willens, E. Corenzwit, G.W. Hull, Superconductivity of Nb_3Ge. Physical Review, 1965. 139(5A): p. A1501-A1503.
[4] J.G. Bednorz, K.A. Müller, Possible high T_c superconductivity in the Ba-La-Cu-O system. Zeitschrift für Physik B Condensed Matter, 1986. 64(2): p. 189-193.
[5] M.K. Wu, J.R. Ashburn, C.J. Torng, P.H. Hor, R.L. Meng, L. Gao, Z.J. Huang, Y.Q. Wang, C.W. Chu, Superconductivity at 93 K in a new mixed-phase Y-Ba-Cu-O compound system at ambient pressure. Physical Review Letters, 1987. 58(9): p. 908-910.
[6] L. Gao, Y.Y. Xue, F. Chen, Q. Xiong, R.L. Meng, D. Ramirez, C.W. Chu, J.H. Eggert, H.K. Mao, Superconductivity up to 164 K in $HgBa_2Ca_{m-1}Cu_mO_{2m+2+\delta}$ (m=1, 2, and 3) under quasihydrostatic pressures. Physical Review B, 1994. 50(6): p. 4260-4263.
[7] H. Hosono, A. Yamamoto, H. Hiramatsu, Y. Ma, Recent advances in iron-based superconductors toward applications. Materials Today, 2018. 21(3): p. 278-302.
[8] P.J. Ray, Master's thesis: Structural investigation of $La_{(2-x)}Sr_{(x)}CuO_{(4+y)}$ - Following staging as a function of temperature. 2016
[9] J. Nagamatsu, N. Nakagawa, T. Muranaka, Y. Zenitani, J. Akimitsu, Superconductivity at 39 K in magnesium diboride. Nature, 2001. 410: p. 63.
[10] D.C. Larbalestier, L.D. Cooley, M.O. Rikel, A.A. Polyanskii, J. Jiang, S. Patnaik, X.Y. Cai, D.M. Feldmann, A. Gurevich, A.A. Squitieri, M.T. Naus, C.B. Eom, E.E. Hellstrom, R.J. Cava, K.A. Regan, N. Rogado, M.A. Hayward, T. He, J.S. Slusky, P. Khalifah, K. Inumaru, M. Haas, Strongly linked current flow in polycrystalline forms of the superconductor MgB_2. Nature, 2001. 410: p. 186.
[11] X.K. Chen, M.J. Konstantinovic, J.C. Irwin, D.D. Lawrie, J.P. Franck, Evidence for two superconducting gaps in MgB_2. Physical review letters, 2001. 87(15): p. 157002.
[12] W. Meissner, R. Ochsenfeld, Ein neuer effekt bei eintritt der supraleitfähigkeit. Naturwissenschaften, 1933. 21(44): p. 787-788.
[13] E. Maxwell, Isotope effect in the superconductivity of mercury. Physical Review, 1950. 78(4): p. 477-477.
[14] M. Tinkham, Introduction to superconductivity. 2004: Courier Corporation.
[15] C.P. Poole, R. Prozorov, H.A. Farach, R.J. Creswick, 2 - Phenomenon of superconductivity, in Superconductivity (Third Edition), C.P. Poole, et al., Editors. 2014, Elsevier: London. p. 33-85.
[16] F. London, H. London, The electromagnetic equations of the supraconductor. Proceedings of the Royal Society of London. Series A, Mathematical and Physical

Sciences (1934-1990), 1935. 149(866): p. 71-88.
[17] P. Mangin, R. Kahn, The non-local pippard equations, in Superconductivity: An introduction, P. Mangin and R. Kahn, Editors. 2017, Springer International Publishing: Cham. p. 49-57.
[18] A.A. Abrikosov, The magnetic properties of superconducting alloys. Journal of Physics and Chemistry of Solids, 1957. 2(3): p. 199-208.
[19] J. Bardeen, L.N. Cooper, J.R. Schrieffer, Theory of Superconductivity. Physical Review, 1957. 108(5): p. 1175-1204.
[20] E.H. Brandt, The flux-line lattice in superconductors. Reports on Progress in Physics, 1995. 58(11): p. 1465-1594.
[21] D. Dew-Hughes, Flux pinning mechanisms in type II superconductors. The Philosophical Magazine: A Journal of Theoretical Experimental and Applied Physics, 1974. 30(2): p. 293-305.
[22] G. Blatter, M.V. Feigel'man, V.B. Geshkenbein, A.I. Larkin, V.M. Vinokur, Vortices in high-temperature superconductors. Reviews of Modern Physics, 1994. 66(4): p. 1125-1388.
[23] A. Campbell, J. Evetts, D. Dew-Hughes, Pinning of flux vortices in type II superconductors. Philosophical Magazine, 1968. 18(152): p. 313-343.
[24] A.I. Larkin, Y.N. Ovchinnikov, Pinning in type II superconductors. Journal of Low Temperature Physics, 1979. 34(3): p. 409-428.
[25] G. Blatter, V.B. Geshkenbein, J.A.G. Koopmann, Weak to strong pinning crossover. Physical Review Letters, 2004. 92(6): p. 067009.
[26] R. Labusch, A statistical theory of solid solution hardening. Physica Status Solidi, 1970. 41(2): p. 659-&.
[27] M. Eisterer, Predicting critical currents in grain-boundary limited superconductors. Physical Review B, 2019. 99(9).
[28] A. Gümbel, J. Eckert, G. Fuchs, K. Nenkov, K.H. Müller, L. Schultz, Improved superconducting properties in nanocrystalline bulk MgB_2. Applied Physics Letters, 2002. 80(15): p. 2725-2727.
[29] T. Matsushita, M. Kiuchi, A. Yamamoto, J.-i. Shimoyama, K. Kishio, Essential factors for the critical current density in superconducting MgB_2: connectivity and flux pinning by grain boundaries. Superconductor Science and Technology, 2007. 21(1): p. 015008.
[30] T. Mousavi, P.S. Grant, S.C. Speller, C. Grovenor, New nanoscale artificial pinning centres for NbTi superconductors. Materials & Design, 2021. 198: p. 109285.
[31] S. Santra, T. Davies, G. Matthews, J. Liu, C.R.M. Grovenor, S.C. Speller, The effect of the size of NbTi filaments on interfacial reactions and the properties of InSn-based superconducting solder joints. Materials & Design, 2019. 176: p. 107836.
[32] D.K. Namburi, Y. Shi, A.R. Dennis, J.H. Durrell, D.A. Cardwell, A robust seeding technique for the growth of single grain (RE)BCO and (RE)BCO–Ag bulk superconductors. Superconductor Science and Technology, 2018. 31(4): p. 044003.

[33] A. Pomar, J. Gutiérrez, A. Palau, T. Puig, X. Obradors, Porosity induced magnetic granularity in epitaxial $YBa_2Cu_3O_7$ thin films. Physical Review B, 2006. 73(21).
[34] T. Matsushita, J. Tanigawa, M. Kiuchi, A. Yamamoto, J.I. Shimoyama, K. Kishio, Effect of packing density on critical current density at high magnetic fields in polycrystalline MgB_2 superconductors. Japanese Journal of Applied Physics, 2012. 51.
[35] M. Eisterer, J. Emhofer, S. Sorta, M. Zehetmayer, H.W. Weber, Connectivity and critical currents in polycrystalline MgB_2. Superconductor Science and Technology, 2009. 22(3).
[36] J.M. Rowell, The widely variable resistivity of MgB_2 samples. Superconductor Science and Technology, 2003. 16(6): p. R17-R27.
[37] D. Mou, S. Manni, V. Taufour, Y. Wu, L. Huang, S.L. Bud'ko, P.C. Canfield, A. Kaminski, Isotope effect on electron-phonon interaction in the multiband superconductor MgB_2. Physical Review B, 2016. 93(14).
[38] S.L. Bud'ko, G. Lapertot, C. Petrovic, C.E. Cunningham, N. Anderson, P.C. Canfield, Boron isotope effect in superconducting MgB_2. Phys Rev Lett, 2001. 86(9): p. 1877-80.
[39] MgB_2 Crystal Structure: Datasheet from "PAULING FILE Multinaries Edition – 2012" in Springer Materials. Springer-Verlag Berlin Heidelberg & Material Phases Data System (MPDS), Switzerland & National Institute for Materials Science (NIMS), Japan.
[40] S. Brutti, A. Ciccioli, G. Balducci, G. Gigli, P. Manfrinetti, A. Palenzona, Vaporization thermodynamics of MgB_2 and MgB_4. Applied Physics Letters, 2002. 80(16): p. 2892-2894.
[41] H.J. Choi, D. Roundy, H. Sun, M.L. Cohen, S.G. Louie, The origin of the anomalous superconducting properties of MgB_2. Nature, 2002. 418: p. 758.
[42] T. Yildirim, The surprising superconductor. Materials Today, 2002. 5(4): p. 40-44.
[43] J.H. Durrell, M.D. Ainslie, D. Zhou, P. Vanderbemden, T. Bradshaw, S. Speller, M. Filipenko, D.A. Cardwell, Bulk superconductors: a roadmap to applications. Superconductor Science and Technology, 2018. 31(10).
[44] K.D. Belashchenko, M.v. Schilfgaarde, V.P. Antropov, Coexistence of covalent and metallic bonding in the boron intercalation superconductor MgB_2. Physical Review B, 2001. 64(9): p. 092503.
[45] H.J. Choi, M.L. Cohen, S.G. Louie, Anisotropic Eliashberg theory of MgB_2: T_c, isotope effects, superconducting energy gaps, quasiparticles, and specific heat. Physica C: Superconductivity, 2003. 385(1): p. 66-74.
[46] A. Mialitsin, B.S. Dennis, N.D. Zhigadlo, J. Karpinski, G. Blumberg, Anharmonicity and self-energy effects of the E_{2g} phonon in MgB_2. Physical Review B, 2007. 75(2): p. 020509.
[47] J.M. An, W.E. Pickett, Superconductivity of MgB_2: Covalent bonds driven metallic. Physical Review Letters, 2001. 86(19): p. 4366-4369.
[48] I.I. Mazin, V.P. Antropov, Electronic structure, electron–phonon coupling, and multiband effects in MgB_2. Physica C: Superconductivity, 2003. 385(1): p. 49-65.

[49] K. Vinod, N. Varghese, U. Syamaprasad, Superconductivity of MgB_2 in the BCS framework with emphasis on extrinsic effects on critical temperature. Superconductor Science and Technology, 2007. 20(10): p. R31-R45.
[50] S.C. Erwin, I.I. Mazin, Toward one-band superconductivity in MgB_2. Physical Review B, 2003. 68(13): p. 132505.
[51] A.V. Sologubenko, N.D. Zhigadlo, S.M. Kazakov, J. Karpinski, H.R. Ott, Influence of carbon substitution on the heat transport in single crystalline MgB_2. Physical Review B, 2005. 71(2): p. 020501.
[52] W. Pickett, Mind the double gap. Nature, 2002. 418(6899): p. 733-734.
[53] X.K. Chen, M.J. Konstantinovic, J.C. Irwin, D.D. Lawrie, J.P. Franck, Evidence for two superconducting gaps in MgB_2. Phys Rev Lett, 2001. 87(15): p. 157002.
[54] P. Szabo, P. Samuely, J. Kacmarcik, T. Klein, J. Marcus, D. Fruchart, S. Miraglia, C. Marcenat, A.G. Jansen, Evidence for two superconducting energy gaps in MgB_2 by point-contact spectroscopy. Phys Rev Lett, 2001. 87(13): p. 137005.
[55] S. Tsuda, T. Yokoya, Y. Takano, H. Kito, A. Matsushita, F. Yin, J. Itoh, H. Harima, S. Shin, Definitive experimental evidence for two-band superconductivity in MgB_2. Phys Rev Lett, 2003. 91(12): p. 127001.
[56] T.W. Heitmann, S.D. Bu, D.M. Kim, J.H. Choi, J. Giencke, C.B. Eom, K.A. Regan, N. Rogado, M. Hayward, T. He, J.S. Slusky, P. Khalifah, M. Haas, R.J. Cava, D.C. Larbalestier, M.S. Rzchowski, MgB_2 energy gap determination by scanning tunnelling spectroscopy. Superconductor Science and Technology, 2004. 17.
[57] A. Gurevich, S. Patnaik, V. Braccini, K.H. Kim, C. Mielke, X. Song, L.D. Cooley, S.D. Bu, D.M. Kim, J.H. Choi, L.J. Belenky, J. Giencke, M.K. Lee, W. Tian, X.Q. Pan, A. Siri, E.E. Hellstrom, C.B. Eom, D.C. Larbalestier, Very high upper critical fields in MgB_2 produced by selective tuning of impurity scattering. Superconductor Science and Technology, 2003. 17(2): p. 278-286.
[58] A. Yamamoto, H. Tanaka, J.-i. Shimoyama, H. Ogino, K. Kishio, T. Matsushita, Towards the realization of higher connectivity in MgB_2 conductors: In-situ or sintered ex-situ? Japanese Journal of Applied Physics, 2012. 51(1).
[59] C.E.J. Dancer, P. Mikheenko, A. Bevan, J.S. Abell, R.I. Todd, C.R.M. Grovenor, A study of the sintering behaviour of magnesium diboride. Journal of the European Ceramic Society, 2009. 29(9): p. 1817-1824.
[60] A.G. Bhagurkar, A. Yamamoto, L. Wang, M. Xia, A.R. Dennis, J.H. Durrell, T.A. Aljohani, N.H. Babu, D.A. Cardwell, High trapped fields in C-doped MgB_2 bulk superconductors fabricated by infiltration and growth process. Sci Rep, 2018. 8(1): p. 13320.
[61] J. Zou, M.D. Ainslie, H. Fujishiro, A.G. Bhagurkar, T. Naito, N. Hari Babu, J.F. Fagnard, P. Vanderbemden, A. Yamamoto, Numerical modelling and comparison of MgB_2 bulks fabricated by HIP and infiltration growth. Superconductor Science and Technology, 2015. 28(7): p. 075009.
[62] A.G. Bhagurkar, A. Yamamoto, A.R. Dennis, J.H. Durrell, T.A. Aljohani, H.B.

Nadendla, D.A. Cardwell, Microstructural evolution in infiltration-growth processed MgB_2 bulk superconductors. Journal of the American Ceramic Society, 2017. 100(6): p. 2451-2460.
[63] C.E.J. Dancer, D. Prabhakaran, M. Başoğlu, E. Yanmaz, H. Yan, M. Reece, R.I. Todd, C.R.M. Grovenor, Fabrication and properties of dense ex situ magnesium diboride bulk material synthesized using spark plasma sintering. Superconductor Science and Technology, 2009. 22(9): p. 095003.
[64] C.Q. Jin, S.C. Li, J.L. Zhu, F.Y. Li, Z.X. Liu, R.C. Yu, High critical current density of a MgB_2 bulk superconductor high-pressure synthesized directly from the elements. Journal of Materials Research, 2002. 17(3): p. 525-527.
[65] S. Mizutani, A. Yamamoto, J.I. Shimoyama, H. Ogino, K. Kishio, Self-sintering-assisted high intergranular connectivity in ball-milled ex situ MgB_2 bulks. Superconductor Science and Technology, 2014. 27(11).
[66] T. Naito, Y. Endo, H. Fujishiro, Optimization of vortex pinning at grain boundaries on ex-situ MgB_2 bulks synthesized by spark plasma sintering. Superconductor Science and Technology, 2017. 30(9).
[67] G.A.B. Matthews, S. Santra, R. Ma, C.R.M. Grovenor, P.S. Grant, S.C. Speller, Effect of the sintering temperature on the microstructure and superconducting properties of MgB_2 bulks manufactured by the field assisted sintering technique. Superconductor Science and Technology, 2020. 33(5).
[68] A. Mesquita, M.I.B. Bernardi, V.R. Mastelaro, M.H. Lente, J.A. Eiras, M.R. Gallas, T.M.H. Costa, Nanograined ferroelectric ceramics prepared by high-pressure densification technique. Journal of the American Ceramic Society, 2009. 92(8): p. 1679-1683.
[69] D. Lahiri, V. Singh, G.R. Rodrigues, T.M.H. Costa, M.R. Gallas, S.R. Bakshi, S. Seal, A. Agarwal, Ultra high-pressure consolidation and deformation of tantalum carbide at ambient and high temperatures. Acta Materialia, 2013. 61(11): p. 4001-4009.
[70] J. Gu, J. Zou, J. Liu, H. Wang, J. Zhang, W. Wang, Z. Fu, Sintering highly dense ultra-high temperature ceramics with suppressed grain growth. Journal of the European Ceramic Society, 2020. 40(4): p. 1086-1092.
[71] B. Matovic, F. Zivic, S. Mitrovic, D. Prsic, V. Maksimovic, T. Volkov-Husovic, R. Kumar, N. Daneu, Ultra-high pressure densification and properties of nanostructured SiC. Materials Letters, 2016. 164: p. 68-71.
[72] L. Liu, X. Li, Q. He, L. Xu, X. Cao, X. Peng, C. Meng, W. Wang, W. Zhu, Y. Wang, Sintering dense boron carbide without grain growth under high pressure. Journal of the American Ceramic Society, 2018. 101(3): p. 1289-1297.
[73] P.P. Singh, From E_{2g} to other modes: effects of pressure on electron-phonon interaction in MgB_2. Phys Rev Lett, 2006. 97(24): p. 247002.
[74] F. Liu, D. He, P. Liu, H. Wang, C. Xu, S. Yin, W. Yin, Y. Li, Plastic deformation and sintering of alumina under high pressure. Journal of Applied Physics, 2013. 114(23): p. 233504.

[75] G. Fuchs, B. Holzapfel, K.H. Müller, L. Schultz, Superconductors: Basic properties and materials development of MgB_2, in Encyclopedia of Materials: Science and Technology, K.H.J. Buschow, et al., Editors. 2006, Elsevier: Oxford. p. 1-6.
[76] J.M. Rowell, S.Y. Xu, X.H. Zeng, A.V. Pogrebnyakov, Q. Li, X.X. Xi, J.M. Redwing, W. Tian, X. Pan, Critical current density and resistivity of MgB_2 films. Applied Physics Letters, 2003. 83(1): p. 102-104.
[77] A. Martinelli, C. Tarantini, E. Lehmann, P. Manfrinetti, A. Palenzona, I. Pallecchi, M. Putti, C. Ferdeghini, Direct TEM observation of nanometric-sized defects in neutron-irradiated MgB_2 bulk and their effect on pinning mechanisms. Superconductor Science and Technology, 2008. 21(1).
[78] I. Pallecchi, M. Putti, Properties of irradiated MgB_2, bulk and wires, in MgB_2 Superconducting Wires. 2015, WORLD SCIENTIFIC. p. 455-483.
[79] M. Putti, R. Vaglio, J.M. Rowell, Radiation effects on MgB_2: a review and a comparison with A15 superconductors. Superconductor Science and Technology, 2008. 21(4).
[80] C. Tarantini, H.U. Aebersold, V. Braccini, G. Celentano, C. Ferdeghini, V. Ferrando, U. Gambardella, F. Gatti, E. Lehmann, P. Manfrinetti, D. Marré, A. Palenzona, I. Pallecchi, I. Sheikin, A.S. Siri, M. Putti, Effects of neutron irradiation on polycrystalline $Mg^{11}B_2$. Physical Review B, 2006. 73(13): p. 134518.
[81] G.K. Perkins, Y. Bugoslavsky, A.D. Caplin, J. Moore, T.J. Tate, R. Gwilliam, J. Jun, S.M. Kazakov, J. Karpinski, L.F. Cohen, Effects of proton irradiation and ageing on the superconducting properties of single crystalline and polycrystalline MgB_2. Superconductor Science and Technology, 2003. 17(1): p. 232-235.
[82] Y. Bugoslavsky, L.F. Cohen, G.K. Perkins, M. Polichetti, T.J. Tate, R. Gwilliam, A.D. Caplin, Enhancement of the high-magnetic-field critical current density of superconducting MgB_2 by proton irradiation. Nature, 2001. 411(6837): p. 561-563.
[83] V. Sandu, A.M. Ionescu, I. Ivan, L. Craciun, G. Aldica, Effect of proton fluence on the superconducting properties of MgB_2 irradiated with protons of high energy. Physica C: Superconductivity and its Applications, 2020. 578: p. 1353734.
[84] M. Eisterer, Influence of disorder on H_{c2}-anisotropy and flux pinning in MgB_2. physica status solidi (c), 2005. 2(5): p. 1606-1614.
[85] M. Eisterer, M. Zehetmayer, S. T nies, H.W. Weber, M. Kambara, N.H. Babu, D.A. Cardwell, L.R. Greenwood, Neutron irradiation of MgB_2 bulk superconductors. Superconductor Science and Technology, 2002. 15(2): p. L9-L12.
[86] G. Faraji, H.S. Kim, H.T. Kashi, Introduction, in Severe plastic deformation, G. Faraji, H.S. Kim, and H.T. Kashi, Editors. 2018, Elsevier. p. 1-17.
[87] O. Roberto, L. Roberta, L. Antonio Mario, C. Giacomo, 12 - Mechanochemically activated powders as precursors for spark plasma sintering (SPS) processes, in High-Energy Ball Milling, M. Sopicka-Lizer, Editor. 2010, Woodhead Publishing. p. 275-303.
[88] W. Häßler, H. Hermann, M. Herrmann, C. Rodig, A. Aubele, L. Schmolinga, B. Sailer, B. Holzapfel, Influence of the milling energy transferred to the precursor powder

on the microstructure and the superconducting properties of MgB_2 wires. Superconductor Science and Technology, 2013. 26(2).
[89] W. Häßler, B. Birajdar, W. Gruner, M. Herrmann, O. Perner, C. Rodig, M. Schubert, B. Holzapfel, O. Eibl, L. Schultz, MgB_2 bulk and tapes prepared by mechanical alloying: influence of the boron precursor powder. Superconductor Science and Technology, 2006. 19(6): p. 512-520.
[90] S. Sugino, A. Yamamoto, J.-i. Shimoyama, K. Kishio, Enhanced trapped field in MgB_2 bulk magnets by tuning grain boundary pinning through milling. Superconductor Science and Technology, 2015. 28(5): p. 055016.
[91] S. Mizutani, A. Yamamoto, J.-i. Shimoyama, H. Ogino, K. Kishio, Self-sintering-assisted high intergranular connectivity in ball-milled ex situ MgB_2 bulks. Superconductor Science and Technology, 2014. 27(11): p. 114001.
[92] P. Mikheenko, E. Martínez, A. Bevan, J.S. Abell, J.L. MacManus-Driscoll, Grain boundaries and pinning in bulk MgB_2. Superconductor Science and Technology, 2007. 20(9): p. S264-S270.
[93] G.A.B. Matthews, J. Liu, C.R.M. Grovenor, P.S. Grant, S. Speller, Design and characterisation of ex situ bulk MgB_2 superconductors containing a nanoscale dispersion of artificial pinning centres. Superconductor Science and Technology, 2020. 33(3).
[94] S. Soltanian, J. Horvat, X.L. Wang, P. Munroe, S.X. Dou, Effect of nano-carbon particle doping on the flux pinning properties of MgB_2 superconductor. Physica C: Superconductivity, 2003. 390(3): p. 185-190.
[95] G. Pasquini, A. Serquis, A.J. Moreno, G. Serrano, L. Civale, Carbon nanotubes effects on the relaxation properties and critical current densities of MgB_2 superconductor. Journal of Applied Physics, 2013. 114(2).
[96] G. Aldica, M. Burdusel, S. Popa, Y. Hayasaka, P. Badica, Graphene addition to MgB_2 superconductor obtained by ex-situ spark plasma sintering technique. Materials Research Bulletin, 2016. 77: p. 205-211.
[97] B.J. Senkowicz, J.E. Giencke, S. Patnaik, C.B. Eom, E.E. Hellstrom, D.C. Larbalestier, Improved upper critical field in bulk-form magnesium diboride by mechanical alloying with carbon. Applied Physics Letters, 2005. 86(20): p. 202502.
[98] M.A. Susner, S.D. Bohnenstiehl, S.A. Dregia, M.D. Sumption, Y. Yang, J.J. Donovan, E.W. Collings, Homogeneous carbon doping of magnesium diboride by high-temperature, high-pressure synthesis. Applied Physics Letters, 2014. 104(16).
[99] J.S. Hansdah, P.M. Sarun, Doping effect of nano-Ho_2O_3 and naphthalene in MgB_2 superconductor prepared by powder-in-sealed-tube method. Journal of Applied Physics, 2015. 117(11): p. 113903.
[100] J. Kortus, O.V. Dolgov, R.K. Kremer, A.A. Golubov, Band filling and interband scattering effects in MgB_2: Carbon versus aluminum doping. Physical Review Letters, 2005. 94(2): p. 027002.
[101] M. Angst, S.L. Bud'ko, R.H.T. Wilke, P.C. Canfield, Difference between Al and

C doping in anisotropic upper critical field development in MgB_2. Physical Review B, 2005. 71(14): p. 144512.
[102] A.G. Bhagurkar, A. Yamamoto, L. Wang, M. Xia, A.R. Dennis, J.H. Durrell, T.A. Aljohani, N.H. Babu, D.A. Cardwell, High trapped fields in C-doped MgB_2 bulk superconductors fabricated by infiltration and growth process. Scientific Reports, 2018. 8(1): p. 13320.
[103] A. Yamamoto, J.I. Shimoyama, S. Ueda, I. Iwayama, S. Horii, K. Kishio, Effects of B_4C doping on critical current properties of MgB_2 superconductor. Superconductor Science and Technology, 2005. 18(10): p. 1323-1328.
[104] Y. Yang, Influence of chemical doping on microstructures and superconducting properties of MgB_2 wires and bulk samples. 2016
[105] J.Y. Xiang, D.N. Zheng, J.Q. Li, S.L. Li, H.H. Wen, Z.X. Zhao, Effects of Al doping on the superconducting and structural properties of MgB_2. Physica C: Superconductivity, 2003. 386: p. 611-615.
[106] A. Berenov, A. Serquis, X.Z. Liao, Y.T. Zhu, D.E. Peterson, Y. Bugoslavsky, K.A. Yates, M.G. Blamire, L.F. Cohen, J.L. MacManus-Driscoll, Enhancement of critical current density in low level Al-doped MgB_2. Superconductor Science and Technology, 2004. 17(10): p. 1093-1096.
[107] Y.G. Zhao, X.P. Zhang, P.T. Qiao, H.T. Zhang, S.L. Jia, B.S. Cao, M.H. Zhu, Z.H. Han, X.L. Wang, B.L. Gu, Effect of Li doping on structure and superconducting transition temperature of $Mg_{1-x}Li_xB_2$. Physica C: Superconductivity, 2001. 361(2): p. 91-94.
[108] D. Daghero, G.A. Ummarino, M. Tortello, D. Delaude, R.S. Gonnelli, V.A. Stepanov, M. Monni, A. Palenzona, Effect of Li–Al co-doping on the energy gaps of MgB_2. Superconductor Science and Technology, 2009. 22(2): p. 025012.
[109] I. Pallecchi, P. Brotto, C. Ferdeghini, M. Putti, A. Palenzona, P. Manfrinetti, A. Geddo Lehmann, A. Orecchini, C. Petrillo, F. Sacchetti, M. Affronte, G. Allodi, R. De Renzi, S. Serventi, A. Andreone, G. Lamura, D. Daghero, R.S. Gonnelli, M. Tortello, Investigation of Li-doped MgB_2. Superconductor Science and Technology, 2009. 22(9): p. 095014.
[110] C. Shekhar, R. Giri, R.S. Tiwari, O.N. Srivastava, S.K. Malik, High critical current density and improved flux pinning in bulk MgB_2 synthesized by Ag addition. Journal of Applied Physics, 2007. 101(4): p. 043906.
[111] S.M. Kazakov, M. Angst, J. Karpinski, I.M. Fita, R. Puzniak, Substitution effect of Zn and Cu in MgB_2 on T_c and structure. Solid State Communications, 2001. 119(1): p. 1-5.
[112] Z. Ma, Y. Liu, Z. Gao, The synthesis and grain connectivity of lamellar MgB_2 grains by Cu-activated sintering at low temperature. Scripta Materialia, 2010. 63(4): p. 399-402.
[113] N. Varghese, K. Vinod, S. Rahul, K.M. Devadas, S. Thomas, S. Pradhan, U. Syamaprasad, Influence of nano-Cu additive on MgB_2 phase formation, processing

temperature, and transport properties. Journal of Applied Physics, 2011. 109(3).
[114] I.A. Ansari, Study of dynamic behaviors for nano Fe-doped MgB_2 superconductor via ac-susceptibility measurements. Ceramics International, 2019. 45(2, Part A): p. 1523-1527.
[115] W.X. Li, R. Zeng, C.K. Poh, Y. Li, S.X. Dou, Magnetic scattering effects in two-band superconductor: the ferromagnetic dopants in MgB_2. J Phys Condens Matter, 2010. 22(13): p. 135701.
[116] O. Lima, K. Vieira, E. Moschim, V. Awana, H. Kishan, Nano-Ni addition to MgB_2 : effects on the superconducting properties. Journal of Materials Science Letters, 2010. 45(18): p. 4929-4933.
[117] G. Kirat, O. Kizilaslan, M.A. Aksan, M.E. Yakinci, Effect of Co addition on the critical current density of MgB_2 superconductor. Physica B: Condensed Matter, 2014. 445: p. 24-27.
[118] B. Gahtori, R. Lal, S.K. Agarwal, Y.K. Kuo, K.M. Sivakumar, J.K. Hsu, J.Y. Lin, A. Rao, S.K. Chen, J.L. MacManus-Driscoll, Effects of Fe substitution on the transport properties of the superconductor MgB_2. Physical Review B, 2007. 75(18): p. 184513.
[119] S.X. Dou, S. Soltanian, Y. Zhao, E. Getin, Z. Chen, O. Shcherbakova, J. Horvat, The effect of nanoscale Fe doping on the superconducting properties of MgB_2. Superconductor Science and Technology, 2005. 18(5): p. 710-715.
[120] N. Novosel, E. Babić, Influence of magnetic nanoparticles on superconductivity of MgB_2. Physica C: Superconductivity, 2013. 493: p. 119-124.
[121] W.K. Yeoh, X.Y. Cui, B. Gault, K.S. De Silva, X. Xu, H.W. Liu, H.W. Yen, D. Wong, P. Bao, D.J. Larson, I. Martin, W.X. Li, R.K. Zheng, X.L. Wang, S.X. Dou, S.P. Ringer, On the roles of graphene oxide doping for enhanced supercurrent in MgB_2 based superconductors. Nanoscale, 2014. 6(11): p. 6166-72.
[122] W. Li, J. Kang, S. Fu, Y. Hu, P. Hu, M. Zhu, Y. Li, Rare earth doping effects on superconducting properties of MgB_2: A review. Journal of Rare Earths, 2019. 37(2): p. 124-133.
[123] J. Wang, Y. Bugoslavsky, A. Berenov, L. Cowey, A.D. Caplin, L.F. Cohen, J.L. MacManus Driscoll, L.D. Cooley, X. Song, D.C. Larbalestier, High critical current density and improved irreversibility field in bulk MgB_2 made by a scaleable, nanoparticle addition route. Applied Physics Letters, 2002. 81(11): p. 2026-2028.
[124] S.K. Chen, M. Wei, J.L. MacManus-Driscoll, Strong pinning enhancement in MgB_2 using very small Dy_2O_3 additions. Applied Physics Letters, 2006. 88(19): p. 192512.
[125] C. Cheng, Y. Zhao, Enhancement of critical current density of MgB_2 by doping Ho_2O_3. Applied Physics Letters, 2006. 89(25): p. 252501.
[126] M. Gharaibeh, B.A. Albiss, I. Jumah, I.M. Obaidat, Effective incorporation of nanoceria into polycrystalline MgB_2. Journal of Applied Physics, 2010. 107(6): p. 063908.
[127] N. Ojha, G.D. Varma, H.K. Singh, V.P.S. Awana, Effect of rare-earth doping on

the superconducting properties of MgB_2. Journal of Applied Physics, 2009. 105(7): p. 07E315.
[128] C. Yao, X. Zhang, D. Wang, Z. Gao, L. Wang, Y. Qi, C. Wang, Y. Ma, S. Awaji, K. Watanabe, Doping effects of Nd_2O_3 on the superconducting properties of powder-in-tube MgB_2 tapes. Superconductor Science and Technology, 2011. 24(5): p. 055016.
[129] K. Vinod, N. Varghese, U. Syamaprasad, Shipra, A. Sundaresan, Structural and superconducting properties of bulk MgB_2 with added nano Tb_4O_7. Superconductor Science and Technology, 2008. 21(2): p. 025003.
[130] X. Pan, C. Cheng, Y. Zhao, Effect of rare-earth oxides doping on the superconductivity and flux pinning of MgB_2 superconductor. Journal of superconductivity and novel magnetism, 2011. 24(5): p. 1611-1616.
[131] H.L. Xu, Y. Feng, Z. Xu, G. Yan, C.S. Li, E. Mossang, A. Sulpice, Effects of TiB_2 doping on the critical current density of MgB_2 wires. Physica C: Superconductivity, 2006. 443(1): p. 5-8.
[132] X. Zhang, Z. Gao, D. Wang, Z. Yu, Y. Ma, S. Awaji, K. Watanabe, Improved critical current densities in MgB_2 tapes with ZrB_2 doping. Applied Physics Letters, 2006. 89(13).
[133] M. Bhatia, M.D. Sumption, E.W. Collings, S. Dregia, Increases in the irreversibility field and the upper critical field of bulk MgB_2 by ZrB_2 addition. Applied Physics Letters, 2005. 87(4).
[134] Y. Yang, M.D. Sumption, E.W. Collings, Influence of metal diboride and Dy_2O_3 additions on microstructure and properties of MgB_2 fabricated at high temperatures and under pressure. Sci Rep, 2016. 6: p. 29306.
[135] E.M. Cherry, P.G. Maxim, J.K. Eaton, Particle size, magnetic field, and blood velocity effects on particle retention in magnetic drug targeting. Medical Physics, 2010. 37(1): p. 175-182.
[136] J.H. Durrell, M.D. Ainslie, D. Zhou, P. Vanderbemden, T. Bradshaw, S. Speller, M. Filipenko, D.A. Cardwell, Bulk superconductors: a roadmap to applications. Superconductor Science and Technology, 2018. 31(10): p. 103501.
[137] B. Polyak, G. Friedman, Magnetic targeting for site-specific drug delivery: applications and clinical potential. Expert Opin Drug Deliv, 2009. 6(1): p. 53-70.
[138] Y.L. Liu, D. Chen, P. Shang, D.C. Yin, A review of magnet systems for targeted drug delivery. J Control Release, 2019. 302: p. 90-104.
[139] M. Muthana, A.J. Kennerley, R. Hughes, E. Fagnano, J. Richardson, M. Paul, C. Murdoch, F. Wright, C. Payne, M.F. Lythgoe, N. Farrow, J. Dobson, J. Conner, J.M. Wild, C. Lewis, Directing cell therapy to anatomic target sites in vivo with magnetic resonance targeting. Nat Commun, 2015. 6: p. 8009.
[140] J. Riegler, J.A. Wells, P.G. Kyrtatos, A.N. Price, Q.A. Pankhurst, M.F. Lythgoe, Targeted magnetic delivery and tracking of cells using a magnetic resonance imaging system. Biomaterials, 2010. 31(20): p. 5366-71.
[141] M.J. Hills, S. Amirkhanlou, V. Bayliss, T.W. Bradshaw, M.R. Crook, G. Damiani,

J.H. Durrell, S. Greenwood, C.R.M. Grovenor, G. Matthews, S.C. Speller, D. Zhou, A compact high field magnet system for medical applications. IOP Conference Series: Materials Science and Engineering, 2019. 502: p. 012164.
[142] C. Wang, Y. Ma, X. Zhang, Z. Gao, D. Wang, C. Yao, C. Wang, H. Oguro, S. Awaji, K. Watanabe, Significant improvement in critical current densities of C-doped MgB_2 tapes made by high-energy ball milling. Superconductor Science and Technology, 2012. 25(7).
[143] C. Wang, Y. Ma, X. Zhang, D. Wang, Z. Gao, C. Yao, C. Wang, H. Oguro, S. Awaji, K. Watanabe, Effect of high-energy ball milling time on superconducting properties of MgB_2 with low purity boron powder. Superconductor Science and Technology, 2012. 25(3).
[144] J.B. Fogagnolo, F. Velasco, M.H. Robert, J.M. Torralba, Effect of mechanical alloying on the morphology, microstructure and properties of aluminium matrix composite powders. Materials Science and Engineering: A, 2003. 342(1): p. 131-143.
[145] C. Suryanarayana, Mechanical alloying and milling. Progress in Materials Science, 2001. 46(1): p. 1-184.
[146] S. Matthews, C. Doyle, B. James, High energy ball milling (HEBM) of high volume fraction hard-phase composite powder: Production and characterisation of Al_4C_3-27 vol.% NiCrAlY composite powder. Powder Technology, 2013. 237: p. 221-227.
[147] R. Orrù, R. Licheri, A.M. Locci, A. Cincotti, G. Cao, Consolidation/synthesis of materials by electric current activated/assisted sintering. Materials Science and Engineering: R: Reports, 2009. 63(4): p. 127-287.
[148] Z.Y. Hu, Z.H. Zhang, X.W. Cheng, F.C. Wang, Y.F. Zhang, S.L. Li, A review of multi-physical fields induced phenomena and effects in spark plasma sintering: Fundamentals and applications. Materials & Design, 2020. 191: p. 108662.
[149] O. Guillon, J. Gonzalez-Julian, B. Dargatz, T. Kessel, G. Schierning, J. Räthel, M. Herrmann, Field-assisted sintering technology/spark plasma sintering: Mechanisms, materials, and technology developments. Advanced Engineering Materials, 2014. 16(7): p. 830-849.
[150] P. Scardi, M. Leoni, Line profile analysis: pattern modelling versus profile fitting. Journal of Applied Crystallography, 2006. 39(1): p. 24-31.
[151] T.a.G. Ungár, Jenő, Nanocrystalline materials studied by powder diffraction line profile analysis. Zeitschrift für Kristallographie, 2007. 222(3-4): p. 114-128.
[152] K.C. Verma, R.K. Kotnala, Lattice defects induce multiferroic responses in Ce, La-substituted $BaFe_{0.01}Ti_{0.99}O_3$ nanostructures. Journal of the American Ceramic Society, 2016. 99(5): p. 1601-1608.
[153] A.L. Ortiz, L. Shaw, X-ray diffraction analysis of a severely plastically deformed aluminum alloy. Acta Materialia, 2004. 52(8): p. 2185-2197.
[154] The Empyrean Tube.
https://www.malvernpanalytical.com/en/products/category/x-ray-

tubes/xrdtubes/empyreantube/
[155] L. Ingemarsson, M. Halvarsson, SEM/EDX analysis of boron. High Temperature Corrosion Centre-Chalmer University of Technology: Gothenburg, Sweden, 2011.
[156] J.I. Goldstein, D.E. Newbury, J.R. Michael, N.W.M. Ritchie, J.H.J. Scott, D.C. Joy, X-Rays, in Scanning Electron Microscopy and X-Ray Microanalysis, J.I. Goldstein, et al., Editors. 2018, Springer New York: New York, NY. p. 39-63.
[157] Periodic table of elements and X-ray energies. Bruker. https://www.bruker.com/en/products-and-solutions/elemental-analyzers/handheld-xrf-spectrometers/TRACER-5.html
[158] AZtec Live In Depth: TruMap. https://nano.oxinst.com/library/app-note-library.
[159] J.I. Goldstein, D.E. Newbury, J.R. Michael, N.W.M. Ritchie, J.H.J. Scott, D.C. Joy, Quantitative Analysis: The SEM/EDS elemental microanalysis k-ratio procedure for bulk specimens, step-by-step, in Scanning Electron Microscopy and X-Ray Microanalysis, J.I. Goldstein, et al., Editors. 2018, Springer New York: New York, NY. p. 309-339.
[160] R. Borrajo-Pelaez, P. Hedström, Recent developments of crystallographic analysis methods in the scanning electron microscope for applications in metallurgy. Critical Reviews in Solid State and Materials Sciences, 2018. 43(6): p. 455-474.
[161] S. Zaefferer, N.-N. Elhami, Theory and application of electron channelling contrast imaging under controlled diffraction conditions. Acta Materialia, 2014. 75: p. 20-50.
[162] J. Liu, S. Lozano-Perez, A.J. Wilkinson, C.R.M. Grovenor, On the depth resolution of transmission Kikuchi diffraction (TKD) analysis. Ultramicroscopy, 2019. 205: p. 5-12.
[163] D.R. Steinmetz, S. Zaefferer, Towards ultrahigh resolution EBSD by low accelerating voltage. Materials Science and Technology, 2010. 26(6): p. 640-645.
[164] D. Chen, J.C. Kuo, W.T. Wu, Effect of microscopic parameters on EBSD spatial resolution. Ultramicroscopy, 2011. 111(9-10): p. 1488-94.
[165] P.W. Trimby, Y. Cao, Z. Chen, S. Han, K.J. Hemker, J. Lian, X. Liao, P. Rottmann, S. Samudrala, J. Sun, J.T. Wang, J. Wheeler, J.M. Cairney, Characterizing deformed ultrafine-grained and nanocrystalline materials using transmission Kikuchi diffraction in a scanning electron microscope. Acta Materialia, 2014. 62: p. 69-80.
[166] H. Yuan, E. Brodu, C. Chen, E. Bouzy, J.J. Fundenberger, L.S. Toth, On-axis versus off-axis Transmission Kikuchi Diffraction technique: application to the characterisation of severe plastic deformation-induced ultrafine-grained microstructures. Journal of Microscopy, 2017. 267(1): p. 70-80.
[167] F. Niessen, A. Burrows, A. Fanta, A systematic comparison of on-axis and off-axis transmission Kikuchi diffraction. Ultramicroscopy, 2018. 186: p. 158-170.
[168] R. Prozorov, V.G. Kogan, Effective demagnetizing factors of diamagnetic samples of various shapes. Physical Review Applied, 2018. 10(1).
[169] E. Bartolomé, X. Granados, V. Cambel, J. Fedor, P. Kováč, I. Hušek, Critical

current density analysis of ex situ mgb_2 wire by in-field and temperature hall probe imaging. Superconductor Science and Technology, 2005. 18(8): p. 1135-1140.
[170] C.P. Bean, Magnetization of high-field superconductors. Reviews of Modern Physics, 1964. 36(1): p. 31-39.
[171] D.X. Chen, R.B. Goldfarb, Kim model for magnetization of type-II superconductors. Journal of Applied Physics, 1989. 66(6): p. 2489-2500.
[172] Y.B. Kim, C.F. Hempstead, A.R. Strnad, Magnetization and critical supercurrents. Physical Review, 1963. 129(2): p. 528-535.
[173] F. Hengstberger, M. Eisterer, H.W. Weber, Thickness dependence of the critical current density in superconducting films: A geometrical approach. Applied Physics Letters, 2010. 96(2): p. 022508.
[174] D.X. Chen, A. Sanchez, J.S. Muñoz, Exponential critical-state model for magnetization of hard superconductors. Journal of Applied Physics, 1990. 67(7): p. 3430-3437.
[175] M. Eisterer, M. Zehetmayer, H.W. Weber, Current percolation and anisotropy in polycrystalline MgB_2. Phys Rev Lett, 2003. 90(24): p. 247002.
[176] D.R. Tilley, The Ginsburg-Landau equations for anisotropic alloys. Proceedings of the Physical Society, 1965. 86(2): p. 289-295.
[177] M. Eisterer, Magnetic properties and critical currents of MgB_2. Superconductor Science and Technology, 2007. 20(12): p. R47-R73.
[178] M. Eisterer, C. Krutzler, H.W. Weber, Influence of the upper critical-field anisotropy on the transport properties of polycrystalline MgB_2. Journal of Applied Physics, 2005. 98(3): p. 033906.
[179] A. Malthe-Sorenssen, Percolation and disordered systems - A numerical approach. 2015: Springer.
[180] M.A. Grigoroscuta, V. Sandu, A. Kuncser, I. Pasuk, G. Aldica, T.S. Suzuki, O. Vasylkiv, P. Badica, Superconducting MgB_2 textured bulk obtained by ex situ spark plasma sintering from green compacts processed by slip casting under a 12 T magnetic field. Superconductor Science and Technology, 2019. 32(12).
[181] M.A. Grigoroscuta, G. Aldica, I. Pasuk, M. Burdusel, V. Sandu, A. Kuncser, T.S. Suzuki, O. Vasylkiv, P. Badica, Partially-oriented MgB_2 superconducting bulks with addition of B_4C and cubic BN obtained by slip casting under high magnetic field and spark plasma sintering. Materials Research Bulletin, 2021. 134.
[182] J. Horvat, S. Soltanian, A.V. Pan, X.L. Wang, Superconducting screening on different length scales in high-quality bulk MgB_2 superconductor. Journal of Applied Physics, 2004. 96(8): p. 4342-4351.
[183] J. Horvat, W.K. Yeoh, J.H. Kim, S.X. Dou, Transport and magnetic critical current in superconducting MgB_2 wires. Superconductor Science and Technology, 2008. 21(6).
[184] J. Zou, M.D. Ainslie, H. Fujishiro, A.G. Bhagurkar, T. Naito, N. Hari Babu, J.F. Fagnard, P. Vanderbemden, A. Yamamoto, Numerical modelling and comparison of MgB_2 bulks fabricated by HIP and infiltration growth. Superconductor Science and

Technology, 2015. 28(7).
[185] H. Mochizuki, H. Fujishiro, T. Naito, A.F. Albisetti, G. Giunchi, Trapped field properties of a concentric-circled MgB_2 bulk composite magnetized by pulsed field and field cooling. Superconductor Science and Technology, 2015. 28(10).
[186] H.P. Wiesinger, F.M. Sauerzopf, H.W. Weber, On the calculation of J_c from magnetization measurements on superconductors. Physica C: Superconductivity, 1992. 203(1): p. 121-128.
[187] T.A. Prikhna, M. Eisterer, H.W. Weber, W. Gawalek, V.V. Kovylaev, M.V. Karpets, T.V. Basyuk, V.E. Moshchil, Nanostructural inhomogeneities acting as pinning centers in bulk MgB_2 with low and enhanced grain connectivity. Superconductor Science and Technology, 2014. 27(4).
[188] T.A. Prikhna, W. Gawalek, Y.M. Savchuk, T. Habisreuther, M. Wendt, N.V. Sergienko, V.E. Moshchil, P. Nagorny, C. Schmidt, J. Dellith, U. Dittrich, D. Litzkendorf, V.S. Melnikov, V.B. Sverdun, The inclusions of Mg–B (MgB12?) as potential pinning centres in high-pressure–high-temperature-synthesized or sintered magnesium diboride. Superconductor Science and Technology, 2007. 20(9): p. S257-S263.
[189] Y. Takano, H. Takeya, H. Fujii, H. Kumakura, T. Hatano, K. Togano, H. Kito, H. Ihara, Superconducting properties of MgB_2 bulk materials prepared by high-pressure sintering. Applied Physics Letters, 2001. 78(19): p. 2914-2916.
[190] E. Martínez, P. Mikheenko, M. Martínez-López, A. Millán, A. Bevan, J.S. Abell, Flux pinning force in bulk MgB_2 with variable grain size. Physical Review B, 2007. 75(13): p. 134515.
[191] S. Li, T. White, K. Laursen, T.T. Tan, C.Q. Sun, Z.L. Dong, Y. Li, S.H. Zho, J. Horvat, S.X. Dou, Intense vortex pinning enhanced by semicrystalline defect traps in self-aligned nanostructured MgB_2. Applied Physics Letters, 2003. 83(2): p. 314-316.
[192] A.F. Goncharov, V.V. Struzhkin, Pressure dependence of the Raman spectrum, lattice parameters and superconducting critical temperature of MgB_2: evidence for pressure-driven phonon-assisted electronic topological transition. Physica C: Superconductivity, 2003. 385(1): p. 117-130.
[193] W.H.F. S. I. Schlachter, K. Grube, W. Goldacker, High Pressure Studies of T_c and Lattice Parameters of MgB_2. Preprint, 2001. cond-mat/0107205.
[194] P. Bordet, M. Mezouar, M. Núñez-Regueiro, M. Monteverde, M.D. Núñez-Regueiro, N. Rogado, K.A. Regan, M.A. Hayward, T. He, S.M. Loureiro, R.J. Cava, Absence of a structural transition up to 40 GPa in MgB_2 and the relevance of magnesium nonstoichiometry. Physical Review B, 2001. 64(17): p. 172502.
[195] 2 - Evolution of Dislocation Substructures During Creep, in High Temperature Deformation and Fracture of Materials, J.S. Zhang, Editor. 2010, Woodhead Publishing. p. 14-27.
[196] R.M. German, Coarsening in sintering: Grain shape distribution, grain size distribution, and grain growth kinetics in solid-pore systems. Critical Reviews in Solid

State and Materials Sciences, 2010. 35(4): p. 263-305.
[197] J.C. Maya, F. Chejne, S.K. Bhatia, Novel model for the sintering of ceramics with bimodal pore size distributions: Application to the sintering of lime. AIChE Journal, 2017. 63(3): p. 893-902.
[198] F.F. Lange, Sinterability of agglomerated powders. MRS Proceedings, 1983. 24: p. 247.
[199] P.A. Manohar, M. Ferry, T. Chandra, Five decades of the Zener equation. ISIJ International, 1998. 38(9): p. 913-924.
[200] Z.Z. Fang, H. Wang, Sintering of ultrafine and nanosized particles, in Sintering of Advanced Materials, Z.Z. Fang, Editor. 2010, Woodhead Publishing. p. 434-473.
[201] C.C. Wang, R. Zeng, X. Xu, S.X. Dou, Superconducting transition width under magnetic field in MgB_2 polycrystalline samples. Journal of Applied Physics, 2010. 108(9).
[202] C.P. Bean, Magnetization of hard superconductors. Physical Review Letters, 1962. 8(6): p. 250-253.
[203] M. Takahashi, M. Okada, T. Nakane, H. Kumakura, The influence of magnesium grain size and ball milling time on the phase formation of MgB_2 tapes. Superconductor Science and Technology, 2009. 22(12).
[204] G. Fuchs, W. Häßler, K. Nenkov, J. Scheiter, O. Perner, A. Handstein, T. Kanai, L. Schultz, B. Holzapfel, High trapped fields in bulk MgB_2 prepared by hot-pressing of ball-milled precursor powder. Superconductor Science and Technology, 2013. 26(12): p. 122002.
[205] S. Sugino, A. Yamamoto, J.-i. Shimoyama, K. Kishio, Enhanced trapped field in MgB_2 bulk magnets by tuning grain boundary pinning through milling. Superconductor Science and Technology, 2015. 28(5).
[206] O. Perner, J. Eckert, W. Häßler, C. Fischer, K.H. Müller, G. Fuchs, B. Holzapfel, L. Schultz, Microstructure and impurity dependence in mechanically alloyed nanocrystalline MgB_2 superconductors. Superconductor Science and Technology, 2004. 17(10): p. 1148-1153.
[207] A. Kario, R. Nast, W. Häßler, C. Rodig, C. Mickel, W. Goldacker, B. Holzapfel, L. Schultz, Critical current density enhancement in strongly reactive ex situ MgB_2 bulk and tapes prepared by high energy milling. Superconductor Science and Technology, 2011. 24(7).
[208] H. Fujii, A. Ishitoya, S. Itoh, K. Ozawa, H. Kitaguchi, Improved critical current density in ex situ processed MgB_2 tapes by the size reduction of grains and crystallites by high-energy ball milling. Cryogenics, 2017. 82: p. 15-24.
[209] W. Häßler, J. Scheiter, P. Hädrich, S. Kauffmann-Weiß, B. Holzapfel, M. Oomen, K. Nielsch, Properties of ex-situ MgB_2 bulk samples prepared by uniaxial hot pressing and spark plasma sintering. Physica C: Superconductivity and its Applications, 2018. 551: p. 48-54.
[210] G.A.B. Matthews, Design and characterisation of MgB_2 bulk superconducting

magnets containing Y_2O_3 and Mg additions. DPhil thesis, 2020
[211] A. Yamamoto, J. Shimoyama, S. Ueda, Y. Katsura, I. Iwayama, S. Horii, K. Kishio, Universal relationship between crystallinity and irreversibility field of MgB_2. Applied Physics Letters, 2005. 86(21): p. 212502.
[212] S.J. Ye, A. Matsumoto, Y.C. Zhang, H. Kumakura, Strong enhancement of high-field critical current properties and irreversibility field of MgB_2 superconducting wires by coronene active carbon source addition via the new B powder carbon-coating method. Superconductor Science and Technology, 2014. 27(8).
[213] M.R. Koblischka, A. Wiederhold, A. Koblischka-Veneva, C. Chang, Pinning force scaling analysis of polycrystalline MgB_2. Journal of Superconductivity and Novel Magnetism, 2020. 33(11): p. 3333-3339.
[214] A.M. Ionescu, G. Aldica, S. Popa, M. Enculescu, V. Sandu, I. Pasuk, A. Kuncser, L. Miu, P. Badica, Spark plasma sintered MgB_2 co-added with c-BN and C60. Materials Chemistry and Physics, 2016. 170: p. 201-209.
[215] P. Badica, G. Aldica, M. Burdusel, S. Popa, R.F. Negrea, M. Enculescu, I. Pasuk, L. Miu, Significant enhancement of the critical current density for cubic BN addition into ex situ spark plasma sintered MgB_2. Superconductor Science and Technology, 2014. 27(9).
[216] C.H. Jiang, T. Nakane, H. Kumakura, Enhanced J_c-B performance in MgB_2/Fe tapes with nanometre Si_3N_4 addition. Superconductor Science and Technology, 2005. 18(6): p. 902-906.
[217] S. Li, K. Wang, L. Sun, Z. Wang, A simple model for the refinement of nanocrystalline grain size during ball milling. Scripta Metallurgica et Materialia, 1992. 27(4): p. 437-442.
[218] V. Zamora, A.L. Ortiz, F. Guiberteau, M. Nygren, L.L. Shaw, On the crystallite size refinement of ZrB_2 by high-energy ball-milling in the presence of SiC. Journal of the European Ceramic Society, 2011. 31(13): p. 2407-2414.
[219] Z.K. Liu, D.G. Schlom, Q. Li, X.X. Xi, Thermodynamics of the Mg-B system: Implications for the deposition of MgB_2 thin films. Applied Physics Letters, 2001. 78(23): p. 3678-3680.
[220] J. Karpinski, S.M. Kazakov, J. Jun, M. Angst, R. Puzniak, A. Wisniewski, P. Bordet, Single crystal growth of MgB_2 and thermodynamics of Mg-B-N system at high pressure. Physica C: Superconductivity, 2003. 385(1): p. 42-48.
[221] B.P. Singh, G. Nover, G. Will, High pressure phase transformations of cubic boron nitride from amorphous boron nitride using magnesium boron nitride as the catalyst. Journal of Crystal Growth, 1995. 152(3): p. 143-149.
[222] N.D. Zhigadlo, Crystal growth of hexagonal boron nitride (hBN) from Mg-B-N solvent system under high pressure. Journal of Crystal Growth, 2014. 402: p. 308-311.
[223] Deepika, L.H. Li, A.M. Glushenkov, S.K. Hait, P. Hodgson, Y. Chen, High-efficient production of boron nitride nanosheets via an optimized ball milling process for lubrication in oil. Scientific Reports, 2014. 4(1): p. 7288.

[224] G. Han, X. Zhao, Y. Feng, J. Ma, K. Zhou, Y. Shi, C. Liu, X. Xie, Highly flame-retardant epoxy-based thermal conductive composites with functionalized boron nitride nanosheets exfoliated by one-step ball milling. Chemical Engineering Journal, 2021. 407.
[225] K. Zhang, Y. Feng, F. Wang, Z. Yang, J. Wang, Two dimensional hexagonal boron nitride (2D-hBN): synthesis, properties and applications. Journal of Materials Chemistry C, 2017. 5(46): p. 11992-12022.
[226] W. Li, J. Kang, Y. Liu, M. Zhu, Y. Li, J. Qu, R. Zheng, J. Xu, B. Liu, Extrinsic two-dimensional flux pinning centers in MgB_2 superconductors induced by graphene-coated boron. ACS Appl Mater Interfaces, 2019. 11(11): p. 10818-10828.
[227] N. Izyumskaya, D.O. Demchenko, S. Das, Ü. Özgür, V. Avrutin, H. Morkoç, Recent development of boron nitride towards electronic applications. Advanced Electronic Materials, 2017. 3(5).
[228] C.A. Galán, A.L. Ortiz, F. Guiberteau, L.L. Shaw, High-energy ball milling of ZrB_2 in the presence of graphite. Journal of the American Ceramic Society, 2010. 93(10): p. 3072-3075.
[229] M. Mustapić, K.S.B. De Silva, S.H. Aboutalebi, S. Barua, X. Xu, J. Wang, M.S. Hossain, J. Horvat, S.X. Dou, Improvements in the dispersion of nanosilver in a MgB_2 matrix through a graphene oxide net. The Journal of Physical Chemistry C, 2015. 119(19): p. 10631-10640.
[230] Y. Liu, S. Mateti, C. Li, X. Liu, A.M. Glushenkov, D. Liu, L.H. Li, D. Fabijanic, Y. Chen, Synthesis of composite nanosheets of graphene and boron nitride and their lubrication application in oil. Advanced Engineering Materials, 2018. 20(2): p. 1700488.
[231] P. Tang, V.M. Puri, Methods for minimizing segregation: A review. Particulate Science and Technology, 2004. 22(4): p. 321-337.
[232] K.S.B. De Silva, X. Xu, S. Gambhir, X.L. Wang, W.X. Li, G.G. Wallace, S.X. Dou, Flux pinning mechanisms in graphene-doped MgB_2 superconductors. Scripta Materialia, 2011. 65(7): p. 634-637.
[233] Z. Ma, Y. Liu, Y. Han, Q. Zhao, Z. Gao, Variation of the enhancement mechanism in the critical current density of Cu-doped MgB_2 samples sintered at different temperatures. Journal of Applied Physics, 2008. 104(6).
[234] Z. Ma, Y. Liu, Q. Shi, Q. Zhao, Z. Gao, The improved superconductive properties of MgB_2 bulks with minor Cu addition through reducing the MgO impurity. Physica C: Superconductivity, 2008. 468(22): p. 2250-2253.
[235] J.C. Grivel, A. Abrahamsen, J. Bednarčík, Effects of Cu or Ag additions on the kinetics of MgB_2 phase formation in Fe-sheathed wires. Superconductor Science and Technology, 2008. 21(3).
[236] S.B. Güner, B. Savaşkan, K. Öztürk, Ş. Çelik, C. Aksoy, F. Karaboğa, E.T. Koparan, E. Yanmaz, Investigation on superconducting and magnetic levitation force behaviour of excess Mg doped-bulk MgB_2 superconductors. Cryogenics, 2019. 101: p. 131-136.

[237] R. Zeng, L. Lu, J.L. Wang, J. Horvat, W.X. Li, D.Q. Shi, S.X. Dou, M. Tomsic, M. Rindfleisch, Significant improvement in the critical current density of in situ MgB_2 by excess Mg addition. Superconductor Science and Technology, 2007. 20(8): p. L43-L47.
[238] M. Jirsa, M. Rameš, M. Miryala, P. Svora, J. Duchoň, O. Molnárová, S.S. Arvapalli, M. Murakami, Flux pinning and microstructure of a bulk MgB_2 doped with diverse additives. Superconductor Science and Technology, 2020. 33(9).
[239] G. Aldica, S. Popa, M. Enculescu, P. Badica, Te and SiC co-doped MgB_2 obtained by an ex situ spark plasma sintering technique. Scripta Materialia, 2013. 68(6): p. 428-431.
[240] Z. Ma, Y. Liu, L. Yu, Q. Zhao, The accelerated formation of MgB_2 phase with high critical current density by Cu and SiC multidoping during the low-temperature sintering process. Journal of Applied Physics, 2008. 104(11).
[241] K.P. Gupta, The Cu-Mg-Ni (Copper-Magnesium-Nickel) System. Journal of Phase Equilibria and Diffusion, 2004. 25: p. 471-478.